UNIVERSITY OF CALIFORNIA
IRVINE

A Study of Ultra High Energy Radiation Associated with Hercules X-1

DISSERTATION

Submitted in partial satisfaction of the requirements for the degree of

DOCTOR OF PHILOSOPHY

in Physics

by

Steven Douglas Biller

Dissertation Committee:

Professor Gaurang B. Yodh, Chair
Professor Frederick Reines
Professor Henry W. Sobel
Professor Jonas Schultz

1992

The dissertation of Steven Douglas Biller is approved,
and is acceptable in quality and form
for publication on microfilm:

Committee Chair

University of California, Irvine

1992

DISCLAIMER

Portions of this document may be illegible in electronic image products. Images are produced from the best available original document.

DEDICATION

In memory of my first advisor,
Herbert H. Chen: an exceptional
physicist and mentor whose
invaluable lessons continue to
influence me.

And to my current advisor,
Gaurang B. Yodh, for his
incomparable generosity,
encouragement and enthusiasm.

Table of Contents

List of Figures

List of Tables

Acknowledgments

I would like to thank my advisor, Gaurang Yodh, and all the members of the CYGNUS collaboration for providing me with such an excellent working environment. Special thanks goes to Cyrus "Skids" Hoffman, Mike "Mikey" Potter, Todd "Doogie" Haines, Gus "Boots" Sinnis and Jordan "&*%#@!!" Goodman.

Thanks also to Dave Williams, Weiping Zhang, Dan Weeks, Darragh Nagle and, of course, to Scott Delay for keeping the experiment running smoothly and for giving me directions to the electronics trailor. I would also like to thank all of the other graduate students on CYGNUS, especially Dimitris Alexandreas for letting me know when he was driving so that I could stay safely off the road. I have also benefitted greatly from the all too brief interactions I have had with visiting "Cygnoids" Jeremy Lloyd-Evans and P. R. Vishwanath. One of my major ambitions is to one day be able to pronounce all of Vish's name.

I would also like to take this opportunity to thank those who have played a key role in getting me to this stage, starting with high school teachers Mark Waldman and Shirley Citron; my college roommate and long time friend Dave Chasson; Dave Newman and Larry Sulak who hired me as a "know-nothing" undergraduate at the University of Michigan to work part-time on their experiments, giving me my first real taste of physics outside of the classroom. A special thanks to the UCI Liquid Argon TPC crew of Peter Doe, Gerhard Bühler, Dick Allen, and Wayne Johnson. This group was directed by my first advisor, Herb Chen, to whom I owe a tremendous debt of gratitude for teaching me how to do physics by his example. Herb passed away in 1987 after a struggle with leukemia, but his memory is still with me. A very special thanks also goes to my fellow classmates at Irvine, whose

comradeship contributed to my education there more than any other single factor: Steve Riley, Siamak Katal (wherever you are!), Lynn McCarty, Pete Nelson, and Jim Means.

Los Alamos has been one of the most comfortable places that I have ever been privilaged to live. The close community, spectacular scenery of northern New Mexico, and the friends that I have made here have been responsible for this (did I mention that the ski hill is only 10 minutes from the town?). For making me feel welcome, I would like to thank Cy and Jane Hoffman for allowing me to be "the son they never wanted," and a very special thanks goes to Kate and the rest of the Blewett clan for letting me feel like a part of their family.

Finally, this would not have been possibly without the support of my parents, Ken and Marilyn Biller (without whom I would not have been possible), and my sister Lisa, who put up with me while I was growing up. Thanks!

Financial support was provided by the United States Department of Energy and the National Science Foundation.

Steven Douglas Biller

Department of Physics
University of California, Irvine
Irvine, CA 92717

PERSONAL

Date of Birth:	[redacted]
Place of Birth:	[redacted]
Current Home Address:	3980 B Sandia Drive, Los Alamos, NM 87544
Mailing Address:	MS H831, LANL, Los Alamos, NM 87545
Home Phone:	(505) 662-0455
Work Phone:	(505) 665-2358
Bitnet Address:	BILLER@LAMPF

EDUCATION

Sept., 1992	Ph.D., Physics , University of California, Irvine
Oct., 1986	Master of Science, Physics, University of California, Irvine
June, 1984	Bachelor of Science (with Honors), Physics University of Michigan
June, 1980	graduated Oak Park High School, Oak Park, Michigan

EMPLOYMENT

June, 1986 - Present	Research Assistant, Department of Physics, University of California, Irvine
Sept., 1984 - June, 1986	Teaching Assistant, Department of Physics, University of California, Irvine
June, 1982 - Aug., 1984	Undergraduate Research Assistant, Department of Physics, University of Michigan

Field of Ph.D. Research: Particle Astrophysics
Topic: *A Study of Ultra High Energy Radiation Associated with Hercules X-1*
Advisor: Gaurang B. Yodh

JOURNAL PUBLICATIONS

- "A Large Scale Purification System for a Liquid Argon Time Projection Chamber," P.J. Doe *et al.*, Nuc. Inst. and Meth. in Physics Research, **A258**:170-176 (1987).
- "Statistics of Charge Collection in Liquid Argon and Liquid Xenon," J. Thomas, D.A. Imel, and S. Biller, Phys. Rev. A **38**:5793-5800 (1988).
- "Effects of Oxygen and Nitrogen on Drifting Electrons in a Liquid Argon TPC," S.D. Biller *et al.*, Nuc. Inst. and Meth. in Physics Research, **A276**:144-150 (1989).
- "A Study of Cygnus X-3 at Ultra High Energies During the 1989 Radio Outbursts," D.E. Alexandreas *et al.*, Phys. Rev. Lett. **64**, 2973(1990).
- "Observation of Shadowing of Ultra High Energy Cosmic Rays by the Moon and the Sun," D.E. Alexandreas *et al.*, Phys. Rev. D **43**, 1735(1991).
- "Phase Coherence for TeV/PeV Binary Sources," D.A. Lewis, R.C. Lamb, and S.D. Biller, Astrophysical Journal, **369**: 479-484 (1991).
- "The CYGNUS Extensive Air-Shower Experiment," D.E. Alexandreas *et al.*, Nucl. Inst. and Meth. in Physics Research, **A113**, 350 (1992).
- "A Search of the Northern Sky for Ultra High Energy Point Sources," D.E. Alexandreas *et al.*, Astrophysical Journal Letters, **383**, L53 (1991)
- "A Daily Search for Ultra High Energy Radiation from Point Sources," D.E. Alexandreas *et al.*, accepted by Astrophysical Journal
- "Point Source Search Techniques in Ultra High Energy Gamma Ray Astronomy," D.E. Alexandreas *et al.*, submitted to Nucl. Instr. and Meth.

CONFERENCE PRESENTATIONS AND PROCEEDINGS

(principal author)

- "A Large Scale Purification System for a Liquid Argon TPC," Proc. of the 1st International UCLA Workshop on High Resolution Liquid Drift Chambers", University of California, Los Angeles (1987).
- "The UCI Liquid Argon TPC Program," Proc. of the 13th Int'l. Conf. on Neutrino Physics and Astrophysics, J. Schnepps and T. Kafka, eds., Boston, (June, 1988).

- "Relative Muon Content of UHE Showers Associated with Hercules X-1," Proc. of the XXI Int'l. Cosmic Ray Conf., OG 4.2.8, Adelaide, (Jan., 1990).
- "The Showerfront Time-Structure of "Anomalous Muon" Events Associated with Hercules X-1," Proc. of the Int'l. Conf. on High Energy Gamma-Ray Astronomy, Ann Arbor, p.154 (Oct., 1990).
- "Detailed Simulation of the CYGNUS Array's Response to Extensive Air-Showers," Proc. of the XXII Int'l. Cosmic Ray Conf., HE 3.6.29, Dublin, (Aug., 1991).
- "Characteristics of "Anomalous Muon" Events Associated with Hercules X-1," Proc. of the XXII Int'l. Cosmic Ray Conf., OG 4.2.10, Dublin, (Aug., 1991).
- "Differences Between Gamma-Ray and Proton Induced Air-Showers in the Range 1-100 TeV," Proc. of the XXII Int'l. Cosmic Ray Conf., OG 4.7.18, Dublin, (Aug., 1991).

CONFERENCE PROCEEDINGS (contributing author)

Int'l Workshop on the Physics and Experimental Techniques of High Energy Neutrino and VHE and UHE Gamma-Ray Particle Astrophysics, Arkansas, 1989

- "The Status of the CYGNUS Experiment: Past, Present, and Future," T.J. Haines *et al.*, p.244

Meeting of Amer. Phys. Soc. Division of Particles and Fields

- "Astronomy at Ultra High Energies: Results from the CYGNUS Experiment," T.J. Haines *et al.*, 1990
- "Search for Emission of Ultra High Energy Gamma Rays from Point Sources with the CYGNUS Experiment," D.E. Alexandreas *et al.*, 1991

XXI Int'l. Cosmic Ray Conference, Adelaide, Australia, 1990

- "Observations from the CYGNUS Experiment of Cygnus X-3 During the 1989 Radio Burst," T.J. Haines *et al.*, OG 4.1.6
- "Search for Emission of UHE Gamma Rays from the Crab Nebula," D. Berley *et al.*, OG 4.3.9
- "Search for Signals from X-Ray Binaries from the CYGNUS Experiment at Los Alamos," D. Berley *et al.*, OG 4.6.9
- "Search for Diffuse Galactic Emission Anisotropies, and "Unknown" Sources with the CYGNUS Experiment," D. Berley *et al.*, OG 4.7.2
- "A Low Threshold EAS Array for Gamma-Ray Astronomy at Los Alamos," R.L. Burman *et al.*, HE 7.3.11
- "Status of the Expansion of the CYGNUS Array at Los Alamos," D. Berley *et al.*, HE 7.3.12

Int'l. Conf. on High Energy Gamma-Ray Astronomy, Ann Arbor, 1990

- "Recent Data from the CYGNUS Experiment," D.E. Alexandreas *et al.*, p.99
- "UHE Point Source Survey at CYGNUS Experiment," X-Q. Lu *et al.*, p.105
- "A Search for UHE Cosmic Rays from the Crab Pulsar/Nebula," D.E. Alexandreas *et al.*, p.150
- "Search for UHE Emission from 4U0115+63," D.E. Alexandreas *et al.*, p.167

XXII Int'l. Cosmic Ray Conference, Dublin, Ireland, 1991

- "Search for UHE Emission from the Crab Region with the CYGNUS Array," D.E. Alexandreas *et al.*, OG 4.1.8
- "Search for a Daily Excess of Ultra High Energy Air-Showers from Point Sources with the CYGNUS Experiment," D.E. Alexandreas *et al.*, OG 4.3.18
- "Search for UHE Emission 4U0115+63 with the CYGNUS Array," D.E. Alexandreas *et al.*, OG 4.4.11
- "Search for Steady Emission from 41 UHE Sources with the CYGNUS Array," D.E. Alexandreas *et al.*, OG 4.6.4
- "Angular Resolution of the CYGNUS EAS Array from the Shadows of the Moon and Sun," D.E. Alexandreas *et al.*, OG 10.4.4
- "Studies on Improving the Angular Resolution of the CYGNUS Array," D.E. Alexandreas *et al.*, OG 10.4.5

REFERENCES

Prof. Gaurang B. Yodh
Department of Physics
University of California, Irvine
Irvine, CA 92717
(714)856-6975

Dr. Cyrus M. Hoffman
MP-4 Division, MS H846
Los Alamos National Laboratory
Los Alamos, NM 87545
(505)667-5876

Prof. Jordan A. Goodman
Department of Physics and Astronomy
University of Maryland
College Park, MD 20742
(301)454-5312

Dr. Todd Haines
Department of Physics and Astronomy
University of Maryland
Currently: Los Alamos National Laboratory, MS H831
Los Alamos, NM 87545
(505)667-3638

ABSTRACT OF THE DISSERTATION

A Study of Ultra High Energy Radiation Associated with Hercules X-1

by

Steven Douglas Biller

Doctor of Philosophy in Physics
University of California, Irvine, 1992
Professor Gaurang B. Yodh, Chair

Data from the CYGNUS experiment has been used to examine ultra high energy (UHE) radiation associated with the X-ray binary star system Hercules X-1. A search for both pulsed, and unpulsed emission over time scales ranging from minutes to years has failed to yield a result of comparable significance to that of the previously published observation of July 24, 1986. A reassessment of this result in light of the number of hypotheses that have been examined for Hercules X-1 yields a probability estimate of 0.44% that the data is consistent with background fluctuations. If the number of independent source hypotheses is also accounted for, an overall chance probability of 1.8% is assessed for the observations of the CYGNUS experiment.

The extensive air showers corresponding to the episode of July 24, 1986 contain a substantial muon content, in contradiction with traditional predictions for primary gamma-rays. No satisfactory theory has yet been put forward to explain this phenomenon. A further analysis of shower characteristics for events associated with this episode indicates a steeper radial dependence of the showerfront timing width at a chance probability level of 0.16%. This property might be explained by a model that invokes a forward-peaked and/or a deeply interacting component of the hadronic interaction in the atmosphere.

The potential importance of UHE observations of Hercules X-1 is great, however the evidence is not yet compelling. Further observations will be necessary to confirm the potential properties of associated UHE radiation.

Chapter 1

Introduction

"...Alice had not a moment to think about stopping herself before she found herself falling down what seemed to be a very deep well."
- Lewis Carroll -

Extensive Air-Showers

Since its discovery in the 1920's, cosmic radiation has been detected up to energies as high as 10^{20}eV. The fields of Very High Energy (VHE) and Ultra High Energy (UHE) astronomy are primarily concerned with searching for localized astrophysical emissions in the energy regimes of $\sim 10^{12}$eV and $\geq 10^{14}$eV, respectively. The origin and nature of the accelerating mechanisms that produce such particles are largely unknown. Most of these higher energy particles are believed to consist of protons and heavier elements. Due to the presence of interstellar magnetic fields, directions of charged particles will be significantly altered before reaching the earth. Therefore, in order to study "point-sources" of cosmic rays, the primary particle must be neutral, stable enough to reach earth without decaying, and preferably of low mass in order to preserve phase-coherence of any periodicities associated with the source of acceleration. High energy photons are therefore favored as a candidate primary particle for point-source studies.

The relatively low flux of particles at these energies require large-area detectors, making satellite or balloon-based experiments impractical. On the other

hand, earth-based experiments are unable to directly detect the primary particle since it would have to penetrate more than 26 radiation lengths of atmosphere without interacting in order to reach sea level. Therefore, indirect measurements are relied upon to provide information about the primary particle and the properties of its interaction. This is done by detecting the numerous secondary particles that are produced as the primary energy is dissipated through the atmosphere by successive interactions (figure 1.1). For a hadronic primary, this secondary particle *cascade*, or *extensive air-shower* (EAS), is initiated by a nuclear interaction that produces a large number of hadrons and pions. Many of the charged pions decay to produce muons, most of which penetrate directly to ground level. Neutral pions decay into photons, which then initiate electromagnetic cascades. These cascades typically reach maximum development at an altitude of about 7 kilometers. Multiple scattering tends to laterally disperse the electrons and photons, whereas the heavier and more energetic secondaries remain somewhat more concentrated near the central *core* of the shower. If the primary particle is a photon, shower development proceeds almost entirely through electromagnetic cascades, with only occasional photoproduction of heavier particles.

One experimental technique that is widely used in the VHE regime is to detect the Cherenkov light radiated by the charged particles in the EAS as they propagate through the air. This typically involves tracking potential sources with large, focussing mirrors with sensitive photomultiplier tubes (PMTs) to detect the light. Detectors of this kind can only operate on cloudless, moonless nights due to their sensitivity to ambient light, and therefore have a relatively low duty cycle. In addition, only one source can be studied at any given time.

In the UHE regime, a technique typically used is that of the *extensive air-shower array,* which employs a large number of detectors (usually scintillation counters) to directly sample properties of the secondary particles that reach ground-level. The direction of the primary particle is inferred from the arrival-times of the secondaries in the shower front (figure 1.2). By also sampling the fraction of "penetrating" secondaries (using shielded detectors), the muon content can be inferred and used to yield information about the hadronic nature of the primary

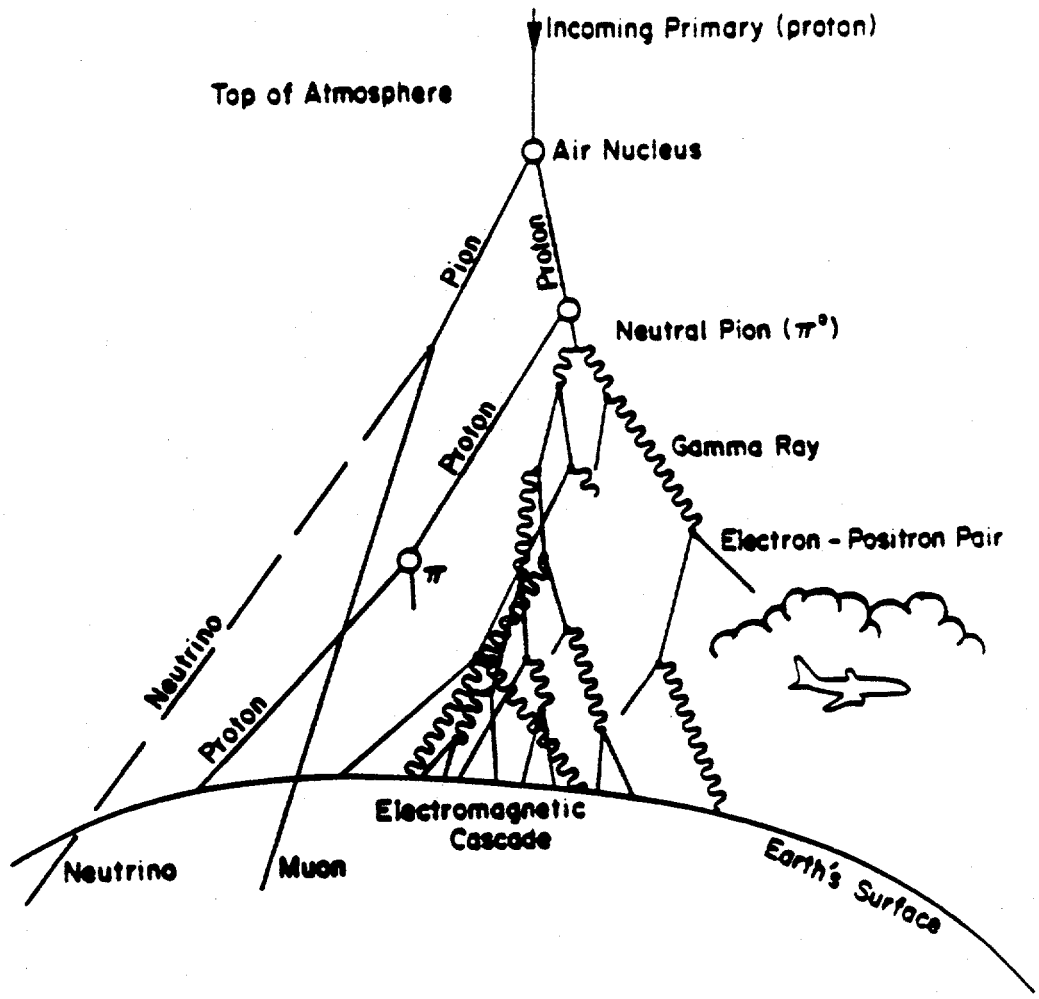

Figure 1.1: Illustration of EAS produced by a primary proton.

interaction. This technique has the advantages of being insensitive to ambient light (thus allowing a 100% duty cycle), and is able to study a large portion of the visible sky at once. The disadvantage is a higher primary energy threshold that is needed to produce a large number of secondary particles that can reach the detector level before the full energy of the shower is dissipated.

The Muon Anomaly

The Kiel group reported the observation of continuous, UHE emission from the X-ray binary Cygnus X-3 during the period of 1978 to 1982 [1]. This emission was modulated at the known orbital frequency of the star system. Using neon flash-tubes shielded beneath a concrete bunker, a substantial muon content was inferred for those events associated with the source. This observed muon content is inconsistent with traditional theories of gamma-ray interactions, as previously described. On the other hand, constraints on the mass, charge, cross-section, and particle lifetime that are necessary to make such a source detection possible (see chapter 9), make it extremely difficult to find alternative particle candidates within the Standard Model to be able to satisfactorily explain the observation.

This source detection was confirmed by the Leeds group, which used a subset of their larger array at Haverah Park to probe the same energy region as the Kiel experiment ($\sim 10^{15}$eV) during the years 1980-1982 [2]. While indicating a somewhat lower flux than that quoted by Kiel, the observation appeared to confirm emission at the same phase of the orbital period. Unfortunately, this array was not able to measure the muon content of these showers.

In 1986, the CYGNUS experiment (named for the source it had hoped to detect), observed short-term ($\sim$ less than 1 "source-day") emission from a similar X-ray binary system, Hercules X-1 [3]. This observation consisted of a substantial excess of events from the direction of Hercules X-1. These events were mainly concentrated in shorter duration "bursts" that occured throughout the source transit, and exhibited a periodicity close to the known frequency of the X-ray pulsar. An anomalously large muon content compared with that expected for a primary gamma-

ray interaction was again indicated. Emission from this object was also detected by the air-Cherenkov telescopes of the Whipple [4] and Haleakala [5] collaborations, in the 2 months prior to the CYGNUS claim. The same pulsed frequency was observed in all three cases, which was slightly shifted from the known frequency of the X-ray pulsar (figure 1.3). This shift is not well understood, but may indicate something about the nature of the acceleration and/or production mechanisms. The air-Cherenkov instruments were incapable of direct muon content measurements. However, the Whipple telescope was capable of giving additional information about the distribution of Cherenkov light that could be used to discriminate gamma-ray interactions from hadronic showers. Use of this technique has allowed the group to make a very compelling observation of VHE gamma-ray emission from the Crab nebula [7] and, more recently, from the active galactic nucleus Markarian 421 [8]. However, when this same technique was applied to the observation of Hercules X-1, the associated Cherenkov images were found *not* to be indicative of gamma-ray primaries. The Whipple collaboration has also reported possible evidence for a number of additional episodes of pulsed emission from Her X-1 occurring throughout the time period 1984-1987 [9]. The air-showers associated with these observations were also found to produce Cherenkov images not indicative of primary gamma-rays.

In recent years, there have been few (if any) convincing observations of these binary sources in the VHE/UHE regime. Therefore, if the previous claims are correct, emission from Hercules X-1 and Cygnus X-3 must be of a highly sporadic nature. In the case of Cygnus X-3, the current failure to observe the flux previously reported by Kiel has lead some to the belief that the source has turned off, and has lead others to skepticism. However, extreme variability of this source at lower energies is well known, and it should be emphasized that the only experiment (Haverah Park) that actually overlapped in time with the Kiel detection, confirmed it. Similarly, despite the recent lack of evidence for further emission from Hercules X-1, the previous observations have remained difficult to explain.

Structure of Forthcoming Chapters

The remainder of the thesis will begin with a discussion of compact binary systems and possible mechanisms capable of producing VHE/UHE emission. This will be followed by a summary of knowledge regarding the Her X-1 system based on X-ray, optical and infra-red observations. A brief description of the CYGNUS air-shower array in Los Alamos will then be given. A detailed discussion of statistical issues related to the analysis of VHE/UHE data will then be presented through a re-analysis of the 1986 Her X-1 observation. This will be followed by a further analysis of the 1986 episode in an attempt to discern any properties of the air showers associated with Her X-1 that might distinguish them from typical background events. In an effort to confirm the observation of UHE emission, a systematic search for additional episodes of emission from Her X-1, with timescales ranging from minutes to years, will be described. Equipped with the knowledge gained from the discussion of statistical issues in chapter 4, a critical evaluation of previous claims of VHE/UHE emission from Her X-1 will then be given. Proposed models related to the nature of claimed emission will next be discussed in light of the experimental results previously presented. Finally, the results of the previous analyses will be placed in context, the major conclusions of the thesis will be summarized, and speculation on possible future directions will be presented.

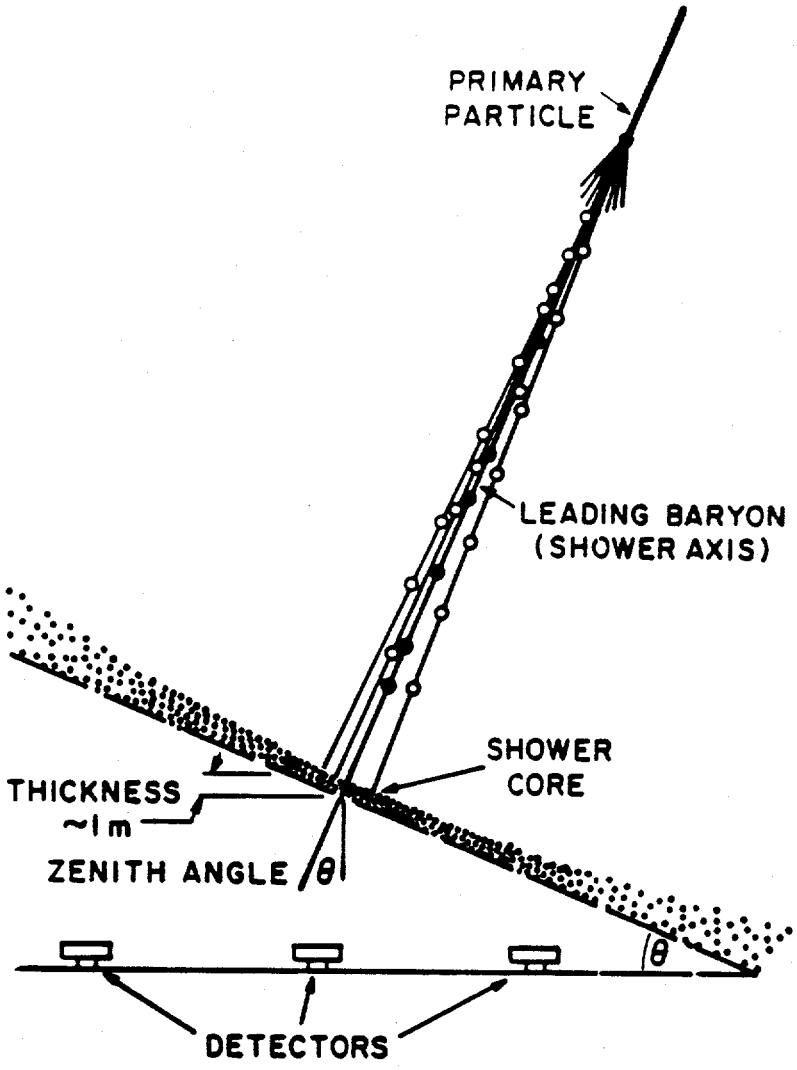

Figure 1.2: Illustration of EAS showerfront

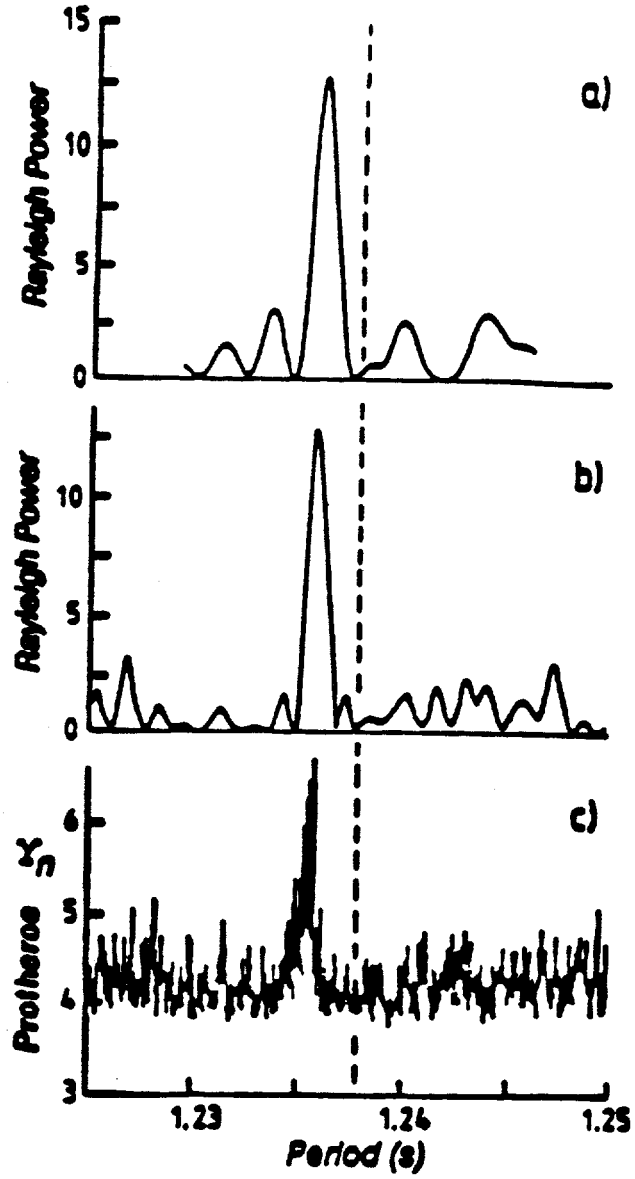

Figure 1.3: Period scans for **a)** the Haleakala observation on May 13, 1986 [5], **b)** the Whipple observation on June 11, 1986 [4], and **c)** the CYGNUS observation on July 23, 1986. The parameter on the ordinate is related to the significance for phase-alignment (see Appendix D). The X-ray pulsar **period** is indicated by the dashed line. (Figure from reference [6])

Chapter 2

Acceleration in Compact Binary Systems

"I am astounded by people who want to 'know' the universe when it's hard enough to find your way around Chinatown."

- Woody Allen -

Evolution of Compact Objects

For stars with masses $M > 1.5M_{\odot}$, the last stages of stellar evolution quickly ensue after hydrogen has been depleted from the convective core of the star, causing it to move off the *main sequence* of development. Without the radiation pressure from the energy released by hydrogen burning to balance the gravitational force, the core collapses until a shell of hydrogen around the core reaches temperatures that are high enough for *hydrogen-shell burning.* If the star is sufficiently massive, this stage will be followed by further core collapse until helium burning is initiated, followed by carbon burning,...etc., until iron is reached. Since iron possesses the largest binding energy per nucleon of all the stable elements, lower energy states cannot be reached through further transmutation of elements beyond this point. For stars with an initial mass $M > 4M_{\odot}$, the energy released in this process is large enough to eject the outer layers of the star, resulting in a *supernova.* If the final mass of the star is approximately within the range $0.9M_{\odot} < M_f < 1.24M_{\odot}$,

further collapse may proceed until the electrons within the star are in their lowest energy state. At this point, the gravitational force is supported by *electron degeneracy pressure*, and the final state is called a *white dwarf*. For larger mass stars, $1.24M_\odot < M_f < 2.5M_\odot$, further collapse will produce a *neutron star*, supported by neutron degeneracy pressure. For stars with $M_f > 2.5M_\odot$, gravitational forces will overcome all degeneracy pressures and collapse will proceed indefinitely to produce a *black hole*.

The three final states just described comprise the catagory known as *compact objects*. Double star, or *binary* systems involving at least one compact object are therefore called *compact binaries* (figure 2.1). Hercules X-1 is believed to be a compact binary system, involving a $\sim 2M_\odot$ main-sequence star in orbit with a $\sim 1.3M_\odot$ neutron star. In order to understand the possible acceleration mechanisms capable of producing VHE/UHE cosmic rays that may be at work in such a system, first it is necessary to understand the environment within the vicinity of the neutron star.

Environment of Neutron Stars

Neutron stars have typical radii of ~10km, spin periods ranging from 0.01 to several seconds, and surface magnetic fields of $\sim 10^{12}$Gauss. These rapidly-spinning fields can, in principle, induce a potential of $\sim 10^{18}$ volts [10]. However, Goldreich and Julian [11] have shown that the induced electric field is strong enough to remove electrons, and possibly ions, from the stellar surface so as to create a charge-separated plasma, or *magnetosphere* in the vicinity of the neutron star (figure 2.2). This plasma tends to neutralize much of the potential drop. In a plasma of infinite conductivity, magnetic field lines tend to be tied to charged particles. Beyond the radius $r_l = \frac{c}{\Omega}$, where c is the speed of light and Ω is the rotation frequency of the neutron star, these magnetic field lines can therefore no longer corotate with the neutron star. This radius defines the *light cylinder*. In addition, charged particles can only escape along open field lines. Such field lines emanate from the "polar cap" region of the star. If the magnetic field of the neutron star is misaligned with

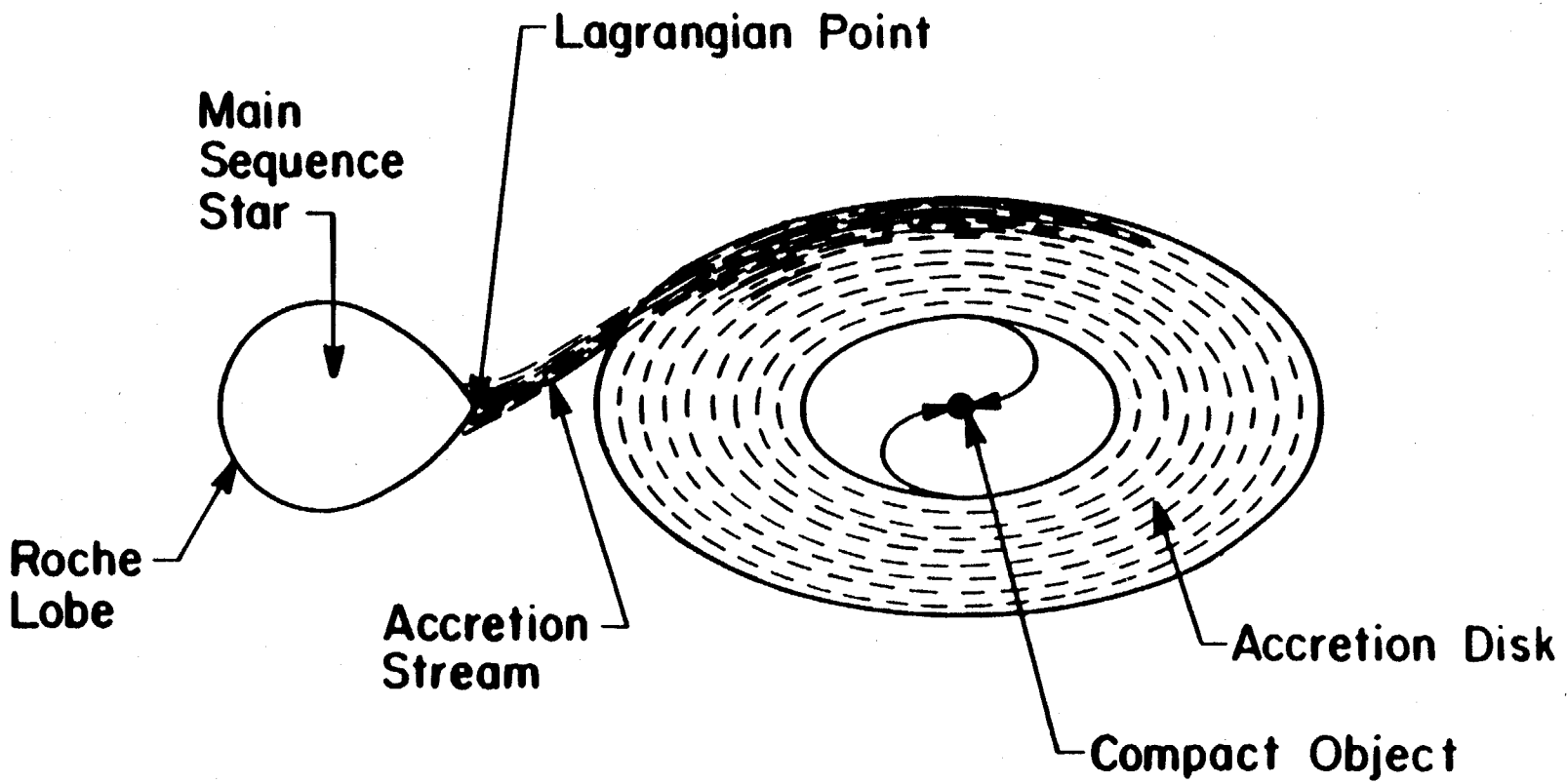

Figure 2.1: Illustration of an accreting compact binary system [63].

the axis of rotation, energetic emission from the polar regions may regularly sweep through an observer's line of sight, producing apparent pulsations. Such objects are known as *pulsars*.

If isotropic emission is assumed, an upper limit to the star's luminosity can be calculated by equating the inward gravitational force (acting mainly on protons) with the outward radiation pressure (acting mainly on electrons). Due to electrostatic attraction, interactions of protons and electrons are coupled. The resulting quantity is the *Eddington Luminosity*, and has a value of $\sim 10^{38}$ergs/sec.

In a binary system, matter may be transferred to the neutron star from the companion either by stellar wind or by Roche lobe overflow. The latter case occurs when the radius of the companion is large enough that matter can flow directly through the first Lagrange point to the neutron star. The angular momentum imparted to matter during Roche lobe transfer and the viscous stress on accreting matter results in the formation of an *accretion disk* of material that gradually spirals in to the neutron star. A description of accretion disk dynamics was first attempted by Shakura and Sunyaev [12], and later by Ghosh and Lamb [13], who included the effects of magnetic coupling with the neutron star (figure 2.3). The Alfven radius, r_A, defines the distance from the star within which the motion of accreting matter is dominated by the magnetic field. Accretion cannot occur if $r_l < r_A$, which constrains accreting pulsars to have periods greater than about 31ms. A boundary layer at $\sim 0.41 r_A$ defines where plasma leaves the plane of the disk and is funneled towards the poles of the neutron star. Beyond the Alfven radius is an outer transition region where motion is essentially Keplarian, but magnetic coupling is still important. Beyond the transition region, the magnetic field is completely screened from the disk and flow is unperturbed.

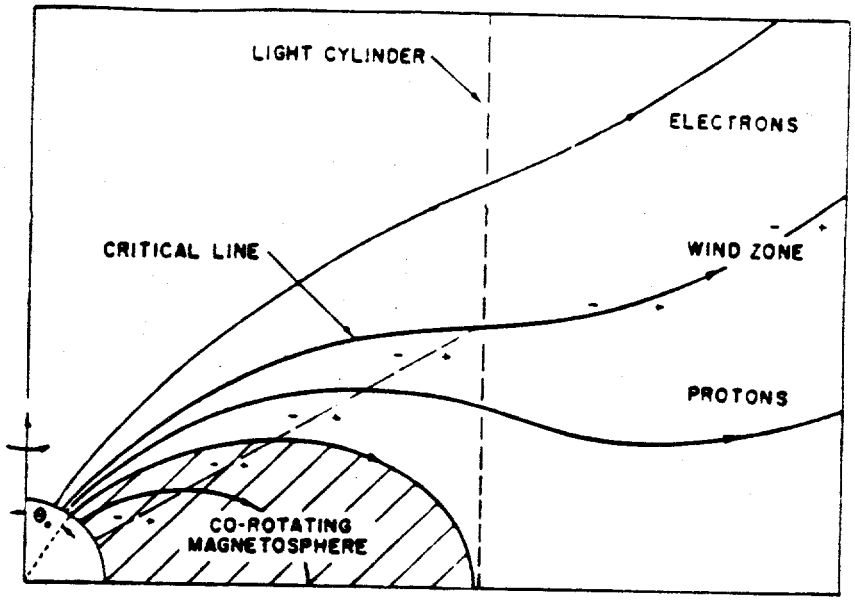

Figure 2.2: Schematic diagram showing the corotating magnetosphere. Star is at lower left [11].

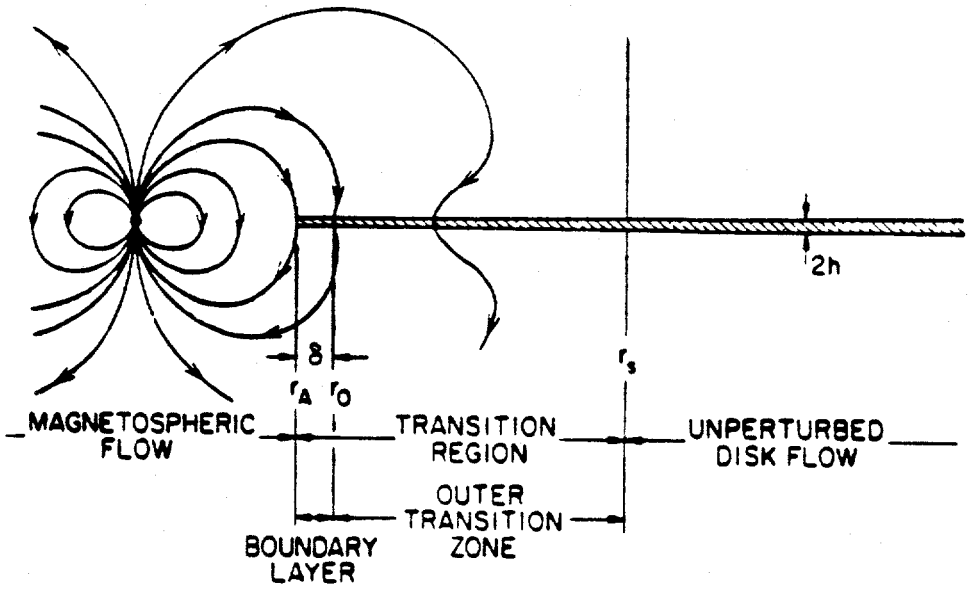

Figure 2.3: Schematic picture of neutron star and accretion disk [13].

Acceleration Mechanisms

The two principle mechanisms that have been suggested to explain VHE/UHE emission from compact objects are acceleration by induced electric fields, or "Dynamo," and first-order Fermi, or "Shock" acceleration. In addition to these, stochastic acceleration (second-order Fermi mechanism) and magnetic reconnection models have also been proposed. A summary of these models is given in table 2.1, taken from Harding, 1990 [14].

Dynamo

Acceleration along open field lines from the potential difference between the pole and the edge of the cap can, in principle, produce particle energies of $\sim 10^{13}$eV. However, acceleration by induced electric fields must take place in regions of relatively low plasma density since, as previously mentioned, charged plasma tends to neutralize differences in potential. Consequently, acceleration along open field lines must take place far outside the light cylinder of the star, making coherent pulsation impossible. Thus, only unpulsed emission is predicted in this scenario.

Sturrock [15], and later Ruderman and Sutherland [16] considered the possibility of acceleration if a gap were to form between the neutron star and magnetosphere near the pole. The height of such a gap is limited to about 1 meter by e^+-e^- pair-creation within the gap from photons interacting with the radiation field. In fact, due to the strength of the magnetic field near the neutron star surface, the radiation field tends to degrade photon energies so as to make high-energy photon production impossible. In order to avoid such difficulties, Cheng, Ho and Ruderman [17] proposed an "outer gap" model, in which a stable gap is assumed to have formed in the outer magnetosphere along the last closed field line. The available potential (again limited by γ-γ interactions) has been estimated to be capable of accelerating protons and nuclei up to $\sim 10^{14}$eV, and electrons up to $\sim 10^{13}$eV (limited by synchrotron and inverse Compton losses).

POWER SOURCE	ACCELERATION MECHANISM			
	Dynamo	Shock	Reconnection	Plasma Turbulence
	$E_p^{max} \simeq e \frac{v \times B}{c} R$	$E_p^{max} \simeq e \frac{v_1}{c} B R$,	$E_p^{max} < e \frac{v_A}{c} B R$	$E_p^{max} \simeq e B R$
Pulsar Rotation $L < 10^{43}$ erg/s	$< 10^{14}$ eV	$< 10^{18}$ eV		
Accretion $L_{NS} < 10^{38}$ erg/s	$< 10^{16}$ eV	$< 10^{16}$ eV	$< 10^{14}$ eV	$< 10^{16}$ eV

Table 2.1: Acceleration models for UHE gamma-ray sources [14].

For a perfectly conducting disk threaded by magnetic field lines, differential rotation between the inner and outer edges will induce large electric fields. Originally proposed by Lovelace [18] and Blandford [19] in relation to massive black holes believed to comprise active galactic nuclei (AGN's), the concept of the *unipolar inductor* was extended to neutron stars by Chanmugam and Brecher [20]. In principle, a maximum potental drop of $\sim 10^{17}$eV is available for acceleration. Since plasma will tend to "short-out" these electric fields, acceleration may only take place just above the disk if plasma is deficient there. However, the tendancy for plasma to be pulled from the disk is not clear. Ruderman *et al.* [21] have proposed applying the unipolar inductor model to the transition region between magnetospheric corotation and Keplarian velocities. The available potential maximizes at $\sim 10^{16}$eV when r_A is at the surface of the neutron star. Therefore, the model works only for stars with relatively low magnetic fields.

Shock

First-order Fermi acceleration operates by imparting energy from converging shock fronts to charged particles via progressive magnetic scatterings across the shock boundary [22]. Eichler and Vestrand [23] have proposed that radiation pressure from the neutron star may result in the formation of a collisionless shock front in the accretion column above the polar regions of the star. Shock acceleration, limited by synchrotron loss in the strong magnetic field, might thus accelerate protons to energies as high as $\sim 10^{16}$eV. Kiraly and Meszaros [24] have proposed a similar mechanism in which the formation of the shock occurs further from the star, at a radius of $\sim r_A$ above the pole (see figure 2.4). Since this radiation is "beamed" from the polar regions, it will be modulated by the pulsar frequency. In the case of accretion by stellar wind, Kazanas and Ellison consider a spherical accretion shock formed at the Alfven radius to provide a similar vehicle for proton acceleration [25]. The emission would be more symmetric and, thus, predominantly unpulsed.

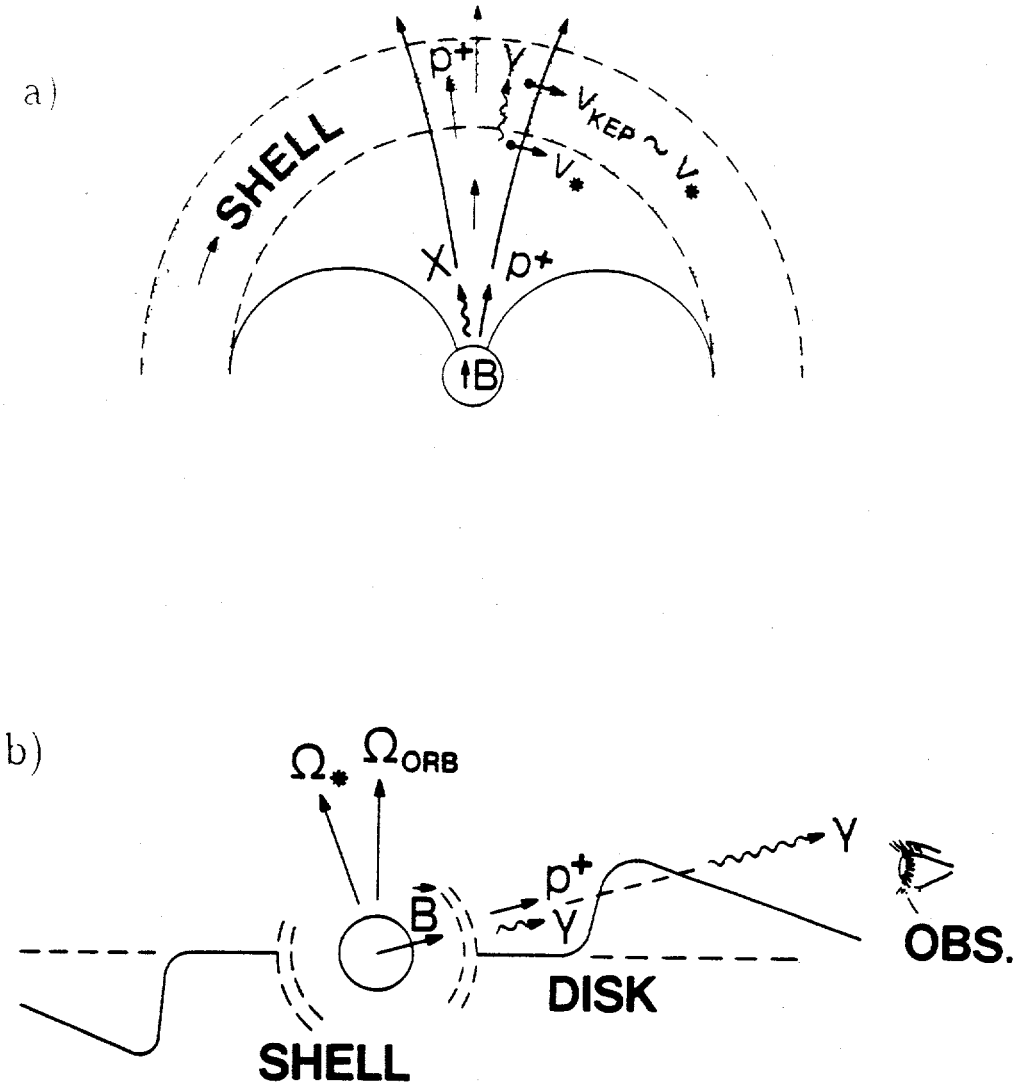

Figure 2.4: **a)** Accretion shell and shock acceleration region (dashed lines); **b)** a possible configuration for the disk system with respect to the observer [24].

Harding and Gaisser [26] have also proposed the formation of a shock through the confinement of the pulsar wind by the companion star of the binary system (figure 2.5). One might therefore expect an orbital periodicity to be associated with such a mechanism.

Due to synchrotron radiation losses, protons are more efficiently accelerated to higher energies than electrons in shock mechanisms. Protons interacting with the surrounding material will then produce (among other things) neutral pions, which will then decay into gamma-rays. In this so-called "beam-dump" model, the target material must be ~ 1 radiation length thick so as to efficiently "convert" the protons without significantly attenuating the gamma-rays thereby produced. In some cases this might be achieved by grazing the edge of the accretion disk or the companion star. If the alignment of such targets are only transitory in nature, short bursts of gamma-rays might thus be expected under these scenarios.

Others

Alternate mechanisms include that proposed by Katz and Smith [27], which uses plasma turbulences in the accretion flow to cause protons to be accelerated stochastically (second-order Fermi acceleration [28]). Energies as high as $\sim 10^{16}$eV are predicted. Wang [29] also considers turbulent accretion flows, but invokes magnetohydrodynamic instabilities in the magnetosphere to result in magnetic reconnection of field lines, producing electric fields with potentials of $\sim 10^{14}$eV.

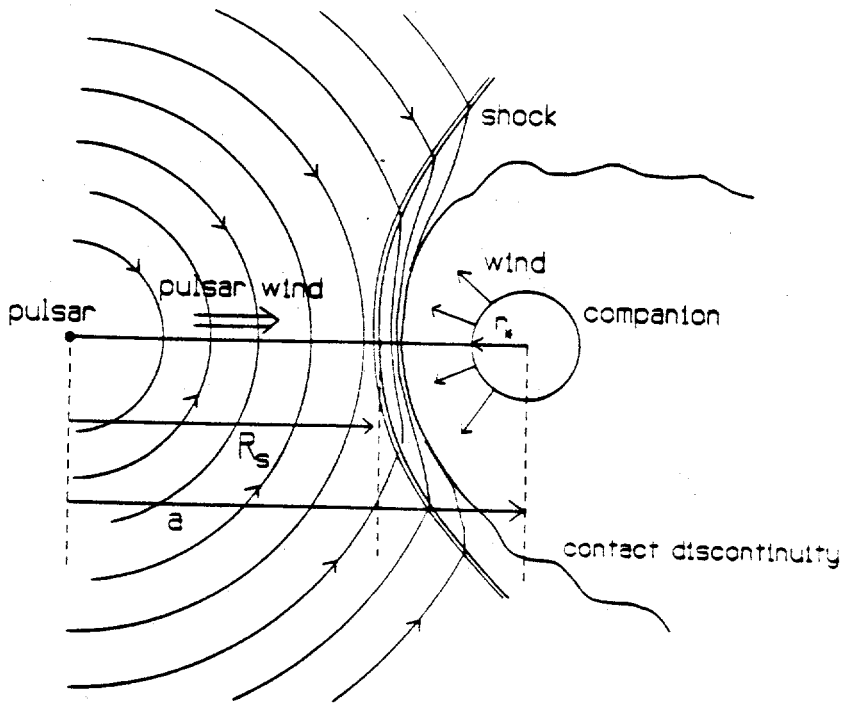

Figure 2.5: Schematic view of pulsar wind shock formation in a binary system for the case of confinement by the companion star wind [26].

Chapter 3

Hercules X-1

"Scientists estimate that one light year is equivalent to 6 trillion miles."
- UPI -

X-Ray Observations

Hercules X-1 (or Her X-1, originally 2U 1705+34), was the second X-ray binary system, after Cen X-3, to be discovered by the Uhuru satellite in 1971 [30],[31]. Observations have indicated a variety of periodicities associated with Her X-1, allowing the determination of numerous system parameters and the development of detailed, dynamical models. Some of the basic parameters of the Her X-1 system are given in table 3.1.

Original observations revealed a 1.24 second (1.2368±0.0006s) regular pulsation, with a 1.7 day (1.70017±0.00004d) variation in the average intensity. The 1.7 day cycle could be divided into a 1.43 day "high state," in which at least 80% of the power was pulsed at 1.24 seconds, and a 0.24 day "low state," with the transition taking place in less than 0.025 days. This cycle is indicative of an occulting binary system. Measurements of a sinusoidal modulation of the 1.24 second periodicity, when viewed in terms of Doppler shifts, were also found to be consistent with a nearly circular orbit (eccentricity < 0.1) with a 1.7 day period (figure 3.1). The amplitudes of these modulations further indicated a projected orbital radius

Quantity	Value
Right ascention (1950 epoch)	254.0 degrees
Declination (1950 epoch)	35.4 degrees
Distance from earth	5 kiloparsecs
Age of system	$\sim 10^7$ years
Surface magnetic field of pulsar [32]	$\sim 4 \times 10^{12}$ Gauss
Pulsar period (epoch JD2445778.56) [33]	$1.23779200 \pm 0.00000005$ sec
Time derivative of pulsar period [33]	$(-2 \pm 1) \times 10^{-13}$
Orbital period (epoch JD2442859.73) [34]	$1.70016779 \pm 0.00000001$ days
Time derivative of orbital period [34]	$< 2 \times 10^{-10}$
Projected orbital radius ($a\sin i$) [34]	13.1831 ± 0.0003 light-sec
Projected orbital velocity ($v\sin i$)[34]	169.049 ± 0.004 km/sec
Eccentricity [34]	< 0.0003
Eclipse half-angle [34]	24.56 ± 0.03 degrees
Mass function [34]	$0.8520 \pm 0.0001 M_\odot$
Angle of inclination (i) [35]	87 ± 3 degrees
Mass ratio ($\frac{M_{HZ\,Her}}{M_{Her\,X-1}}$) [35]	1.68 ± 0.1
HZ Her mass [35]	$2.18 \pm 0.11 M_\odot$
Her X-1 mass [35]	$1.3 \pm 0.14 M_\odot$
Avg. disk-precession(?) period (epoch JD2442408.9) [36]	34.928 ± 0.001 days

Table 3.1: Parameters of Her X-1 system.

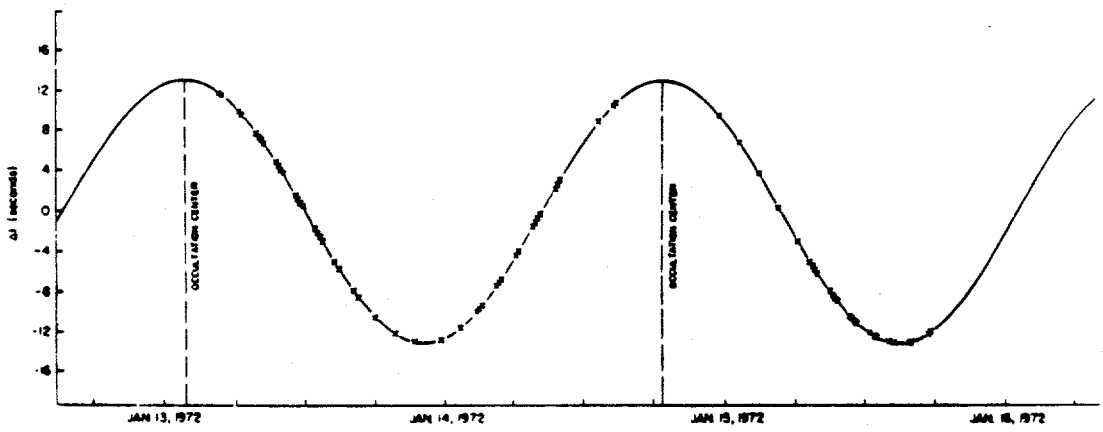

Figure 3.1: Difference δT between the time of occurence of a pulse and the time predicted for a constant period as a function of time [31].

of 13.19±0.03 light-seconds, leading to an estimated projected orbital *velocity* of 169.2±0.4 km/s and a *mass function* of 0.85 $M_{\odot}$. The mass function is defined as

$$m = \frac{(M_2 sin(i))^3}{(M_1 + M_2)^2}$$

where i is the angle of inclination of the orbit relative to the earth, and M_1, M_2 are the binary star masses.

A balloon experiment by Trümper *et. al.* indicated the presence of cyclotron lines in the energy spectrum that would correspond to a surface magnetic field of $\sim 4 \times 10^{12}$ Gauss [32]. This value is consistent with that expected from models of neutron star development.

Further observations by the Uhuru satellite [37] indicated a decrease in the 1.24 second pulsation period amounting to about 4.5 μs over 6 months. This change in period is consistent with predictions for the "spin-up" rate of an accreting neutron star due to the transfer of angular momentum [38], [39]. Since then, the pulsar has been seen to undergo a series of changes in spin rate [40], as shown in figure 3.2.

In addition to the periodicities mentioned above, a longer-timescale variation of 35 days was found in which pulsed emission occurred for 11 days, and was consistent with zero during the rest of the cycle. Subsequent observations [41], [42],[43] revealed the presence of lower-level emission during a "low-on" state, occuring within the phase interval $0.45 < \phi_{35} < 0.6$, where the peak of the "high-on" state is defined to have a phase of zero (figure 3.3). The peak intensity of the low-on state was found to be about 30% that of the high-on state, with pulsed fraction measurements ranging from 10-30% (low-on) as compared with 40-80% (high-on).

Later observations by EXOSAT suggested a 180 degree phase-shift of the 1.24 second cycle during the low-on state relative to the high-on state [33]. One possible explanation is that emission associated with different poles of the neutron star has been seen.

Uhuru data also revealed the presence of regular dips in X-ray intensity correlated with the orbital phase, and occuring progressively earlier as the end of the 11 day high-on state is approached (figure 3.4). These intensity dips have been

interpreted as being due to absorption by gas that is streaming into the system. The mechanism behind the 35 day periodicity has not been firmly established. The favored hypothesis invokes a precessing, twisted accretion disk to periodically occult the source from the field of view of the earth [44],[45],[46]. An alternate model attempts to explain the periodicity in terms of a precession of the neutron star [47],[48][49],[50]. One weakness of the latter class of theories is the difficulty in explaining the relatively poor stability of the 35 day period (which can vary by about 5% over 10 cycles [33]), although the "unpinning" of magnetic field lines attached to the superfluid crust of the neutron star has been suggested as a possible mechanism. One particular model that invokes bi-polar emission [32] has difficulty explaining the complete disappearence of observed emission during the off-state without also invoking an occultation of some kind. Lending support to an accretion-disk based model are the EXOSAT observations of a possible correlation between changes in the 1.24 second period and time variations in the onset of the 35 day cycle [33]. This could be interpreted as indicating the dependence of the pulsar spin-up rate on the accretion rate of matter from the surrounding disk.

From June 28, 1983 to March 1, 1984, EXOSAT observed what appeared to be an extended low state, lasting for about 8 times the average 35-day cycle [51]. This episode seemed to be preceeded by a increase of the pulsar period [52], suggestive of a change in accretion rate. This change may have resulted in a thickening of the accretion disk, thus causing the pulsar to be obscurred during the extended low state.

Optical and Infra-Red Observations

Shortly after the X-ray discovery of Her X-1, the optical counterpart of the binary system, HZ Herculis, was identified [54], [55],[56]. A detailed study of optical pulsations by Middleditch and Nelson [35] allowed the derivation of several parameters under the assumption of a simple, geometric model. This model employs X-ray heating of target material (principally the companion star, HZ Her) to reprocess emission from Her X-1 into optical light. The fact that the intensities of

optical observations appear to be only weakly correlated with the 35 day cycle is consistent with this model, since the orientation of the accretion disk with respect to earth should not greatly effect X-ray heating of the companion star.

Based on precise measurements of Doppler-shifted pulsar frequencies and their time derivatives, three distinct regions of emission were proposed (figures 3.5 and 3.6): regions I and II associated with the surface of the companion star, and region III with the accretion disk. Analysis of the 1.7 day light curve (primarily the lack of emission from regions I and II at orbital phase 0.5) was used to associate the companion star with a filled Roche lobe, (figure 3.7). From the asymmetry of Doppler-shifted pulsar frequencies on either side of orbital phase 0.5, prograde orbital motion (*i.e.* in the same direction as the neutron star's rotation) was implied. Further model calculations indicated a ratio of companion to pulsar mass (which determines the separation of the binary components) of 1.68 ± 0.1, where the error estimation includes both statistical uncertainties in the data, and uncertainties in the specific nature of the model. Given the mass ratio and the fact that the Roche lobe is filled, the size of the Roche lobe can be determined. This, along with the duration of orbital eclipse from X-ray observations, can then be used to determine the inclination angle of the orbit with respect to the earth. The value thus implied is 87 ± 3 degrees. Knowledge of the mass function from X-ray observations can then be used to assign masses to the binary components of $M_{HerX-1} = 1.3 \pm 0.14 M_{\odot}$, and $M_{HZHer} = 2.18 \pm 0.11 M_{\odot}$. The implied mass for Her X-1 is above the Chandrasekhar limit for white dwarfs and below the expected mass regime of black holes, and is therefore quite consistent with the picture that Her X-1 represents a neutron star.

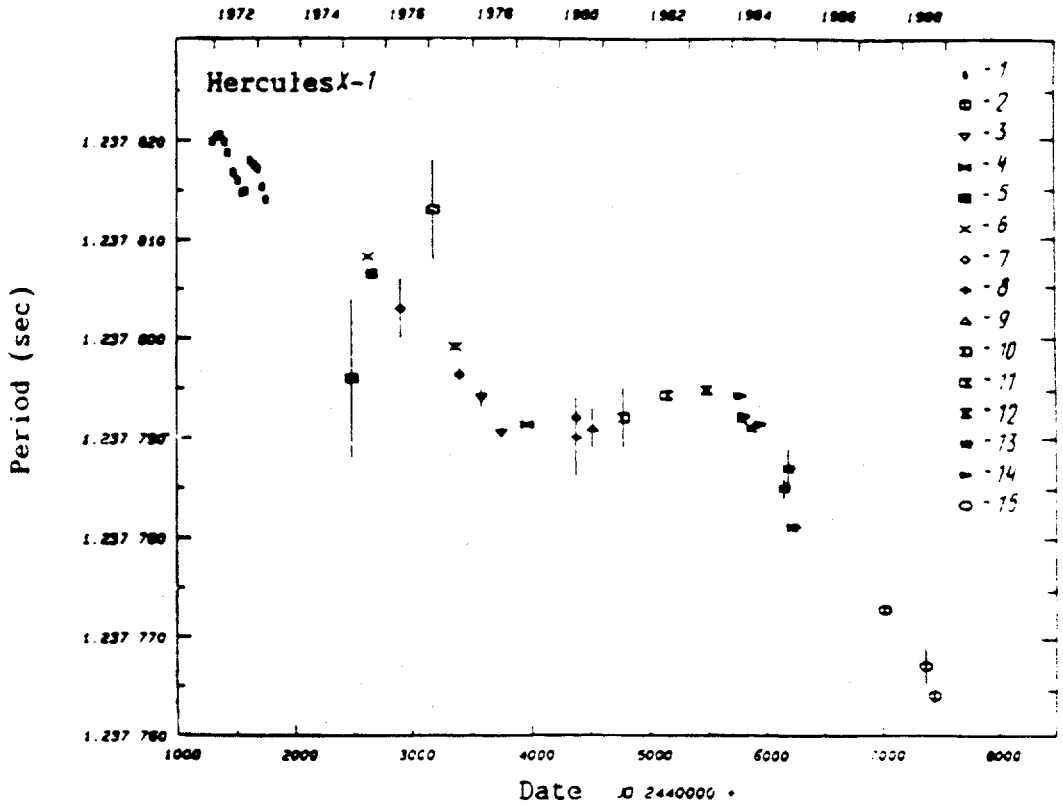

Figure 3.2: Measured X-ray period versus time (compilation by Gil'fanov *et al.* [40]).

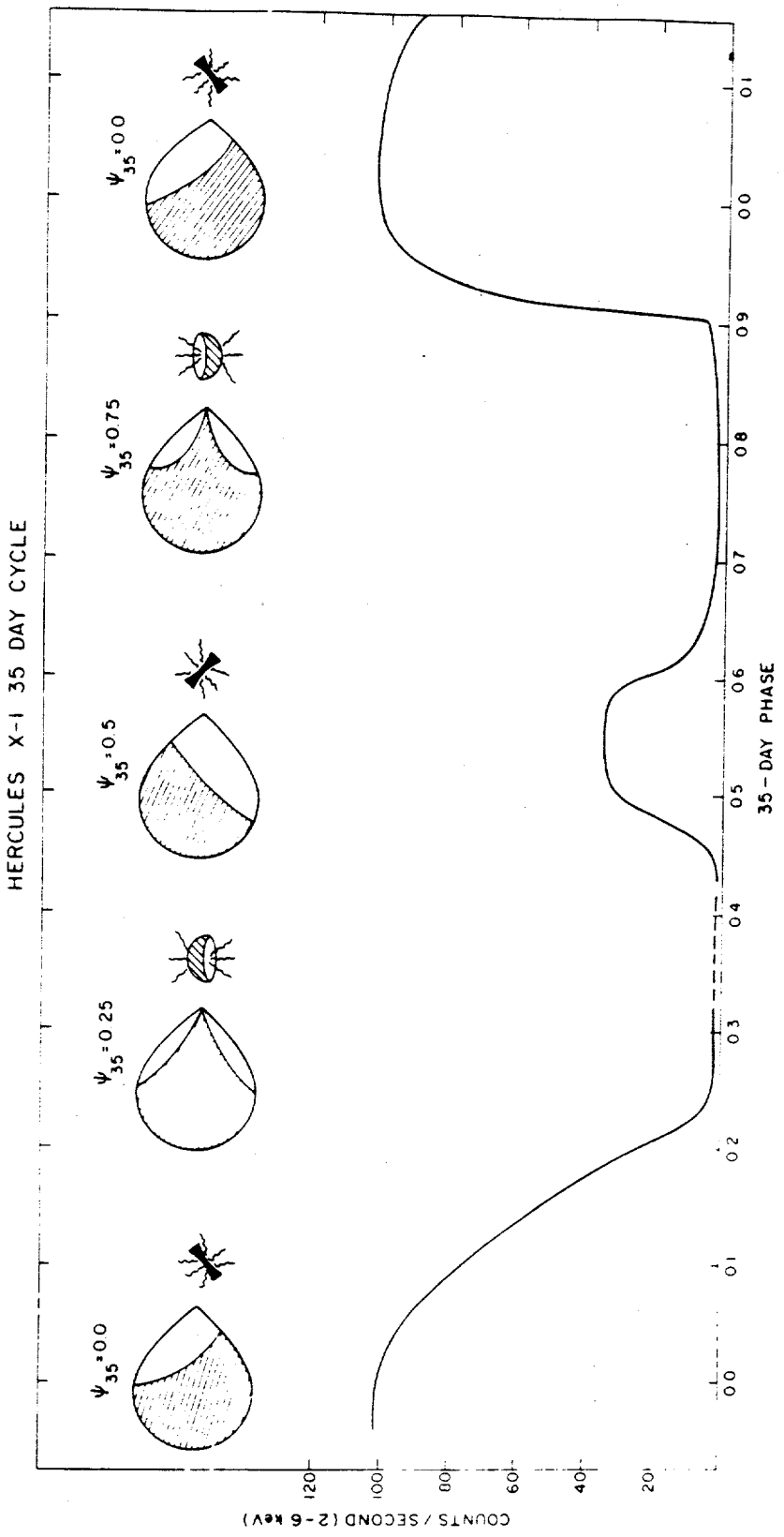

Figure 3.3: Her X-1 35 day cycle. The upper portion of the figure shows a model for the "precessing" orientation of the accretion disk[43].

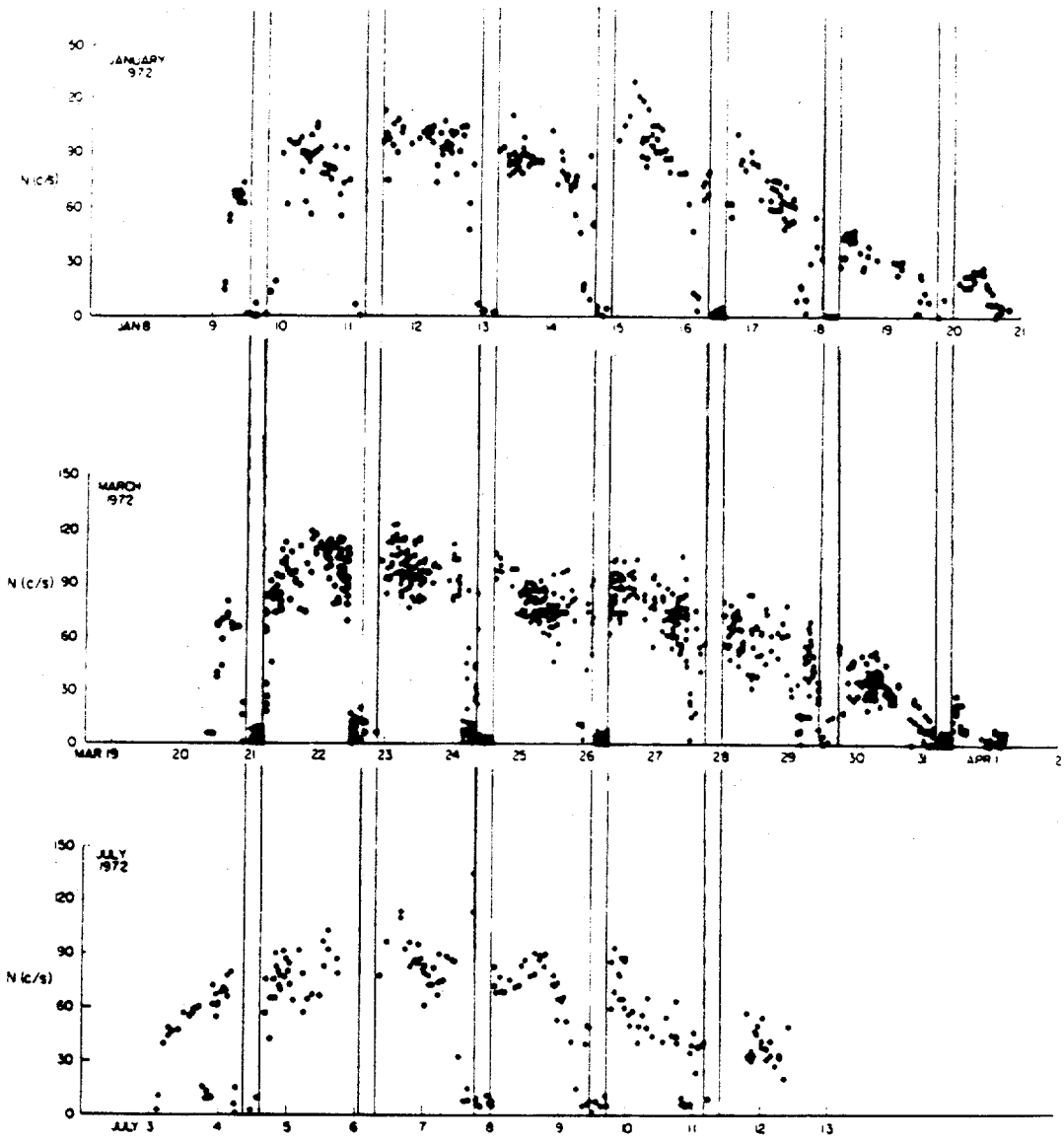

Figure 3.4: Her X-1 X-ray intensity dips data during 3 "ON" states. The vertical lines represent orbital eclipses [37].

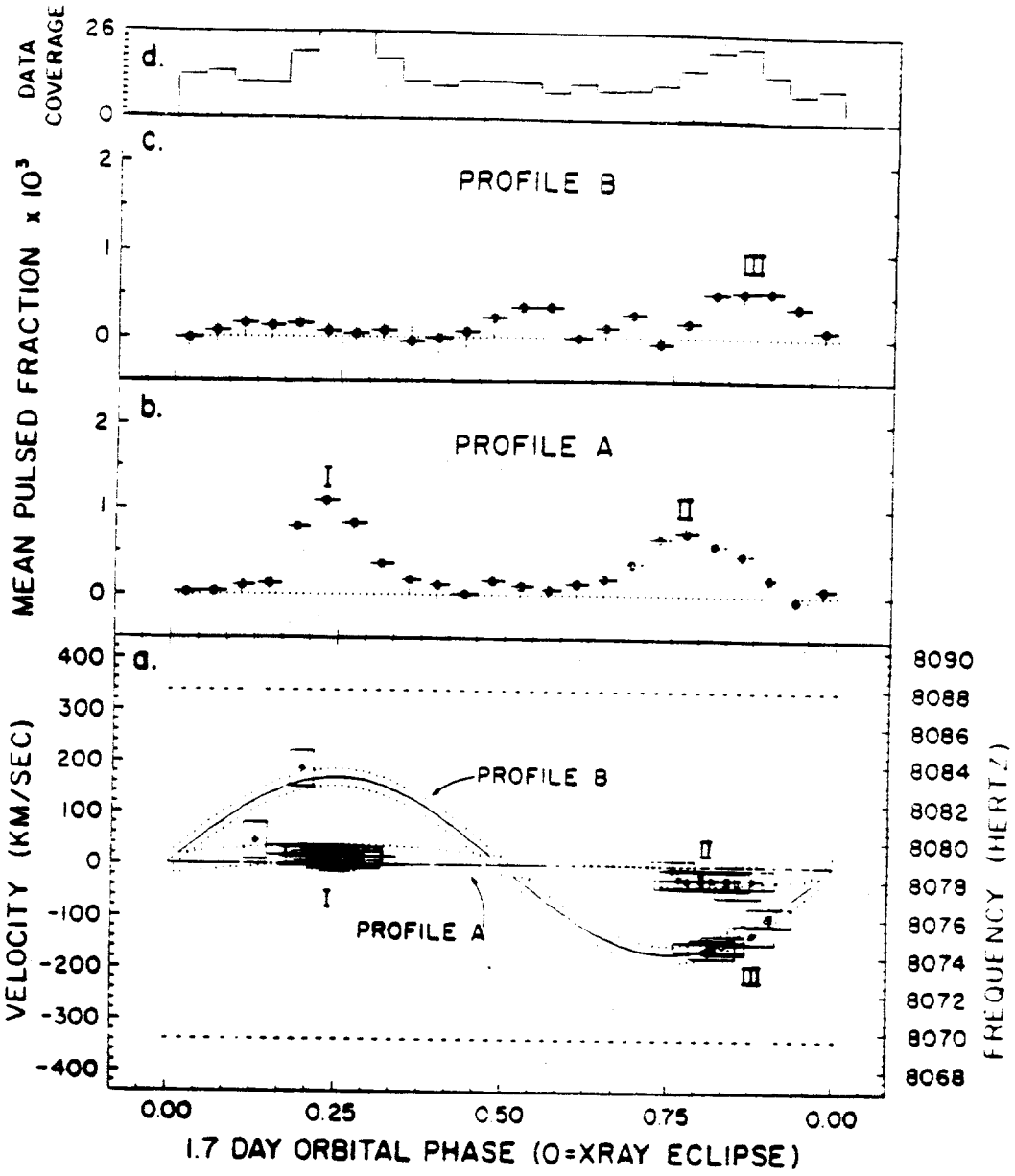

Figure 3.5: Evidence for 3 regions of optical emission from Her X-1 [35]

(*a*) The significant bins chosen from all of the power spectra are shown plotted as boxes on the orbital phase-frequency plane. Features I, II, and III are labeled. The horizontal solid line and the solid sine curve indicate the average pulse frequency of Her X-1 and its Doppler-shifted pulse frequency, respectively. The horizontal dashed lines at the top and bottom of the frame indicate the frequency region examined and are at twice the extent of the maximum Her X-1 Doppler shift. The dotted lines indicate the regions on the phase-frequency plane which were applied to all of the spectra to calculate the amplitude profiles in (*b*) and (*c*). (*b*) The profile of amplitude versus orbital phase for Features I and II from HZ Her. (*c*) The amplitude profile following the Doppler track of Her X-1. Feature III is indicated near phase 0.85. (*d*) The data coverage histogram over 24 equal parts of the 1.7 orbital phase. The profiles in (*b*) and (*c*) have had this unevenness normalized out.

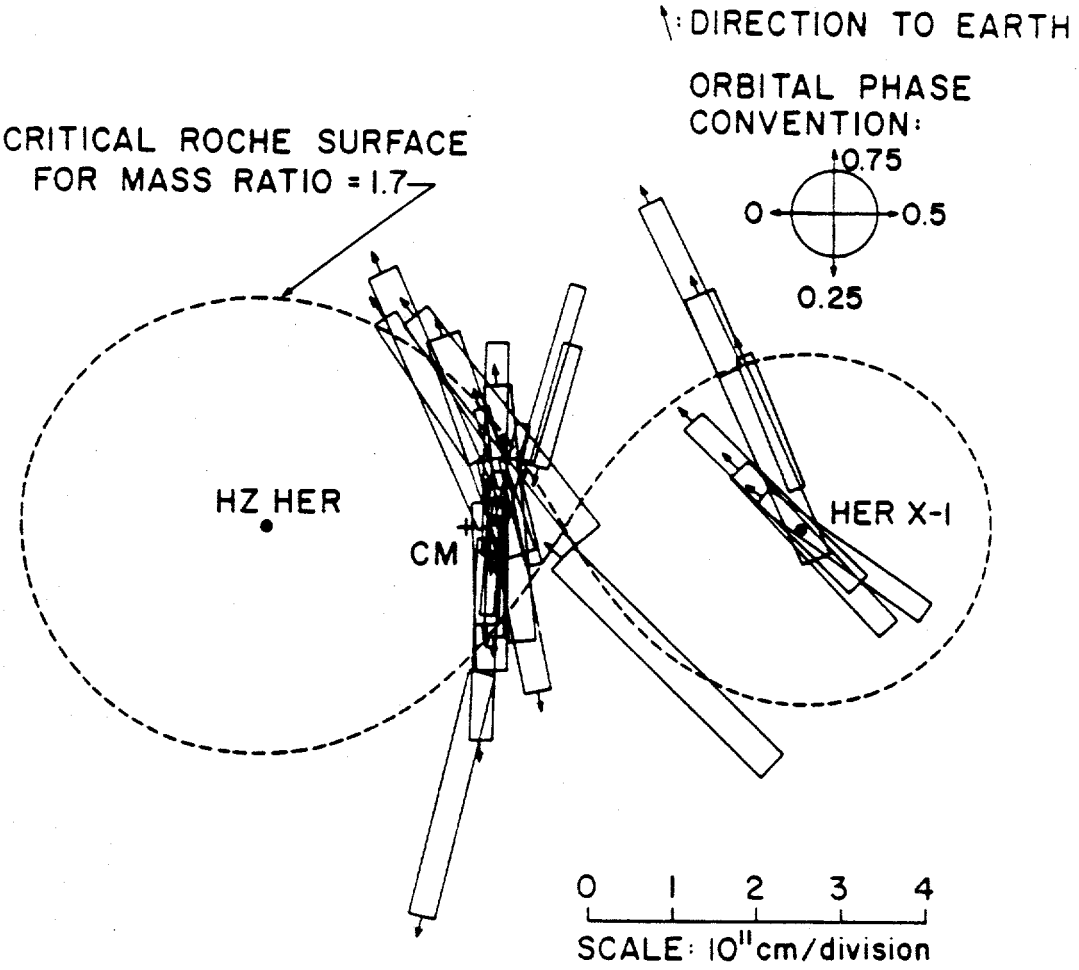

Figure 3.6: Evidence for 3 regions of optical emission from Her X-1 [35]

The locations in the orbital plane (as projected for $i = 90°$) of the strong pulsation events as derived from the precise measurements of f and f'. The boxes are fixed with respect to the centers of mass of Her X-1 and of the entire binary system. The positions of the center of mass of HZ Her and the dashed critical Roche lobe contour depend on the value of the mass ratio which was arbitrarily set equal to 1.7 (with HZ Her as the more massive component). The box lengths are set by the $\pm 1\sigma$ errors for the values of f'; the widths, by the $\pm 2\sigma$ errors for the f-values. The arrows at the ends of the boxes indicate the direction of the Earth and (equivalently) the orbital phases at the midpoints of the runs. The scale is given at the lower right.

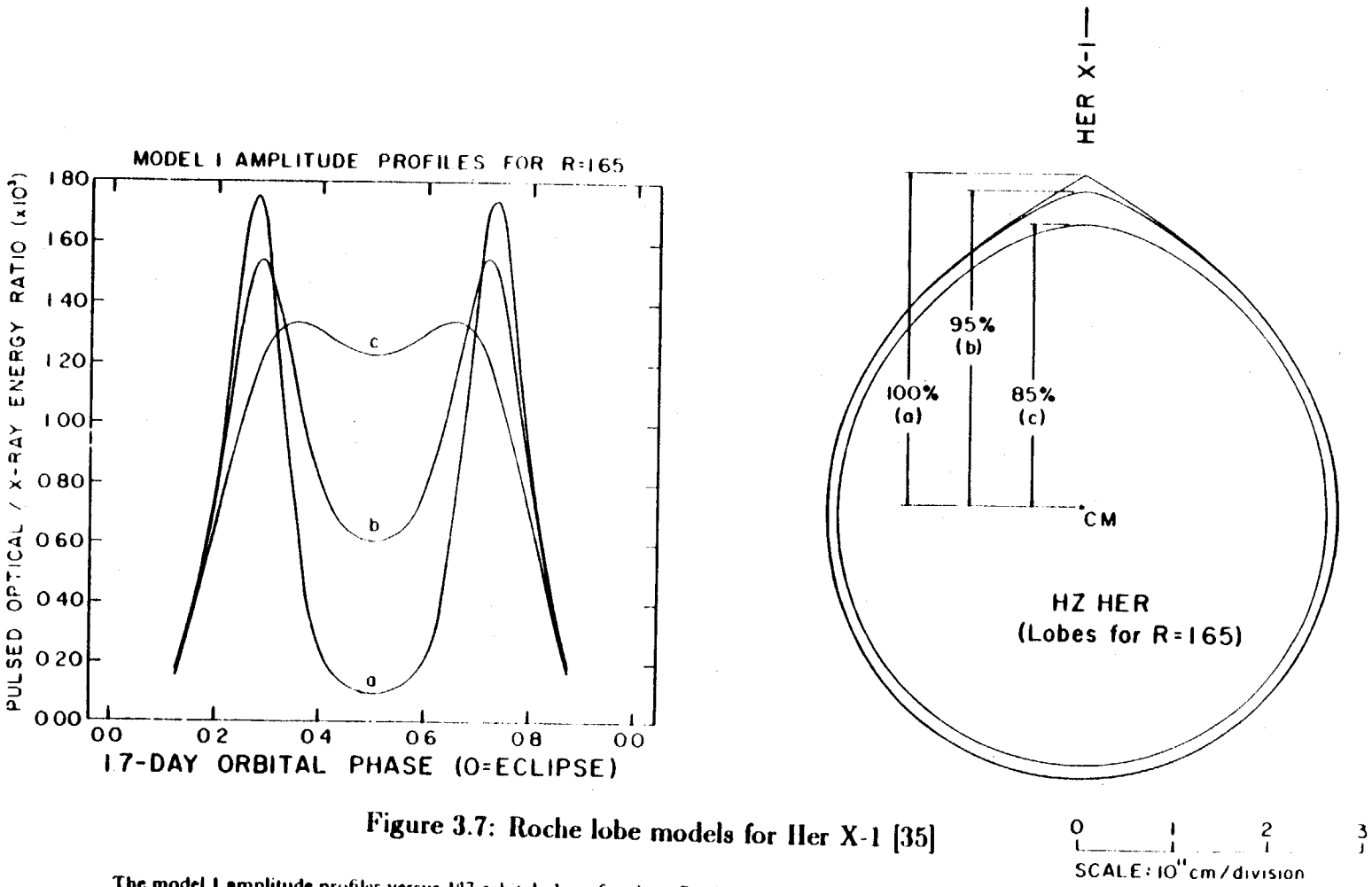

Figure 3.7: Roche lobe models for Her X-1 [35]

The model I amplitude profiles versus 1.7 orbital phase for three Roche equipotential contours with $R = 1.65$ are plotted together on the left for comparison. The right-hand side shows the three contours associated with the profiles *a*, *b*, and *c* labeled according to their extent from the HZ Her center of mass toward Her X-1 along the mass axis. The critical Roche lobe defines 100% for this extent.

Simultaneous optical and infra-red observations of pulsed emission were made during the extended X-ray low period [57]. Correlated measurements of a weak "anomalous feature," believed to be associated with X-ray illumination of the mass transfer stream in the binary system [58], indicated a flow velocity of ~65 km/sec towards the pulsar. In addition, one episode involving an unusually red-shifted pulsar periodicity was seen that corresponded to a relative velocity of ~209 km/sec, directed away from the earth. This may be due to X-ray reprocessing from material circulating in the rim of the accretion disk. Along with an apparent decrease in the amplitude of pulsations from region I, and the appearance of a second harmonic, this may reflect a change in the accretion disk structure responsible for the extended X-ray low state.

Chapter 4

The CYGNUS Array

"This signal must be detected above the intrinsic noise associated with the detector system, i.e., cavity, amplifier, coaxial feeds, graduate students, etc."
- Edward Kolb and Michael Turner -

The CYGNUS EAS (Extensive Air-Shower) array has been in continuous operation since April of 1986, and has collected a total of more than 3.5×10^8 events to date. The original purpose of the experiment was to construct an instrument capable of readily confirming the Kiel observation of localized emission from Cygnus X-3 and unambiguously determining whether the muon content of the associated air-showers were, in fact, in disagreement with predictions for gamma-ray primaries. Consequently, the design goals were: **1)** To attain an energy threshold for primary particles that was factor of 10 lower than that of the Kiel experiment. This would greatly improve the sensitivity to emission if the energy-dependence of the signal flux extended to these lower energies without modification; **2)** To achieve an angular resolution of better than $\sim$1 degree for reconstructing the directions of primary particles in order to identify localized emission associated with point sources: and **3)** To encorporate a large, well-shielded detector within the array to measure the muon content associated with the detected air-showers. Since the initial configuration in 1986 (which achieved all of these goals), a series of modifications have been affected to further lower the energy threshold, increase the collection area, enhance the muon detection capability, and improve the angular resolution.

Since part of this thesis is concerned with the details of the 1986 Her X-1 result, the initial array configuration relevant to that detection will now be discussed. This will then be followed by a brief description of various modifications that have since taken place. A more detailed list of these modifications is presented in Appendix F.

Initial Configuration

In 1986, the CYGNUS array consisted of 50 scintillation detectors deployed over an area of $\sim 10^4$ m^2 (figure 4.1) at an altitude of 2310 meters (corresponding to an atmosperic overburden of 800 gm/cm^2) at Los Alamos National Laboratory in northern New Mexico. Each of these detectors (figure 4.2) is comprised of a light-tight, fiberglass enclosure, housing a circular piece of scintillator that is viewed by a photomultiplier tube (PMT). The PMT is located at a position $\sim$ 0.7m above the plane of the scintillator to reduce the spread in flight-times for photons produced in different regions of the scintillator. The scintillator (previously used in the Volcano Ranch array during cosmic ray studies of the late 1950's and 1960's [60]) is 10 cm thick and 1 meter in diameter. At the time it was manufactured, it produced a yield of 6700 photons per MeV of deposited energy with an exponential response time of 4 nanoseconds. Since then, the scintillator has noticibly yellowed, taking on an effective attenuation length for visible light of $\sim$7cm (see Appendix A). The PMT (Amperex model 2262) is a 2 inch diameter, 12-stage, high-gain tube with a fast risetime of <2 nanoseconds. The fiberglass enclosures are white on the outside to minimize temperature fluctuations, and white on the inside to increase light collection at the PMT. A minimum-ionizing particle passing through the scintillator results in 20-25 detected photoelectrons. The separation between detectors in 1986 varied from 3 meters near the center of the array, to about 20 meters at the array boundaries. The detector locations were surveyed to an accuracy of <5cm.

The scintillation counters were deployed around the E225 detector, located next to the beam-stop at the end of the LAMPF linear accelerator [61]. This detector, then operating to measure the ν_e-e elastic-scattering cross-section, employed

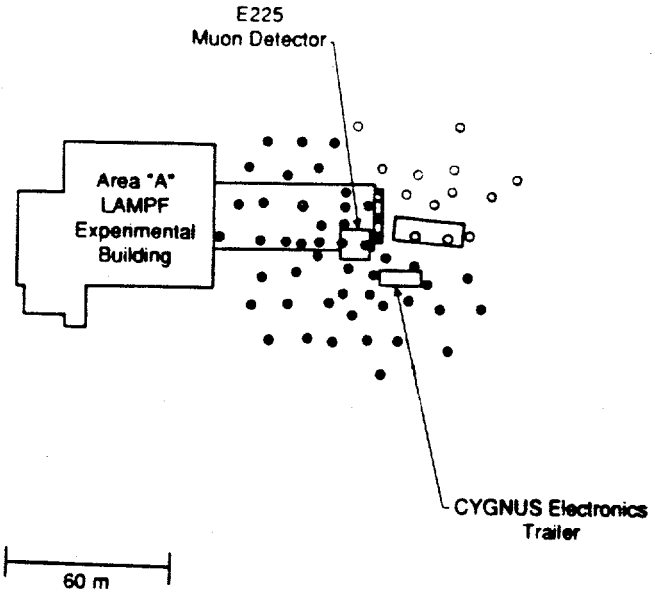

Figure 4.1: Original configuration of CYGNUS array (1986): 64 scintillation detectors deployed, 50 operational (filled circles).

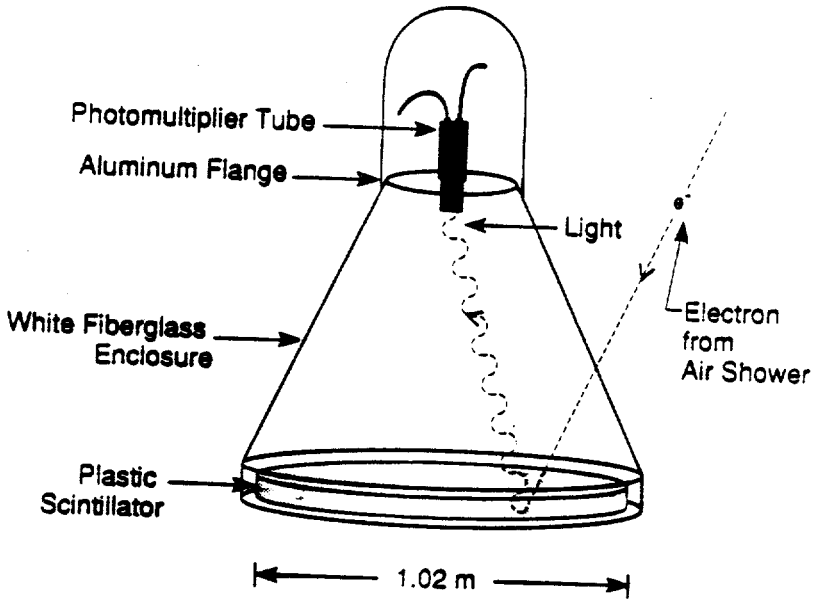

Figure 4.2: Schematic view of a CYGNUS scintillation counter [59].

a cosmic-ray veto-shield consisting of a $6\times6\times6m^3$ cube of multi-wire proportional chambers (MWPCs). This veto-shield was used by CYGNUS to detect muons associated with recorded air-showers (figures 4.3 and 4.4). The inner flash-chamber of the experiment also provided additional muon information for a subset of events that triggered CYGNUS when E225 was not otherwise occupied with beam-associated data. Detector shielding (figure 4.5) provides an average muon energy threshold of $\sim$2GeV, and virtually eliminates the possibility of electromagnetic "punch-through." Further information on the use of the E225 detector by the CYGNUS collaboration is provided in reference [62].

A simplified schematic of the data acquisition system is shown in figure 4.6. The PMT signals traversed 70-150 meters of RG-58 cable before reaching the electronics trailer where they were discriminated at a level of 1-2 photoelectrons (50 millivolts) to minimize dispersive effects. After a passive split of the signal, $\frac{1}{4}$ was directed to an analog-digital converter (ADC) to record pulse-height information (integrated over 700 ns), and the remaining $\frac{3}{4}$ to both the trigger logic and a time-digital converter (TDC) for timing information. The trigger logic required that 20 detectors fire above the discrimination level within a time-window of 300 nanoseconds. This coincidence level of 20 detectors was chosen to eliminate random triggers (caused by the chance time-coincidence of particle detections not associated with a single air-shower), and also to provide a data set of recorded showers whose properties (angle of incidence, core location, lateral extent etc.) could be easily reconstructed. In addition, software "taping cuts" were applied by requiring a subset of the triggered counters to have large pulse heights in order to further constrain the quality of accepted events. A secondary "smart trigger" was also employed to gain additional muon information by triggering the central flash chamber of E225 for showers with directions corresponding to the vicinity of particular sources.

The array was calibrated with the use of a separate pair of overlapping, thin scintillators (15cm$\times$25cm$\times$1.3cm), each connected to a PMT via a light pipe attached to the edge of the scintillator. This set of scintillator *paddles* could be positioned beneath any of the detectors in the array. Using a coincidence of signals from both scintillators of the paddle to reduce accidental triggers due to a fluctuation in

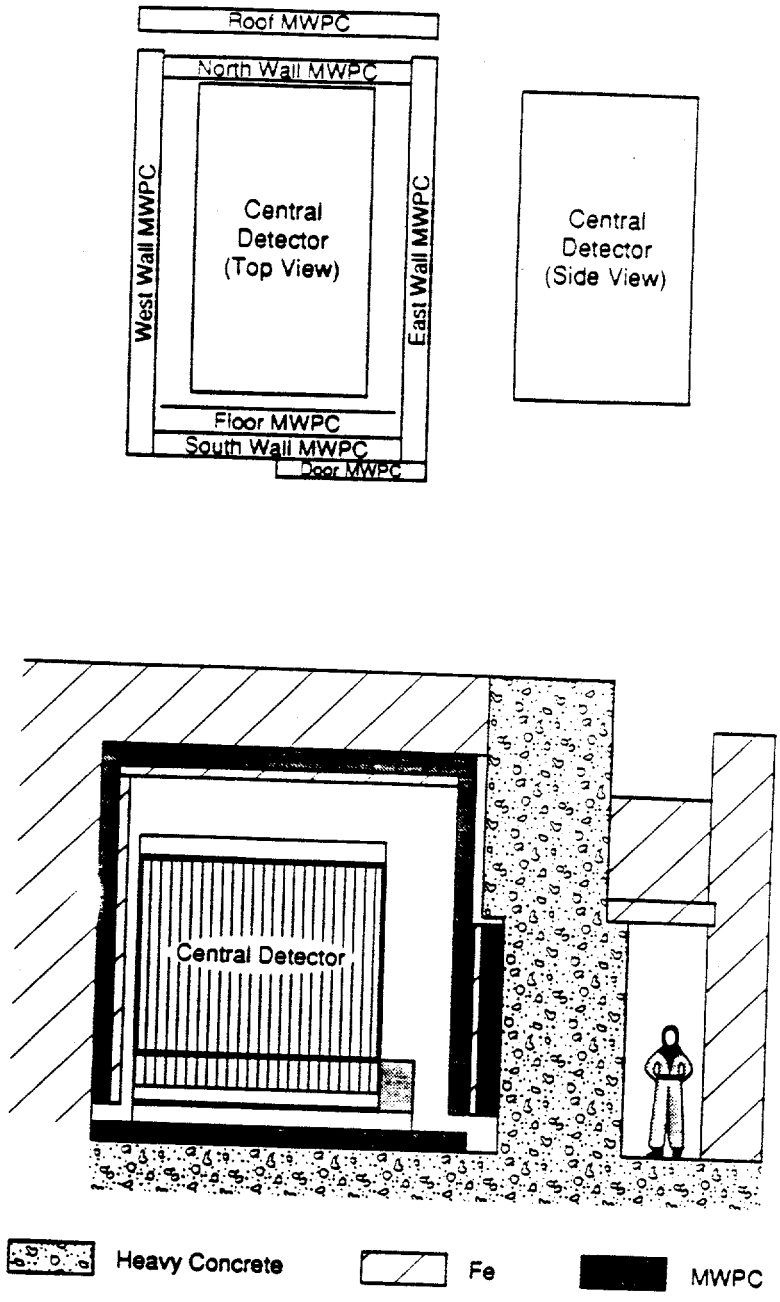

Figure 4.3: E225 muon detector and shielding [59].

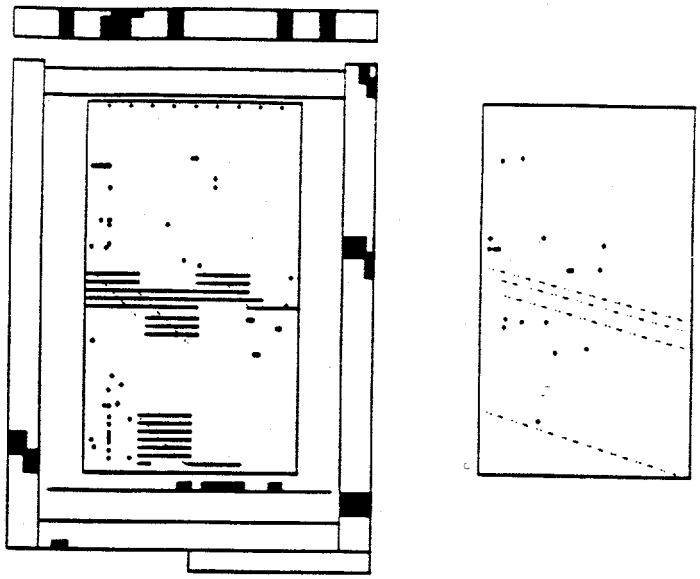

Figure 4.4: A display of muons detected by the E225 central detector and MWPC veto-shield for an event that triggered the CYGNUS array [59].

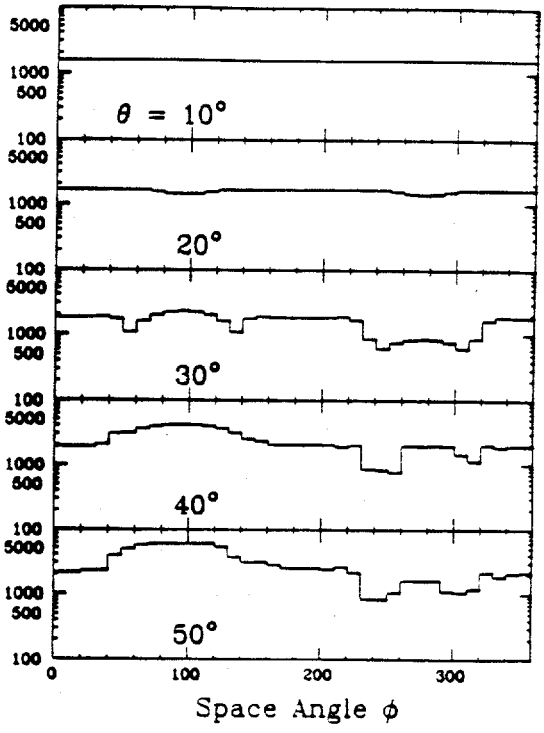

Figure 4.5: E225 shielding (gms) as a function of zenith and azimuthal angles [62].

electronic noise level, the simultaneous measurement of a signal in the detector under which it was placed indicated the passage of a through-going particle, most likely a muon. Histograms of counts for ADC and TDC channels were then collected. ADC histogram entries gated by paddle triggers that are due to accidental triggers (*i.e.* the chance coincidence of noise level fluctuations) established the ADC pedestals. The PMT gains were then adjusted to give a spread of ~10 channels between the ADC pedestal and the distribution median for through-particle triggers (roughly corresponding to the 1-particle peak). Since TDC information for each detector is taken relative to triggers generated by the same set of paddles, the values of the TDC distribution medians measures the relative counter-to-counter time differences that are due to varying cable lengths, electronic delays, etc.

Paddle calibrations are performed once or twice per year, but since the relative time offsets are sensitive to slight variations in cable temperature and PMT/electronics response, more continuous monitoring and occasional adjustment of TDC offsets is required. This has been accomplished by the use of iterative software techniques applied to air-shower data to extrapolate offset values from the previous paddle calibration. These software techniques are either based on the distribution of particle arrival times in each counter relative to the best-fit position of the showerfront or on the distribution of time differences recorded for neighboring detectors triggered by the same showers. Distributions of the differences between TDC offsets determined by extrapolation and by direct paddle calibration have been found to have typical widths of ~1.5 nanoseconds.

Modifications

Several modifications to the CYGNUS experiment have taken place since 1986. These changes are documented in Appendix F. The current array consists of two principal sections (figure 4.7): CYGNUS I, an expansion of the original array from 50 to 108 scintillation detectors with a physical area of $2.2 \times 10^4 m^2$; and CYGNUS II, a contiguous addition of 96 detectors with counter separations graded from 20 to 35 meters over an area of $6.2 \times 10^4 m^2$ for sensitivity to larger showers.

CYGNUS II is separately triggered by coincident signals from at least 16 detectors. In addition, at least 3 coincident signals are required from a given *sub-array* (6 geographically and logically separated regions), for that particular sub-array to be read out. The muon detector in CYGNUS II, named "Anasazi" (after the ancient, cave-dwelling Indians of the region), consists of 70m^2 of plastic scintillation counters located in 15 holes, each 0.9m in diameter and 12.2m deep, drilled into the bottom of a 10m high cliff of volcanic tuff (figure 4.8). This provides an overburden of about 700 gm/cm^2. Due to current reconstruction and calibration uncertainties associated with the CYGNUS II array, only CYGNUS I information is considered in this thesis.

As a result of further studies on the ability to effectively reconstruct events in CYGNUS I, taping cuts are no longer employed. Also, in order to improve the sensitivity to the photon component of air-showers, lead sheets of $\sim$1 radiation length vertical thickness have been placed over the detectors in both arrays. This was done to enhance the probability for a photon to pair-produce an electron and positron, which are more readily detected by scintillation counters. These various changes have resulted in a higher CYGNUS I trigger rate ($\sim$3.5 Hz, as compared to the original 0.25 Hz), and a reduction in energy threshold by a factor of $\sim$2.5 (a median primary energy for simulated triggers of $\sim$130TeV versus 320TeV). The passive split in CYGNUS I now directs $\frac{1}{7}$ (verses $\frac{1}{4}$) of the signal to the ADCs, and the 1-particle peak in the ADC spectrum is set to be $\sim$5 channels (versus 10) above the pedestal. A detailed schematic of the current electronic configuration is shown in figure 4.9. Muon detection in CYGNUS I has been augmented by 45m^2 of plastic scintillation detectors located in the basement of the Bio-Medical facility, adjacent to the E225 detector.

In addition to these changes, an array of 5 water-Cherenkov detectors ($\sim$42m^2 each) have been installed within CYGNUS I to investigate the application of this technology to air-shower arrays. Preliminary results are very encouraging, however directional reconstruction incorporating information from these detectors has not yet been integrated into the standard data-processing procedure.

Software Reconstruction Algorithms

Event reconstruction consists of **1)** locating the core of the shower; **2)** removing the effects of "sampling" and "curvature" from the measured showerfront arrival times; **3)** fitting the corrected arrival-time measurements to a plane wave whose normal defines the direction of the primary particle that initiated the shower; and **4)** fitting the lateral density distribution of equivalent through-going, minimum-ionizing particles to extract an effective shower size (total number of electrons reaching the observation level) and age (steepness of the lateral distribution). The latter step is not currently implemented as part of the standard reconstruction procedure, but is subsequently applied to pre-processed data files according to the needs of a given analysis.

Core location and lateral distribution fitting is described in detail in Appendix B, and sampling/curvature corrections to the showerfront arrival times are described in Appendix E. The shower direction fit is accomplished by minimizing the χ^2 function [63]:

$$\chi^2 = \sum_{n=1}^{N} w_n(c(t_n - t_0) + ix_n + jy_n + kz_n) \tag{4.1}$$

where (i, j, k) is the unit vector normal to the shower plane, (x_n, y_n, z_n) is the geographical location of the nth counter, c is the speed of light, t_n is the corrected arrival time in the nth counter, t_0 is the absolute arrival time of the shower, and w_n is the weight given to the time measurement in the nth counter (based on sampling of the showerfront width... see Appendix E).

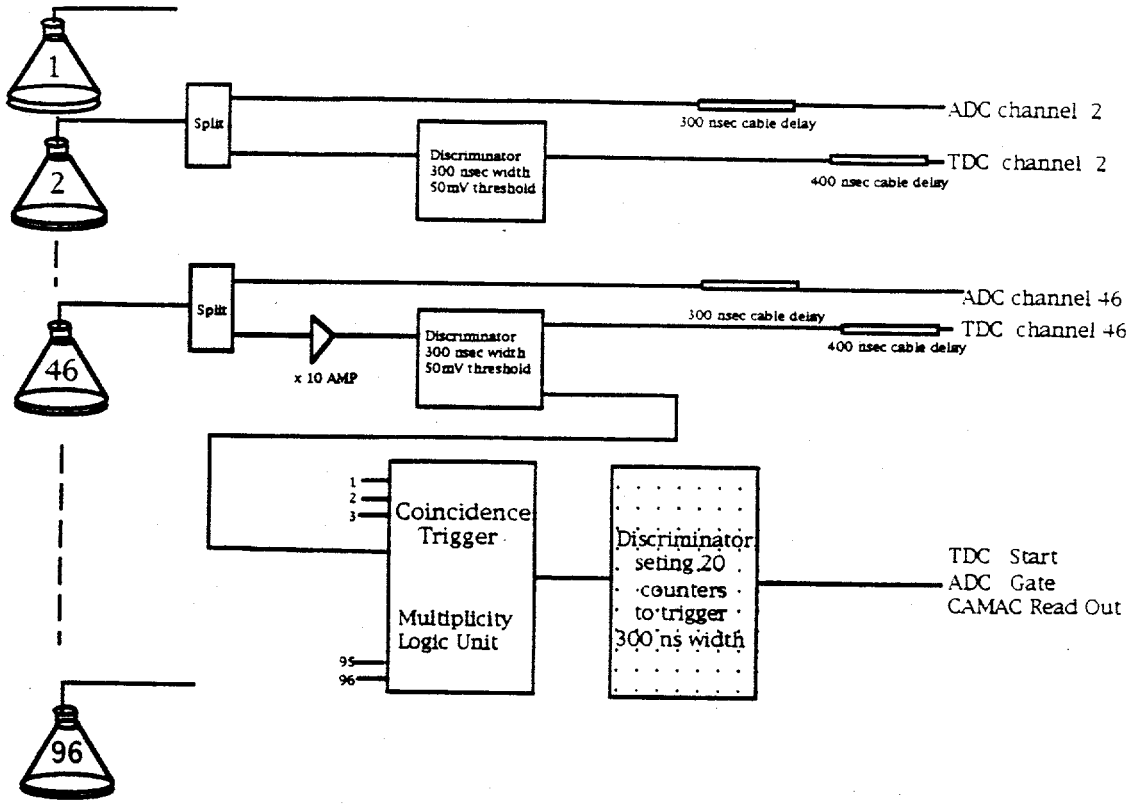

Figure 4.6: Simplified CYGNUS I logic diagram [63].

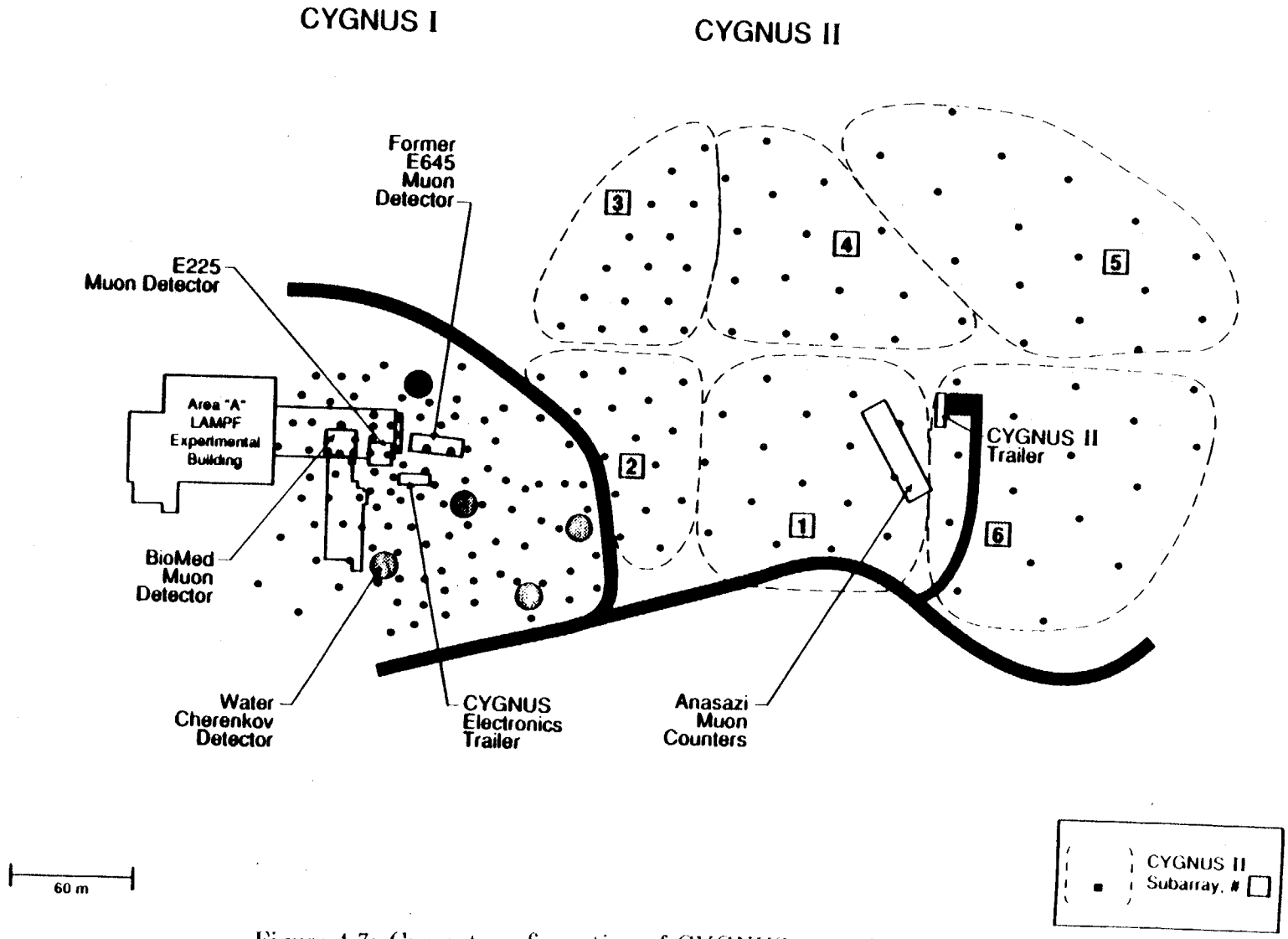

Figure 4.7: Current configuration of CYGNUS array (1992).

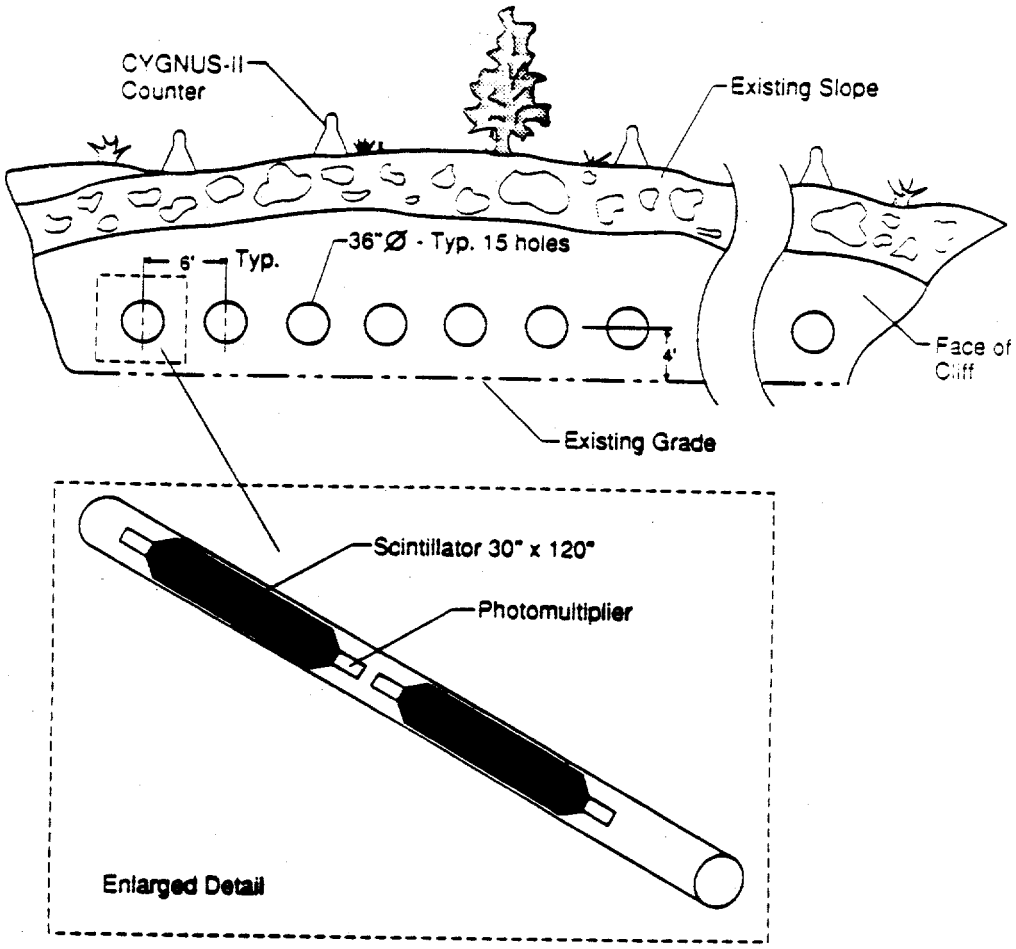

Figure 4.8: Schematic view of an Anasazi muon counter and the holes in which the counters are located [59].

LOGIC DIAGRAM OF CYGNUS I

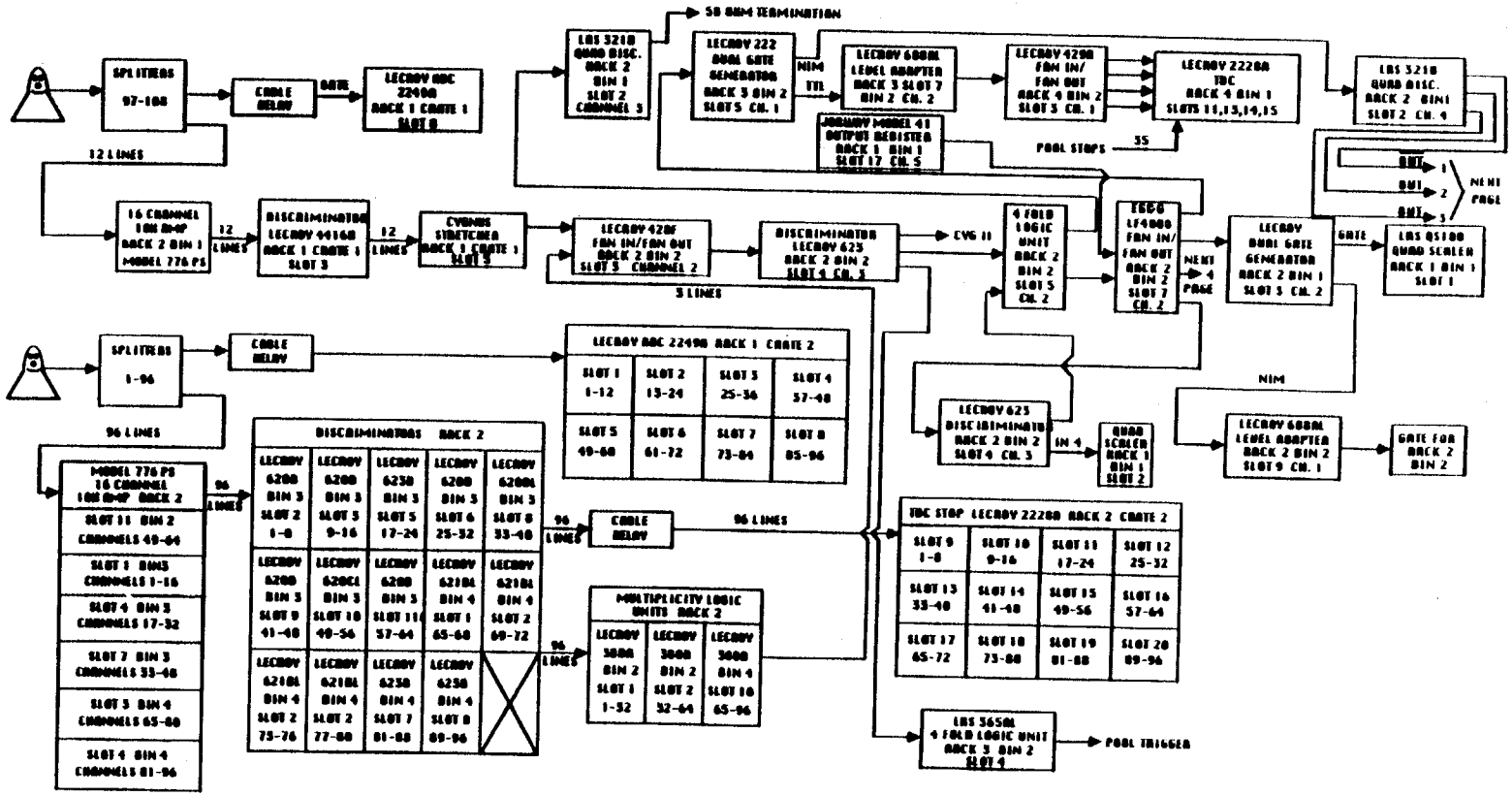

Figure 4.9: Detailed CYGNUS I logic diagram [64].

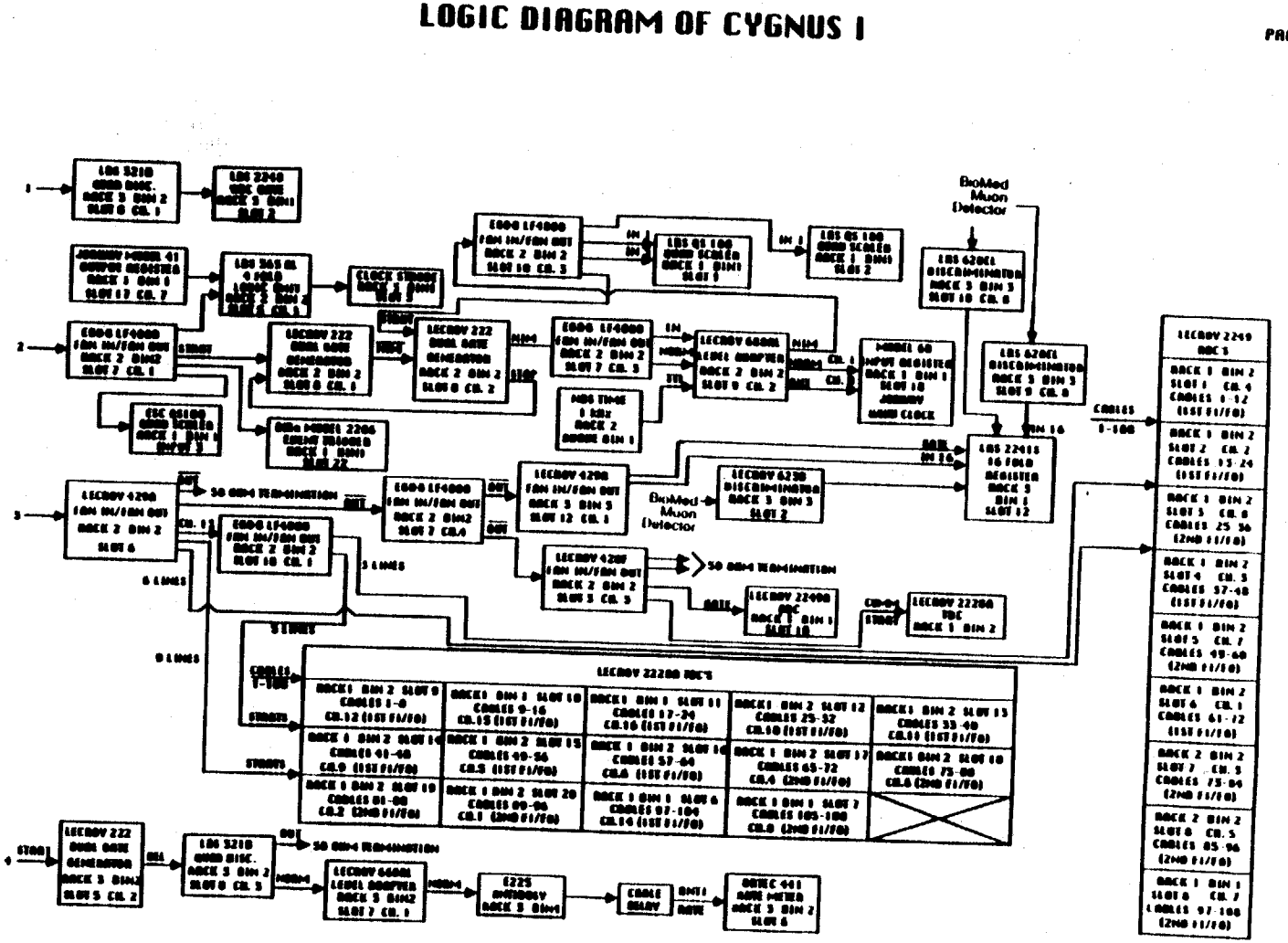

Figure 4.9: Detailed CYGNUS I logic diagram [64]. PAGE 2

Chapter 5

Statistical Analysis of UHE Data: Example and Discussion

"There are three kinds of lies -
lies, damned lies, and statistics."
- Mark Twain -

More so than in many fields of physics, current studies in UHE/VHE astronomy require a detailed knowledge of statistical issues. Due to the large, continuous, isotropic flux of hadronic primaries whose trajectories possess little or no directional information related to their origin, background rejection is a key issue. UHE/VHE astronomy is an *observational* science, and results cannot often be easily confirmed by repeating the measurement under identical conditions. It is therefore crucial to properly assess the significance of discoveries made in any given data set. In addition, there are no clear guidelines regarding potential source types, emission characteristics, atmospheric interaction models, or even primary particle species. As a consequence, data analyses often tend to be somewhat open-ended as they attempt to address a broad range of questions. This naturally leads to concerns that an objective calculation of the significance of a given observation may be compromised by the application of *a posteriori* logic to redefine the question being asked. To guard against such biases, it is therefore important 1) that each procedural step of the analysis can be justified through either physical or mathematical arguments that are independent of the specific data set under consideration, and 2) that each prob-

ability calculation related to a particular question is properly placed in context with all other questions that have been asked during the global analysis of the data. The following sections will address these issues in detail through a re-analysis of the 1986 observation of Hercules X-1, previously reported by the CYGNUS collaboration [3].

Clearly, if UHE observations of point-sources were well-established and self-consistent, much of the following discussion would be unnecessary. However, such is not the case, and this lack of consistency has cast serious doubt on the validity of previous claims. Since an obvious explanation lies in the possible misestimate of significance levels, it is incumbent upon us to re-examine the analysis procedures that have lead to these claims. The following discussion of the 1986 observation is therefore both an attempt to re-evaluate that particular claim in light of the knowledge and experience that have been gained since its publication, and also a "springboard" from which to discuss general approaches to the statistical analysis of UHE data that will be referred to in later chapters.

Review of the 1986 Analysis of Hercules X-1

As of July 1987, 340 transits of the X-ray binary system Hercules X-1 had been recorded by the CYGNUS experiment. This data set was then examined for evidence of UHE emission on the time scale of $\sim$ 1 source transit. The following section briefly reviews the original analysis of Her X-1. Further details will be discussed at length in the forthcoming section, *Discussion and Re-Analysis.*

Calculation of Event Excess

The first step of the analysis involved searching for days with an unusually large number of events associated with the source as compared with expectation. "Association" of events with a potential source is defined by air-showers with reconstructed primary directions that are within a pre-selected angular region of the sky, centered on that source. The angular region chosen was a square "bin," 2.3 degrees on a side. This region is approximately optimum for maximizing the significance of a

signal, assuming point source emission as seen by an array with an intrinsic angular resolution of 0.8 degrees. The average number of background events expected to have reconstructed directions that place them within the source bin was estimated from *off-source* bins of equal angular area that traversed the same region of sky.

The most significant daily excess occurred on July 24, 1986 (UT), when 17 events were observed during a single source transit where 6 ± 0.4 were expected (based on the observed number in 40 off-source bins). This corresponds to a probability of 1.7×10^{-4} for a chance fluctuation to result in an excess at least this large on a *particular* day. Since 340 days had been studied, and there was no *a priori* reason to examine this particular day alone, one must assess the probability to observe a fluctuation at least this large in 340 attempts. More generally, when choosing the most "interesting" result from a series of studies, one must account for each *independent* hypothesis tested in assessing the final significance of that result. This is done by applying the binomial probability function:

$$P_n = \frac{N!}{n!(N-n)!} p^n (1-p)^{N-n} \qquad (5.1)$$

This equation gives the probability, P_n, to observe n successes in N attempts, where the probability for each success is p per trial. Therefore, if $p = 1.7 \times 10^{-4}$, $N = 340$, and $n = 1$, the formula above will give the chance probability to observe *exactly* 1 occurance of the event excess corresponding to p in 340 trials. However, one must also account for ensembles of similar experimental measurements that would have yielded 2 or more successes (since these cases also clearly qualify as having an occurence of an excess at least as large as that observed). It is therefore necessary to calculate the ***cumulative*** binomial probability:

$$P_{\geq 1} = \sum_{n=1}^{N} \frac{N!}{n!(N-n)!} p^n (1-p)^{N-n} = 1 - P_0 = 1 - (1-p)^N \qquad (5.2)$$

This is approximately equal to $N \times p$ for cases when this product is much less than 1. In the discussions that follow, N will be referred to as the *trials* or *trial factor* that is needed to account for the number of independent hypotheses tested. In some instances the independence of several hypotheses may not be clear. For these cases, techniques such as Monte Carlo calculation will be used to estimate an *effective* trial

factor so that the formula above will produce the correct probability distribution under the $H0$ assumption of zero signal. The value of p will be referred to as the *pre-trial* chance probability, and $P_{\geq 1}$ will thus be referred to as the *post-trial* chance probability.

For the case at hand, 340 days had been examined. The post-trial chance probability for a fluctuation to result in an excess of events at least as large as that observed on *any* day during the observation period is therefore

$$P_{excess} = 1 - (1 - P_{pre-trial})^{340} \sim 340 \times P_{pre-trial} = 0.06 \qquad (5.3)$$

Search for "Bursts"

The next part of the analysis procedure was to prepare for a study of source periodicity by separating out a segment of the data where the relative amount of potential signal is largest. This separation was accomplished in two steps: First, the angular size of the source bin was increased to include more potential signal by maximizing the observed excess. This maximum occurred for a bin of dimensions $4.1° \times 4.1°$ in which 46 events were observed when 24 were expected. Assuming that the distribution of signal from a point source can be described by a 2-dimensional Gaussian distribution with σ=0.8 degrees (the predicted angular resolution of the array), this bin size is expected to contain ~98% of the signal, as opposed to the ~72% expected in the 2.3 degree bin. The second step was then to look for additional structure in the distribution of event arrival times within this bin during the day in an effort to locate possible "bursts" of shorter term emission. An integral rate plot (**figure** 5.1) indicated two bursts, each about 30 minutes in duration. Burst **A** occurred at ~ 35° from the zenith, as the source was rising, and consisted of 7 events when 0.5 were expected. Burst **B** occurred near zenith and consisted of 10 events when 2.6 were expected. Neither the chance probability for the event excess observed in the larger 4.1 degree bin, nor for the observed burst structure were accounted for in the final assessment of significance due to the *a posteriori* nature of these searches.

Periodicity Study

The 17 events of bursts **A** and **B** were then examined for evidence of pulsar periodicity. A period range of ±0.3% about the X-ray pulsar period (1.2378 seconds) was considered in order to take into account possible deviations from this period suggested by other experiments [4],[5]. Individual event times were adjusted to account for the motion of the neutron star in the Hercules X-1 binary system relative to the solar system according to the ephemeris of Deeter, Boyton and Pravdo [34]. An additional correction for the earth's motion relative to the solar system barycenter was taken from the approximate expression (accurate to ~0.1 seconds) given by the same authors. The Protheroe statistic [65] was then chosen *a priori* to characterize the significance of the observed phase alignment at any given period.

The most significant phase alignment for burst **A** was found at the period 1.23572±0.0004 seconds, and for burst **B** at the period 1.23575±0.0003 seconds. The "errors" quoted for the period measurements correspond to $\frac{1}{2}$ of an independent Fourier interval relevant to the duration of each burst. The final significance for these observations was obtained by first performing a single period analysis on the combination of events found in bursts **A** plus **B**. For the combined data, a period of 1.23568 was found to result in a pre-trial probability of 3×10^{-7} for a chance fluctuation to result in a phase alignment at least this strong at any *particular* period. Due to the time separation of the two bursts, alignment of the relative phase between them tends to be more probable than if a continuous time segment were being analyzed. Such an alignment may not necessarily be a characteristic of the signal, but can simply be an artifact of the global time structure of the data collected [66]. This effect was taken into account by obtaining the post-trial significance of the observed Protheroe power with a data-specific Monte Carlo calculation in which random fractions of the pulsar period were added to each event time. In this way, the phases of individual events can be randomized while still preserving the global time structure of the data. This Monte Carlo calculation was used to obtain an effective trial factor of 390 for the period scan. An additional factor of 3 was also assessed for choosing the most significant of the following analysis scenarios: 1)

Period analysis of burst **A** only; **2)** Period analysis of burst **B** only; **3)** "Coherent" period analysis of bursts **A** plus **B**. The final post-trial chance probability resulting from the periodicity analysis was therefore given as:

$$P_{periodicity} =\sim 390 \times 3 \times P_{pre-trial} = 3.3 \times 10^{-4} \tag{5.4}$$

Combination of Probabilities

Because the pulsar period is much shorter than the observation time of one source transit, the probabilities $P_{periodicity}$ and P_{excess} are independent, and may be combined as such. Multiplication of these probabilities will not, by itself, result in a correct estimate of the significance for the combination (as was incorrectly presented in the 1988 publication of this result). If this were the correct estimate, one would always gain significance by combining the results of independent measurements in this way, even if they were individually 90% probable. One must take into account the fact that a *critical* value of the probability product (the value above which the result is considered "interesting"), can be arrived at in several ways. This is illustrated in figure 5.2 [67], which plots the probability combinations of P_1 and P_2 whose product equals some fixed value α. The chance probability for the product $P_1 \times P_2$ to result in a value of α or less, is then given by integrating the area below the curve shown. This results in the expression:

$$P_{combined} = P_1 P_2 (1 - log(P_1 P_2)) \tag{5.5}$$

For the more general case of combining n probabilities in this manner, the overall probability is derived according to the Fisher test [68] from the quantity $-2log(\prod_{i=1}^{n} P_i$ which is distributed as χ^2_{2n}.

Circumstances may arise where the full range of probabilities for P_1 and/or P_2 are not relevant owing to physics constraints. For example, the degree of phase alignment (characterized by $P_{periodicity}$) must be consistent with the estimated number of signal events (*i.e.* the observed event excess). For the case of combining two probabilities, P_1 and P_2, each restricted in their upper bounds by constraints c_1 and

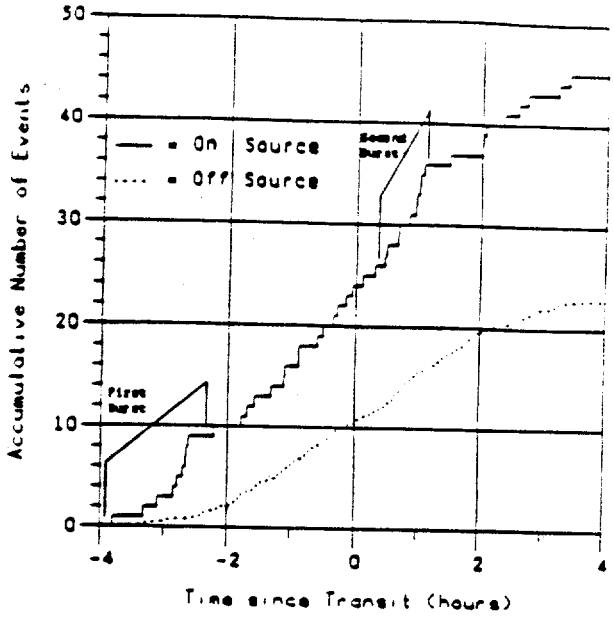

Figure 5.1: Cumulative number of events versus time for data from the direction of Her X-1 on July 24, 1986 and for data from neighboring off-source bins at the same declination [3].

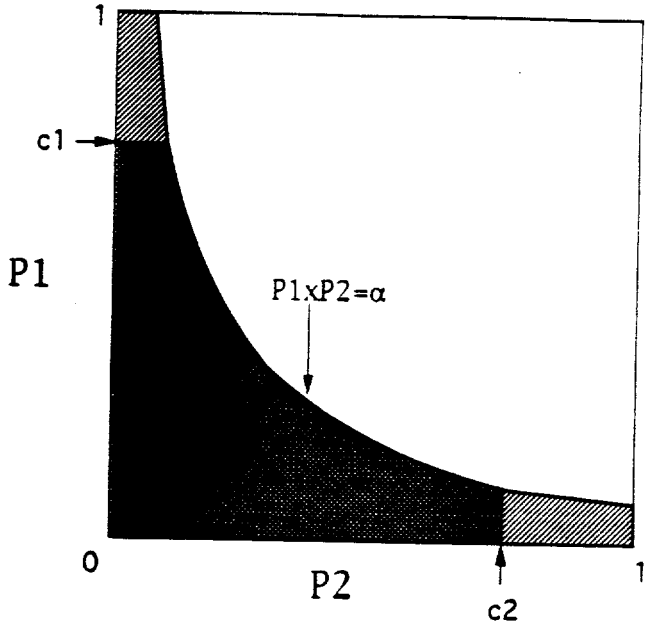

Figure 5.2: Range of probabilities bounded by a critical value of α, defined as the product of probabilities P1 and P2. C1 and C2 are *a priori* restrictions on the ranges of P1 and P2 respectively. The probability associated with α is given by integration of the shaded region.

c_2 that have been decided upon *a priori*, integration of the appropriate contour of figure 5.2 yields:

$$P_{combined} = P_1 P_2 (1 - log(P_1 P_2) + log(c_1 c_2)) \tag{5.6}$$

This modification has little effect on the final result unless the product of the constraints is of the same order of magnitude as the product of the individual probabilities. For the example of insuring consistency between phase alignment and event excess, this is rarely the case. Questions may also be raised as to what *a priori* choices for these constraints are reasonable. An alternative (and possibly less ambiguous) approach for this particular situation is to avoid using any constraints in the combination of probabilities, and then to address the question of consistency between phase alignment and event excess as a separate issue. Several statistics are available for such a consistency test, including those of Lewis [69].

Taking this latter approach, the combination of P_{excess} with $P_{periodicity}$ yields a final chance probability of 2.3×10^{-4} (about an order of magnitude larger than the previously published value). Due to the burst selection, which enhanced the amount of potential signal in the data subset used for periodicity analysis to $\sim$80%, consistency between the observed phase alignment and the event excess in that data subset (17 when $\sim$3 were expected) is guaranteed.

Discussion and Re-Analysis

Details of the analysis presented in this section will be interwoven with extended discussions of statistical issues. For clarity, a brief review of the analysis procedure will therefore be presented in the concluding section of this chapter.

Special Treatment of Source Events

In the original analysis of Her X-1, a variety of criteria were imposed on air showers in the data set in an effort to filter out events reconstructed with relatively poor angular resolution. First, the space-angle difference between event directions

reconstructed with independent, detector subsets of the array were used as an indicator of angular resolution. Events with unusually large or unreconstructable values of this parameter were eliminated from the data set under consideration. Secondly, the average squared-deviation of particle arrival times measured in each detector from a fit to the showerfront plane was used as another indicator of angular resolution. Events with unsually large values of this parameter were also eliminated from consideration. However, even if the events that do not pass these criteria possess somewhat worse angular resolution, significance may still be lost in removing them owing to the potential number of signal events in this class that may still have been reconstructed to be within the source bin. In fact, this rationale has been used to justify the inclusion of events with ill-defined core locations in source analyses [59]. Such arguments have recently been justified in studies of cosmic-ray occultation by the sun and the moon [70]. Furthermore, all other analyses of the CYGNUS data set have been performed without imposing the requirements mentioned above.

Another example of special treatment of the data associated with potential sources involves the use of the measured showerfront arrival times in reconstructing the direction of the primary particle. When fitting the arrival times of particles in the showerfront, a "curvature" correction must be made to account for the fact that the measured arrival time in a given detector depends on the measured pulse height as well as the radius of that detector from the core of the shower (see Appendix E). A technique that was employed at that time of the Hercules observation was to allow the degree of curvature correction to be a variable parameter in the showerfront fit on an event-by-event basis. In order to reduce computation time, this additional parameter was fit only for showers that were initially reconstruction to be in the vicinity of selected sources. Application of the computer simulation described in Appendix A indicates that this procedure of curvature variation

does not improve the angular resolution, but actually degrades it to some extent. The reason for this is that the curvature correction does not significantly change in form from event to event, so that allowing its value to vary relaxes a valid constraint of the χ^2 minimization.

The re-analysis of the Hercules X-1 data that will be performed in following sections will employ a fixed value of curvature and no additional selection of recorded events. As a result, slight changes in angular reconstruction and event excess calculations should be expected.

Optimal Sizes for Angular Bins

Assessing the probability for emission typically involves tests of event excess (Poisson probability), and/or periodicity studies (usually Rayleigh or Protheroe tests). A question naturally arises as to the choice of the angular bin size that determines the acceptance of events for a given test, assuming some intrinsic angular resolution of the experimental apparatus. More specifically, one would like to make an *a priori* choice of angular bin size that will, on average, maximize the significance of a true signal based on the predicted relative abundances of signal and background events within that angular bin.

In the limit of large numbers of expected events, it is well known that the correct quantity to maximize in the case of the Poisson test is $\frac{\#Signal}{\sqrt{\#Background}}$, where the signal is assumed to follow a two-dimensional Gaussian distribution and the background increases as the area of the angular bin. Most periodicity tests also approach this dependence in the limit of large statistics. If the angular resolution is defined by the standard deviation (σ) of the two-dimensional Gaussian distribution, then optimization of this quantity results in a bin size corresponding to a circle with a radius of $\sim 1.6\sigma$. However, this argument breaks down for small numbers of expected events, where the form for the dependence of significance on signal and background changes. This limit of small numbers becomes particularly important when searching for emission over short time intervals, where the expected number of background event may be quite small.

Simulation studies have been carried out to determine empirical parameterizations of the optimal angular bin radius as a function of expected number of background events for the cases of Poisson, Rayleigh and Protheroe tests. The results are as follows:

Test	Radius of Optimal Bin (units of σ)
Poisson	$1.6 + 0.7e^{-0.88N^{0.36}}$
Rayleigh	$1.6 + 7.4e^{-2.29N^{0.14}}$
Protheroe	$1.6 + 3.9e^{-1.76N^{0.19}}$

Table 5.1: Optimal bin radius for various tests.

Where N is the number of background events expected to fall within a circle with a radius of 1 unit of angular resolution (σ). Note that these formulas asymptotically approach the expected value of 1.6σ for large N. Any possible dependence of the optimal bin size on signal strength and/or signal phase width (for the cases of Rayleigh and Protheroe tests) was found to be weak. These formulas are shown graphically in figure 5.3.

The use of a square bin (as is often more convenient) equal in area to the optimal circular bin will result in only a slightly reduced estimate of significance. When expressed as the number of predicted standard deviations from a normal distribution, the use of a square bin reduces the average significance of a signal detection by about 1.5%.

Since the 1986 Hercules observation, additional information regarding the angular resolution of the array has been obtained based on the observed shadowing of cosmic rays by the sun and the moon [70] (figure 5.4). This indicates an average angular resolution of 0.7 (as opposed to 0.8) degrees. However, application of the formula above for Poisson excess predicts an optimal bin of radius 1.8σ (as opposed to 1.6σ). These effects compensate each other and the net result leads to a predicted optimal, square bin length of 2.3 degrees on a side, as was originally chosen.

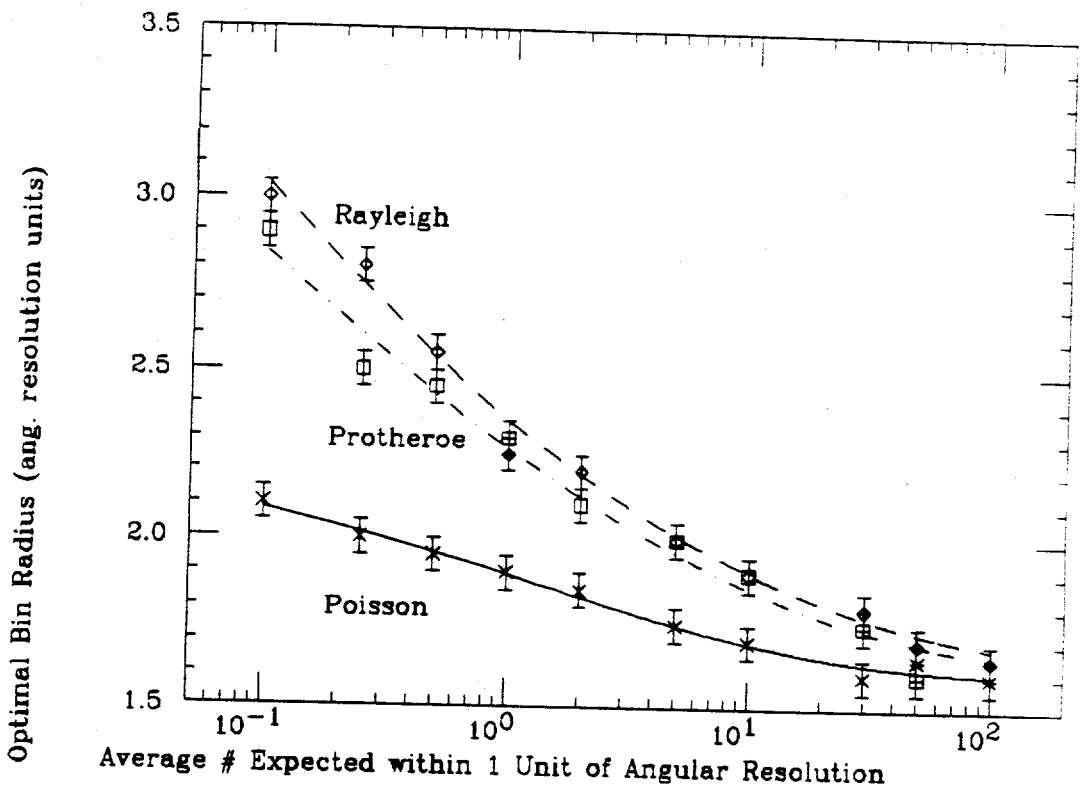

Figure 5.3: Optimal bin radius for various tests as a function of background expected in a circular bin 1 angular resolution unit in radius. Note: 1 angular resolution unit is defined as σ of a 2-D Gaussian that best reflects uncertainties in angular reconstruction.

The Shadow of the Sun

I long to touch the vacuum rare (although the smell is deafening),
For tracks of Leprechauns are there, which form a straight, uncurving ring.
There I'd fish in solid stone, and use for bait my finest catch;
Together then I'd go alone, to watch the eggs of flowers hatch.
I like to read by dark of night, and remember what I can't recall
About directions left of "right," the length of "wide," the width of "tall."
And so I dig down to the sky, to quench my thirst with hot, dry air,
And always answer questions, "why?" and look for things that are not there.
You'll find that all these lies are true, when you begin what has been done;
So always buy your antiques new, and seek the shadow of the sun.

- S.B. -

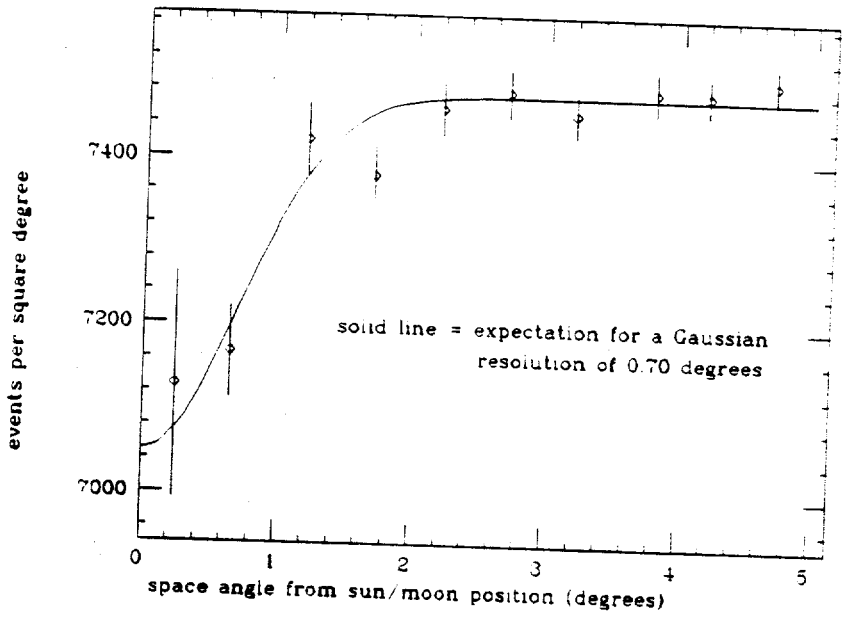

Figure 5.4: Events per square degree as a function of reconstructed space angle from the sun/moon position. The deficit to the left is due to the shadowing of cosmic rays by the sun/moon. The solid line shows the expected result for a Gaussian angular resolution of 0.70 degrees (derived from a maximum likelihood analysis). The data includes all showers with directions reconstructed to within 5 degrees of the sun/moon position that have been collected up to May of 1991.

For the periodicity analysis of the bursts, where $\sim$ 3 background events were expected in a square bin 4.1 degrees on a side, the formula for the Protheroe tests given above indicates an optimal bin of radius 2.6σ. This corresponds to an equal-area square bin of length 3.2 degrees on a side.

Estimation of Significance in a Binned Analysis of Event-Excess

The determination of the number of background events expected within a selected angular bin is usually based on the number observed in "off-source" bins of equal area that traverse a similar region of sky. Care must be taken to insure equal exposure and uniform detector response during the transit of on-source and off-source bins. The implementation of these constraints typically involves data selection (resulting in the loss of some portion of the data), and often limits the accuracy to which the background can be determined by limiting the number of off-source bins that can be used.

An alternate approach involves a Monte Carlo integration of the measured background event rate over the source bin [71], [72],[74]. This is accomplished by associating the direction of each measured event in local coordinates (θ, ϕ) with N different event times randomly sampled from the measured rate distribution of all detected events. In celestial coordinates, this process amounts to a simple translation in right ascention. The expected background is then just the number of translated events that are placed within the source-bin, divided by N. The accuracy of the integration improves approximately as $\frac{1}{\sqrt{N}}$, and is limited by the number of independent direction-time associations that can be made from the data. Since the actual distribution of measured event times is used, all aspects of detector rate variations (air-pressure changes, detector off-times, etc.) are automatically taken into account. It is assumed that the number of signal events is small compared to the background events that populate the declination band of the source (i.e. those events capable of being translated into the source bin), and that the angular dependence of the event rate does not change over the course of the integration.

Given the measured and predicted number of events within an angular bin centered on the source, one must then determine the chance probability for any observed excess above expectation. The problems involved in such a determination, including an accurate accounting of the uncertainty in the background estimation, have been described in detail by Li and Ma [75]. In their paper, Li and Ma derive the following likelihood ratio:

$$\lambda = [\frac{\alpha}{1+\alpha}(\frac{N_{on}+N_{off}}{N_{on}})]^{N_{on}}[\frac{1}{1+\alpha}(\frac{N_{on}+N_{off}}{N_{off}})]^{N_{off}} \qquad (5.7)$$

The quantity $-2log(\lambda)$ asymptotically follows a χ^2 distribution with 1 degree of freedom [76], so that $\sqrt{-2log(\lambda)}$ is approximately distributed as a standard, normal variable. This parameterization breaks down for small numbers of events, although it stills does suprisingly well on the positive tail of the distribution as indicated in figures 5.5a and 5.5b. The non-zero average that is typical of the distribution of Li-Ma standard deviations approaches zero as the number of expected events increase, as shown in figure 5.6.

Avoiding Bins: Maximum Likelihood

Although the choice of bin sizes used in the original analysis can be justified with the arguments previously given, an un-binned approach that avoids such choices would be preferable and less ambiguous in appearance. An obvious candidate for such an approach is that of *Maximum Likelihood*. Since hypothesis discrimination in such a test involves more specific information regarding the background and source hypotheses, it is a more powerful technique than the binning method previously described (provided that signal and background behave as predicted). The average gain in significance for a true signal is about 10% in the number of standard deviations [77], which corresponds to a factor of about 5 for the case of the 1986 burst observation. A Maximum Likelihood approach also leads to a more "stable" estimate of significance under alternate analysis scenarios, as will be discussed below. However, the application of this technique can become time-consuming in

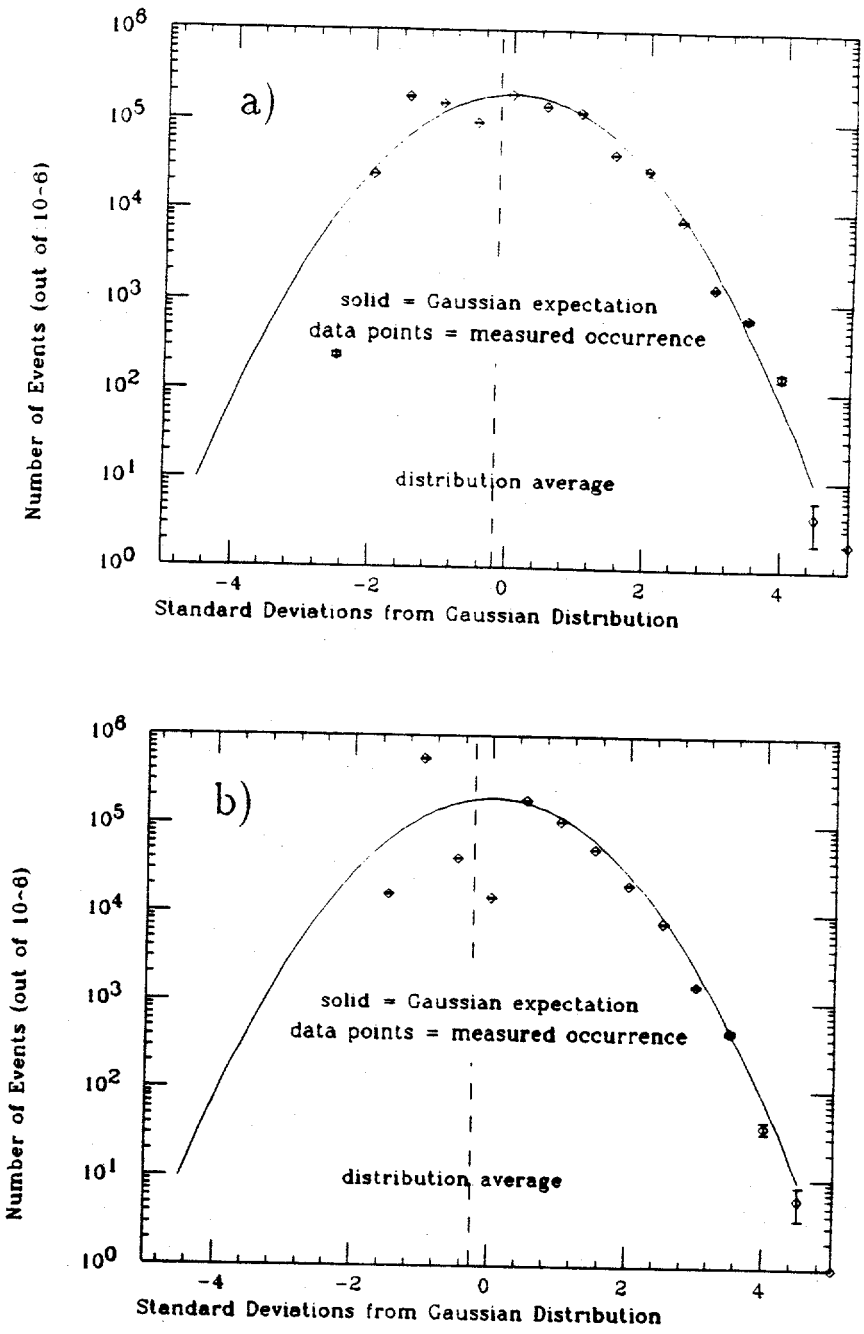

Figure 5.5: Observed occurence of standard deviations calculated by the formula of Li and Ma under $H0$ compared to the Gaussian expectation: a) 1 source bin, 5 background bins, with an average of 1 event expected in each; b) 1 source bin, 20 background bins, with an average of 0.5 events expected in each.

some cases. Therefore, the following approach will be adopted for source searches: binned analyses will be used to initially estimate the significance of possible emission. Those episodes that are deemed to be "interesting" will then be subjected to further scrutiny via maximum likelihood, and it is this test that will be used to assess the final level of significance for the episode.

For the application discussed here, the *Likelihood Ratio* will be defined as follows:

$$L = \frac{\prod_{i=1}^{N}(N_s P_s(i) + (N - N_s)P_B(i))}{\prod_{i=1}^{N} N P_B(i)} \tag{5.8}$$

Where N= the total number of detected events, N_s= the number of signal events assumed for this hypothesis, $P_s(i)$= the probability for the ith event to result from a distribution of signal, $N - N_s$= the number of background events assumed, and $P_B(i)$= the probability for the ith event to result from a distribution of background. The value of L characterizes the likelihood of the hypotheses H1 (signal+background) relative to H0 (background only). The value of N_s is varied so as to maximize L. In practice, not all detected events need be considered, as long as a sufficiently large region of the sky around the source is used so as to guarantee that $N_s << N$, so long as the probability distributions for P_s and P_B are properly normalized within this region. Figure 5.7 shows the predicted relative gain in significance compared to a standard, binned analysis as a function of the radius chosen to define the likelihood region. A radius of greater than $\sim$7 times the rms angular resolution is suggested by the figure, or a region of radius 5° for an estimated average angular resolution of 0.7°. The angular distribution of source events is assumed to follow the 2-dimensional Gaussian function

$$P_s = \frac{\theta}{\sigma^2} exp(-\frac{\theta^2}{2\sigma^2}) \tag{5.9}$$

where θ is the space-angle between a given event and the source position, and σ is the rms angular resolution due to the uncertainty in the reconstructed direction of the event. For the purposes of this study, σ is taken to be 0.7° for all events. This technique can be improved if the angular resolution is characterized on an event-by-event basis, although the relative improvement in sensitivity is typically small.

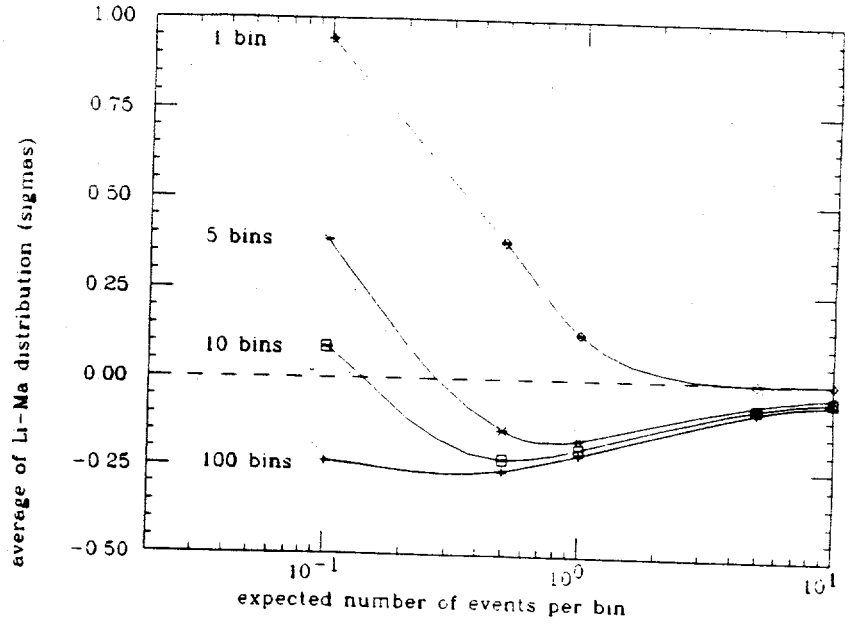

Figure 5.6: Average of the distribution of standard deviations calculated by the method of Li and Ma for various numbers of background bins as a function of expected background per bin.

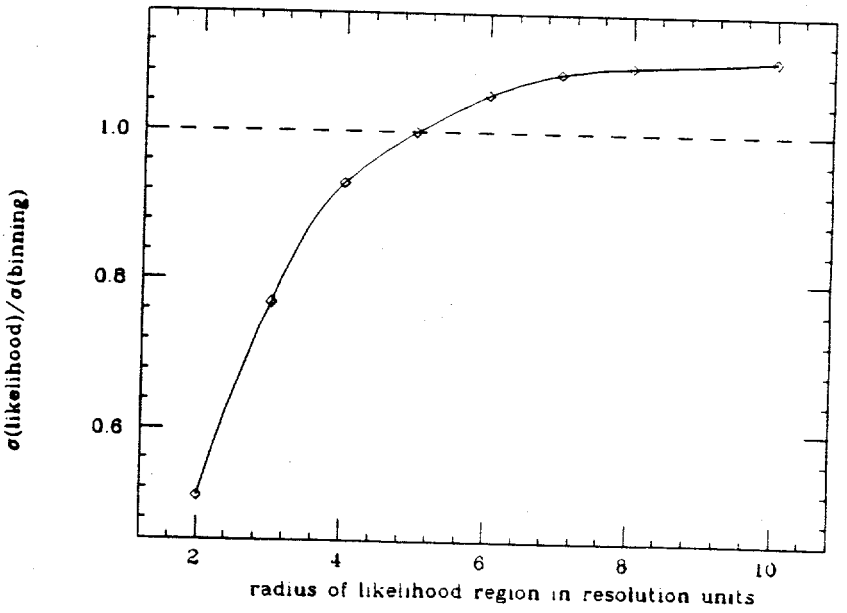

Figure 5.7: Fractional gain in the number of standard deviations for a hypothetical signal obtained for a maximum likelihood approach compared to binning. This gain is plotted as a function of the radial extent of the angular region used in the likelihood analysis.

One indication of this is shown in figure 5.8, which shows the predicted average significance of a hypothetical signal versus the ratio of assumed to true resolution, for both likelihood and binning techniques. Note that the likelihood approach is less susceptible to an error in the assumed resolution than binning techniques.

A related point has to do with the *stability* of a particular result for a given change in the assumed angular resolution. For example, consider a given data set containing signal that is first analysed using the true angular resolution of the array, and is then re-analysed with an assumed angular resolution that is 50% larger. Given this re-analysis, it is of interest to know what typical variations (as opposed to the average change) in the significance level can be expected. Figure 5.9 shows the variation in estimated significance, in terms of the fractional change in the number of standard deviations above background, for both binning and likelihood approaches under the scenario just described. Note that the distribution is substantially narrower for the likelihood case, indicating that the estimate of significance is more stable under a re-analysis of the data.

Given the *probability density function* (PDF) for source events (equation 5.9), a similar definition must be made for background. If background events were distributed uniformly throughout the sky, the number of such events within a given angular radius from the source would scale as the square of that radius. However, this form is modified is due to the fact that the event rate is a strong function of zenith angle. The functional form for this rate can be parameterized as follows :

$$Rate \simeq cos^{\alpha}(\theta) exp(-\frac{\beta}{cos\theta}) \tag{5.10}$$

where α is -0.79 and β is 7.6 for the CYGNUS data [78]. For simplicity, however, this form will not be used to account for the rate dependence. Instead, the data itself will be used to find the expected number of events as a function of the space-angle from the source position, which provides a more natural coordinate system than zenith and azimuth.

From an examination of off-source events using the Monte Carlo integration technique described in the previous section, the integral density distribution of background events as a function of space-angle, θ, from the source position is shown

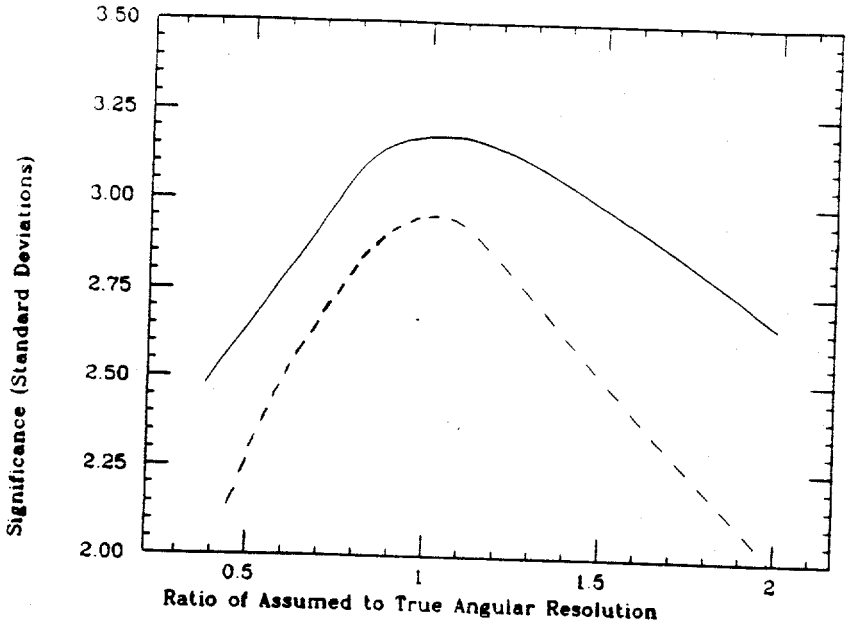

Figure 5.8: Predicted average significance of a hypothetical signal versus the ratio of assumed to true resolution for likelihood (solid) and binning (dashes) techniques.

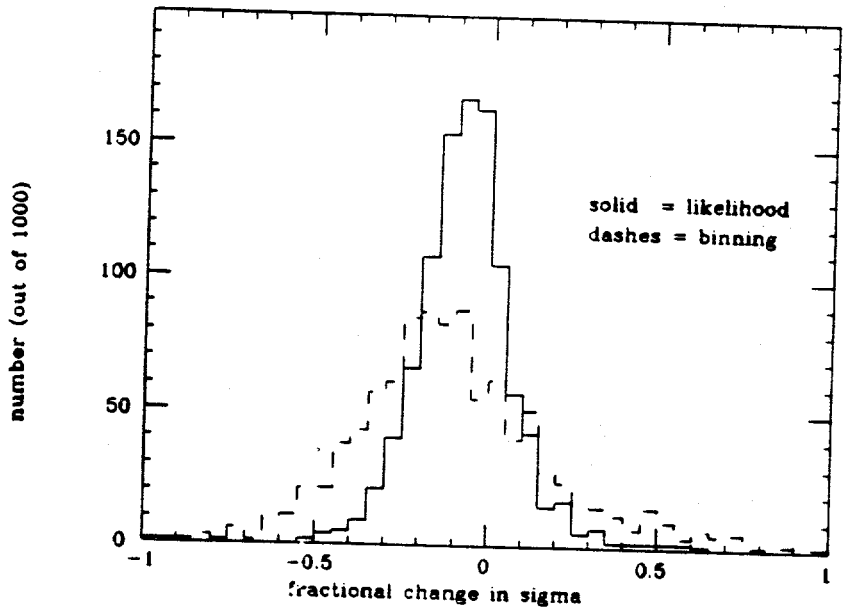

Figure 5.9: Distribution of fractional changes in the number of standard deviations for a hypothetical, 3σ average signal, under a re-analysis using a 50% larger assumed resolution for both maximum likelihood (solid) and binning (dashes) approaches.

in figure 5.10. It has been normalized to $\rho = 1$ at θ=5 degrees. This distribution can be parameterized by $\rho_{integral} = 0.0426\theta^{1.96}$, indicating that the zenith-dependent event rate does not significantly effect the naive θ^2 expectation. The normalized *differential* probability density for background events is thus:

$$P_B = \rho_{diff} = 0.083\theta^{0.96} \tag{5.11}$$

Given these probability densities, figure 5.11 shows the results of applying the likelihood ratio test to the Hercules X-1 data of July 24, 1986. In this figure, $-2log(L)$ is plotted as a function of the trial number of signal events. The maximum occurs for a value of N_s=19 events, in good agreement with the excess of events that was observed in the 4.1 degree bin of the original analysis. This corresponds to a flux of

$$\Phi = \frac{19}{(4hr)(10^4 m^2)} = 10^{-11} cm^{-2} s^{-1} \tag{5.12}$$

The results for three assumed resolutions other than 0.7° are also shown for comparison. Note that, as previously indicated, the significance level is not critically dependent on the specific choice of angular resolution. Given the inherent uncertainties, the angular distribution of these events is not at all inconsistent with the predicted resolution. The chance probability for the observed maximum likelihood ratio is obtained from the parameter $-2log(L_{max})$, which is asymptotically distributed as a χ^2 distribution with "n" degrees of freedom, where "n" is the number of parameters that were varied to obtain L_{max} [76]. In this case, $n = 1$ (only the number of possible signal events was varied), and $-2log(L_{max})$=20.5 . This corresponds to a chance probability of 6×10^{-6}. In fact, since physical constraints require that only *positive* signals be considered (*i.e.* we are not interested in event deficits associated with the source), this number should be divided by 2 to yield a final pre-trial probability of 3×10^{-6}. This number has been verified by application of a data-specific Monte Carlo calculation that involved sampling the measured angular distribution of background events. The answer is about a factor of 50 more significant than that quoted in the original analysis. The lack of both the additional

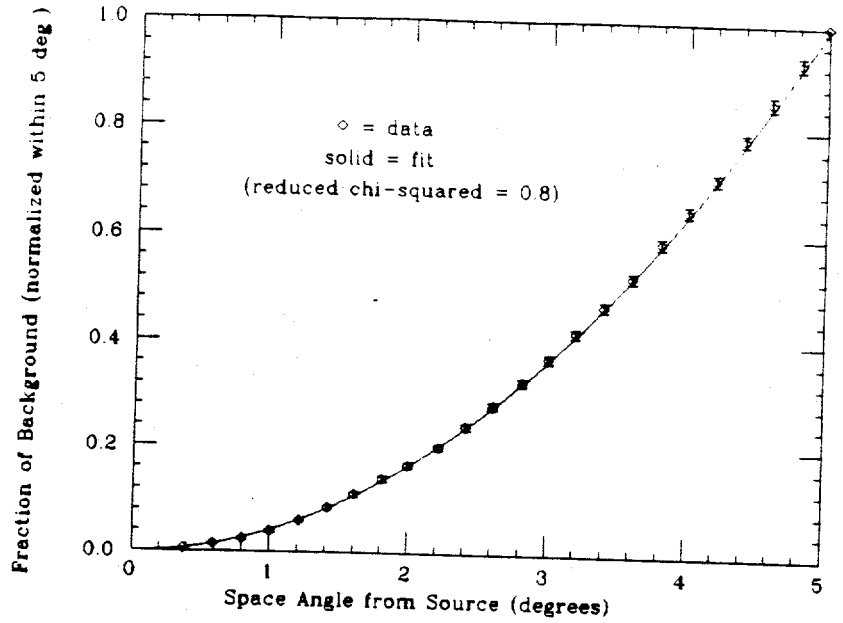

Figure 5.10: Integral density distribution of background as a function of space-angle from the source position. The reduced χ^2 for the fit parameterization (solid line) is 0.8.

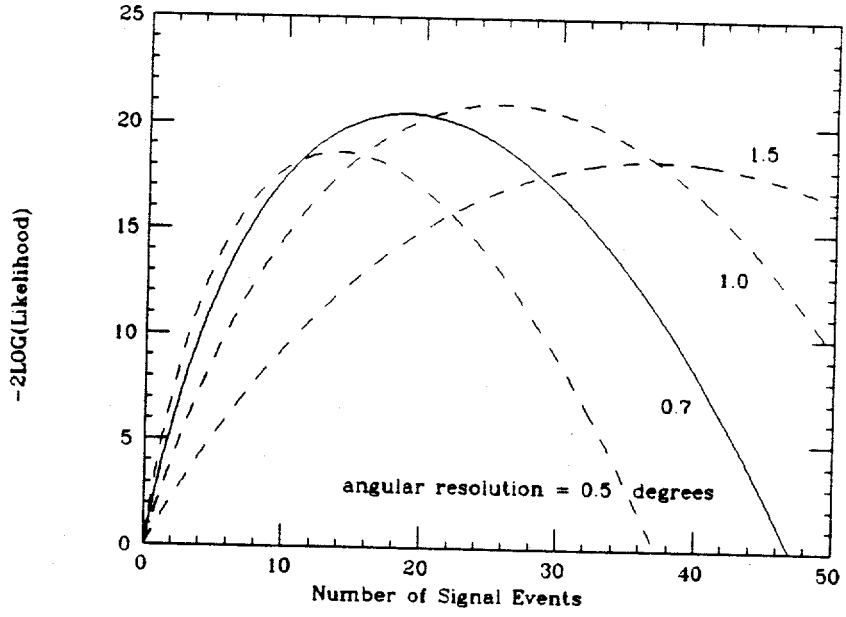

Figure 5.11: $-2log(L)$ versus number of trial signal events for the *a priori* chosen resolution of 0.7 degrees (solid), and for resolutions of 0.5, 1.0, and 1.5 degrees (dashes).

event selection criteria and variable curvature fits accounts for a gain of a factor of 5 in significance in the standard binned analysis. The rest of the gain (an additional factor of $\sim$10), is a result of the likelihood analysis.

A Monte Carlo calculation has been used to estimate the expected gain in significance due to the application of a maximum likelihood tests, under the $H1$ hypothesis (signal+background), for the specific scenario of the observed event excess corresponding to the original binned analysis. Assuming that the average angular resolution for the source event reconstruction is as predicted, the observed gain in significance due to the application of the Maximum Likelihood analysis is expected to occur 30% of the time (see table below).

Occurance	Minimum Relative Gain in Significance from Likelihood vs Binned Analysis
90%	0.3
80%	0.7
70%	1.4
60%	2.4
50%	4.1
40%	6.8
30%	13.2
20%	29.3
10%	87.0

Table 5.2: Predicted gain in significance based on a Monte Carlo calculation of the July 24, 1986 scenario

Ethics of Re-Analysis

The results of the previous section raise an important question regarding the re-analysis of data: "Is such a study *a posteriori* and, if so, are there trial factors associated with manipulating the data in this manner to achieve a more significant result?" Recall that trials must be assessed for each ***independent*** hypothesis that is tested. The two analyses of event excess discussed above are clearly ***not*** indepen-

dent. In fact, the question being addressed in both cases is identical: "What is the probability that the observed density distribution of events resulted from a background as opposed to a signal distribution?" In both cases information regarding the expected distribution of signal events was used to optimize the test statistic (*e.g.* the choice of bin size in the original analysis). In the case of maximum likelihood, this information was used in a more explicit manner, leading to the expectation of better hypothesis discrimination.

Questions might also be raised as to the use of different event selection criteria (or lack thereof), and different curvature corrections. However, arguments have been presented to indicate that the method of analysis presented here is more consistent with our present understanding of both the array response and of the predicted behavior of any potential signal.

Clearly, the true answer as to whether the data represents UHE, point-source emission from Hercules X-1 is unknown. The best that can be expected is to *estimate* the probability relevant to this question. This probability estimate should be a *dynamic* quantity, that changes as better information relevant to the question is obtained. If *a priori* evidence exists that a particular test will provide a better estimate of this probability as compared with that used in a former analysis, this new test should be applied and the result adopted, whether it is more or less significant, as the current best estimate of the chance probability. Since the actual question regarding source emission has not changed, a trial factor to account for the choice of a more sensitive test statistic is not relevant. As a more extreme example, one should not have to pay a statistical penalty for correcting an analysis that is later found to have been insensitive or incorrect.

Selection of Bursts

In preparation for an analysis of source periodicity, the next step is to use the distribution of event excess to identify portions of the data that are likely to contain the highest percentage of signal events. This is based on looking for shorter duration "bursts" of higher intensity emission occuring throughout the source day.

The two bursts of the original Hercules analysis were initially chosen by visually scanning the integral rate plot of figure 5.1 for the fixed bin length of 4.1 degrees. Computer algorithms designed to find bursts were then developed as "independent" checks of this selection. One such algorithm [63] required a minimum number of events per burst, chosen so that a perfect phase alignment of this minimum number would result in a "sufficient" power to reject $H0$. This requirement is no longer relevant if a coherent analysis of the events in several bursts is to be considered. Another algorithm [79] involved variables that could be adjusted to choose bursts of various types, such as those already selected by visual scanning. As such, this algorithm cannot be considered to be a truely independent method. Neither approach assigns a chance probability level to potential bursts, making it difficult to determine which bursts should be judged to be "significant".

An alternate approach to searching for emission over a range of arbitrary time scales will be described in detail in chapter 8. This technique has been applied in the present case to produce a distribution of burst probabilities based on the observed event excess, for timescales of 10, 30 and 90 minutes. This method relies on a binned approach, where the bin size is chosen according to the formula given in table 5.1.

These probabilities are trial-corrected for the effective number of independent intervals in each timescale, as well as for searching the 3 different timescales. The choice of a *critical* probability level, P_{crit}, is still needed to decide whether or not a particular burst is "interesting" enough to be used in the periodicity analysis. In an effort to eliminate the arbitrary nature of this choice, the following approach was adopted: First, the distribution of pre-trial event-excess probabilities was scanned for each time scale to choose a *critical probability level* corresponding to the most significant occurance of n or more episodes with chance probabilities of P_{crit} or less (similar to the technique described in Appendix C). This corresponds to selecting those episodes that contribute most to the distortion in the expected distribution of burst probabilities at each timescale. Only those bursts with pre-trial burst probabilities less than the value of P_{crit} for each timescale are shown in figure 5.12. The next step is to select the most significant, non-overlapping intervals in this figure for

periodicity analysis. In the present case, 4 independent episodes of higher emission are observed. The first of these (6 obs., 0.6 expct.) is 90 minutes in duration and starts at a zenith angle of $\sim$ 35 degrees as the source is rising; the second (9 obs., 3.65 expct.) is another 90 minute burst that starts $\sim$90 minutes later; the third (3 obs., 0.35 expct.) is a 10 minute burst occurring near zenith; and the fourth (6 obs., 2.3 expct.) is another 90 minute episode occurring at a zenith angle of about 25 degrees as the source is setting. The first and third episodes correspond roughly to bursts **A** and **B** of the original analysis. Note that, according to table 5.1, a slightly larger bin size will be used in the periodicity analysis. The number of events in each burst may therefore change slightly under this analysis.

Choice of Periodicity Test-Statistic

A decision that must be made prior to performing a periodicity study is the choice of the test statistic to characterize the probability for phase alignment. The efficiency of a given test statistic depends on both the form of the light curve (*i.e.* the characteristic distribution of source emission as a function of phase), and on the predicted number of background events. The Protheroe and Rayleigh tests are two of the most frequently used statistics in VHE/UHE experiments, and represent relative extremes in their different operational ranges.

The Rayleigh *Power*, R_p, is defined relative to the Rayleigh statistic, $\bar{R}$, as follows [80]:

$$R_p = N\bar{R}^2 = \bar{S}^2 + \bar{C}^2 \qquad (5.13)$$

where

$$\begin{aligned} \bar{C} &= \frac{1}{N}\sum_i^N cos(2\pi\phi_i) \\ \bar{S} &= \frac{1}{N}\sum_i^N sin(2\pi\phi_i) \\ N &= \text{number of events} \\ \phi_i &= \text{phase of } i_{th} \text{ event} \end{aligned}$$

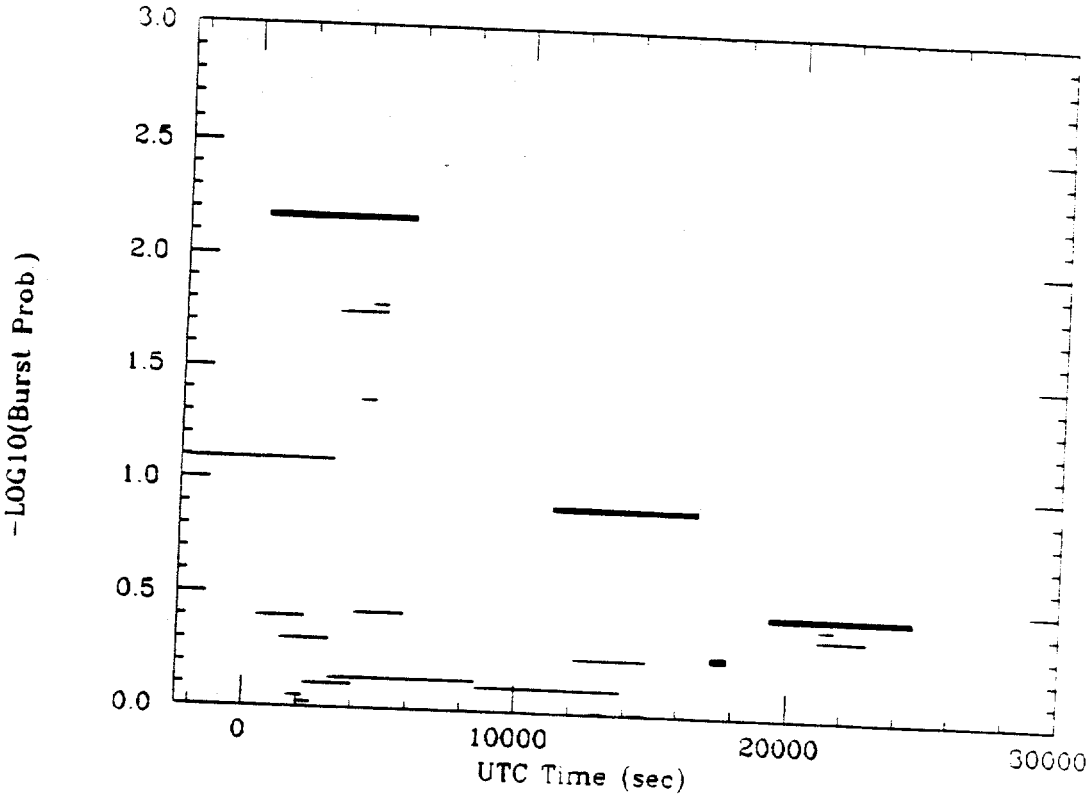

Figure 5.12: Trial-corrected probabilities for most significant bursts on time scales of 10, 30, and 90 minutes. The bold, horizontal lines represent the most significant, non-overlapping bursts within the day.

For large values of N ($\sim$ 100), the chance probability to exceed a given Rayleigh power is approximately e^{-R_P}. For values of N as low as $\sim$ 20, a simple polynomial correction [81] can be applied to extend the reliable range of this approximation. For smaller values of N, a Monte Carlo calculation must be used to determine the significance of phase-alignment (see Appendix D).

The Protheroe statistic is defined as [65]:

$$\Upsilon_N = \frac{2}{N(N-1)} \sum_{j=i+1}^{N} \sum_{i=1}^{N-1} \frac{1}{\Delta_{ij} + \frac{1}{N}} \tag{5.14}$$

where

$$\begin{aligned} \Delta_{ij} &= 0.5 - ||\phi_i - \phi_j| - 0.5| \\ N &= \text{number of events} \\ \phi_i &= \text{phase of } i_{th} \text{ event} \end{aligned}$$

The probability distribution for Υ_n can not be characterized by a simple, closed-form expression due to the fact that the Δ_{ij} terms are not independent. The formula by Uretsky [82] does not properly account for this, and is found to depart significantly from the true probability distribution for probability levels less than about 1%. The correct distribution can be obtained by Monte Carlo calculation. Such a method has been used to extend the previously published table of "critical" Υ_N values to probability levels as low as 10^{-7}, for $2 \leq N \leq 200$ (Appendix D).

The Protheroe test is very efficient for narrow light curves and for small numbers of events, whereas the Rayleigh test is best suited for wide light curves and for a relatively large number of expected events. Note that both tests attain their maximum significance for a δ-function light curve, but the Protheroe test achieves a larger power to reject the null hypothesis ($H0$) relative to the Rayleigh test in this case.

The Protheroe statistic also maintains a reasonable efficiency for detecting multi-modal light curves, unlike the Rayleigh test. Variants of the Rayleigh test, such as the Z_n^2 statistic [83], that involve the investigation of higher harmonics, have been developed for such cases. The Z_n^2 statistic is defined as:

$$Z_n^2 = N \sum_{j=1}^{n} (\tilde{C}^2 + \tilde{S}^2) \tag{5.15}$$

where

$$\begin{aligned} \tilde{C} &= \frac{1}{N} \sum_{i}^{N} cos(2\pi j \phi_i) \\ \tilde{S} &= \frac{1}{N} \sum_{i}^{N} sin(2\pi j \phi_i) \\ N &= \text{number of events} \\ \phi_i &= \text{phase of } i_{th} \text{ event} \end{aligned}$$

For large values of N, this parameter is distibuted as χ^2_{2n}. However, contrary to previous claims [84], the Z_n^2 statistic does not obey a χ^2 distribution for small values of N due to correlations in the phase-alignment at various harmonics.

A variation of the Z_n^2 statistic suggested by DeJager *et al.* [85] is the H_n test. This test essentially involves choosing the value of n in the Z_n^2 statistic that maximizes the significance for a given data set and accounting for the trial factor associated with this choice (note that this trial factor was not properly accounted for in the original incarnation of this test [84]). This test has good sensitivity for large numbers of events comprising a light curve with either a single peak or with small numbers of symmetric, multiple peaks.

Figure 5.13 compares the *power* of the Protheroe, Rayleigh and Z_{10}^2 tests as a function of the phase width of an injected hypothetical signal, assuming 100 background events plus 30 signal events. Symmetric, square-wave light curves of one, two and three phase peaks are considered. The *power* of the test is defined as the probability to reject $H0$ at a given confidence level (in this case 95%). Since it is only sensitive to the relative separation between phases, the Protheroe statistic maintains excellent power under a variety of light curves. The Rayleigh test performs somewhat better for the case of a broad, single-peaked light curve, but is relatively insensitive to multi-modal structures. Also note that for asymmetric, multiply-peaked light curves, the Rayleigh and Protheroe tests will attain slightly larger powers than for the symmetric case, whereas the power of the Z_{10}^2 test will decrease.

For the present case, the relatively small number of events involved indicates that the Protheroe statistic is the best choice. However, for cases involving a larger number of events, and given the potential uncertainties in source characteristics, it may be advantageous to choose a test that maintains a high efficiency over a broad range of light curves. One possible approach is to perform both Rayleigh and Protheroe tests and choose the better result, taking an appropriate statistical penalty for the choice. Monte Carlo calculations have been carried out to determine the trial factor associated with this choice as a function of the number of events. This is shown graphically in figure 5.14, and can be somewhat awkwardly parameterized as follows:

$$Factor = \frac{2arctan(0.009(log(N))^{3.5}) + \pi}{\pi} \tag{5.16}$$

Where N equals the number of events (phases) being analysed. This trial factor is 1 for very small numbers of events, where the value of both statistics are highly correlated, and asymptotically approaches 2 for large numbers of events, which is the maximum penalty to be paid for choosing the better of 2 completely independent hypotheses.

Exposure Bias and Periodicity Tests

The periodicity tests just described assume a uniform background distribution of phases. This is generally the case for periods that are short compared to the on-source exposure time (as is the case with the 1.24 second pulsar periodicity of Her X-1). However, for longer periodicities, exposure time may significantly affect the background phase distribution. One method to account for this is to first convert the measured phases into a new variable ,a "pseudophase", that is uniformly distributed, and to then apply the previously mentioned tests to the pseudophase distribution without modification. This approach has been employed by Meyhandan *et al.* [53]. Specifically, the approach is to assign each on-source event with the probability of obtaining a larger value of phase than what was measured, as determined from an off-source distribution of phases. This probability is then taken to be the pseudophase, and is uniformly distributed between 0 and 1 (by definition).

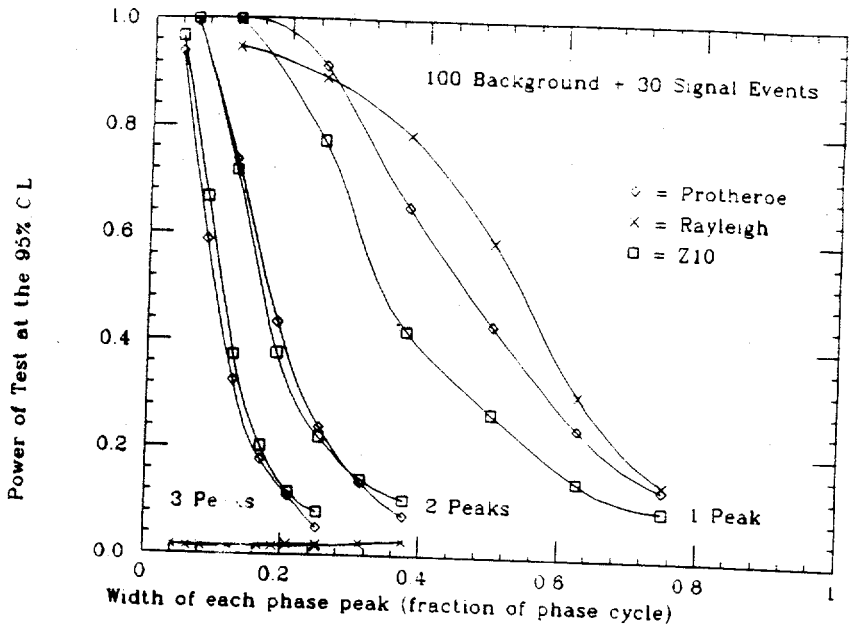

Figure 5.13: Power (at 95% C.L.) of the Protheroe, Rayleigh and Z^2_{10} tests as a function of phase width for an injected hypothetical signal of 30 signal events with 100 background events. Results for symmetric, square-wave light curves involving 1, 2 and 3 peaks are shown.

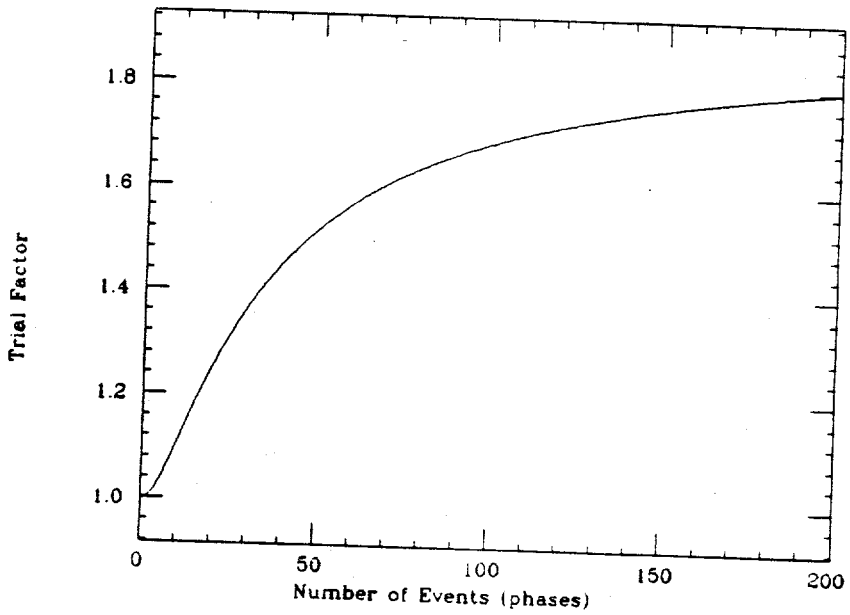

Figure 5.14: Trial factor for choosing the most significant result of Rayleigh and Protheroe tests as a function of the number of phases involved.

Although the light-curve of any potential signal will be appropriately modified in this new variable, standard periodicity tests can then be applied.

Combination of Bursts

Having chosen the statistic that will be used to test for phase-alignment, and having selected 4 bursts from the source day, several different phase analyses are possible: Coherent analysis of all 4 bursts, analysis of each burst separately, or coherent analysis of some combination of selected bursts. In order to remain sensitive to a large range of possible emission scenarios, the following approach will be taken: **1)** Assess the chance probability for coherent phase-alignment in all 4 bursts. **2)** Assess the chance probability for the most significant phase-alignment in any individual burst, or in any combination of bursts, accounting for the appropriate trial-factor for this choice. **3)** Finally, take the more significant result of either **1** or **2**, and assess an additional trial-factor for this choice.

This approach, which ultimately converts the problem into a choice between 2 different hypotheses, is a method of "ranking" possible emission scenarios in a statistically sound manner. Since the simplest scenario is to have significant phase-alignment among all 4 bursts, this hypothesis has been put on an equal footing with the sum of all other emission scenarios.

A Monte Carlo calculation of the specific scenario being considered indicates a trial-factor of 10 to account for the choice involved in **2**, and a factor of 1.5 for the final choice involved in **3**.

Formulation of Period Scan

The Hercules X-1 system (see chapter 3) has several well-established periodicities associated with it: a 1.24 second pulsar period, a 1.7 day orbital period, and a 35 day X-ray cycle associated with a precession of the accretion disk. Since the study currently being discussed is for time scales less than 1 source day, only the 1.24 second cycle is relevant to periodicity searches.

The pulsar period was measured by the X-ray satellite *TENMA* in 1983 [52] to be 1.2377942 seconds. Pulsations near this period were also observed in 1983 by ground-based telescopes at both infra-red and optical frequencies [86]. However, the optical observations indicated periods ranging from 1.2375 to 1.2387 seconds. Previous observations claimed by air-Cherenkov telescopes operating in the TeV energy regime [87], have also claimed periods ranging from 1.2367 to 1.2386 seconds, indicating that a large range of periods should be considered.

The Whipple collaboration has claimed an observation on June 11, 1986, of a 1.2358 second period in the VHE regime [4], blue-shifted by $\sim$ 3 Doppler intervals relative to the X-ray period. The Haleakala experiment, also sensitive in the VHE regime, observed a similar period of 1.2359 seconds on May 13, 1986 [5]. The CYGNUS group became aware of these other observations after an initial data analysis, but prior to the publication of the July 24 observation of a 1.2357 second period [3]. Knowledge of these VHE obsevations was indirectly used to justify the choice of the large period search range in the published version of the CYGNUS analysis. This raises the following question regarding the present re-analysis of the CYGNUS result: "Can knowledge of the Whipple and Haleakala results be legitimately used in formulating a strategy for a period analysis of the CYGNUS data?" Had the knowledge of the VHE observations come prior to the initial data analysis, an approach involving a specific test of the $\sim$1.2358 second period hypothesis would certainly have been justified. In another scenario, had the CYGNUS analysis proceeded prior to knowledge of the VHE results and involved a search for periodicity only at the X-ray period, later knowledge of the lower energy observations would have dictated a further investigation of the data in which the blue-shifted period would again be tested as a separate hypothesis. The question is therefore whether knowledge gained in the initial analysis of the CYGNUS data should effect an analysis strategy that is partially based on the Whipple and Haleakala observations. Clearly the answer depends on whether the probability estimates of the Her X-1 observations by the Whipple or Haleakula collaborations were influenced by knowledge of the CYGNUS result, thus leading to a circular argument. This does not appear to be the case. It is therefore reasonable to adopt an analysis strategy for the CYGNUS

data that takes account of the VHE results, although the results of such an analysis can clearly no longer be considered independent of the VHE observations. As such, a significance level resulting from the combination of the three observations [9] should not be considered. In fact, such a combination is problematical in any case due to the undefined trials associated with choosing only these particular observations for consideration.

An accounting must also be made for the fact that the blue-shifted period hypothesis is not the only one that would be considered in a comprehensive study. There are, in fact, potentially 4 different periodicity hypotheses of interest: **1)** Pulsed emission precisely at the X-ray period (interpolated from satellite observations); **2)** Pulsed emission within 1 Doppler shift of the interpolated X-ray period [86]; **3)** Pulsed emission at a blue-shifted period lying within the uncertainty range of the Whipple and Haleakala results ($\pm$ $\sim$0.0003 seconds); **4)** Pulsed emission that may occur at any in a wide range of frequencies centered on the X-ray period [87]. A more optimal procedure than that used in the original analysis is as follows: First test each of the 4 hypotheses mentioned above, accounting for the appropriate trial factors in each case. Then choose the most significant result and assess an additional trial factor of 4 for this choice. This approach of hypothesis testing is similar to that discussed at the end of the previous section regarding the combination of bursts.

Period Scans in the Absence of Preferred Bounds

Circumstances may arise where a lack of previous observational data, combined with uncertainties in orbital parameters, or uncertainty regarding the particle production and/or acceleration mechanisms may call for a search that extends to a large, undefined distance from some central value of "preferred" period. One approach that accounts for the trials associated with such a search is as follows: First define a large but finite range over which the search is to be performed (e.g. a range encompassing $N_{scan} = 10^4$ independent period hypotheses). Next, assess the chance probability for phase-alignment at each test period and correct for the appropriate trials that correspond to the effective number of independent period hypotheses, n_p,

that separate the test-period from the preferred period. Finally, choose the most significant of these "corrected" probabilities, and assess an additional trial factor to account for this choice. Since the probability of each test period has already been ~multiplied by n_p, the chance that this value will prove to be the smallest (i.e. most significant) in the search will clearly decrease with increasing distance from the preferred period as $\frac{1}{n_p}$. The additional trial factor that is needed to account for the search is therefore

$$Factor = \int_1^{N_{scan}} \frac{1}{n_p} dn_p = log(N_{scan}) \tag{5.17}$$

Oversampling in Periodicity Searches

In performing a period search, it is important to determine the appropriate separation between test periods as well as the relative independence of phase-alignment between these different test periods. If the data spans a length of time, T, then the maximum number of phase cycles of a given period, p, that can be observed is just

$$N_\phi = \frac{T}{p} \tag{5.18}$$

The change in the maximum number of measured phase cycles for a given change in period is then

$$\delta N_\phi = \frac{T}{p^2} \delta p \tag{5.19}$$

This corresponds to the relative change in phase that will occur between events at either end of the time interval for a given change in period. Therefore, when δN_ϕ is greater than 1, the alignment of phases corresponding to periods separated by δp are essentially uncorrolated. The value $\delta p = \frac{p^2}{T}$ thus defines the separation between "independent Fourier freqeuncies" (IFF), or, in this case, "independent Fourier periods" (IFP).

In determining the minimum separation between test periods that should be used, one should choose a value of δp such that the corresponding change in phase-alignment, δN_ϕ, is small compared to the phase-width of the potential signal's light-curve. If the light-curve is sinusoidal, spanning ~0.5 of the phase cycle, a reasonable

tolerance for a shift in phase-alignment might be $\delta N_\phi < 0.1$, corresponding to "10 times oversampling" of an IFP. Narrower light curves require larger oversampling factors.

Typically, it is best to use data-specific Monte Carlo calculations to determine the statistical penalty necessary to account for choosing the most significant phase-alignment of a search. However, assuming a uniform distribution of events within the time window of interest, this penalty can be estimated by the number of IFPs multiplied by an additional factor to account for the oversampling of each Fourier interval. Due to the non-independence of phase-alignment in oversampled periods, the trial factor does not increase linearly with oversampling, but reaches some "saturation" value when oversampled beyond some critical point. Assuming such a critical oversampling, an additional factor of 3 is often quoted as the appropriate value for a Rayleigh test [84]. In fact, Monte Carlo calculations indicate that the saturation value of the trial factor is not strictly constant, but also has some dependence on the pre-trial significance of the largest Rayleigh power. For the Protheroe test, similar calculations indicate a somewhat larger trial factor with a similar dependence on the pre-trial probability for phase alignment. The reason for this larger factor is clear from the previous discussion: the relative independence of phase-alignment between two different periods within an IFP is governed by the shape of the light-curve. For a given δp from the true period, a broad light-curve may not change very much in appearance whereas a δ-function light-curve will look dramatically different. The trial factors associated with oversampling in periodicity searches involving the Rayleigh and Protheroe statistics can be approximately parameterized as follows:

$$Factor(Rayleigh) = 2.2 - 0.5log_{10}(P) \tag{5.20}$$

$$Factor(Protheroe) = 4.1 - 0.5log_{10}(P) \tag{5.21}$$

Where P is the pre-trial chance probability for phase-alignment. These parameterizations have been fit to the results of Monte Carlo simulations involving the pre-trial probability range $0.5 > P > 10^{-6}$. For the case of the Rayleigh statistic, the dependence of the oversampling factor has been analytically derived in a recent

paper by Orford [88], although the exact solution cannot be conveniently expressed in closed form. It does, however, agree well with the above parameterization over the the range of probabilities specified.

Results of Periodicity Analysis of Bursts

The most significant phase alignment occurs for the combination of bursts 1 and 3, at a period of 1.235696 seconds, corresponding to the blue-shifted period hypothesis. A value of 7.07 for the Protheroe statistic was found for this case, corresponding to a probability of 1.5×10^{-6} for the 13 observed events (figure 5.15). A data-specific Monte Carlo calculation (as described earlier) was used to evaluate the effective trial-factor for the period scan. This calculation indicates a factor of 25. An additional factor of 4 is then assessed for the choosing the best of 4 period hypotheses that have been tested, and another factor of 15 for the combination of bursts. The full trial-factor is therefore 1500, resulting in a post-trial chance probability for the periodicity analysis of 2.2×10^{-3}.

Coherence of Bursts

The fact that the most significant test of the Protheroe statisic resulted from the combination of bursts 1 and 3, does not necessarily indicate that the bursts are coherent. The problem of treating bursts (or, more generally, data containing time gaps) as a continuous observation for the purposes of period-search analyses has been addressed in a recent paper by Lewis, Lamb and Biller [66]. The basic difficulty lies in the fact that a period shift that produces a minimal change in the relative phase distributions *within* each burst will still shift the relative phases *between* the 2 bursts according to the length of the burst separation. This enhances the ability to align peaks between bursts in a coherent search. A "search-induced" alignment of this kind is not due to any real coherence, but is simply an artifact of the time distribution of events. This will lead to an overestimate of the significance for phase-alignment unless steps are taken to account for this effect (such as using a data-specific Monte Carlo, as has been done in the current analysis).

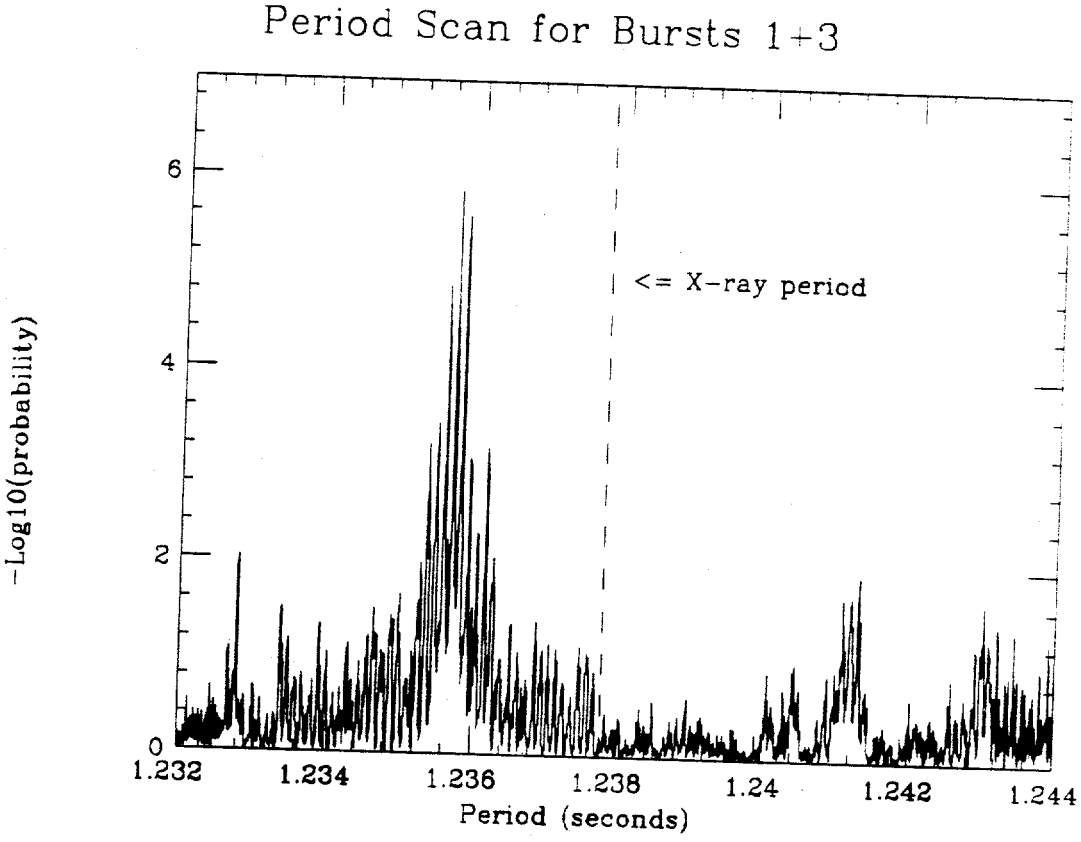

Figure 5.15: Large-window period scan for the combination of the bursts 1 and 3.

One method to determine the extent to which phase-alignment of bursts 1 and 3 can be demonstrated is as follows: Repeat the coherent scan for periodicity, but introduce random fractions of the 1.24 second period to the time-separation *between* bursts. This will randomly change the relative phase between bursts while still preserving the global time structure of the data. The number of such scans that result in a phase-alignment at least as strong as the actual observation will therefore give the probability for the apparent coherence to arise by chance. When this procedure is applied to bursts 1 and 3, this probability is found to be 80%. Therefore, although this does not necessarily indicate that the bursts are not coherent, the data cannot be used to justify the assumption of coherence.

Calculation of Period Uncertainty

The estimated uncertainty in the period determination was taken to be half of an IFP in the original analysis. However, as previous discussions have indicated, the ability to determine the period depends on the nature of the light curve. Several authors [89] [90] have developed parameterizations to approximate "one sigma" uncertainties in the period determination for a given Rayleigh power, assuming a sinusoidal light curve. However, errors in period are rarely distributed normally, and are a function of the actual time distribution of the recorded events (i.e. gapped data will produce more sidelobes in the frequency spectrum). Furthermore, the form of the light curve is generally not known *a priori* and it cannot be determined from the data independent of the choice of period. Finally, since the determination of the uncertainty in period assumes that $H0$ has already been rejected, the probabilities that are relevant to this problem are those related to fluctuations from a *signal* ($H1$), as opposed to a background distribution.

One approach to this problem is that of maximum likelihood, where the likelihood function is maximized for each period over a range of possible light curves.

The ratio of the maximum likelihood value at each period to that of the peak value (corresponding to the most probable period) can then be used to give the relative likelihood for each period under the $H1$ hypothesis. The range of allowed periods for various confidence levels can then be specified.

For the Hercules X-1 case, a parameterization of light curves will be used that allows up to two Gaussian phase peaks (appropriately normalized within the allowed phase region of 0 to 1), each possessing the same width. This width was allowed to vary, along with the phase position and signal content of each peak. There are thus 5 variable quantities: the peak width, the central phases of each peak, and the signal content of each peak. The difference in $-2Log(L_{max})$ with respect to the value at the favored period will therefore follow a χ^2 distribution with 5 degrees of freedom. The background distribution is taken to be uniform in phase. Figure 5.16 shows $-Log(L_{max})$ as a function of period for the coherent combination of the bursts 1 and 3. Both 90% and 99% confidence levels are shown. The spiked structure of this plot is primarily due to the time separation between the bursts. As stated in the previous section, it is principally this separation that prohibits the ability to determine whether the bursts are actually coherent. Consequently, figure 5.17 shows the incoherent sum of the likelihood scans for bursts 1 and 3. The fine structure that is present in this plot is primarily due to the low number of events in burst 3. The 90% confidence level is found to encompass a range of approximately ± 0.0004 seconds.

Note that if one were interested in determining the uncertainty in the light curve instead, this procedure could be inverted by maximizing with respect to the period for each type of light curve. The advantage of this approach over that of the Kernal Density Estimator [84] is that it more properly accounts for the fact that the uncertainty in the light curve is directly related to the uncertainty in the period determination. It also gives the relative probabilities for various light curves (*i.e.* uncertainties in the light curve) in more statistically meaningful terms.

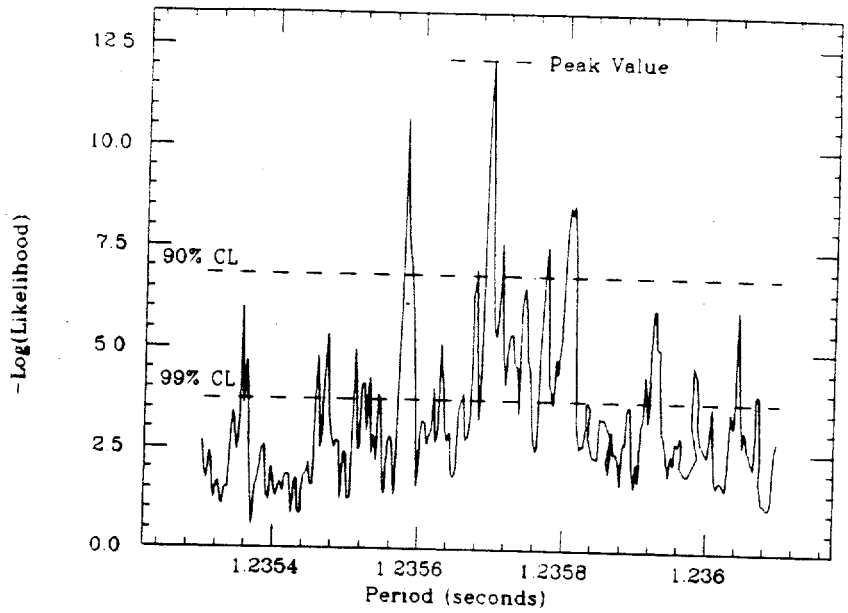

Figure 5.16: $-Log(L_{max})$ as a function of period for the coherent combination of the bursts 1 and 3. The value of likelihood has been maximized over various potential light curves. Both 90% and 99% confidence levels are shown (dashed lines).

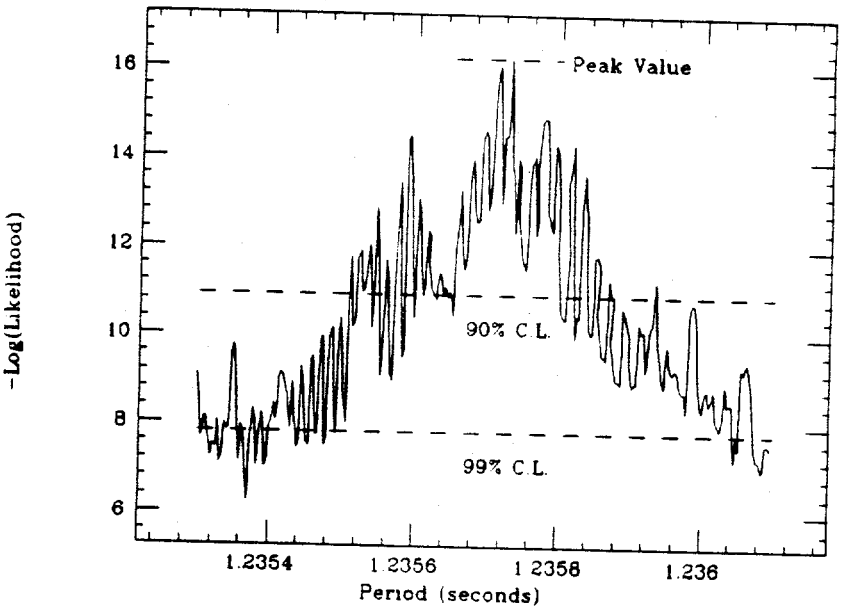

Figure 5.17: $-Log(L_{max})$ as a function of period for the *incoherent* combination of the bursts 1 and 3. The value of likelihood has been maximized over various potential light curves. Both 90% and 99% confidence levels are shown (dashed lines).

Combination of Probabilities

The search strategy that was considered in the original analysis was a two-step procedure: choose the single most significant source day based on event excess, and then perform a period analysis of that day. The idea was to pick out the most likely candidate for source emission on the time scale of one day and avoid the additional trials factor that would be incurred if every day were to be period-analysed. For this scenario, the combination of event excess and periodicity probabilities is calculated according to equation 5.5 as follows:

$$P_{combined} \simeq (N_{days}P_{excess})(N_\phi P_\phi)(1 - log((N_{days}P_{excess})(N_\phi P_\phi))) \qquad (5.22)$$

where P_{excess} is the pre-trial chance probability for the observed event excess; N_{days} is the trial factor for the number of days searched to find P_{excess}; P_ϕ is the pre-trial chance probability for the observed phase alignment; and N_ϕ is the trial factor for the period scan performed to find P_ϕ. The formula above assumes that both $N_{days}P_{excess}$ and $N_\phi P_\phi$ are small compared to one.

Now consider the scenario in which a period analysis is performed *every* day, and the best combination of periodicity and event-excess probabilities is chosen. One would then apply the logarithmic expression to the combination of probabilities examined every day, and then take into account the trials associated with picking the day with the best combination. In other words:

$$P'_{combined} = N_{days} \times (P_{excess})(N_\phi P_\phi)(1 - log((P_{excess})(N_\phi P_\phi)) \qquad (5.23)$$

Note that the only difference between equations 5.22 and 5.23 is the absence of N_{days} in the argument of the *log* in the latter case. This typically results in an additional factor of less than 2 in effective trials for searching every day for periodicity as opposed to only testing the one day with the most significant event excess.

Given the potential gain in sensitivity to weaker signals, this latter approach is clearly worthwhile. It is also, perhaps, a more honest description of the

search procedure initially used to find the source day currently under consideration. Several other days have, in fact, been studied for periodic emission.

Our current data set consists of approximately 1700 source-days for Hercules X-1, as opposed to the 340 that were present during the initial analysis. Application of equation 5.23 therefore results in the following probability estimate for the combination of event excess and periodicity studies:

$$P_{combined} = 1700(3 \times 10^{-6})(0.0022)(1 - log((3 \times 10^{-6})(0.0022)) = 2.2 \times 10^{-4} \quad (5.24)$$

Note that if the value of 340 is used, the chance probability resulting from this alternate analysis procedure is a factor of 5 more significant then the estimate made in the original analysis (with properly combined probabilities).

If the above probability is also corrected by a trial factor of 2 to account for the fact that one could have either tested for pulsed or unpulsed emission, a chance probability of 4.4×10^{-4} results.

Context of Probabilities in an Exhaustive Search for Emission

The previous section quotes the significance level for the observation of pulsed emission on the timescale of $\sim$1 source day from Hercules X-1. However, several other questions can be asked, including the possibly more relevant question of whether or not emission of *any* nature has been observed from *any* of the sources studied.

In the absence of more specific theoretical or observational guidance to indicate which sources are most likely to be emitters of UHE radiation, or to predict the nature of these emission characteristics, many different hypotheses must be examined. Consequently, given the potentially large number of trials associated with such a search, no single probability calculation is meaningful unless it is placed in context with the other questions that have been asked. One method of establishing

this context is to form a "blueprint" for an exhaustive search of the data that both accounts for all analyses that have been performed, and provides a means of incorporating future analyses. As an example, segments from a possible blueprint are shown in figure 5.18, where one specific analysis branch has been followed. Each box in the diagram states the question being addressed, and solid lines connecting the boxes indicate the relationship of these questions. Since the significance of a given analysis depends on an assessment of the related questions on the preceeding level, an accounting must be made for each *independent* hypothesis that has been tested on this level. Dashed boxes represent analyses that have not yet been completed, and dashes lines indicate further analysis branches that have not been followed in this illustration.

Figure 5.19 follows an analysis scenario for the Hercules X-1 branch. The analysis procedure regarding the search for longer term and shorter term emission will be discussed in chapter 8. Limits on continuous emission from Hercules X-1 have been previously published by this group [72]. In order to address the question of whether UHE emission of *any* kind from Hercules X-1 has been observed by the CYGNUS array, two other trial factors must be assessed: First there is a factor of 2 to account for the choice of either considering the single, most significant episode, or for considering several episodes of lesser individual significance that may collectively distort the "tail" of the probability distribution (see Appendix C). Secondly, one must account for the five different analyses that have been performed on the Hercules X-1 data so far; **1)** 1-day emission, **2)** Shorter-term emission (minutes to hours), **3)** Longer-term emission (days to years), **4)** Continuous emission, and **5)** Emission corrolated with other experimental observations. This hypothesis structure also indicates the dynamic nature of the chance probability estimation: note that the significance for UHE emission from Hercules X-1 may change in the future as more source-days are examined, and as more observational correlations are tested. Given that the analysis of July 24, 1986 yields the most significant result of all these tests, the additional trial factors result in a chance probability estimate of $(2 \times 5) \times 0.00044 = 0.0044$.

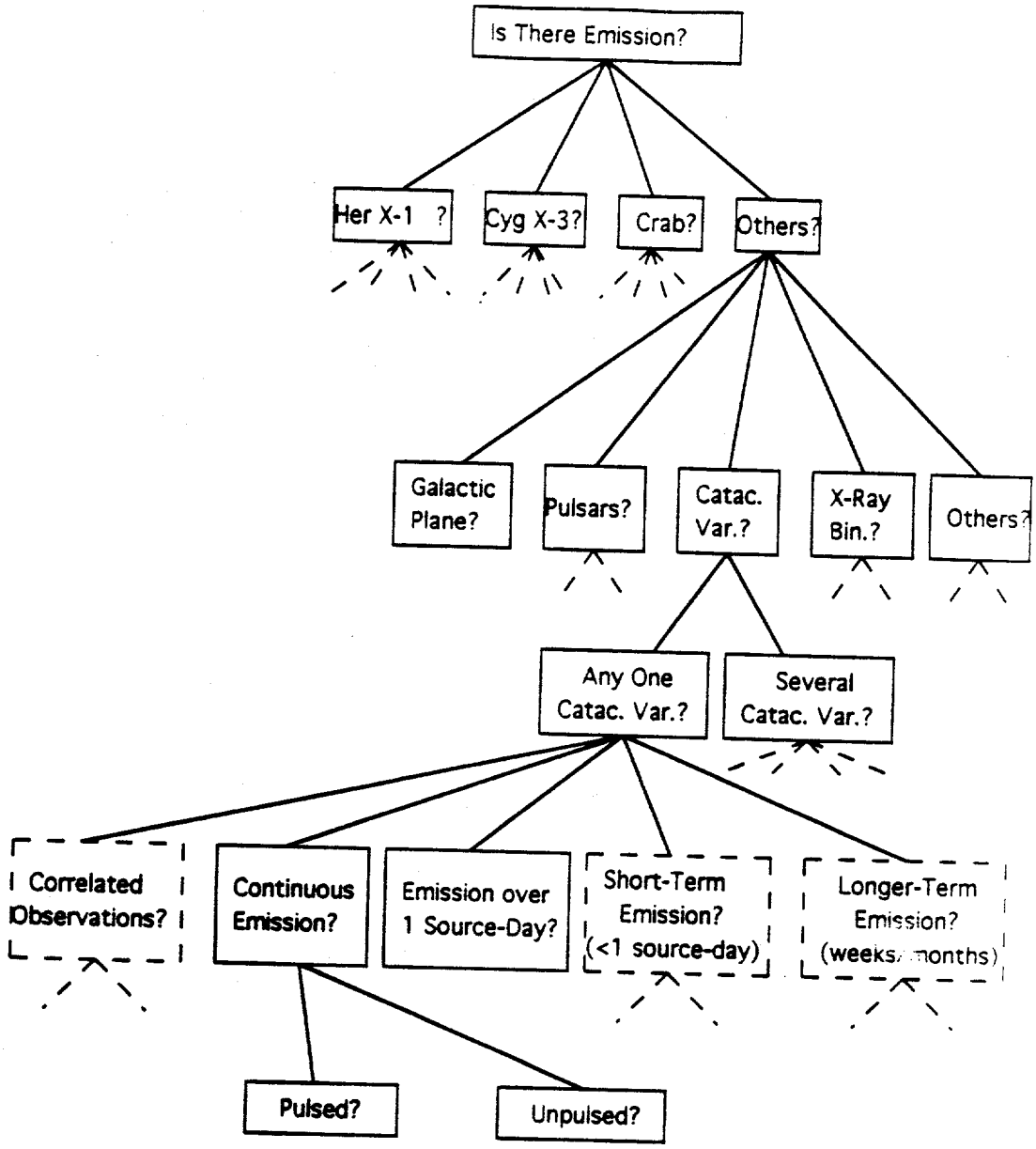

Figure 5.18: Sample logic diagram defining the context of probabilities within an exhaustive search for emission: Each box states a particular question being asked; dashed lines represent results of other tests not shown, and dashed boxes represent analyses not yet performed. To answer a particular question requires that all subordinate questions connected via branches (solid lines) be addressed. These branches, therefore, represent the trials that must be accounted for at each step. An analysis branch related to cataclysmic variable stars is shown here.

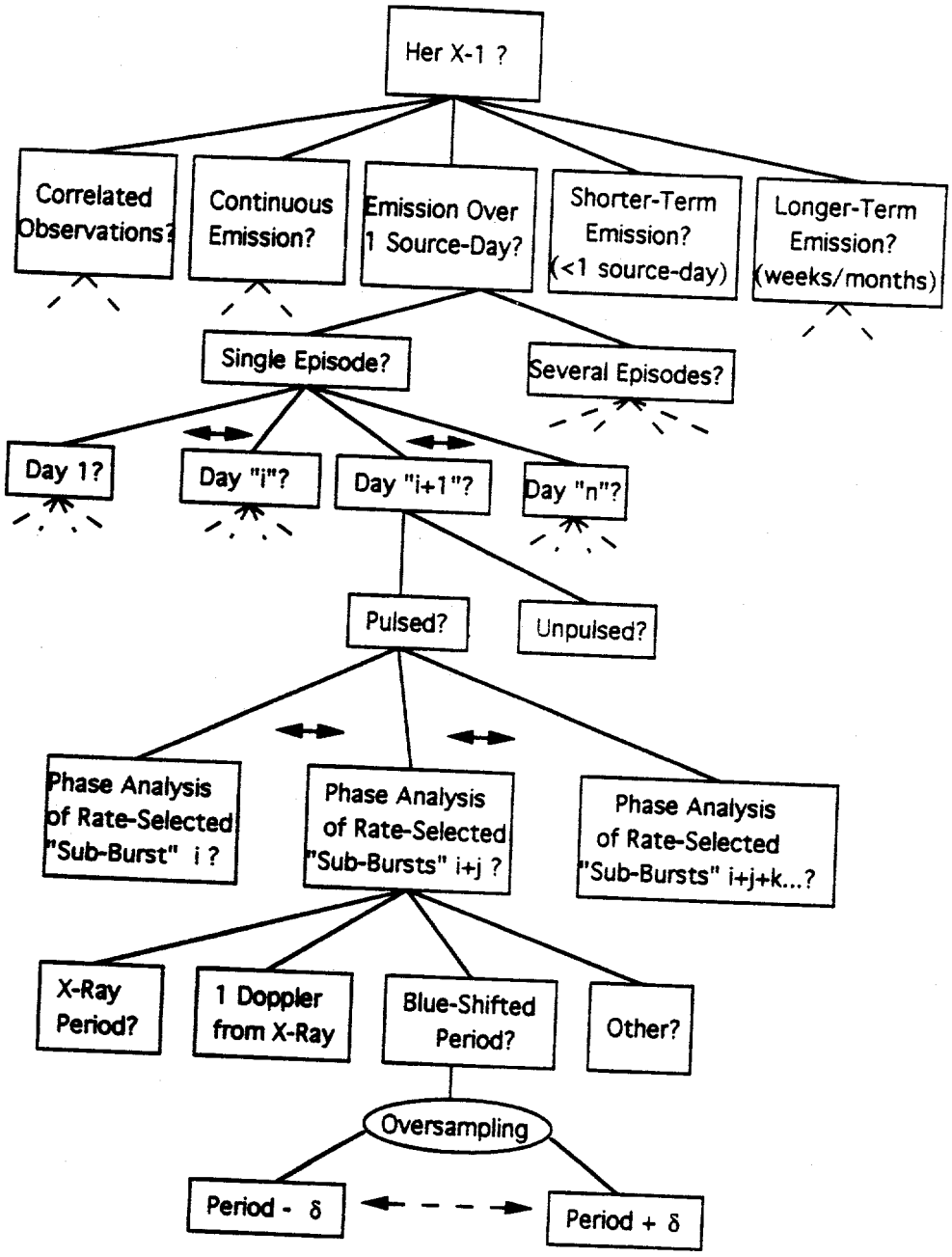

Figure 5.19: Logic diagram depicting the relationship of probabilities within an exhaustive search for emission from Her X-1.

To briefly review the Her X-1 analysis in accordance with the steps outlined in figure 5.19:

(1) A period scan of the combination of bursts 1 and 3 in the blue-shifted frequency range of the Whipple and Haleakala observations yields a value of the Protheroe statistic corresponding to a chance probability of 1.5×10^{-6}. A trial factor of 25 is assessed for the oversampled period scan of that region and results in a chance probability level of $(25)(1.5 \times 10^{-6}) = 3.75 \times 10^{-5}$.

(2) 4 period hypotheses have been examined: Pulsed emission precisely at the X-ray period; Pulsed emission within 1 Doppler shift of the X-ray period; Pulsed emission at the blue-shifted period lying within the uncertainty range of the Whipple and Haleakala results; Pulsed emission that my occur over a wide range of frequencies, centered on the X-ray period. A trial factor of 4 is therefore assessed for choosing the most significant of these tests, resulting in a chance probability level of $(4)(3.75 \times 10^{-5}) = 1.5 \times 10^{-4}$.

(3) For choosing the particular combination of bursts 1 and 3, a trial factor of 15 is assessed. This results in a chance probability level of $(15)(1.5 \times 10^{-4}) = 2.2 \times 10^{-3}$.

(4) A Maximum Likelihood calculation yields a chance probability for the observed event excess on this source day of 3×10^{-6}. This is combined with the chance probability for periodicity according to equation 5.5, where $P_1 = 3 \times 10^{-6}$, and $P_2 = 2.2 \times 10^{-3}$. This yields a combined chance probability of 1.3×10^{-7}. A trial factor of 2 is then assessed for choosing the most significant of either the unpulsed (only the result for event excess) or pulsed (combined) scenario, resulting in a chance probability level of $(2)(1.3 \times 10^{-7}) = 2.6 \times 10^{-7}$.

(5) A trial factor of 1700 for choosing this particular day out of the entire data set results in a chance probability level of $(1700)(2.6 \times 10^{-7}) = 4.4 \times 10^{-4}$.

(6) For choosing the result of a test for the single most significant source day as opposed to a test for several days, a trial factor of 2 is assessed, resulting in a chance probability level of $(2)(4.4 \times 10^{-4}) = 8.8 \times 10^{-4}$.

(7) 5 different emission scenarios have been examined: Emission over 1 source day; Continuous emission over the entire data set; Short-term emission (minutes to hours); Long-term emission (days to years); and emission correlated with other observations. A trial factor of 5 is thus assessed, leading to a final chance probability estimate for the results of the Her X-1 analyses of $(5)(8.8 \times 10^{-4}) = 4.4 \times 10^{-3}$.

In order to address the question of whether or not UHE emission of *any* nature has been observed from *any* of the sources studied, one must first consider the number of different source hypotheses that have been tested. All point-source analyses have been catagorized into 4 basic hypotheses: **1)** Hercules X-1; **2)** Cygnus X-3; **3)** The Crab nebula/pulsar; and **4)** Emission from any of a large list of "secondary" candidate sources. A chance probability corresponding to each of these 4 hypotheses is calculated in a manner similar to that just described for Hercules X-1. As previously discussed, this approach of converting the question into a choice between 4 different hypotheses, is a method of "ranking" possible emission scenarios in a statistically sound manner. A generalization of this technique is presented in Appendix H. As more sources are studied, only the trial-factor corresponding to the fourth hypothesis is effected with this approach. Based on studies that have been performed to date [72] [73], the analysis of Hercules X-1 has yielded the most significant result of the 4 source hypotheses. Therefore, the chance probability associated with the observations is $4 \times 0.0044 = 1.8\%$.

It is worth noting that the total number of trials accounted for in this analysis is $\sim 2 \times 10^8$! This points out both the necessity for a proper accounting of trials, and the difficult nature of trying to isolate a signal in the type of open-ended analysis that is necessary in the absence of more specific theoretical/experimental guidance.

Chapter 6

Further Analysis of the 1986 Hercules Bursts

"Alice laughed: 'There's no use trying,' she said;
'One cannot believe impossible things.'
'I daresay you haven't had much practice,'
said the Queen. 'When I was your age, I always did
it for half-an-hour a day. Why, I've believed in
as many as six impossible things before breakfast."
- Lewis Carroll -

Purpose and Methodology

Based on tests that have been performed on the CYGNUS data, the episode of July 24, 1986 remains the most significant observation to date, with a post-trial probability of ~1% after accounting for all tests that have been performed (chapter 5). The discouraging lack of further observations in recent years leads to one of three conclusions: **1)** The significance of the 1986 episode has been overestimated and UHE emission from Hercules X-1 has not been observed; **2)** The estimate of significance for the 1986 episode is correct, but the observation constitutes a statistical fluctuation and UHE emission from Hercules X-1 has not been observed; **3)** UHE emission has been seen in the past, but the emission is of a highly sporadic nature that may only be observed by EAS detectors during short time intervals occurring every few years. An attempt to address the first of these hypotheses has been made

in chapter 4, and the resulting probability estimate is believed to accurately reflect the current understanding of both data and analysis procedures. While the possibility of a large overestimate in significance cannot be ruled out, potential causes of such errors are not obvious. Likewise, the possibility that the 1986 episode was a fluctuation of background cannot be ruled out, however it cannot be proven either. The results of continued monitoring of point sources will ultimately determine the credibility of this and other claims of UHE emission, although this route is proving to be a long and difficult one.

The process of establishing the validity of UHE emission from point sources would be greatly aided by the formulation of a more specific source hypothesis. The purpose of this chapter is to work towards such a formulation with regard to the nature of the primary particle interaction, based on the properties of air-showers associated with the 1986 episode. Specifically, the goal is to ascertain whether the air-showers associated with Hercules X-1 behave like typical background showers. Such background showers are believed to be initiated predominantly by an isotropic flux of protons and other nuclei. However, if emission has been observed, charged particles such as protons are ruled out because their trajectories would be substantially distorted by the galactic magnetic fields. Thus, there is no reason to assume that the interaction of particles associated with point sources should appear "proton-like." Therefore, despite uncertainties in the sensitivity of EAS measurements to possible differences in the primary interaction, a direct comparison of source events with background events seems warranted.

Because the specific manifestation of potential interaction differences is not known, a number of possible shower parameters must be examined. Other parameters may also suggest themselves in the course of the analysis. A non-standard analysis of this kind clearly raises concerns regarding biases and undefined trial factors that might prevent an accurate assessment of the significance of any differences observed. To avoid such difficulties, the following procedure will be adopted: 1) An exhaustive study will be performed on a subset of the events associated with potential source emission (namely the 11 previously published, in-phase, burst events) for possible differences in shower characteristics compared to sets of similar background

events. **2)** The pre-trial chance probabilities calculated in the first step will be used *only* to choose a single test statistic that maximizes the apparent differences in these showers. These probabilities will not be used to reflect the true significance of the analysis due to the ill-defined nature of the parameter search. **3)** The 11 events examined account for only ~half of the event excess observed (as determined by the maximum likelihood analysis, chapter 5). The remaining on-source events in the day thus constitute an *independent* data set potentially containing signal. Therefore, an identical test of the optimal parameter will be applied to this separate data set, and the chance probability that results will be taken to reflect the true significance of the analysis. Note that as long as the choice of test statistic is based solely on the 11 previously published events, the chance probability assessment for the remainder of the source day is unbiased.

For the purposes of this analysis, the 44 events whose reconstructed primary directions place them within a $4.1° \times 4.1°$ angular bin about Her X-1 during the source day will be considered to be associated with the source. This is the same size bin that was used for the periodicity study in the original analysis and corresponds to an excess of 20 events above expectation, in good agreement with the total number of signal events predicted by the maximum likelihood analysis (19 ± 6) described in chapter 5. As mentioned earlier, the 11 previously published burst events (~1 of which is probably background, based on Monte Carlo calculations) only account for ~half of the this predicted number of signal events While the remaining 33 events are not strongly pulsed at 1.2357 seconds (yielding a Protheroe probability of just 25%, see figure 6.1), there is no reason to assume that all of the emission *should* be pulsed. In fact, a substantial unpulsed fraction is indicated at lower energies [33]. These 33 events, then, comprise the second subset of data potentially containing signal, and will be used to independently confirm any differences in shower characteristics. For the sake of completeness, the results of all shower parameter tests will be given for each of the 44 (11+33) events. However, in strict accordance with the approach outlined above, only the single most significant parameter in the first subset of 11 will be used in the second subset of 33 to assess the overall significance of this analysis.

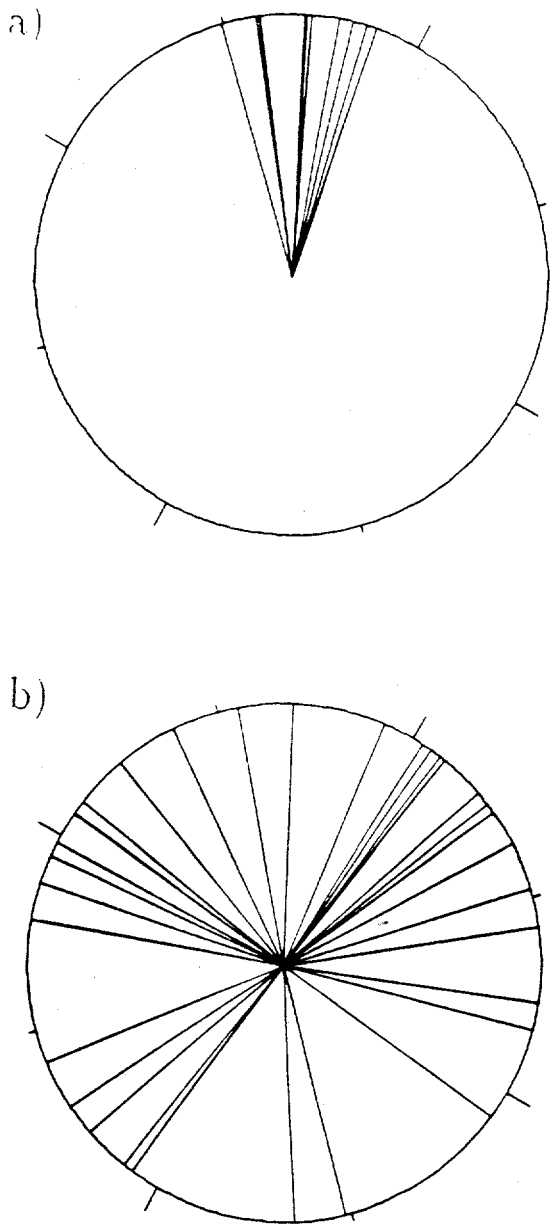

Figure 6.1: Phaseograms for a) the 11 previously published burst events, and b) **the remaining 33 events associated** with Her X-1 for the source day of July 24, 1986 **at the period 1.235696 seconds.** The phases are plotted as vectors on a unit circle **constructed such that 360°** corresponds to 1 phase cycle.

Description of Shower Parameters

Information related to each event has be divided into 3 basic catagories: Orientation, Density/Energy, and Timing. A description of the parameters relevant to each catagory now follows, along with tables giving the values of these parameters for the 44 events in question.

Orientation Parameters

Orientation parameters specify both the physical location of the detected shower within the array, and the reconstructed direction of the primary particle in both local (earth-based) and celestial coordinates. In local coordinates, $\theta = 0$ corresponds to the zenith, and ϕ is defined in a counter-clockwise direction relative to the east. Table 6.1 lists the reconstructed local coordinates of the 44 events under consideration along with the local UTC time of the shower arrival. This is then used to define the celestial coordinates of right ascension (α) and declination (δ), relevant for point-source studies. Table 6.1 also lists the reconstructed location of the shower core within the array (detector positions are given in Appendix F). Simulation studies indicate that the uncertainty in estimated core location is $\sim$3 meters near the array center, and $\sim$8 meters near the perimeter of the array for the configuration and triggering conditions pertinent to this data run. The event number within the run is also given here, along with an event "index" for each of the 44 events to be used for future reference.

Density/Energy Parameters

Table 6.2 lists information on the lateral distribution of the electromagnetic and muon components of each air-shower at the detection level. The method used to fit the electromagnetic lateral distribution is discussed in Appendix B. Relevant quanties are the shower *age*, specifying the steepness of the lateral distribution, and the *size*, giving the estimated number of electrons reaching the ground (in terms of effective minimum-ionizing particles detected in the scintillation counters). The age

ORIENTATION PARAMETERS

Event Index	Event in Run	θ (deg)	ϕ (deg)	Seconds (UTC)	α (deg)	δ (deg)	X-Core (meters)	Y-Core (meters)
1	59190	44.5	18.3	397.364	252.8	36.6	-7.2	-52.1
2	62084	39.2	14.3	2127.512	252.9	35.6	-6.0	36.6
3	63408	37.5	12.5	2920.994	253.6	35.0	16.3	-5.3
4	64899	34.8	22.6	3790.134	253.7	35.2	-43.0	-12.0
5	65235	34.7	8.5	4005.216	253.9	33.5	25.2	-10.2
6	65766	34.5	14.0	4330.360	255.7	36.4	0.1	-20.9
7	66031	32.9	10.6	4486.183	254.3	35.1	-2.2	-18.5
8	66098	31.2	11.4	4527.663	252.8	35.6	-38.6	-56.7
9	66244	33.8	12.5	4608.584	256.2	35.8	-43.6	16.5
10	68753	25.0	11.8	6086.229	251.6	36.8	0.3	-33.8
11	71329	23.6	7.8	7639.644	256.1	35.7	5.6	8.4
12	71874	21.3	4.6	7975.018	254.5	34.2	4.7	-14.7
13	72629	18.0	5.9	8399.307	252.3	35.4	-21.4	-20.6
14	75908	15.5	8.6	9305.017	253.3	36.8	9.4	7.1
15	77304	14.8	2.7	10120.805	255.2	35.4	-8.3	-5.8
16	78638	10.4	354.5	10887.654	252.6	34.3	-20.0	-50.7
17	78640	10.0	347.8	10888.126	252.1	33.5	-6.0	-26.2
18	79432	7.7	355.5	11348.532	251.5	35.1	-18.9	-19.9
19	81051	6.3	5.4	12248.384	254.2	35.9	63.7	-19.7
20	82105	6.1	3.3	12830.636	255.6	36.2	-14.8	-75.4
21	82504	4.5	337.0	13058.569	255.1	34.6	5.9	-20.2
22	83235	3.6	17.6	13488.871	255.2	37.0	12.4	-6.5
23	83826	0.6	262.6	13820.381	252.0	35.1	17.8	-19.7
24	83903	1.9	247.4	13872.319	252.5	34.3	33.7	14.5
25	84870	1.4	287.0	14429.057	254.9	35.0	-5.2	-10.7
26	85068	2.1	125.8	14537.362	254.0	36.2	-12.2	-61.5
27	86098	3.9	181.2	15120.303	253.4	35.8	-34.0	29.7
28	87080	5.2	195.1	15709.434	254.4	34.4	10.2	-13.6
29	87278	5.7	178.5	15822.763	254.3	35.8	23.6	-29.4
30	88320	6.7	195.6	16417.537	255.4	33.9	-1.3	-6.5
31	88445	9.6	180.8	16481.700	251.6	35.6	-38.4	35.3
32	89464	11.4	179.9	17050.577	252.2	35.3	-7.5	9.1
33	90129	12.4	173.1	17419.974	253.2	36.8	35.0	24.5
34	90234	10.3	168.2	17482.940	254.6	37.3	-63.3	2.2
35	90468	12.0	174.9	17610.313	253.3	36.2	-18.8	-20.6
36	90580	11.3	183.4	17683.197	255.1	34.0	2.1	-47.8
37	90825	10.1	190.7	17816.256	256.2	33.5	-42.6	-9.8
38	90959	11.6	188.2	17891.924	255.4	33.5	-26.4	-10.6
39	93479	18.2	175.0	19358.124	254.3	35.2	8.7	11.6
40	96644	23.4	170.4	21258.880	254.3	36.1	47.8	-34.3
41	96675	24.4	174.1	21274.784	253.8	34.5	-31.8	6.2
42	96959	24.7	170.6	21427.679	253.9	35.9	-44.1	-30.5
43	98853	28.5	170.9	22483.737	253.4	35.0	-10.9	-3.8
44	101170	32.5	168.4	23787.488	253.9	35.6	-6.2	-45.9

Table 6.1: Orientation parameters for all events in source day.

DENSITY/ENERGY PARAMETERS

Event Index	Age (±0.1)	Size (10^4) (±30%)	χ^2_{DoF} of fit to Lat. Distrib.	E_{proton} (TEV)	R_{E225} (meters)	Muon Number
1	1.48	3.7	1.3	380	45	NA
2	1.12	10.1	2.9	620	36	NA
3	1.05	6.3	1.6	440	17	>10
4	1.77	7.5	2.1	470	43	6
5	1.22	13.8	1.7	750	26	>10
6	1.23	6.6	3.1	430	17	7
7	1.26	2.5	6.4	230	15	9
8	1.02	26.8	0.9	1310	61	3
9	1.18	10.1	2.2	580	47	4
10	1.33	12.9	2.3	650	28	5
11	1.21	16.8	4.8	810	11	9
12	1.80	181	6.4	8190	12	>10
13	1.12	2.9	1.7	160	26	2
14	1.58	53.7	3.0	2440	12	9
15	1.51	4.8	5.7	240	9	6
16	0.99	9.9	0.9	450	47	3
17	1.38	3.6	1.3	170	22	>10
18	1.57	4.5	2.6	200	24	4
19	1.75	23.7	1.9	1060	66	1
20	1.37	13.4	0.8	600	67	3
21	1.16	2.9	3.2	130	18	2
22	0.96	3.8	1.5	170	13	2
23	1.79	5.8	1.2	250	24	NA
24	0.93	20.4	1.1	910	36	3
25	1.10	1.4	1.0	80	9	1
26	0.80	11.0	2.1	490	54	3
27	1.67	10.3	1.2	460	45	1
28	1.25	3.4	0.6	150	15	3
29	1.45	6.6	1.6	290	35	2
30	1.08	2.4	1.3	110	4	>10
31	1.32	31.7	1.9	1430	52	5
32	1.46	4.3	1.4	200	13	0
33	0.80	14.7	1.1	670	41	0
34	0.80	34.1	2.4	1540	63	0
35	1.28	3.4	2.1	160	24	1
36	1.72	78.7	2.6	3550	41	8
37	1.33	6.1	1.0	280	42	NA
38	1.08	12.9	1.8	590	27	4
39	1.09	1.8	1.0	120	15	0
40	1.79	70.1	1.9	3210	57	4
41	0.99	5.6	1.1	310	33	1
42	1.11	6.0	2.0	330	50	3
43	1.41	7.1	3.8	410	11	8
44	1.45	11.8	2.6	650	40	2

Table 6.2: Density/Energy parameters for all events in source day.

is constrained to lie between 0.8 and 1.8, since studies indicate that values beyond these limits tend to lead to unrealistic values of shower size while making little improvement to the quality of the fit. The age parameter has some sensitivity to the depth of primary interaction and the transverse momentum distribution within the shower (see Appendix A). The shower size, coupled with the known atmospheric overburden (zenith angle, pressure), can provide information related to the energy of the primary interaction. Estimation of the primary energy from this parameter is highly model-dependent in terms of both the nature of the interaction, and the shape of the energy spectrum from which the event is sampled. The latter of these 2 dependences is due to the fact that, with a more rapidly falling spectrum, a given shower size in more likely to have resulted from a lower energy shower that has fluctuated up to the observed size. Such fluctuations can be quite large for a given interaction model; orders of magnitude are not uncommon. Thus, the equivalent proton primary energies obtained from simulation and listed for each shower size and zenith angle should be regarded only as model-dependent, order-of-magnitude approximations.

Since the fitting procedure used to obtain the age and size (Appendix B) involves the use of the data itself to determine the variance of particle density measurements, a value of reduced χ^2 calculated with these variances cannot be relied upon to reflect unusual density fluctuations. For these purposes, a value of reduced χ^2 has been defined that assumes average, Gaussian variations in density of the form $\sigma = \sqrt{N_p + (0.3N_p)^2}$, where N_p is the effective number of particles measured at a given detector. The second term inside the radical accounts for uncertainties in the ADC conversion factors and non-uniformities in scintillator quality from counter to counter. This form breaks down when $N_p < 1$, and so σ is never allowed to drop below its value at $N_p = 1$. The somewhat large values of the resulting reduced χ^2 may reflect deficiencies still present in the model for typical density fluctuations.

Since only one muon detector (the E225 anti-shield) was operating during the time of the 1986 episode, an accurate determination of the muon lateral distribution on an event-by-event basis is not possible. Therefore, table 6.2 merely lists the measured muon number and the distance between the reconstructed shower core

and muon detector for each event. The computer algorithm used to determine the number of muons from the pattern of MWPC hits can easily distinguish between 0,1,2 or 3 muons; has an uncertainty of about ± 1 for larger muon numbers; and has little ability to distinguish between muon numbers greater then 10. Entries listed as "NA" correspond to events where the muon information was not available as a result of the neutrino experiment operation for which the anti-shield was originally built.

Timing Parameters

Information on the time-structure of the showerfront and characteristics of the event arrival times is given in table 6.3. To look for differences in the showerfront curvature of the events, a fit was performed (in accordance with the results of Appendix E) to the form:

$$\Delta T = \frac{2.2}{\sqrt{N}} + 1.8e^{-0.05N} + \alpha R_m N^{-0.25} \tag{6.1}$$

where ΔT is the curvature correction (Appendix E), N is the pulse height in terms of effective particle number, R_m is the radius from the shower core in meters, and α is the "curvature" parameter that was allowed to vary in the fit. The large variations and uncertainties listed in table 6.3 indicate the difficulty in determining this parameter on an event-by-event basis. Note that the standard, fixed value of $\alpha = 0.12$ was used for the remaining studies, not this best-fit value.

The average showerfront timing width was parameterized by the weighted rms deviation of particle arrival times relative to the shower plane. The weighting scheme followed the prescription given in Appendix E, and was employed after removing all data points deviating by more than 5 nanoseconds from the shower plane so as to eliminate the non-Gaussian tails (which can significantly effect the value of the average, squared deviation).

TIMING PARAMETERS

Event Index	Best Fit Curvature (ns/m)	Average $\sigma_{Showerfront}$ (ns)	Inner-Counter $\sigma_{Showerfront}$ (ns)	Inner/Outer Ratio of σ's	Phase at Period 1.2357 sec	Burst Group*
1	1.03±0.57	2.14	0.99	0.150	.745	1
2	0.05 ±0.02	1.53	0.83	0.234	.144	1
3	0.24±0.13	1.86	1.07	0.257	.948	1,A,P
4	0.14±0.06	3.38	2.34	0.292	.957	1,A,P
5	-0.41±0.69	1.40	0.90	0.275	.928	1,A,P
6	-0.06±0.65	1.55	1.01	0.298	.926	1,A,P
7	0.11±0.23	1.50	0.89	0.242	.966	1,A,P
8	0.08±0.05	3.02	1.95	0.278	.518	1,A
9	0.12±0.05	1.26	0.67	0.193	.972	1,A,P
10	0.20±0.14	1.07	0.75	0.380	.208	
11	0.22±0.06	1.56	0.66	0.145	.765	
12	-2.51±3.5	0.71	0.46	0.400	.053	
13	2.03±1.76	0.92	0.55	0.242	.268	
14	0.34±0.08	2.34	1.30	0.296	.922	
15	0.28±0.18	1.34	1.11	0.561	.846	
16	0.03±0.02	1.19	0.59	0.133	.191	
17	0.93±0.97	0.70	0.40	0.229	.573	
18	0.12±0.05	1.29	0.64	0.205	.024	
19	0.08±0.73	3.18	1.60	0.169	.981	2
20	0.91±0.98	1.84	0.75	0.122	.014	2
21	0.04±0.05	0.90	0.71	0.429	.411	2
22	1.64±0.88	2.00	1.45	0.368	.524	2
23	-0.32±0.95	4.94	2.96	0.303	.718	2
24	-0.65±0.38	2.52	1.37	0.203	.736	2
25	0.03±0.06	2.33	2.09	0.571	.144	2
26	0.19±0.08	0.49	0.13	0.068	.766	2
27	-0.09±0.10	2.10	1.23	0.213	.379	2
28	0.03±0.03	1.62	1.30	0.470	.007	2,B
29	0.79±0.33	2.21	0.98	0.165	.695	2,B
30	0.09±0.03	2.04	1.20	0.223	.896	2,B,P
31	0.04±0.39	2.50	1.88	0.444	.807	2,B
32	-1.10±1.37	1.67	0.65	0.138	.062	B
33	0.02±2.66	1.03	0.39	0.076	.931	3,B,P
34	0.22±0.05	2.83	1.96	0.283	.874	3,B,P
35	0.08±0.05	1.33	0.40	0.080	.928	3,B,P
36	0.27±0.41	2.68	1.91	0.430	.898	3,B,P
37	1.39±2.50	4.88	4.50	0.631	.553	
38	0.22±0.20	1.78	0.93	0.204	.774	B
39	0.15±0.07	2.04	1.60	0.414	.068	4
40	0.19±0.26	2.32	1.43	0.282	.021	4
41	0.24±0.81	1.13	0.29	0.060	.888	4
42	1.27±1.18	0.99	0.68	0.357	.604	4
43	0.30±0.22	1.77	1.28	0.414	.120	4
44	0.14±0.61	2.14	1.72	0.461	.091	4

*Groups 1-4: events selected for bursts 1-4 (re-analysis)
Groups A,B: events selected for bursts A,B (original analysis)
Group P: "in-phase" burst events (original analysis)

Table 6.3: Timing parameters for all events in source day.

To investigate possible differences in the radial dependence of the showerfront width, a radius from the shower core for each event was first defined so as to encompass half the number of counters recording a particle arrival time. An "inner-counter" and "outer-counter" rms timing deviation was then computed (as previously described) for each half, and the ratio of these values was then taken.

Finally, table 6.3 lists the phase corresponding to the arrival time for each event relative to the period of 1.2357 seconds (corresponding to the peak Protheroe power of the burst search in chapter 5), and also designates the burst groups selected both by the original analysis and by the re-analysis described in chapter 5.

Analysis of the 11 Previously Published, Burst Events

Hypotheses and Background Selection

Given the values of various parameters for each event in burst group P, the hypotheses that will be considered involve the probabilities for an ensemble of otherwise similar background events to possess **1)** a smaller or equal age; **2)** a larger size; **3)** a larger value of χ^2 for the lateral distribution fit; **4)** a larger or equal number of muons; **5)** a greater showerfront curvature; **6)** a smaller average showerfront width; **7)** a smaller ratio of inner-counter to outer-counter showerfront widths; and **8)** a steeper muon lateral distribution.

For all but hypotheses **2, 4** and **8**, ensembles of background events were accumulated by separating all events into catagories defined by: zenith angle intervals of 5°; **10** meter radial intervals (relative to the center of the array) for core location; and size intervals (in units of 10^4 particles) of 0-5, 5-10, 10-15, 15-20, 20-30, 30-40, 40-60, 60-80, 80-120 and >120. For hypothesis **2**, only zenith angle catagories were used. The ensembles were accumulated for runs 167-175 (encompassing 10 source-days) over which time the detector configuration was nominally constant.

Typically ~1000 background events were accumulated for each ensemble. For each source event, the rank of a given parameter value within the appropriate ensemble then gives the probability for that parameter. A number of alternate approaches involving more stringent criteria for event selection and background studies based specifically on the data of July 24, 1986 yielded consistent results and indicated no evidence of bias in the determination of probabilities.

For the muon studies (hypotheses **4** and **8**), a more event-specific selection of background was employed due to concerns that the probability associated with a single-position measurement of muon density might be more susceptible to biases. For these hypothesis tests, a background event was considered part of a source event's ensemble if it matched the zenith angle to within 5°; the azimuthal angle to within 30°; the core distance relative to the muon detector to within 5 meters; and the shower size to within 30%. Once more, studies of alternate selection criteria indicated that these choices were sufficient.

Results

The resulting probabilities for each event in burst group P under hypotheses **1-7** are given in table 6.4. For each hypothesis tested, a final probability for the ensemble of source events must be calculated. For the test of a flatter distribution of shower sizes, one would expect the probabilities calculated to cluster closer to zero as the primary energy spectrum becomes flatter (assuming a simple power law). A Fisher test is thus employed for this case [68]. Under the signal hypothesis for the remaining parameters, one might well imagine a systematic clustering of probabilities **within** the ensemble about some arbitrary value (*i.e.* the values for the age **parameter** might all be systematically lower than the average by 20%). Therefore, a Kolmorgorov-Smirnov (K-S) test has been chosen [91]. This test assesses a significance based on the observed deviations from an expected integral distribution of values. For the present case, the integral distribution employed consists of the fraction of ensemble events with chance probabilities less than some critical value, versus that critical value of probability. The expected background distribution would sim-

ply be a straight line from (0,0) to (1,1) of that plot. Taking the test statistic to be the maximum, positive deviation from the expected distribution (D^+), the chance probability for the "upper tail" ($P < 15\%$) is approximately given by

$$P = e^{-2z^2} \tag{6.2}$$

$$\text{where } z = (\sqrt{N} + 0.12 + \frac{0.11}{\sqrt{N}})D^+$$

$$\text{and } N = \text{number of values}$$

For larger values of chance probabilities, Monte Carlo calculations can be employed. The resulting chance probabilities for each hypothesis are given at the bottom of table 6.4. These hypotheses have been defined so as to yield the maximum value of D^+, *i.e.* one could have just as easily asked for the probability of obtaining a *smaller* value of showerfront curvature. Thus, an additional factor of 2 for this choice yields the probability level given in parentheses at the bottom of the table. In the case of the muon hypothesis, the quantization of measured muon number must be taken into account in deriving the significance level. This was done with the use of a Monte Carlo calculation that sampled muon numbers from each background ensemble.

A test of the muon lateral distribution (hypothesis 8) is not available on an event-by-event basis since only a single muon density measurement was possible. However, the relative muon content in the ensemble of source events, with cores at different distances from the muon detector, can provide information related to this question. The principle difficulty is to compensate for the different shower sizes, zenith angles, etc. of the these events so that a direct comparison of the muon content can be made. A model-independent method for doing this is to look for a correlation between the distance from the muon detector and the previously calculated probability to obtain an equal or greater muon content (which already takes into account the effects mentioned above). A plot of these 2 quantities is shown in figure 6.2 for the 11 events of burst group P. Once again, the quantization of measured muon number must be taken into account in deriving the significance level. A Monte Carlo calculation involving the sampling of muon numbers from each background ensemble indicates a chance probability of 4% to obtain a linear corrolation coefficient as large or larger, suggesting a possible corrolation.

PROBABILITIES OF VARIOUS PARAMETERS

Event Index	≤Age	>Size	$> \chi^2$ (Lat. Dist.)	≥Muons	>Curv.	$< \sigma$ (Showerfront)	$< \sigma_{ratio}$ (Showerfront)
3	0.102	0.513	0.565	0.069	0.195	0.430	0.168
4	0.895	0.443	0.277	0.147	0.295	0.856	0.357
5	0.251	0.228	0.437	0.073	0.795	0.240	0.220
6	0.502	0.502	0.094	0.251	0.669	0.404	0.240
7	0.622	0.881	0.015	0.065	0.334	0.393	0.180
9	0.258	0.331	0.256	0.541	0.343	0.059	0.110
30	0.338	0.901	0.587	0.034	0.418	0.790	0.225
33	0.048	0.232	0.721	1.000	0.657	0.034	0.008
34	0.140	0.070	0.146	1.000	0.254	0.545	0.314
35	0.583	0.802	0.188	0.705	0.396	0.350	0.013
36	0.938	0.020	0.114	0.063	0.188	0.812	0.375
Prob. of Ensemble	0.34 (×2 = 0.68)	0.23 (×2 = 0.46)	0.046 (×2 = 0.09)	0.007 (×2 = 0.014)	0.10 (×2 = 0.20)	0.34 (×2 = 0.68)	0.0001 (×2 = 0.0002)

Table 6.4: Probabilities of various parameters for 11 previously published, burst events.

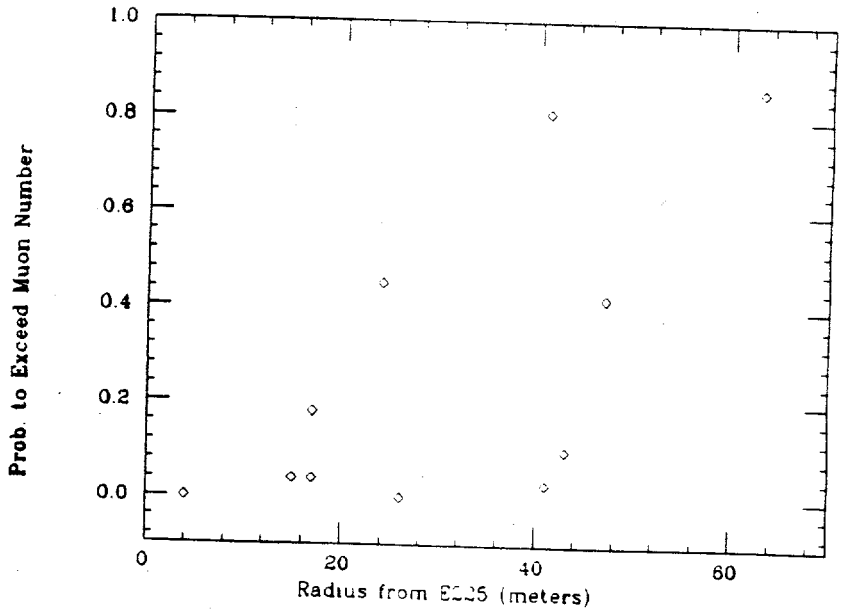

Figure 6.2: Probability for a larger muon number versus radius for the 11 previously published, burst events.

However, the most significant result by far is associated with the ratio of inner-counter to outer-counter showerfront widths. This K-S plot is shown in figure 6.3. It should be noted that the 8 hypotheses tested are not entirely independent. For example, a smaller ratio of timing widths will necessarily affect the curvature.

Analysis of the Remaining Source Events

Table 6.5 lists the probabilities associated with each hypothesis for the remaining 33 events of the source-day. A test of the muon lateral distribution, relative to the best-fit linear dependence for the 11 events of burst group P, yields a chance probability of 12%. The results of all hypotheses are given for the sake of completeness although, as previously stated, only the probability for the most significant test of burst group P will be used here to assess an overall probability for the analysis. The parameter associated with this test is the ratio of inner-counter to outer-counter timing widths and yields a chance probability of 0.0016 for an ensemble of similar events to produce smaller ratios. This, is taken to represent the chance probability for the shower characteristics of a set of similar background events to deviate as much from expectation.

Discussion

Based on the results just presented, the general statement can be made that the source events from the 1986 episode appear to behave differently from background. In keeping with the goals of this chapter, an attempt will now be made to interpret these results in terms of an empirical model of the air-shower development. For this, the results of all 8 hypothesis tests will be drawn upon without regard to trial factors, since no attempt will be made to assess the probability of such a speculative model.

The most significant parameter, the smaller ratio of inner-counter to outer-counter showerfront widths, may indicate a higher energy and/or a lower production depth for electromagnetic particles associated with the core of the shower

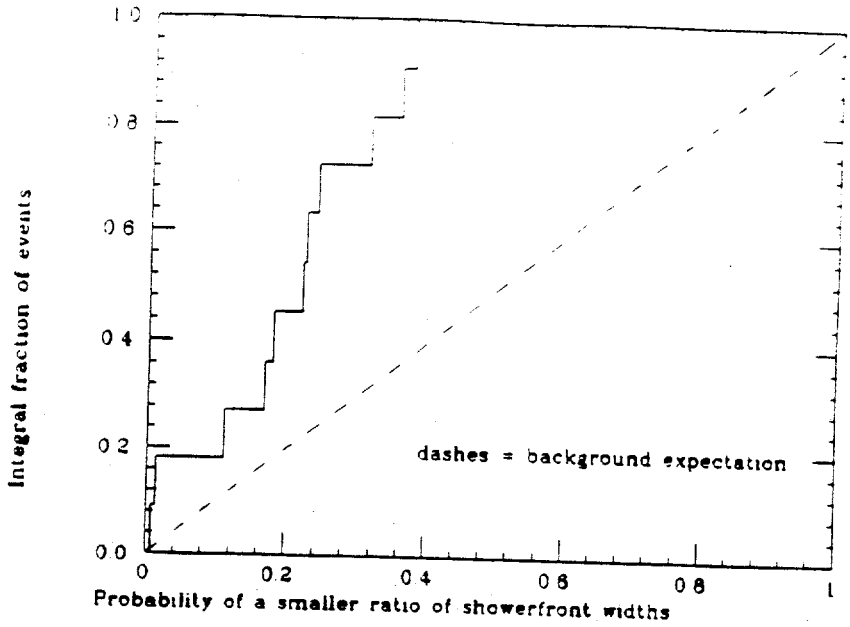

Figure 6.3: K-S (integral fraction) plot of inner-counter to outer-counter timing width probabilities for the 11 previously published, burst events. The abscissa is the probability for a smaller value, and the ordinate is the integral fraction of events less than this probability.

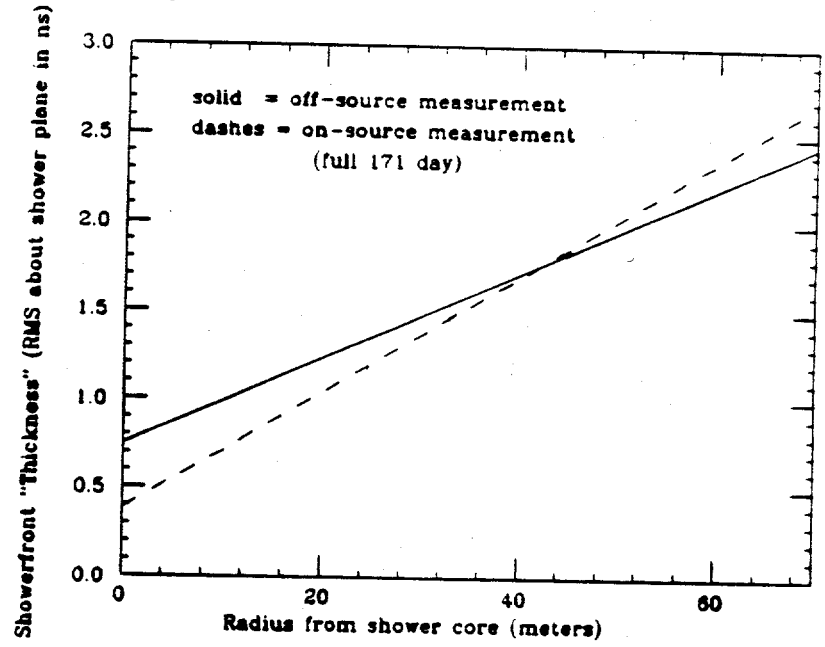

Figure 6.4: Illustration of showerfront thickness effect: "average" rms showerfront thickness versus radius is shown for both on-source (dashes) and off-source (solid) events.

PROBABILITIES OF VARIOUS PARAMETERS

Event Index	≤Age	>Size	$> \chi^2$ (Lat. Dist.)	≥Muons	>Curv.	$< \sigma$ (Showerfront)	$< \sigma_{ratio}$ (Showerfront)
1	0.724	0.716	0.810	NA	0.071	0.610	0.109
2	0.248	0.318	0.143	NA	0.530	0.140	0.189
8	0.232	0.086	0.906	0.549	0.407	0.648	0.242
10	0.567	0.272	0.232	0.434	0.230	0.097	0.339
11	0.287	0.190	0.023	0.415	0.255	0.408	0.026
12	1.000	0.001	0.010	0.500	0.848	0.030	0.290
13	0.315	0.848	0.342	0.336	0.027	0.094	0.260
14	0.400	0.025	0.077	0.727	0.200	0.654	0.200
15	0.940	0.646	0.010	0.256	0.175	0.424	0.711
16	0.108	0.376	0.863	0.294	0.614	0.111	0.090
17	0.740	0.759	0.541	0.087	0.080	0.026	0.239
18	0.947	0.663	0.094	0.142	0.328	0.335	0.232
19	0.903	0.119	0.230	0.843	0.468	0.681	0.112
20	0.586	0.281	0.940	0.368	0.055	0.223	0.055
21	0.381	0.810	0.039	0.537	0.564	0.097	0.566
22	0.105	0.723	0.384	0.620	0.028	0.726	0.492
23	0.907	0.561	0.569	NA	0.848	0.949	0.402
24	0.122	0.162	0.703	0.628	0.898	0.561	0.183
25	0.323	0.994	0.821	0.583	0.536	0.882	0.721
26	0.047	0.328	0.168	0.188	0.213	0.005	0.014
27	0.805	0.352	0.657	0.768	0.837	0.358	0.285
28	0.533	0.761	0.972	0.345	0.541	0.548	0.633
29	0.657	0.498	0.371	0.483	0.084	0.675	0.148
31	0.494	0.076	0.255	0.238	0.649	0.488	0.613
32	0.829	0.714	0.533	1.000	0.878	0.515	0.104
37	0.481	0.593	0.808	NA	0.025	0.961	0.788
38	0.219	0.269	0.282	0.240	0.273	0.524	0.116
39	0.235	0.968	0.820	1.000	0.267	0.693	0.573
40	0.883	0.021	0.315	0.886	0.286	0.402	0.299
41	0.073	0.580	0.807	0.742	0.205	0.111	0.003
42	0.167	0.546	0.289	0.394	0.026	0.050	0.497
43	0.701	0.471	0.057	0.260	0.192	0.522	0.446
44	0.637	0.293	0.161	0.710	0.825	0.551	0.590
Prob. of Ensemble	0.69	0.09	0.08	0.09	0.01	0.09	0.0016

Table 6.5: Probabilities of various parameters for the remaining 33 events.

This might result from a high energy, extremely forward-directed component of the hadronic core that then feeds some fraction of its energy into smaller electromagnetic cascades at lower depths. This might also lead to an underestimate of the primary energy based on shower size, since the energies of the hadronic core and the electrons are not measured by the scintillation detectors. Simulations of more standard interaction schemes have been examined, and indicate that a primary interaction occurring deep in the atmosphere, but appearing otherwise proton-like, will not explain the observations for two reasons: 1) the lateral density distribution becomes significantly steeper (smaller age parameter) before any showerfront effect is noticeable, and this predicted distortion of the age distribution is not seen; 2) At lower interaction depths, a proton-like interaction appears to produce only an overall narrowing of the showerfront, and not the radial-dependent trend observed. The first of these problems can be alleviated by invoking the production of hadrons with a larger fraction of transverse momentum (*e.g.* an iron-like interaction) to compensate for the steepening of the lateral distribution. However, a deep, iron-like interaction still only results in an overall narrowing of the showerfront. Based on the data, a graphical representation of the "typical" difference in the radial-dependence of the showerfront thickness between source and background events is shown in figure 6.4. Note that although typical deviations are only ~fractions of a nanosecond, this accuracy is within reach of the average rms as determined from several counter measurements.

With further regard to the age parameter, it should be noted that the results presented here contradict the Kiel claim that larger ages are associated with muon-rich showers from point sources [1]. This statement assumes, of course, that the same interaction model is responsible for the showers associated with Cyg X-3 as for Her X-1. It also assumes that the Kiel study of shower ages was done in an unbiased manner so as to accurately reflect the steepness of the lateral distribution.

Slight differences in the overall showerfront width and curvature (weakly indicated) are probably artifacts of the smaller inner-counter to outer-counter ratio of timing widths. In the case of curvature, this would certainly bias the sampling of particle arrival times so as to produce the general trend observed (a slightly larger effective curvature).

Evidence for a flatter primary energy spectrum based on shower size is not compelling. However, assuming an integral source spectrum of $E^{-1.0}$ (as opposed to the background spectrum of $E^{-1.7}$), a Monte Carlo calculation indicates that chance probability levels as large as those obtained in tables 6.4 and 6.5 will occur roughly 20% and 50% of the time, respectively. In other words, the ability to discriminate between different energy spectra is limited, so that the results are consistent with either the background or with a typical source hypothesis.

Interpretation of the muon measurements is highly dependent on the assumptions made. Assuming that these showers possess the same lateral distribution and primary energy spectrum as background showers, there are indications of a larger muon content and this may indicate increased pion production in the primary interaction compared with proton-like interactions. If a flatter source energy spectrum is assumed (not inconsistent with the data), the apparent muon excess has been somewhat overestimated since showers sampled from a steeper distribution of background for comparison will have a greater tendancy to result from lower energy showers (lower muon content) that have fluctuated high in size. If a steeper muon lateral distribution is assumed (possibly indicated by the data), the overall muon content could be consistent with or even less than that produced by a proton-like interaction. The possibility of a steeper muon lateral distribution is consistent with the notion of a forward-peaked or a more deeply-interacting component of the hadronic interaction. It is also consistent with the claim of a steeper muon lateral distribution made by the Kiel group with respect to muon-rich showers associated with Cyg X-3 [1].

To summarize: the air-showers associated with Her X-1 in the 1986 episode appear to behave differently from otherwise similar background showers at a chance probability level of 0.1%. In particular, a steeper radial dependence of the shower-

front timing width is indicated. In a speculative attempt to link this and other possible possible differences with physical processes, a hypothetical model has been considered that principally invokes a forward-peaked and/or a more deeply-interacting component of the hadronic interaction as compared with proton or iron-like interactions.

Chapter 7

Search for Emission Over Arbitrary Time Scales

"They hunted till darkness came on, but they found
Not a button, or feather, or mark,
By which they could tell that they stood on the ground
Where the Baker had met with the Snark"
- Lewis Carroll -

Introduction

Standard analyses of the CYGNUS data have involved searching for either daily or continuous UHE emission. However, several groups have reported possible emission on time scales of several days [100] to several years [1], [2]. Still other observations indicate short duration "bursts," lasting from 10 to 60 minutes [3], [4], [5]. The difficulty in searching for emission over arbitrary time scales in the presence of background lies in the assessment of trial factors to account for the number of independent hypotheses tested. If this statistical penalty is too large, sensitivity to emission will be lost. One must therefore be prudent in choosing a search strategy.

A method to look for emission over an arbitrary range of time scales will now be described. One shortcoming of the technique is that it only gives the probability for the single most significant "burst" within the interval of data being considered. An approach for combining several bursts is discussed separately in chapter 5.

Episodic Search Technique

Brief Outline of Approach

The basic approach is essentially one of "brute force": **1)** For a given interval of data, choose the range of time scales to be tested; **2)** Span this data interval with a series of consecutive time "windows" corresponding first to the smallest time scale for emission that is of interest; **3)** Within each time window, assess the probability for emission (based either on event excess, periodicity, or the combination); **4)** Repeat the procedure with offset time-window boundaries to account for emission that may not be centered in a given window; **5)** Determine the chance probability of the most significant interval for this time scale (accounting for the number of independent intervals searched and for the search with offset window boundaries); **6)** Repeat the whole procedure for time windows of increasing length, until the entire range of time scales has been investigated; **7)** Choose the time scale corresponding to the most significant result, and account for the trials associated with that choice; **8)** Having obtained the chance probability for the most significant burst within a given interval of data (*e.g.* one source day), the entire process may then be applied to additional data intervals (*e.g.* other source days), so that the distribution of burst probabilities may be tested against the null hypothesis.

A diagram for the sequence of logic behind the trial assessment for a hypothetical scenario is shown in figure 7.1. Typical values for various trial factors are given in brackets. Precise accounting for effective trial factors is a highly data-specific endevour, and is virtually impossible in practice. The approach adopted here is to approximate these trials with general parameterizations of typical scenarios, and to use these parameterizations as a first-order correction. A further refinement to this correction can then be made with background studies.

It is conceivable that alternate techniques might be found that are as efficient in selecting the emission time scale and window boundaries, but incur fewer trials for this selection. A typical value for the trial factor associated with the com-

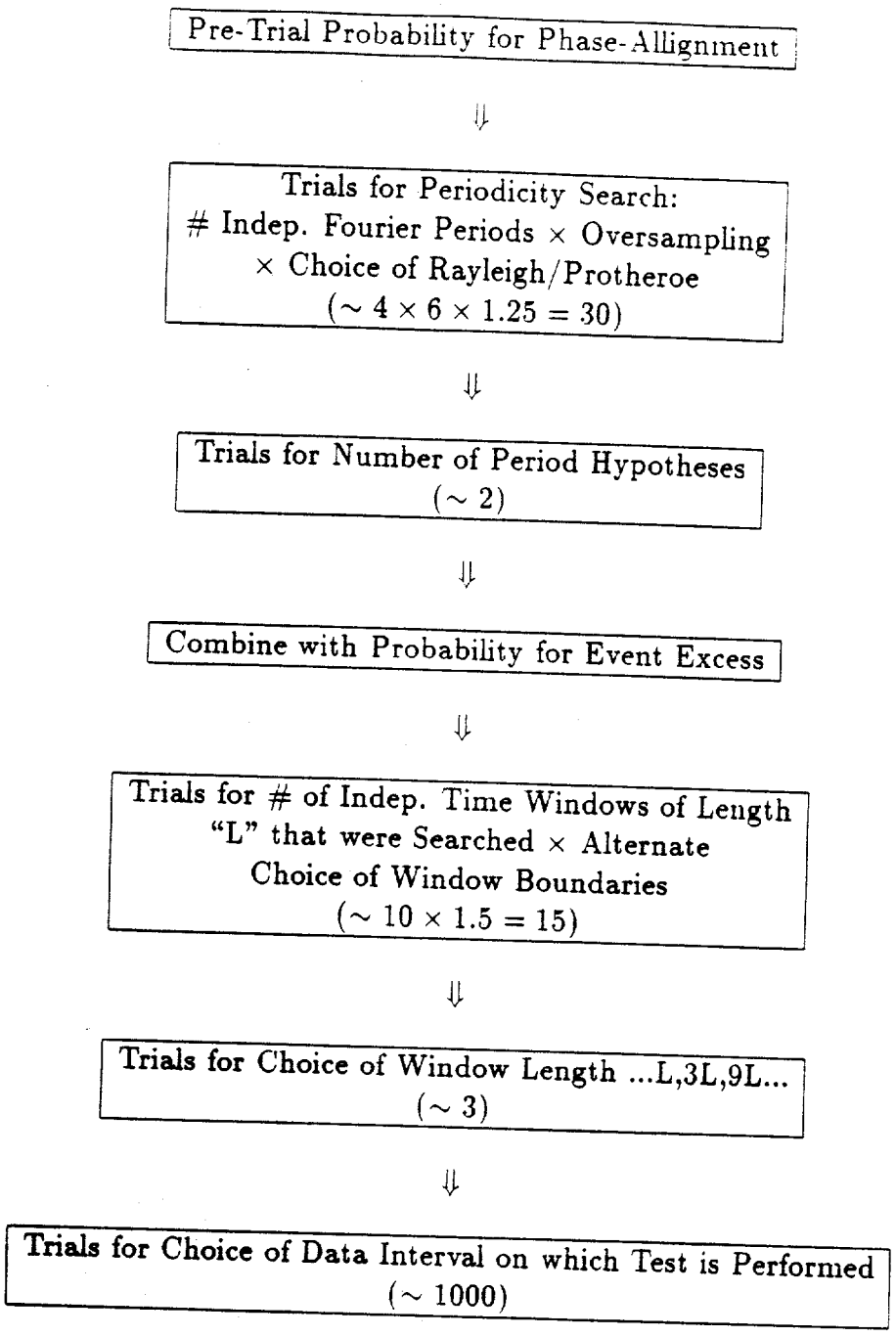

Figure 7.1: Hypothetical logic diagram for burst search. Typical values for trial factors are given in parentheses.

bination of these two choices is ~5 for the technique described here. It is difficult to see how significant improvement could be made in other areas of the search method since the other trial factors involved appear to be inherent to the problem itself.

Time-Window Oversampling

This section addresses how many different overlapping windows of a given, fixed duration should be tested in order to account for emission that may not be centered in any one particular window.

The first step involved in answering this question is to determine the appropriate trial factor that must be taken for searching a given set of overlapping, fixed-length windows. For this purpose, a simulated data set was generated assuming Poisson fluctuations around a constant background rate. This data set was then divided into 10 intervals to represent consecutive windows of a given time scale. A particular value of window offset was then chosen in terms of a percentage of the original window size. A sequence of similar sets of 10 time windows, each offset by this chosen value relative to the previous set, were then constructed until the total offset equaled the length of the initial time window (at which point the series of sets will repeat). This is schematically illustrated in figure 7.2.

The pre-trial probability for the most significant excess of events in a given time window is then calculated, and a first-order correction for the number of *independent* time intervals (10) is determined. Finally, an additional multiplicative correction to this trial factor is then calculated so as to produce a statistically correct distribution when applied to the pre-trial probability. Table 7.1 gives empirical parameterizations for this additional correction as a function of the pre-trial chance probability (as calculated within a single time window), for offsets of 50%, 25% and 10%. This study was also performed for cases where the Rayleigh test for phase- alignment is used within each time window (as opposed to using the probability for event excess), and for testing the combination of phase-alignment (using the Protheroe statistic) and event excess. In the latter case, the combination was

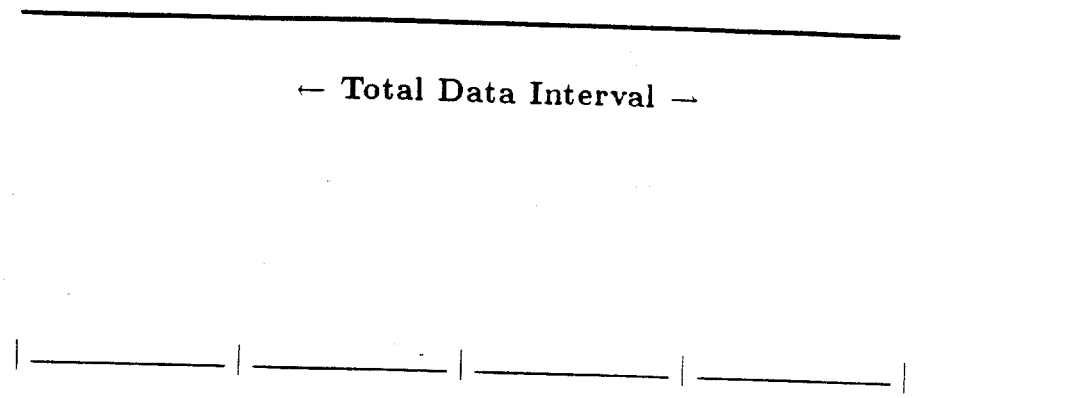

Figure 7.2: Illustration of time-window oversampling.

computed with the formula

$$P_{combined} = P_{\phi} P_{excess}(1 - log(P_{\phi} P_{excess})) \tag{7.1}$$

The trial parameterization for $P_{combined}$ was found to also depend on the number of events within the time window. These parameterizations are also given in the following table:

Offset	Poisson (event excess)	Rayleigh	Protheroe×Poisson
50%	$1.8 - 0.78P^{0.36}$	$1.96 - 0.46P^{0.26}$	$1.36N^{0.07} - 0.5P^{0.11}$
25%	$2.7 - 1.6P^{0.17}$	$2.56 - 0.97P^{0.33}$	$1.92N^{0.07} - 1.0P^{0.11}$
10%	$5.6 - 4.39P^{0.07}$	$5.08 - 3.14P^{0.09}$	$3.09N^{0.07} - 2.5P^{0.11}$

Table 7.1: Parameterization for multiplicative correction to the trial factor corresponding to the number of independent time-windows searched to account for time-window oversampling.

where P is the pre-trial probability within a given window, and N is the average number of events per window. The value given by these formulas, when multiplied by the number of *independent* time windows, gives the final, effective trial factor for the search.

In order to assess the effect of various time-window "oversamplings", square-wave signals of various durations were introduced. Figure 7.3 shows the probability for rejecting $H0$ (power of the test) at the 90% confidence level based on finding the time window that gives the single most significant event excess, as a function of the relative duration of the injected signal. This figure shows the cases of trial-corrected searches involving no offsets, and offsets of 50%, 25% and 10%. Note that although one continues to gain sensitivity with increased oversampling, the largest relative gain by far results from using a search involving 50% offsets, as opposed to using no offsets at all. Similar results are shown in figure 7.4 for tests of various scenarios using a combination of Protheroe and Poisson probabilities within each time window. Therefore, it is reasonable to choose a search that only involves an alternate choice of window boundaries that are offset by 50%.

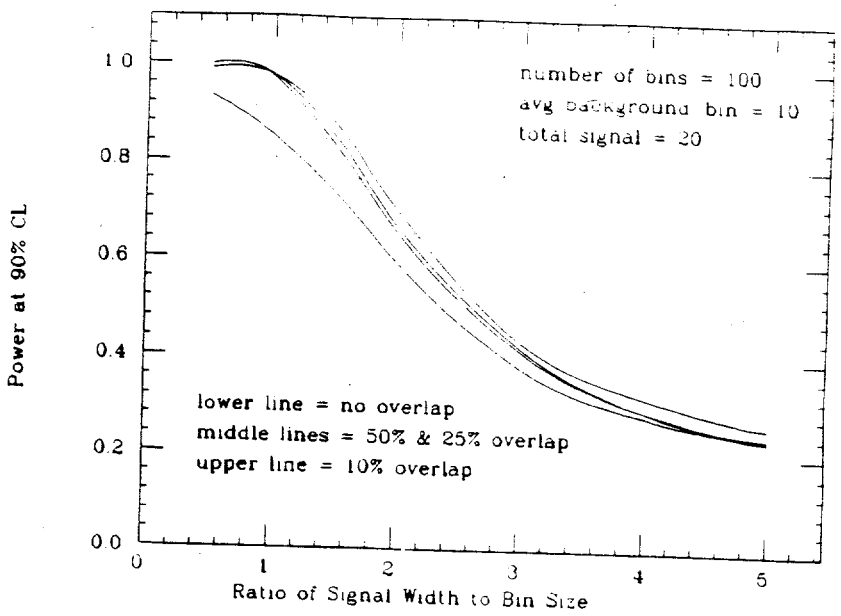

Figure 7.3: Probability for rejecting $H0$ (power of the test) at the 90% confidence level based on event excess for various time-window oversamplings as a function of the relative duration of an injected, hypothetical signal.

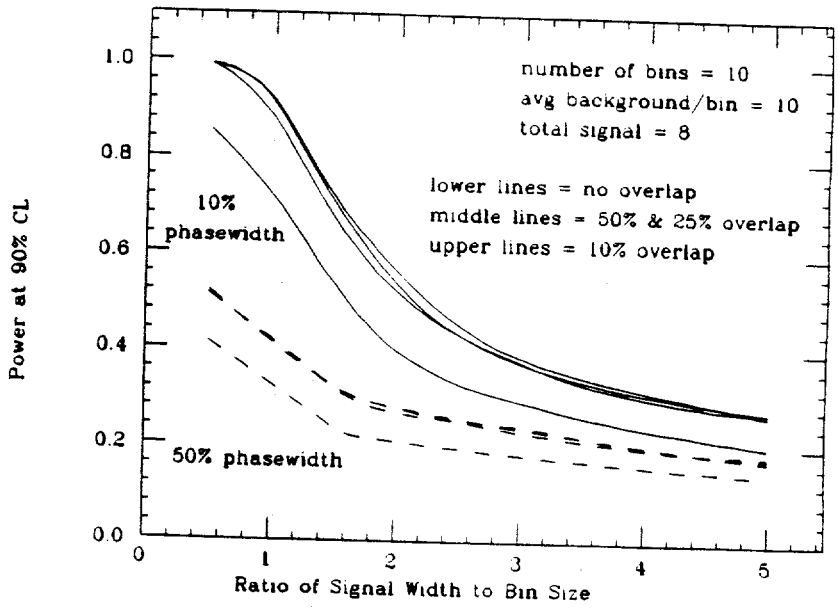

Figure 7.4: Probability for rejecting $H0$ (power of the test) at the 90% confidence level based on event excess and periodicity (Protheroe test) for various time-window oversamplings as a function of the relative duration of an injected, hypothetical signal. Results for 10% and 50% phase widths are shown.

Increase of Window Length

The next step is to determine the relative increase in the length of time windows to be taken in the process of searching for emission over larger time intervals. In principle, one would like to search over a continuous range of time scales, but computation time imposes practical considerations. The choice of the factor by which to increase the test time scale in successive searches thus involves some degree of subjectivity. Through simulation of a variety of test scenarios, it has been found that the sensitivity of the search technique is not significantly compromised if a factor of 3 increase in successive time scales is used.

Monte Carlo calculations were used to determine trial factors associated with choosing the time scale that contains the most significant interval of event excess (Poisson) as a function of the number of time scales searched. This was found to be approximated by 1 (for the first time scale) plus 0.5 for each additional time scale searched (where each additional time scale is 3 times the length of the previous one). The factor associated with testing the combination of phase-alignment (Protheroe) and event excess (Poisson) was found to be approximated by 1 plus 0.6 for each additional time scale searched.

Application to the Hercules X-1 Data Set

The following analyses refer to data taken by the CYGNUS I extensive air shower array between April 2, 1986 and January 11, 1992. CYGNUS II information is not used for reasons described in chapter 4.

Short-Term Emission

The episodic search technique previously described has been applied to the CYGNUS data to search for evidence of pulsed emission from Hercules X-1 on time scales of 10 minutes, 30 minutes, 90 minutes and 1 source day. Two sets of intervals, the second offset by 50% from the first, were used for each time scale. In each data interval, 4 different periodicity hypotheses were tested (as described in

chapter 5): **1)** Pulsed emission precisely at the interpolated X-ray period; **2)** Pulsed emission within 1 Doppler shift of the interpolated X-ray period ; **3)** Pulsed emission at a blue-shifted period lying within the uncertainty range of the 1986 results ; **4)** Pulsed emission that may occur over a wide range of frequencies, arbitrarily chosen to encompass a range of $\pm 0.5\%$ of the pulsar period. The significance of each periodicity hypothesis was assessed using the Protheroe statistic, with approximate corrections for the number of independent periods and oversampling relevant to each case. The most significant result was then taken, and a trial factor of 4 was assessed for this choice. Next, the chance probability for the observed event excess in the data interval was computed according to the prescription of Li and Ma, where the background was determined by the Monte Carlo integration method described in chapter 5, using 20 time-associations per event. This was then combined with the chance probability for periodicity according to equation 7.1. The most significant interval for a given time scale was then selected, and a trial factor was assessed according to table 7.1. The most significant result of the 4 time scales was then chosen, and the trial-corrected probability was associated with that source day.

As previously mentioned, a precise accounting of trials is difficult and the parameterizations used represent only approximations. Therefore, the same analysis was performed on background regions, from which it was determined that a multiplicative trial correction of $\sim$1.3 was needed. The distribution of the resulting probabilities is shown in figure 7.5, the dashed line shows the form of the expected distribution for background. A test of the upper 10% of the distribution (Appendix C) yields a chance probability of 54%. A similar analysis was performed to search for purely unpulsed signals. Background studies indicated that no additional trial correction was necessary, suggesting that the factor of 1.3 needed in the previous study may have been due to an underestimate of the number of independent periods searched. The distribution of most significant burst probabilities based on event excess alone is shown in figure 7.6, and a similar test of this distribution yields a chance probability of 82%. Note that this is not independent of the previous result, since the former employs event excess information as well.

The scenario of emission on the time scale of exactly one source-day has

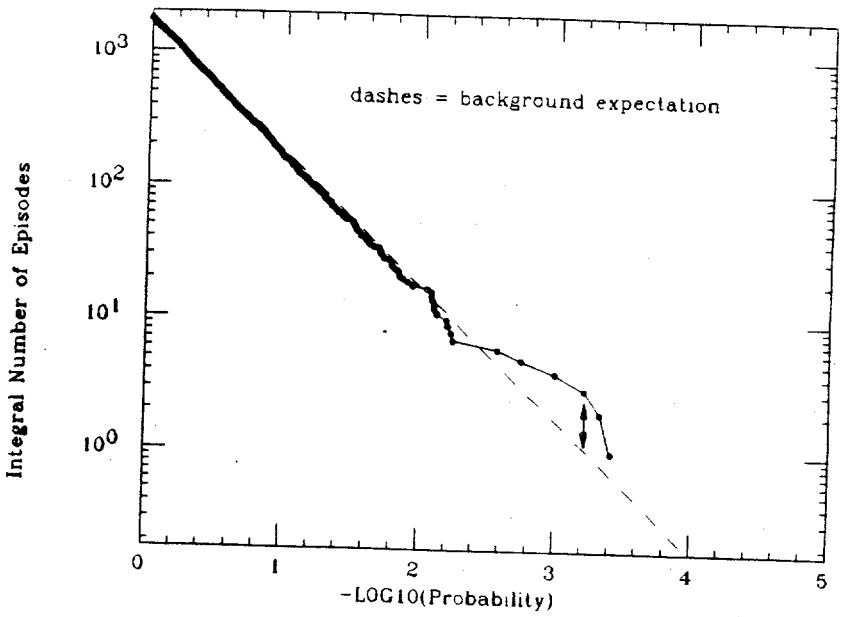

Figure 7.5: Integral probability distribution of burst episodes involving event excess and periodicity tests. The dashed line shows the background expectation. The deviation indicated by arrows corresponds to a chance probability of 54%.

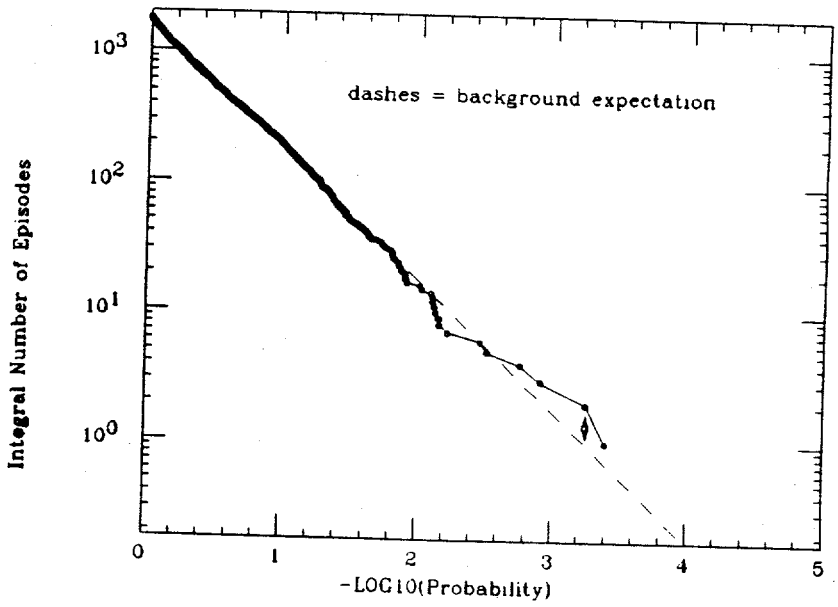

Figure 7.6: Integral probability distribution of burst episodes involving event excess tests only. The dashed line shows the background expectation. The deviation indicated by arrows corresponds to a chance probability of 82%.

also been treated as a separate hypothesis, as discussed in chapter 5. Therefore, the distribution of daily probabilities based on the combination of event excess and periodicity is shown in figure 7.7 (after a background-based trial correction of 1.25). A test of the distribution results in a 8.5% chance probability. A similar plot for event excess alone is shown in figure 7.8, corresponding to a chance probability of 36%. Once more, these probabilities estimates are not independent.

Figure 7.9 shows the upper limits for source fluxes from Her X-1 above 100 TeV for emission on time scales of 1 day. These limits are based solely on the observed event excesses (*i.e.* no periodicity information is used), and are calculated according to the prescription given in Appendix G. The higher values of flux limits that deviate from the main part of the distribution are primarily due to low numbers of expected events resulting from interrupted data acquisition.

The 5 most significant episodes for each of these 4 scenarios are given in table 7.2. The lack of independence of these tests is clear. Run 171, corresponding to the 1986 claim (discussed in chapter 5), is the most significant in all 4 hypotheses. Note that the post-trial chance probability for run 171 that results from these numbers is less significant than the assessment given in chapter 5. However, as has been stated before, the analysis approach taken is to select episodes that are potentially interesting based on an initial, relatively quick analysis, and then to re-examine these episodes with a more time-consuming, detailed approach. Aside from the study of run 171 represented in table 7.2, analyses such as maximum likelihood estimation of event excess and periodicity studies of combined bursts within the day have not yet been taken into account.

Based on table 7.2, the two additional runs (975 and 2361) that contribute to the most significant deviation in figure 7.7 have undergone further analysis, similar to that described in chapter 5. A summary of the results is as follows: for run 975, a likelihood analysis of the event excess yielded an increased significance by a factor of 2 compared to the binned approach. Coherent phase-analysis of burst combinations for this run failed to yield a more significant result than what was already found, so trial factors for the search ultimately resulted in a decrease of the significance by a factor of 4. A net decrease in the significance of a factor of 2 is therefore found.

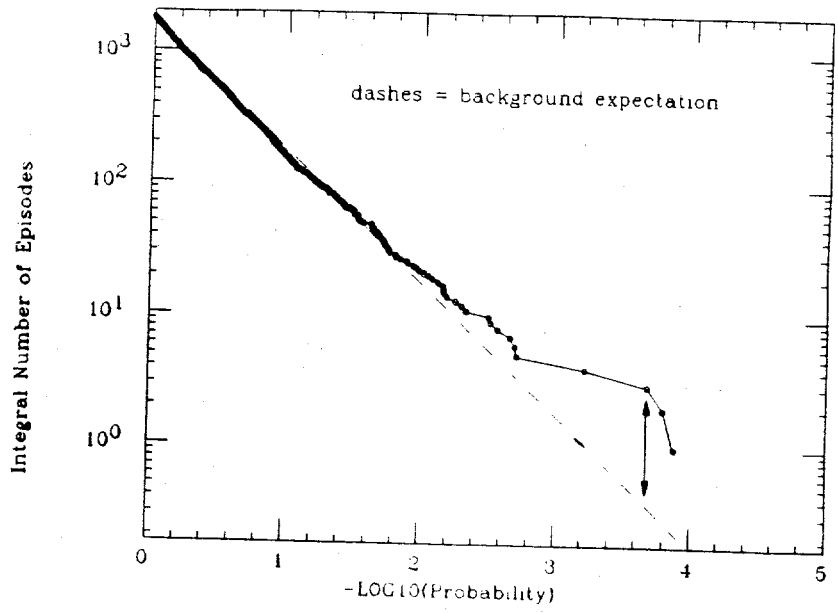

Figure 7.7: Integral probability distribution of day-long episodes involving event excess and periodicity tests. The dashed line shows the background expectation. The deviation indicated by arrows corresponds to a chance probability of 8.5%.

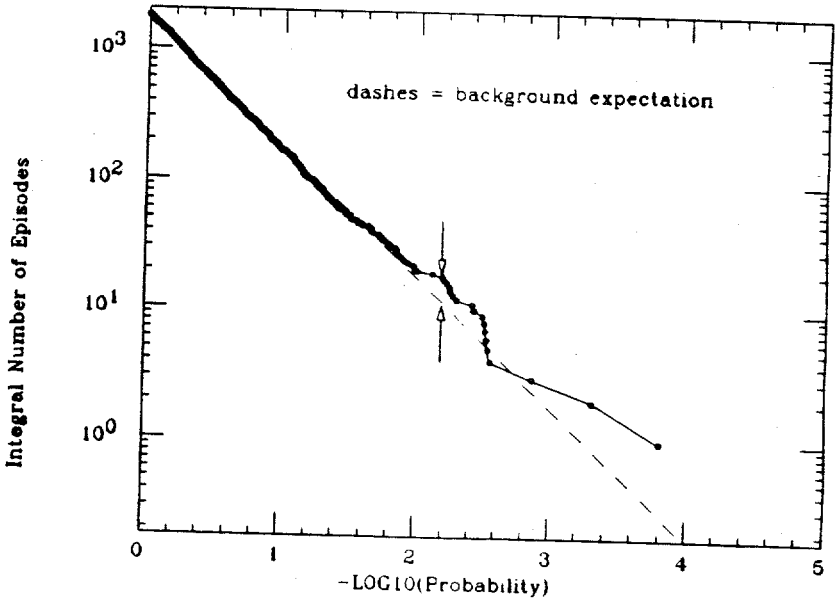

Figure 7.8: Integral probability distribution of day-long episodes involving event excess tests only. The dashed line shows the background expectation. The deviation indicated by arrows corresponds to a chance probability of 36%.

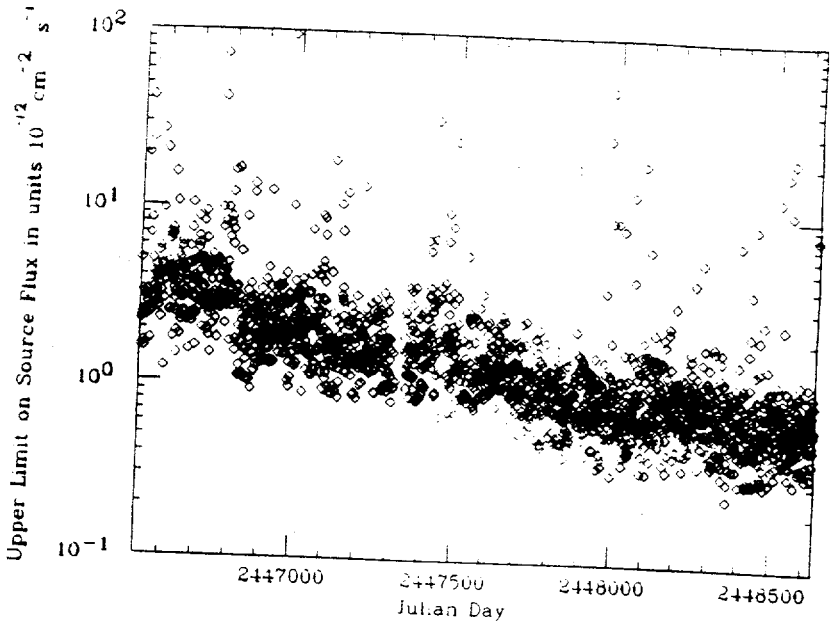

Figure 7.9: Upper limits for source fluxes from Her X-1 above 100 TeV for emission on time scales of 1 day. Flux limits are quoted in units of $10^{-12} cm^{-2} s^{-1}$. The higher values of flux limits that deviate from the main part of the distribution are primarily due to low numbers of expected events resulting from interrupted data acquisition.

Emission Scenario	Julian Day	Run	Start Time (UTC Sec)	Duration	Period	Chance Prob. for Jul. Day
1-Day, Pulsed	2446635.5	171	-	-	1.23571	1.3E-04
	2447416.5	975	-	-	1.23547	1.6E-04
	2448165.5	2361	-	-	1.23677	2.1E-04
	2448292.5	2819	-	-	1.23844	6.0E-04
	2447896.5	1512	-	-	1.23569	2.0E-03
1-Day, Unpulsed	2446635.5	171	-	-	-	1.6E-04
	2447416.5	1501	-	-	-	5.0E-04
	2448165.5	2361	-	-	-	1.4E-03
	2448324.5	2936	-	-	-	2.8E-03
	2447730.5	1318	-	-	-	3.0E-03
Burst, Pulsed	2446635.5	171	-	Full Transit	1.23571	3.9E-04
	2447416.5	975	-	Full Transit	1.23547	3.9E-04
	2448165.5	2361	-	Full Transit	1.23677	6.0E-04
	2447532.5	1116	51196	30 Minutes	1.23779	1.0E-03
	2448292.5	2819	-	Full Transit	1.23844	1.8E-03
Burst, Unpulsed	2446635.5	171	-	Full Transit	-	3.9E-04
	2447686.5	1268	17909	10 Minutes	-	5.6E-04
	2448165.5	1501	-	Full Transit	-	1.2E-03
	2447280.5	835	26955	10 Minutes	-	1.7E-03
	2447673.5	1250	38611	30 Minutes	-	3.1E-03

Table 7.2: 5 most significant episodes in each emission scenario tested. The probabilities quoted account for trials associated with specific day in question and not for the number of days searched.

resulting in a post-trial chance probability for run 975 of 49% under the hypothesis of 1-day, pulsed emission. For run 2361, a likelihood analysis for event excess yielded the same significance as the binned approach. A coherent phase-analysis of 5 smaller bursts resulted in an improvement in significance by a factor of 2 after trial factors for the burst combination are taken into account. A net improvement of a factor of 2 in significance therefore results, yielding a post-trial chance probability for run 2361 of 16% under the hypothesis of 1-day, pulsed emission. Clearly, neither of these runs are significant enough to warrant any further claim of observed emission.

Long-Term Emission

A search has also been conducted to look for emission on time scales greater than 1 source-day. Specifically, the significance of event excesses were examined for time scales of 2,6,18,54,164 and 486 days according to the prescription previously described. The most significant observation is a 6-day interval, beginning at run number 816, on the Julian Day 2447257.5 . The post-trial probability after accounting for the number of 6-day intervals, time-window oversampling, and choice of the time interval is 20%. Again, no claim of emission is thus warranted.

Chapter 8

Results from Other VHE/UHE Experiments: A Critical Review

"I deserve respect for the things I did not do."
- Dan Quayle -

"It's no exaggeration to say that the undecideds could go one way or another."
- George Bush -

Durham

The first claim of detected VHE emission (~1 TeV) from Hercules X-1 is attributed to the Durham air-Cherenkov telescope (then located in Dugway, Utah) in 1983 [92]. A 3 minute burst was reported to have occurred on April 17 of that year, consisting of a 3 standard deviation event excess pulsed at a period consistent with that of the X-ray measurements. The telescope was operated in "drift-scan" mode, where the candidate source is allowed to drift past an aperture of ~ 2 deg. The chance probability for phase alignment was given as 4×10^{-4}, and a final significance (excess and phase alignment) of 7×10^{-5} was then quoted.

The ~3 standard deviation event excess, consisting of approximately 30 events, corresponds to a chance probability of 1.5×10^{-3}. The quoted chance probability for phase-alignment does not take into account the oversampling of the 1 IFP

interval around the X-ray period that was considered. This factor of about 4 increases the probability to 1.6×10^{-3}. Combining this with the chance probability for the observed event excess according to equation 5.5, yields a value of 3.3×10^{-5}. However, a trial factor must be assessed for the choice of the 3 minute interval. As this was not done in the published analysis, it will be estimated here based on the approach discussed in chapter 8: Since 4 scans, each 40 minutes in duration were considered in this analysis, 53 independent 3-minute intervals are possible. An additional factor of $\sim$2 should be assessed for optimizing the relative "start time" that defines the position of the 3-minute interval, and another factor of $\sim$3.5 for choosing the value of 3 minutes (assuming that values of 1-120 minutes would have been considered). The final, "post-trial" chance probability is therefore given by:

$$P = (3.3 \times 10^{-5})(53 \times 2 \times 3.5) = 1.2\%$$

However, the events used in the periodicity analysis do not appear to exactly correspond to those of the event excess. A plot of the rate excess during the burst indicates $\sim$118 recorded events, whereas the phase plot that is presented only contains 98 entries. The text further states that,"The excess ocurred $\sim$5 min before the object was in the centre of the field of view of the telescope. Inter-detector fast timing indicates that the pulsed events in the excess arrived from a direction $\sim$ 1 deg below the centre of the field of view coinciding with the position of Her X-1." This indicates that the periodicity was optimized in an *a posteriori* manner by event selection. The significance of this result is therefore impossible to judge, although the chance probability is clearly greater that 1.2%. Thus, it does not appear that this observation can be considered to be a demonstration of source emission.

The Durham group has also claimed a 28 minute simultaneous observation with the Whipple air-Cherenkov telescope of VHE emission from Hercules X-1 on April 4, 1984 [93]. During this time, an analysis of the Whipple data resulted in a large Rayleigh power in the vicinity of the X-ray period with a pre-trial probability of 8×10^{-4}. Over the same 28 minute interval, the Durham group observed a Rayleigh power with a pre-trial chance probability level of 0.003 at a period consistent with that of the Whipple result. Taking period oversampling trials into

account, along with the scan over 3 independent periods typically performed by the Whipple group, these probabilities become 0.009 and 0.01 for Whipple and Durham respectively. Given the number of time intervals that have been tested by each group separately, it is clear that neither observation is able to stand on its own as a claim of detection. Likewise, it is impossible to assess the significance of a possible simultaneous detection without a knowledge of the number of intervals over which coincident observations of source emission by both experiments were possible. It is known that the Whipple data base contains approximately 600 observation intervals on Hercules X-1 of 28 minutes duration for the years 1984-1987. Similar numbers have not been published regarding the Durham data, let alone times of overlapping observation intervals. A further complication is the fact that the Durham claim is not based on an analysis of the exact 28 minute interval reported by Whipple, but results from the consideration of data taken during an 60 minute time span that included the Whipple time interval. It has therefore not been demonstrated that the Durham data indicates any significant phase alignment *during* the precise interval specified by Whipple. Given these uncertainties, the significance of the claimed simultaneous detection cannot be determined.

Ooty

The collaboration associated with the Ooty EAS array, located in Ootacamund, India, has claimed the observation of 3 episodes of coherently pulsed, phase-locked emission in 1986 occurring on July 1, August 8-9, and November 21 respectively [94]. The assertion of phase-locked emission over these timescales raises several difficulties: **1)** The level of period stability indicated is in contradiction with X-ray measurements of the underlying pulsar (figure 3.2); **2)** the measured Ooty period, 1.2357701 seconds, lies outside the 90% confidence level of the CYGNUS result under the assumption of coherence (figure 5.16); **3)** the average phase for each of the 1986, blue-shifted bursts claimed by the CYGNUS, Whipple, and Haleakala collaborations (discussed below) do *not* line up with those of the Ooty bursts at their predicted period. This is shown in figure 8.1, where the ephemeris of Deeter.

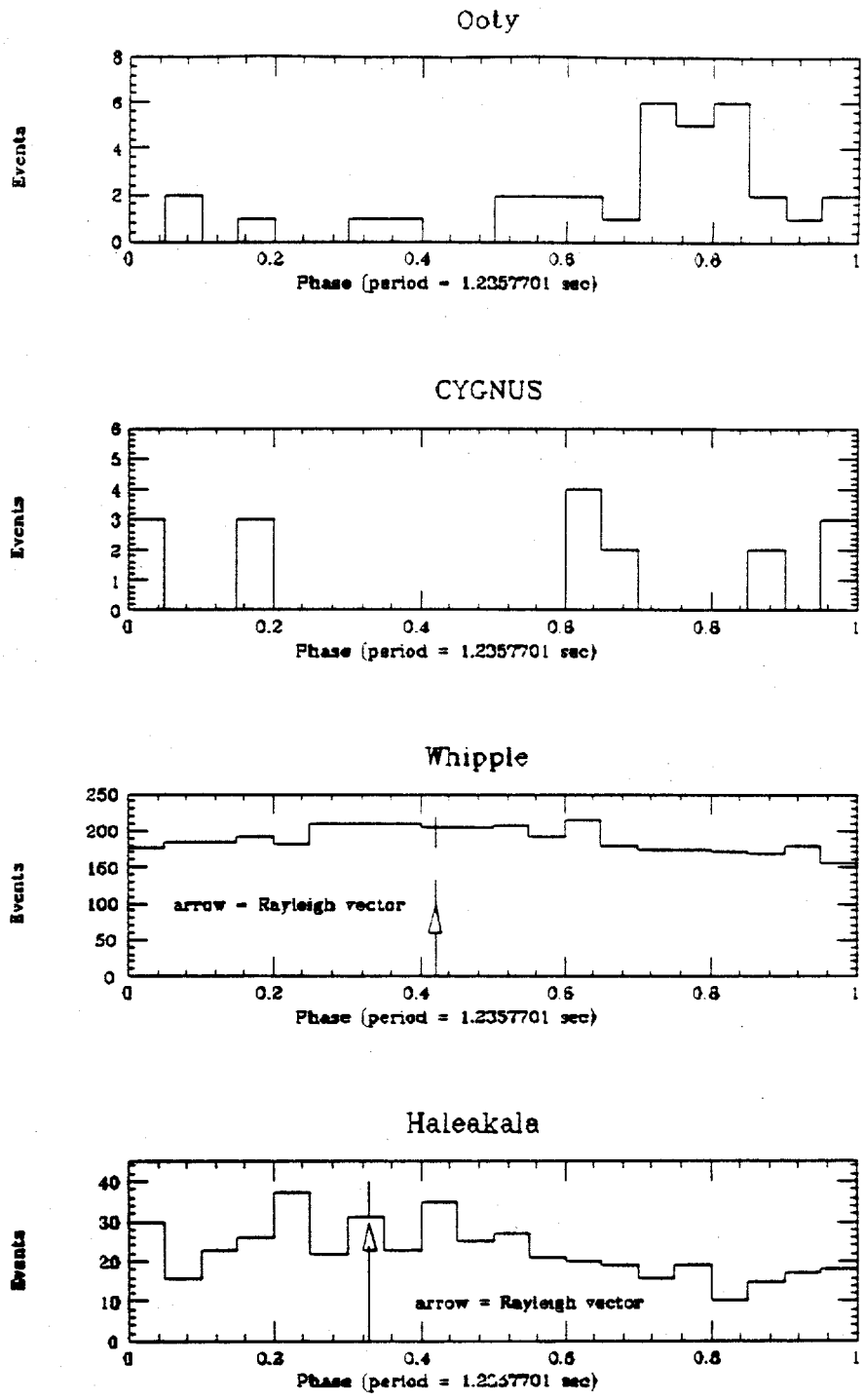

Figure 8.1: Histograms of the phase distribution for the Ooty, CYGNUS, Whipple and Haleakala observations of Her X-1 at the period specified by the Ooty collaboration.

Boyton and Pravdo [34] has been applied in conjunction with the MIT PEP311 solar barycenter correction [95] to the unprocessed times for each experiment. The directions of the Rayleigh vectors are indicated on each plot for the Ooty period. Note further that the pre-trial Protheroe probability for the CYGNUS data at this period is ~3%, more than 4 orders of magnitude less significant than the phase alignment at the period 1.2357 seconds.

In addition to these problems, the significance of the Hercules observation by Ooty depends on the specific manner in which the three episodes are combined, as no single episode is particularly significant either in terms of event excess, or phase-alignment. The combination of the 3 episodes appears to rely on two questionable arguments: First, the fact that no additional trials are assessed for examining other potential source-days is justified based on an ill-defined, *a posteriori* selection of "interesting" episodes prior to the periodicity analysis. This is especially difficult to understand since it is clear from the published account that at least 4 additional days were examined. Secondly, no trials were associated with a period-scan of the second and third episodes because coherence was *assumed*, even though this had not yet been demonstrated.

In a follow-up paper on the Hercules X-1 result, the group uses the angular distribution of events within the 3 episodes to measure of the angular *resolution* of the array [96] and to claim futher consistency with the $H1$ (signal) hypothesis. However, this distribution is also consistent with $H0$, since the selection criteria regarding event excess for these episodes biases the angular distribution to peak in the vicinity of the source, even if the event excess is due to a fluctuation of background. In this regard it should be noted that it is the stated policy of the Ooty collaboration to test for the $H1$ hypothesis, rather than testing to reject $H0$ [97]. In other words, a signal is *assumed*, and tests are then performed to elucidate the nature of the signal. Given this approach to data analysis, the results presented by the Ooty group cannot be used to determine whether or not the observations of Hercules X-1 are consistent with background expectation.

Gulmarg

The Gulmarg collaboration has reported the possible observation of a 15 minute burst from Hercules X-1 on June 12, 1988 at energies above 2 TeV, from data taken with their air-Cherenkov telescope [98]. The claim is based on an initial search of 16 half-hour intervals, using the Rayleigh statistic to scan over 11 independent periods. One interval was found to yield to a Rayleigh power of 9.5, or a pre-trial probability of 7.5×10^{-5}. After taking 11×16 trials, a probability of 1.3% is quoted. However, this does not account for the trials associated with oversampling the independent periods, which raises the probability to 5.5%. The trials associated with the further scan that was performed to pick the optimum 15 minute interval are not clear. In their publication, these trials are overestimated with respect to the number of independent 15 minute intervals but underestimated with respect to the method by which the period of 1.237625 seconds was chosen for the Rayleigh test. Taking the value of 5.5%, which further assumes that Hercules data was only taken for the reported observation period during 1988, a strong claim of source detection cannot be made.

Pachmarhi

The Pachmarhi group employs an array of 18, seperately tracking, parabolic mirrors equipped with fast photomultuplier tubes. On April 11, 1986, a 30 minute rate increase in recorded events of 54% was observed while tracking Hercules X-1 [99]. This correspond to a 42 standard deviation effect, and indicates a flux of 1.8×10^{-8} particles per cm^2 per second above 0.4 TeV. If this flux is scaled to 100 TeV according to an E^{-1} integral spectrum, it would to be consistent with the instantaneous flux observed by the CYGNUS EAS array during the bursts of July 24. Periodicity analysis did not reveal any significant power, although such an analysis was hampered by hardware problems associated with the large rate increase. Accidental rates and visible night sky activity appeared to be normal during the episode. If systematic effects due to electronics or background light can be ruled out, the sta-

tistical significance of this result is clearly beyond question. However, it is difficult to rule out such systematic effects with complete certainty, particularly for a system that was not designed to handle the large rate increase that was observed. This fact is recognized by the authors by their caveat,"*Barring any electronic noise or celestial or terrestrial optical phenomenon with time structure similar to that of atmospheric Cerenkov phenomenon*, we ascribe the increase to TeV gamma rays from Her X-1." In light of this, the Pachmarhi observation will not be cited as a detection in this thesis, although it remains a curiosity.

Fly's Eye

The Fly's Eye experiment in Dugway, Utah reported a detection of Hercules X-1 in July of 1983 while operating in "Cherenkov blast mode" [100]. This mode of operation allowed for the observation of air-Cherenkov signals above an energy threshold of about 200 TeV, with nearly full-sky coverage. An excess of 29 events, corresponding to a 1.8 standard deviation effect, was observed over the 5 nights of Hercules data recorded in this mode during 1983. On one of these nights, July 11, a high degree of phase-alignment was indicated at the X-ray period of 1.2377872 seconds, extrapolated from satellite measurements performed in May of 1983. The data from this night was then further divided into two halves, and the pulsation was found to be concentrated primarily in the first half of that night. To calculate the probability for phase-alignment, a 10-bin histogram of phases was first constructed. Four different bin-boundary positions were examined, and the probability for the single largest bin excess was computed. This bin was found to contain 15 events when ~3 were expected, yielding a pre-trial probability of 7×10^{-7}. After trials for the number of phase bins, bin-boundary positions, and data intervals examined, a post-trial probability of 2×10^{-4} is quoted.

A potential problem with binned phase analyses is that the visual appearance of the resulting histogram is often used to dictate how the probability is to be assessed, resulting in a biased calculation. For example, if the excess is contained in a single bin, the probability is typically calculated with respect to a single "source"

bin. If several neighboring bins contain the excess, the probability is often calculated with respect to those few bins, or a Rayleigh test is used. In order to avoid such biases, bin-independent tests (such as those discussed in chapter 5) are recommended. Based on the published phase histogram, the Rayleigh test is predicted to result in a chance probability of ~8%, and a $Z10$ test is predicted to yield $\sim 5 \times 10^{-5}$. Taking a trial factor of ~ 1.5 for the choice of these two statistics, and a factor of 10 for the number of half-nights (note that a factor of 7 for 5 full nights plus 2 half nights is incorrect since *any* of the 5 nights would have been further divided if it initially appeared to be interesting), a chance probability level of 7.4×10^{-4} results. Note that this alternate analysis yields a number that is only a factor of ~ 4 larger than the published value, indicating that the effect cannot be explained as a bias in the binning procedure.

The event excess associated with Hercules X-1 for the full night of July 11 is estimated to be 88 where 83.9 are expected [101]. However, for the half of the night indicating periodicity, 41 events were observed where 29.2 were expected, in good agreement with the observed phase excess. The energy spectrum of events constituting the main phase peak appears to be consistent with that of the cosmic ray background, although it should be noted that it is difficult to distinguish an $E^{-1.7}$ integral spectrum from a spectrum such as $E^{-1.0}$ based on ~12 events, especially considering that the energy of each event may only be known to within a factor of ~2. The episodic integral flux corresponding to the observed excess has been estimated to be $3.3 \times 10^{-12} cm^{-1} sec^{-1}$ above an energy of 200 TeV.

A potential difficulty of the observation is the fact that the Durham air-Cherenkov telescope, observing at the same time with a lower energy threshold, failed to observe any significant excess [102]. While this could be explained by invoking a very flat primary energy spectrum, the explanation is not very satisfying.

Subsequent blast-mode observations by the Fly's Eye group have failed to yield additional candidate detections. However, the additional trial factor for these later searches would most likely only decreases the significance of the 1983 observation by less than an order of magnitude, which is not enough to classify the result as being consistent with background fluctuations. Furthermore, since

subsequent blast-mode operations have employed different triggering criteria, the consistency of observations between data sets is difficult to judge. In any case, this observation remains difficult to explain in terms of the $H0$ hypothesis.

Whipple

The Whipple air-Cherenkov detector, located at an altitude of 2.3 km on Mt. Hopkins in Arizona, has been operating as an "imaging" telescope since 1983 [103]. The telescope consists of a composite, 10m diameter, optical reflector that directs the Cherenkov light from air-showers onto an array of phototubes at the focal plane. This "camera," possessing a 3.5° field of view, is able to provide information on the specific angular distribution of Cherenkov light associated with air-showers. This distribution is predicted to be different (essentially narrower) for photon-induced showers compared to hadronic interactions, which tend to produce a more disperse image due to the transverse momentum associated with such interactions [104]. This imaging technique has been applied as a background discriminant to data associated with the Crab nebula, resulting in a very compelling observation of continuous, VHE emission from that source [7].

Since 1984, Hercules X-1 has been tracked for a total of 512 hours under two primarily different experimental conditions: From 1984-1987, a "medium resolution" camera was used, consisting of 37 PMTs, each with a diameter of 5cm and a 0.5° field of view. In 1988, the detector was upgraded to a "high resolution" camera, using 91 PMTs, each of 2.5cm diameter and with a 0.25° field of view, plus an outer ring of 18 PMTs with 5cm diameters [105]. Both systems were triggered when two adjacent tubes recorded pulse heights above some preset discrimination level. This requires a certain level of image "compactness" for triggered events (especially for lower energy showers), effectively resulting in a slight hardware bias towards photon-like interactions. This bias is stronger in the case of the high-resolution camera due to the closer PMT spacing. A recent review of the Hercules X-1 data set has been published in which the data corresponding to each detector configuration were analysed separately [9].

The distribution of peak Rayleigh powers obtained during 30 minute observation intervals was tested (see Appendix C) to assess the significance of a collection of potential burst observations within the context of the Whipple data set. Note that the result of this type of analysis is not independent of previously reported claims of burst observations [87]. Shown below is a reproduction of a table presented in the Whipple review paper that gives the results of the distribution test for 4 ~independent hypotheses considered for the 1984-1987 data set, and for 4 hypotheses considered for the 1988-1989 data set. Two aspects of this table are

Table 8.1: Results of Her X-1 periodicity analyses from the Whipple experiment [9].

Data Base	Frequency Search Range (Indep. Fourier Freq.)	Image Selection	Chance Probability
1984-1987	fundamental (X-ray) ±1	no	0.0025
1984-1987	fundamental (X-ray) ±1	yes	0.2628
1984-1987	2nd harmonic ±1	no	0.2171
1984-1987	2nd harmonic ±1	yes	0.3243
1988-1989	fundamental (X-ray) ±1	no	0.2321
1988-1989	fundamental (X-ray) ±1	yes	0.3498
1988-1989	fundamental -1-4 (blue-shifted)	no	0.4548
1988-1989	fundamental -1-4 (blue-shifted)	yes	0.0633

worth note: First is the significance of the chance probability level indicated with regard to the 1984-1987 data base for non-image-selected data in the vicinity of the fundamental X-ray period. Second is the fact that all 8 of the probabilities are less than 50%. While this latter effect may be indicative of weak signals present in several emission hypotheses, it may also indicate the presence of a slight systematic overestimate of the significance level. In light of both this and the discussion in Appendix C regarding the Fisher versus the binomial approach to testing the distribution, the results of a re-analysis of several distributions will be presented here using the binomial test of the upper 10% of these distributions (see Appendix C).

Before proceeding with this re-analysis, it should first be noted that an additional hypothesis is relevant to the 1984-1987 Whipple data set. In their paper.

the Whipple collaboration states that, while there appears to also be an excess of large Rayleigh powers associated with a blue-shifted period, there is no *a priori* justification to consider this hypothesis. It is therefore only considered for the 1988-1989 data set. However, the 1986 result [4] related to the contemporaneous observations of a blue-shifted period does, in fact, provide a justification to search for *other* blue-shifted bursts. As long as the observation of June 11, 1986 is removed, a search for other episodes of blue-shifted emission provides a well-defined, independent test of that hypothesis.

The following table lists the results of the re-analysis of those Whipple data sets for which the observed and expected Rayleigh power distributions could be extracted from published tables or graphs. For the 1984-1987 data, both the

Table 8.2: Alternate analysis of Whipple results

Data Base	Search Range (IFF)	Image Selection	Power Thresh	obs/expct Num > Thresh	Chance Prob
1984-1987	X-ray ±1	no	7.6	7/1	0.0095
1984-1987	X-ray ±1	yes	9.8	1/0.11	0.79
1984-1987	blue-shifted	no	6.8	12/4	0.0125
1988-1989	X-ray ±1	no	5.8	13/7	0.20
1988-1989	X-ray ±1	yes	4.3	32/25	0.47
1984-1989	X-ray ±1	no	6.0	26/12.4	0.0070

non-image-selected searches near X-ray and blue-shifted periods indicate possible emission at about the 1% chance probability level. Recall that the June 11, 1986 interval has been removed from the blue-shifted data set. The chance probability associated with this interval has been separately assessed to be somewhat less than 1% [4]. The combined non-image-selected X-ray results for the years 1984-1989 is also given. This indicates that, contrary to statements made in the Whipple paper, the effect is *not* less significant when the 6 years of data are taken as a whole.

Although a distortion of a probability distribution may indicate the presence of signal, it does not necessarily indicate which specific episodes contain this

signal. One method to further discriminate such episodes is to check for the consistency between the event excess and Rayleigh power for a given interval under the signal hypothesis [69]. For most of the intervals associated with Hercules X-1, the event excess was estimated from deviations of the measured rate distribution from the entire night, fit as a smooth function of zenith angle. With the application of this technique, a number of the episodes involving large Rayleigh powers were found to be inconsistent under $H1$. However, due to the lack of actual off-source data in most of these cases, the estimate of event excess would give misleading results if a more continuous, unpulsed component of emission were present throughout some fraction of the night in addition to an occasional pulsed episode. In this case, the true quantity of signal events may be obscured by simply changing the overall normalization of the zenith angle fit to the rate distribution. This scenario, is not inconsistent with the observations by the Fly's Eye and CYGNUS collaborations, in which the event excess present in pulsed "bursts" did not account for all of the excess seen during a larger observation interval that encompassed these bursts.

For one particular episode in the 1984-1987 data set that resulted in a Rayleigh power of 7.7 in in the vicinity of the X-ray period for non-image-selected events, the estimate of event excess gave a 4.45σ result, or a chance probability of 4.3×10^{-6}. The chance probabilty level for the Rayleigh power after trials for the period scan only is 2.3×10^{-3}. Combining these probabilities according to equation 5.5 yields a value of 1.9×10^{-7}. Taking trials for the total number of intervals searched during the 6 years of Hercules X-1 observations that have been reported (578+486) results in a final chance probability estimate of 2×10^{-4} for the "hottest" interval of the observation period. Also note that the hypothesis corresponding to this number is essentially independent of the hypotheses previously discussed. However, this result once again depends on whether an accurate assessment of event excess can be made based on a zenith-angle fit to on-source event rates. The Whipple group feels that there is currently not sufficient confidence in understanding the systematics of this approach to warrant a claim of detection here. As previously stated, this also casts some doubt on the ability of the group to judge the consistency of phase-alignment with event excess during other episodes.

Taken as a whole, it is difficult to explain the Whipple data set associated with Hercules X-1 in terms of the null hypothesis. If emission has been observed, the lack of such emission related to image-selected events (a proven technique for emission associated with the Crab nebula) appears to lead to the conclusion that the particles associated with Hercules X-1 are not gamma rays. However, this conclusion is based on several assumptions: **1)** The image-selected data quality with regard to the specific nights in question is sufficient to selectively reject hadronic background. While one tends to believe that this is probably true, it has not yet been explicitly demonstrated. **2)** The primary energies of the source events lie within a range where image-selection is effective. For example, higher energy events are known to be more difficult to discriminate via image-selection in the current Whipple configuration due to PMT saturation. **3)** Somewhat related to this last point is the assumption that the visible energy associated with a given event can be used to accurately determine the total energy of the primary interaction. If an appreciably large fraction of the interaction energy is "hidden" (e.g. by producing highly energetic muons or neutrinos), models associated with a modification of photon interactions at much higher energies cannot be ruled out.

Based on the 1988-1989 observations, one is tempted to conclude that the effect is not present in the data associated with the high-resolution camera. If this is true, then either **1)** the apparent observations of the earlier data are not confirmed by further studies; or **2)** the upgraded camera is biased against the type of interaction associated with Hercules X-1 events. This former possibility would occur if, for example, the interactions of source events produced very dispersed Cherenkov images. However, as indicated by the results for the combined data sets for searches near the X-ray period, there is not yet compelling evidence to suggest that the results from the high-resolution camera are inconsistent with those of the earlier data.

Curiously enough, the conclusion stated by the Whipple group based on this data was that,"...no statistically significant evidence for TeV gamma-ray emission was found in the Whipple Observatory data base when the 6 years of data are taken as a whole." This conclusion appears to be unwarranted based on the

data as presented. In fact, if the information provided by the group is correct, the Whipple data base appears to provide one of the most compelling indications of emission from Hercules X-1. Whether or not these observations are consistent with gamma-ray emission remains an open question.

Haleakala

The Haleakala air-Cherenkov telescope [106] operated from 1985-1991 [107]. The original telescope consisted of 6 mirrors, each 1.5 meters in diameter. These mirrors were viewed by a total of 36 PMTs, 18 of which looked on-source, while the remaining 18 looked at a background region 3.6 degrees off-source. The telescope also had the capability to operate in a "wobble" mode, in which the two sets of PMTs alternately viewed the on-source and off-source regions every 15 minutes. The energy threshold of the telescope has been estimated to be approximately 200 GeV, with an angular resolution of better than 0.5 degrees. During 1988, the instrument was upgraded by replacing the 6 mirrors with 26 smaller (0.85 meter diameter) mirrors. Two episodes of interest associated with Hercules X-1 were observed during the operation of the telescope.

For the 1986 data, 416 intervals of 15 minute duration were examined for evidence of pulsed emission from Hercules X-1. The most significant result occured on May 13, where a Rayleigh power of 12.7 was associated with a period of 1.23593 ± 0.00018 seconds [5]. This result is one of the previously mentioned contemporaneous observations in 1986 that included the Whipple and CYGNUS experiments. Taking a trial factor of 416 for the number of intervals examined in that year, a factor of 3 for the number of independent periods searched, and a factor of 5 (as opposed to 3) for the period oversampling, the resulting chance probability is about 2%. In their paper, the Haleakala group also combines this with the probability for the observed 1.4σ excess for that interval. However, this combination is done according the approach of equation 5.22, as opposed to equation 5.23. If the latter approach is used, the result remains about 2%.

In 1987, a 15 minute interval was observed that yielded a Rayleigh power of

11.9, associated with a period of 1.23578±0.0002. Once again taking a trial factor of 3×5 for the oversampled period scan, and a factor of 292 for the number of interval examined during 1987, a chance probability of 3% results.

If a test of the distribution, similar to that described in the previous section, is used to place these observations within the context of the entire data set, the following result is found: Given the 903 total intervals associated with Hercules X-1 that have been examined from 1985-1989, the binomial probability to observe 2 such intervals with "pre-trial" chance probability levels less than $\frac{0.03}{292} = 1 \times 10^{-4}$ (from the 1987 observation) is 0.0038. The trial factor for a test of the upper 10% of the distribution is 12.5 for this case, yielding a final chance probability estimate of 5% for the entire data set.

Further doubt has been cast on these observations by the fact that neither of the two episodes discussed above appear to have a corresponing event excess that is consistent with the observed Rayleigh power under $H1$. However, as both of these particular observations were performed in a continuous tracking mode, the caveat discussed in the previous section regarding the accurate assessment of event excess applies.

In addition to a burst search, the 1989 data was taken entirely in the "wobble" mode, allowing for an investigation of continuous emission. An excess of 2.25σ was observed, or a chance probability of 1.2%. This would correspond to a flux of about $6 \times 10^{-11} cm^{-2} sec^{-1}$ above 150 GeV. A search for a 1.7 day and 35 day periodicity yielded no significant result. If trials for these tests are taken, the probability level is raised to about 3%.

While the fact that both a pulsed, burst analysis and a test for continuous emission yielded chance probabilities of less than 5% may be considered interesting (particularly in light of the association with the Whipple and CYGNUS observations of 1986), neither result can be considered as compelling evidence for emission when taken by itself.

1.7 Day and/or 35 Day Correlations?

Given the lower energy measurements described in chapter 3, an obvious question to consider is whether UHE/VHE emission might occur at preferred phases of either the 1.7 day orbital period, or the 35 day period. In addressing this question, and based on the previous discussion, consideration will only be given to the following claims of observation: **1)** the 1983 Fly's Eye result; **2)** the 1986 CYGNUS result, along with the comtemporaneous results of **3)** Haleakala and **4)** Whipple; and **5)** the distribution of "lesser" bursts in the 1984-1987 Whipple data base. The following table lists the orbital and 35 day phases corresponding to each of these measurements:

Observation	35 Day Phase	1.7 Day Phase
Fly's Eye	0.63	0.66
Cygnus	0.23	0.90
Haleakala	0.22	0.81
Whipple (1986)	0.04	0.71
Whipple (1984-1987)	0.35	0.95

Table 8.3: 35 day and 1.7 day phases for selected observations.

For the 1984-1987 distribution of Whipple bursts, those episodes corresponding to the most significant deviation from the integral probability distribution for X-ray and blue-shifted periodicities (excluding the 1986 contemporaneous episode, which is treated separately) have been chosen. This amounts to 19 episodes (7 at X-ray and 12 at blue-shifted periods: see table 8.2). Figures 8.2 and 8.3 show histograms of the 1.7 day and 35 day phases of these episodes, respectively. The dashed line in each of these plots shows the relative exposure time to each phase bin, as taken from reference [108], and is scaled to the total number of episodes in the each plot. The entries in table 8.3 correspond to the peak in each of these plots above expectation. The probability for the peak in figure 8.2 (at a phase of 0.95) corresponds to a chance probability of 14%, and the less prominent peak in figure 8.3 (at a phase of 0.35) has a chance probability of 63%. These probabilities were

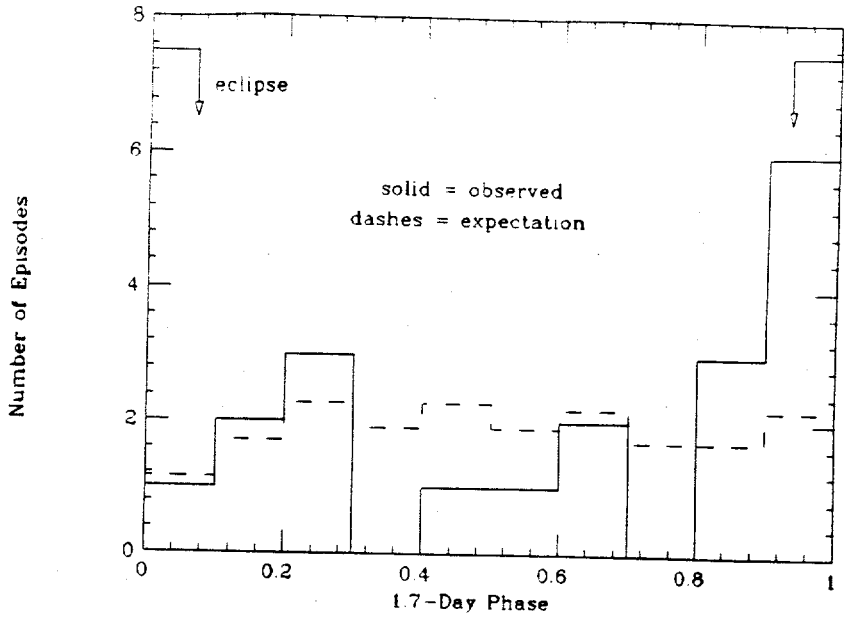

Figure 8.2: Histogram of 1.7 day phases corresponding to the 19 episodes contributing most to the distortion in the integral distribution of Rayleigh powers at both X-ray and blue-shifted periods for Whipple data during 1984-1987 [108]. The dashed line indicates the on-source exposure to each phase interval.

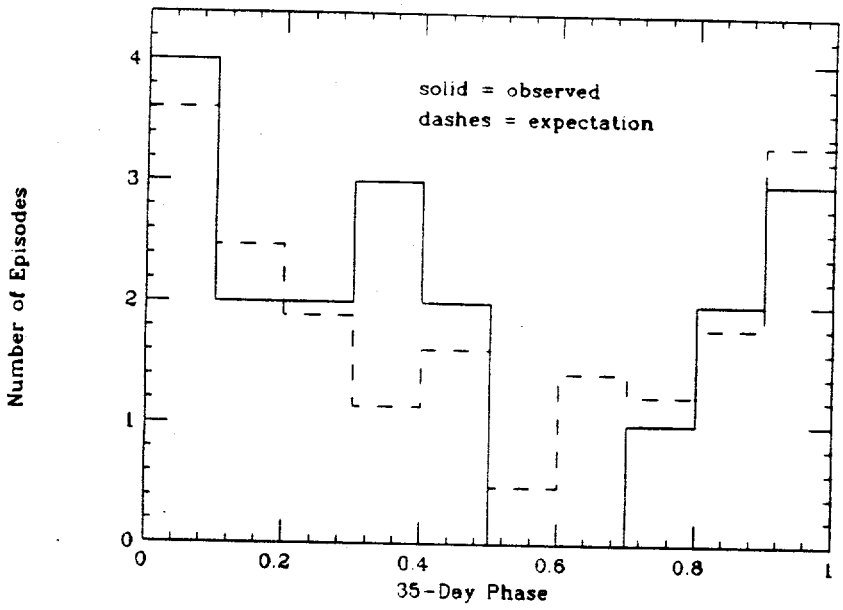

Figure 8.3: Histogram of 35 day phases corresponding to the 19 episodes contributing most to the distortion in the integral distribution of Rayleigh powers at both X-ray and blue-shifted periods during 1984-1987 [108]. The dashed line indicates the on-source exposure to each phase interval.

determined using the Protheroe statistic applied to an exposure-corrected phase distribution, as described in chapter 5. This group of 19 episodes has been put on equal footing with the individual observations of table 8.3 since their significance results from the *collection* of chance probabilities, rather than from that of any one particular episode.

Phase coverages of the 1.7 day and 35 day cycles for the Haleakala observation (extracted from reference [90]) are shown in figures 8.4 and 8.5, respectively. Similarly, the relatively short 5-day observation interval of the Fly's Eye result limits the range of possible 35 day phases to between 0.6-0.74, and the 1.7 day phases to the values of 0.07, 0.25, 0.43, 0.66 and 0.84 . The observed phases cannot, therefore, be treated as random variables over the range of 0-1 in the assessment of preferred phases of emission. On the other hand, due to the nearly continuous duty cycle of the Cygnus array, phase-coverage for both periodicities is ~uniform over the course of this experiment.

Figure 8.6 plots the 1.7 day versus 35 day phases for each of the observations listed in table 8.3. The significance for the possible clustering of observations near some preferred phase has been calculated by first computing a Protheroe statistic, and then obtaining the chance probability by a Monte Carlo in which phases were sampled from the appropriate distribution of on-source exposure for each of the 5 observations. This method yields a chance probability of 7.5% for a 1.7 day clustering, and a 40% chance probability for a 35 day dependence. The probability of a correlated 1.7 day - 35 day grouping has not been calculated due to a lack of information regarding correlated exposure biases for most of the observations in table 8.3.

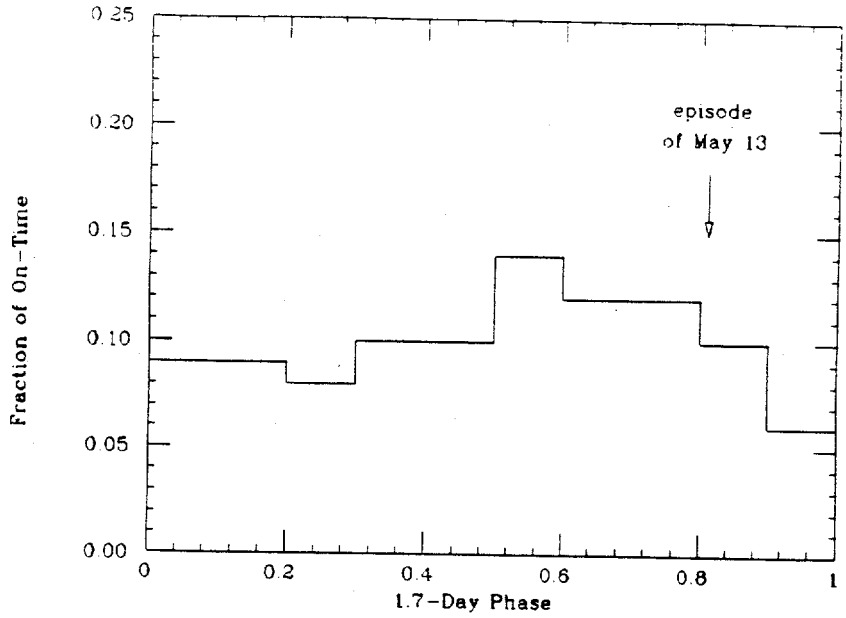

Figure 8.4: 1.7 day phase coverage related to the 1986 Haleakala observation (indicated by the arrow) [90].

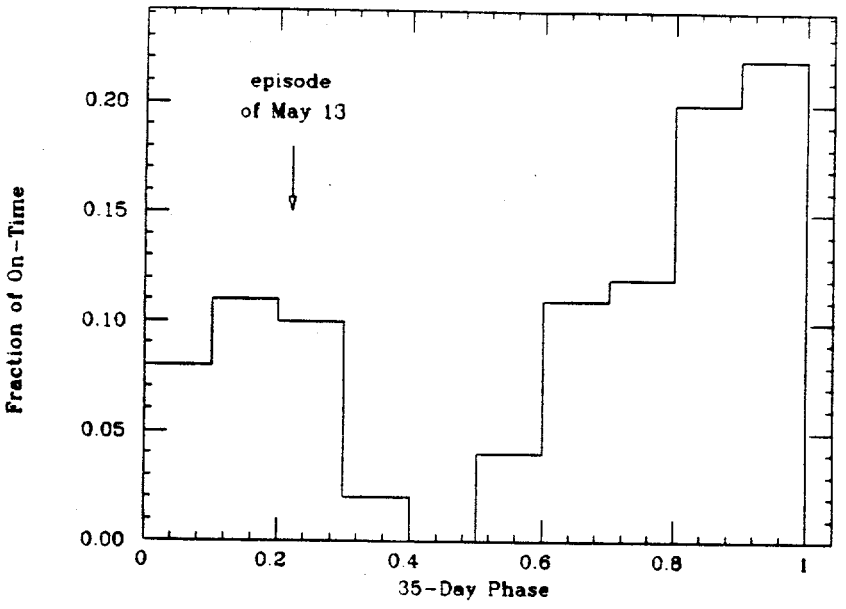

Figure 8.5: 35 day phase coverage related to the 1986 Haleakala observation (indicated by the arrow) [90].

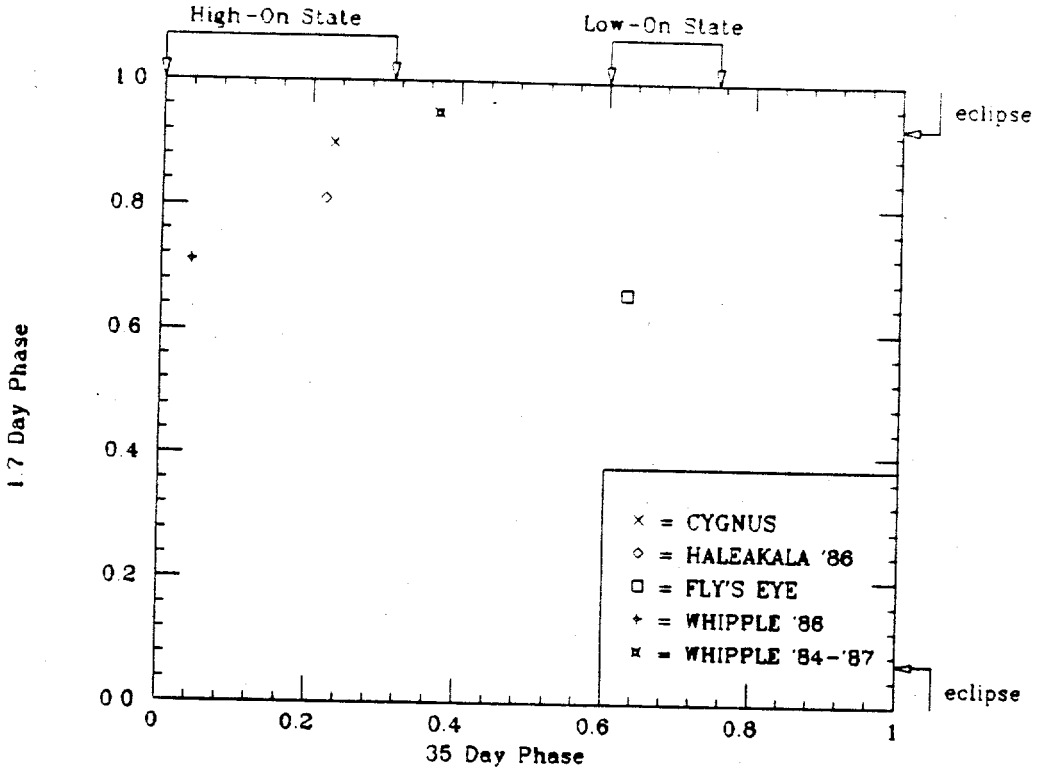

Figure 8.6: 1.7 day versus 35 day phases for various observations.

Chapter 9

Theoretical Models

"The wonderful thing about science is that you get such a wholesale return of conjecture for such a trifling investment of fact."
- Mark Twain -

The Muon Anomaly

To date three basic particle models have been proposed to explain the apparent observation of muon-rich showers associated with point-sources: 1) The interaction is that of a new particle. This invokes physics beyond the "Standard Model," and necessitates unusual conservation and/or interaction rules in order to avoid limits on such particles set by accelerator experiments. 2) The primary particle is a neutrino that develops a ~strong interaction cross section beyond some energy threshold due to the onset of new physics (*i.e.* compositeness of quarks and leptons). 3) The primary particle is, indeed, a gamma-ray, but either hadron photoproduction becomes significantly enhanced at higher energies due to contributions from the gluon structure function of the photon, or the nature of electromagnetic interactions changes due to the onset of new physics.

Constraints

From previous discussions, characteristics of the primary particle may be constrained as follows: First, it must be neutral in order to preserve directional information. Secondly, the mass of the primary must be small enough that energy-dependent velocities do not destroy the observed phase coherence. Namely,

$$\frac{d}{c}(\frac{1}{\beta_1} - \frac{1}{\beta_2}) < P\delta\phi \tag{9.1}$$

where

$$\beta_1 = \sqrt{1 - (\frac{M}{E_{min}})^2}$$

$$\beta_2 = \sqrt{1 - (\frac{M}{E_{max}})^2}$$

d is the distance to Her X-1; c is the speed of light; P is the observed periodicity; $\delta\phi$ is the width of the observed phase peak; M is the mass of the primary; E_{min} is the minimum primary energy observed; and E_{max} is the maximum primary energy observed.

Assuming a proton-like interaction and an energy spectrum that is not too different from background, the shower size can be readily related to the primary energy. Within the main phase peak of bursts 1 and 3, E_{min} is about 200 TeV, and E_{max} is about 3000 TeV. However, since the events in the phase peak may contain 1, or possibly 2 background events, a more conservative choice is to take the second lowest and highest energies. These are approximately 250 TeV and 1500 TeV, respectively. $\delta\phi$ may be taken to be the width of the main phase peak of bursts 1 and 3 ($\sim$0.1), but since the true light curve is not known, a more conservative choice of twice that value will be chosen. This leads to a mass limit of $M < 200$ MeV/c^2. As indicated from the caveats previously stated, this limit is weakened if one assumes either an interaction that causes a gross underestimate of primary energy based on shower size (*e.g.* by "hiding" more of the energy in less visible muons, hadrons or neutrinos), or that the source energy spectrum is more monochromatic. As an example, assume that the energies have been underestimated by an order of magnitude, and that the true spread in energies is only a factor of 2. The mass limit

would then be $M < 1$ GeV/c^2. Given the model uncertainties and large fluctuations in shower size for a given energy, such a scenario is not at all unreasonable. If the Whipple observations are interpreted as resulting from the same phenomenon at energies of $\sim$1 TeV, a mass of less than $\sim$1 MeV/c^2 is inferred for the primary particle.

In addition to the charge and mass constraints, the primary particle must have a lifetime, τ, greater than $\sim \frac{d}{\gamma c}$. For both mass scenarios discussed above, this yields $\tau \geq 4 \times 10^5$sec.

If the particle production mechanism is assumed to stem from an accretion-powered proton beam interacting with nearby material, a lower limit for the interaction cross section can be estimated by comparing the observed and limiting source luminosities. Specifically, if isotropic emission is assumed with some average energy E, then the observable source luminosity is

$$L_{obs} = \Phi E(4\pi R^2) \tag{9.2}$$

where Φ is the observed source flux and R is the distance to Her X-1. If $\Phi = 10^{-11} cm^{-2} s^{-1}$ (chapter 5, equation 5.12), E =300 TeV (480 ergs), and R = 5kpc, then equation 9.2 yields $L_{obs} = 10^{37}$ ergs/s. The limiting source luminosity for isotropically accelerated protons powered by spherical accretion is given by the Eddington limit of $\sim 10^{38}$ ergs/s. For asymmetric accretion and emission it is possible to exceed this limit. Therefore, a limiting source luminosity of 1000 times the Eddington limit, or $L_{lim} = 10^{41}$ ergs/s, will be assumed as an order-of-magnitude estimate. It will further be assumed that the production efficiency for source particles in the 100 TeV regime is 100%. This leads to a lower limit for the fraction of the primary source particles that interact in the atmosphere of $\frac{L_{obs}}{L_{lim}} = 10^{-4}$, corresponding to an atmospheric thickness of 10^{-4} interaction lengths. At the altitude of the CYGNUS experiment, this yields an interaction length of $8 \times 10^6 \frac{gm}{cm^2}$. The cross section is then obtained from

$$\sigma = \frac{1}{N\lambda} \tag{9.3}$$

where λ is the interaction length and N in air is given by

$$N = \frac{6.02 \times 10^{23} mole^{-1}}{14.5 \frac{gm}{mole}} = 4 \times 10^{22} gm^{-1} \tag{9.4}$$

This yields a lower limit for the interaction cross section in air of $\sim 3 \times 10^{-30} cm^{-2}$, or $\sim 3\mu$b. This number is clearly based on several assumptions regarding both the nature of the particle production mechanism at the source and the ability to infer the primary energy from the measured shower size.

If the interaction of the source particle in the atmosphere is assumed to be proton-like, a more stringent limit on the interaction cross section can be gained from the age distribution of signal events. Simulations indicate that the ages of showers produced by protons injected at an atmospheric depth of 400 gm/cm^2 are noticibly smaller than for protons injected at the top of the atmosphere (Appendix A, figure A.32). The fact that the age distribution of source events is consistent with that of background (chapter 6) thus indicates an interaction cross section no smaller than $\sim \frac{1}{2}\sigma_{p-air} = \sim$ 150mb.

New Particle?

Collins *et al.* [109] have proposed a set of models to accomodate a new particle with these properties in a technicolor-like extension of the Standard Model. The new particle, dubbed the "cygnet," is assumed to be the bound state of more fundamental particles ("snarks"), held together by a "new" strong interaction that is mediated by the gluons of a new symmetry group. The snarks would possess a mass on the order of a few GeV, and the lower mass cygnet is a Goldstone boson of some symmetry possessed by the snarks. Cygnets are assumed to couple only to snarks, and not to quarks or gluons in order to avoid their detection in previous accelerator beam-dump or neutrino experiments. In their model, cygnets are expected to have a small cross section for interaction compared to protons, and thus will initiate air-showers deep in the atmosphere. A larger transverse momentum is associated

with this interaction, and will tend to broaden the shower. This effect may therefore offset the extent to which the observed lateral distribution would otherwise be narrowed (smaller age) by the deeper primary interaction point.

As indicated by the authors themselves, the model suffers from two principal drawbacks: First, the model appears very contrived, as is necessary in order to avoid limits on new particles already obtained from accelerator data. In the context of the experimental results presented in this thesis, the balance between primary interaction depth and transverse momentum that is necessary to explain the observed age distribution (*i.e.* consistent with that of background showers) raises further doubts. In addition, it is difficult to conceive of any plausible production mechanism at the source that would not also produce a significant (if not overwhelming) number of UHE/VHE gamma rays that would also be detected. These difficulties appear to be generic to any model that attributes the UHE/VHE observations to a new particle.

Strongly-Interacting Neutrino?

Domokos *et al.* [110],[111], have proposed that the muon-rich showers associated with point-sources might result from an onset of new physics that causes the neutrino cross section to dramatically rise. They consider a simple model of lepton and quark compositeness in which leptons contain colored constituents, or *preons* (figure 9.1). The energy scale required to probe this composite structure is taken to be $\sim$1 TeV.

Consequences of one particular version of this model have been simulated by Mrenna [112]. Compared with proton-induced showers of the same energy, the following differences in observed shower characteristics were noted: **1)** A significantly narrower electromagnetic lateral distribution (smaller shower age); **2)** A narrower muon lateral distribution; **3)** A smaller ($\frac{1}{3}$) average energy per muon; **4)** A 50% smaller ratio of photon-to-electron density; **5)** A rapid decline in the electromagnetic energy beyond 10m from the shower core; 6) A muon-to-electron ratio that is a factor of 1.5 to 4 times larger. Many of these characterics are simply due to the significantly

lower average depth of primary interaction that results from the assumed cross section (between 0.1 and 10 mb). The first of these predictions is in disagreement with the observed distributions of shower age for both the CYGNUS and Kiel data (note that Kiel actually claims to have observed a *larger* shower age than normal), and therefore casts serious doubt on this particular version of the model.

In general, this class of models is plagued by the same concerns raised in the previous section regarding its contrived nature and the need for a "photon-poor" production mechanism should the interaction cross section be too large.

Gamma-Ray?

The Bethe-Heitler cross section for a gamma ray to produce an e^+-e^- pair is $\sim$ 500mb in air. Muons can be produced in an electromagnetic interaction either directly via muon pair-production, or indirectly via hadron photoproduction. The cross sections for these two processes are $\sim 12\mu b$ and $\sim 1 - 2mb$ in air, respectively. Since these numbers are small compared to the Bethe-Heitler cross section, muon production is suppressed in an electromagnetic cascade. For gamma ray primaries, calculations predict a muon content $\sim$10% that of an air-shower induced by a proton of the same energy [113].

As has been previously stated, the muon content of the showers associated with the 1986 bursts is open to interpretation if the primary energy spectrum and, especially, the muon lateral distribution is allowed to vary. A substantially steeper lateral distribution can actually result in a muon content similar to that predicted for gamma rays. As an example, figure 9.2 plots a possible modification to the muon lateral distribution that is consistent with the CYGNUS data, and yet leads to an integrated muon content that is only 15% of that expected for a proton primary. However, simulations indicate that the muon lateral distribution resulting from showers induced by gamma-rays is actually *wider*, rather than narrower than that from proton-induced showers [114]. The observed behavior of the muon component in the 1986 bursts is therefore definitely inconsistent with traditional expectations for gamma-ray primaries.

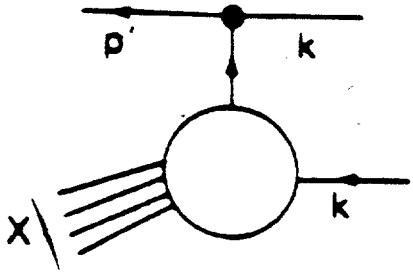

Figure 9.1: Schematic diagram of the process ν + quark $\rightarrow$ lepton + X [110].

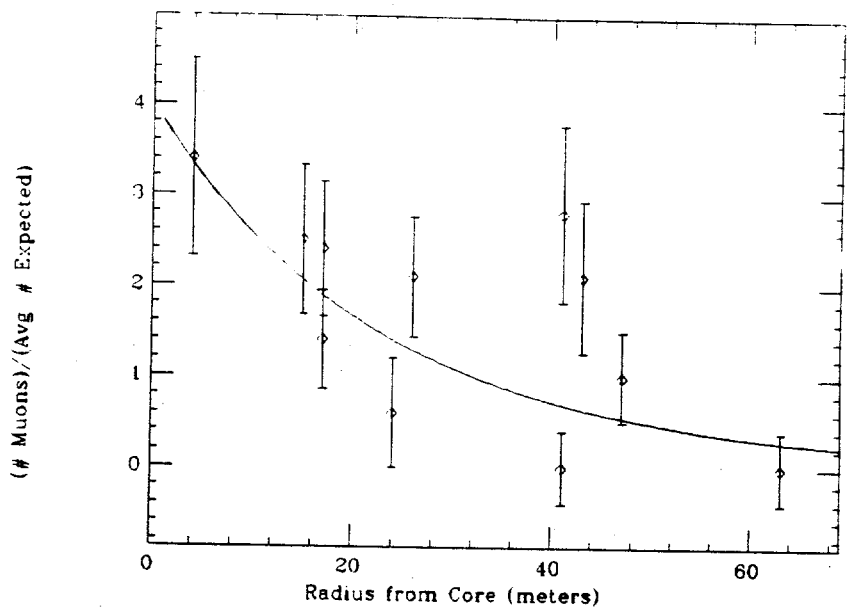

Figure 9.2: Fractional excess in measured muon number over that expected from background showers for each of the 11 previously published, burst events as a function of radius from the shower core. The solid line represents a hypothetical modification to the muon lateral distribution (Greisen formula) that would be constistent with the data, while yielding a smaller overall muon content than background showers.

If the primary particle is a gamma ray, a modification of the electromagnetic interaction is required to alter the muon-production cross section. Drees and Halzen [115] have pointed out that photons will tend to take on a larger cross section for strong interactions at high energies through the associated cloud of virtual gluons (figure 9.3). The degree to which this effect will manifest itself depends on the probability to impart a given fraction of the initial photon momentum to a gluon, which is determined by the gluon structure function of the photon. Since current data on $\gamma - p$ scattering does not exists for center-of-mass energies $\sim$ 1 TeV, extrapolations for the gluon structure function of the photon must be employed. Two of the most common models are those of Duke and Owens [116], and of Drees and Grassie [117]. The resulting predictions for the contribution to the total $\gamma - p$ cross section as a function of center-of-mass energy are shown in figure 9.4 for an assumed minimum jet p_T of 2 GeV. Most regard the Duke and Owens parameterization as an upper bound due to the uncomfortably large cross sections predicted at higher energies. Taking this model, a $\gamma - p$ photoproduction cross section of $\sim$ 4mb is found for a center-of-mass energy of 1 TeV (lab energy of $\sim$500TeV). Scaling by $A^{0.9}$ (the exponent is to account for shadowing in the nucleus), where $A = 14.4$ for air, this yields a photoproduction cross section of $\sim$ 45mb in air. This value is about an order of magnitude below the Bethe-Heitler cross section. This, along with the strong energy dependence of the photoproduction cross section assumed, typically means that the enhanced photoproduction will either manifest itself in the first or second interactions, or not at all. As such, only a fraction of the UHE gamma ray interactions will appear to be "muon-rich" (see figure 9.5).

In order to account for the observations, the photoproduction cross section must become larger than the Duke and Owens extrapolation by about an order of magnitude, which seems unlikely within the standard model, though not impossible. Alternately, one may invoke new physics to dramatically increase the photoproduction cross section at higher energies. Experiments are currently underway at HERA, involving the collision of 800 GeV protons on 30 GeV electrons. Preliminary data indicates a γ-p total cross section of $160\mu b$ at a center-of-mass energy of 200 GeV [119]. This value is in good agreement with more conventional extrapolations from

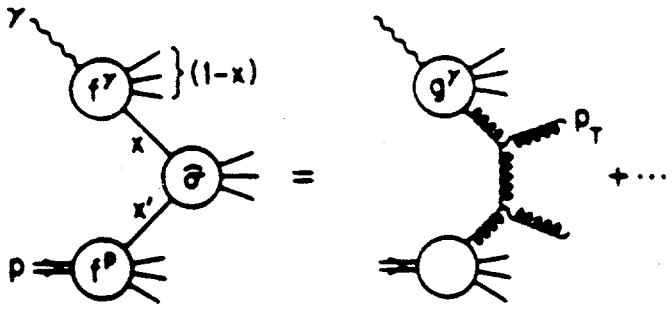

Figure 9.3: Feynman diagram for those contributions to $\gamma - p$ scattering where the photon is resolved into quarks and gluons [115].

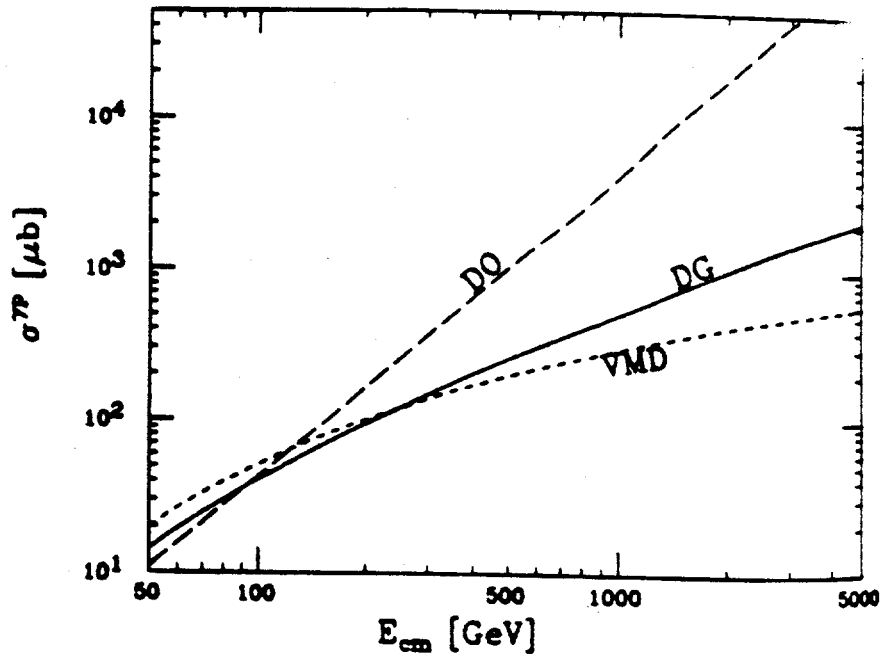

Figure 9.4: Contribution to the total $\gamma - p$ cross section versus center-of-mass energy as predicted by the photon structure function parameterizations of Duke and Owens (long dashes), Drees and Grassie (solid), and the vector-meson dominance model (short dashes) [115].

lower energy data (for example, reference [120]). While this does not rule out the possibility of a much higher cross section at centers-of-mass in the TeV range, a drastic change in the energy dependence of the cross section would be necessary. Once again, if the Whipple observations are interpreted as resulting from the same phenomenon (*i.e.* not standard gamma-ray interactions) at lower energies, this model is ruled out.

Blue-Shifted Pulsar Periodicity

Three different models have been proposed to account for the significantly shifted period associated with the 1986 results. Ground-based, optical measurement made by Middleditch in May and September of 1986 [121] yielded a pulsar period consistent with previous X-ray observations, and rules out the possibility that the blue-shifted period seen by the VHE/UHE experiments is due to an actual change in the pulsar spin rate. All of the models discussed below involve proton beams impinging on targets rotating within the accretion disk to produce UHE gamma-rays. Conventional particle physics at the source is assumed.

Cheng-Ruderman Model

This approach invokes an outer gap-type acceleration mechanism (chapter 2) in which protons are guided by magnetic field lines to a target region in the accretion disk [122]. The target region here is considered to be a localized window of lower density to allow gamma rays to escape. If this window moves radially inward as matter from the disk is accreted onto the pulsar, it will select out progressively shorter magnetic field lines and, hence, shorter paths to the photon production site. In this way, any pulsation associated with proton beam will appear to be foreshortened, resulting in a smaller apparent period. The geometry is illustrated in figure 9.6.

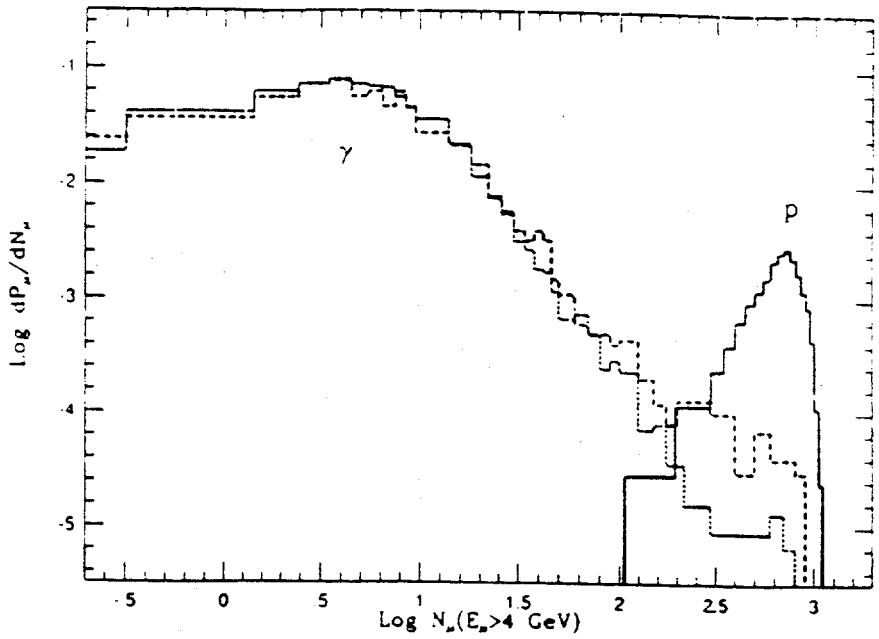

Figure 9.5: Frequency of simulated 100 TeV showers as a function of the total number of muons above 4 GeV. The 3 curves correspond to photons with conventional (dots) and enhanced (dashes) photoproduction, and to protons (solid) [118].

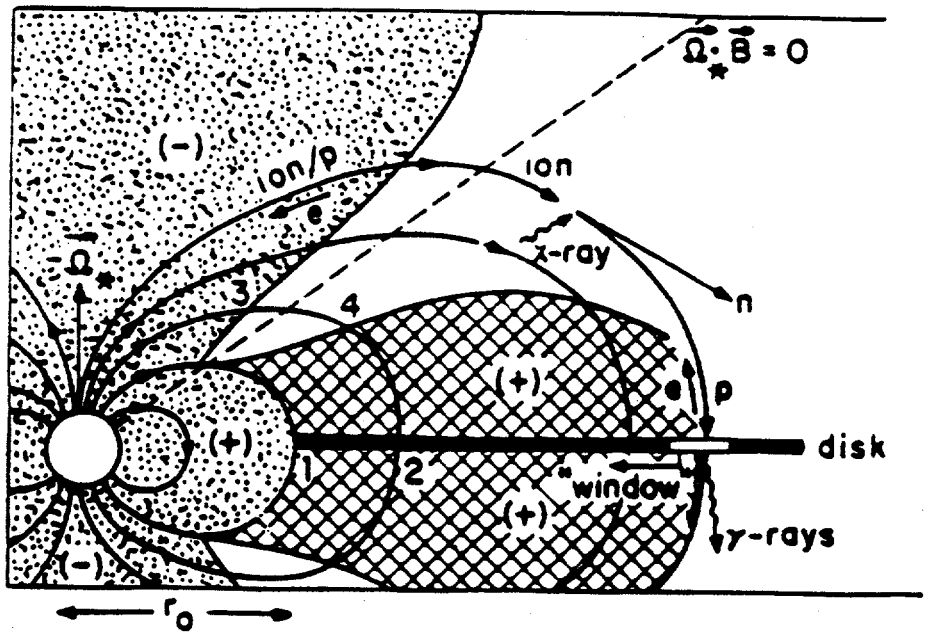

Figure 9.6: Cheng and Ruderman model for producing a blue-shifted periodicity: an "outer-gap" acceleration of protons impinging upon an inwardly moving target region ("window") within the accretion disk [122].

Slane-Fry Model

The model of Slane and Fry [123] associates the shifted period with a localized target of material circulating near the edge of the magnetosphere, where the accretion disk velocity is nearly Keplarian. It does not seem unreasonable that an instability might form at this interface, occasionally giving rise to temporary outcroppings of plasma above the accretion disk that act as a conversion target for a proton beam. If the initial proton beam is sufficiently wide, the relative allignment between the beam, the circulating target, and the earth will appear to "slip" in phase with each successive orbit. Two periodicities would thus be seen: that of the proton beam and that of the target material. The relative strengths of the periodicities are determined by the widths of these two elements. Since no significant peak was observed at the pulsar frequency during the 1986 observations, this would indicate that the width of the initial proton beam is on the order of 2π, or effectively unpulsed. The narrow light curve (a duty cycle of $\sim$10%) associated with the UHE observation at the shifted period, would likewise indicate an effective target region width of about $\frac{2\pi}{10}$ radians. The geometry is indicated in figure 9.7.

Aharonian-Atoyan Model

The model of Aharonian and Atoyan [124] employs scattering from dense, magnetic "clouds" ejected from the companion star. These clouds follow various trajectories under the gravitational influence of the neutron star. Large-angle scattering of a proton beam by these clouds at various points along a given trajectory could thus result in a changing path length to the earth, thereby altering the apparent frequency of beam-associated pulsations. This is illustrated in figure 9.8. However, the production and stability of such clouds is highly questionable, especially considering the magnitude of magnetic fields within the clouds necessary to substantially effect the trajectory of a 10^{15}eV proton beam. This model, therefore, seems to be the least likely of the three previously described.

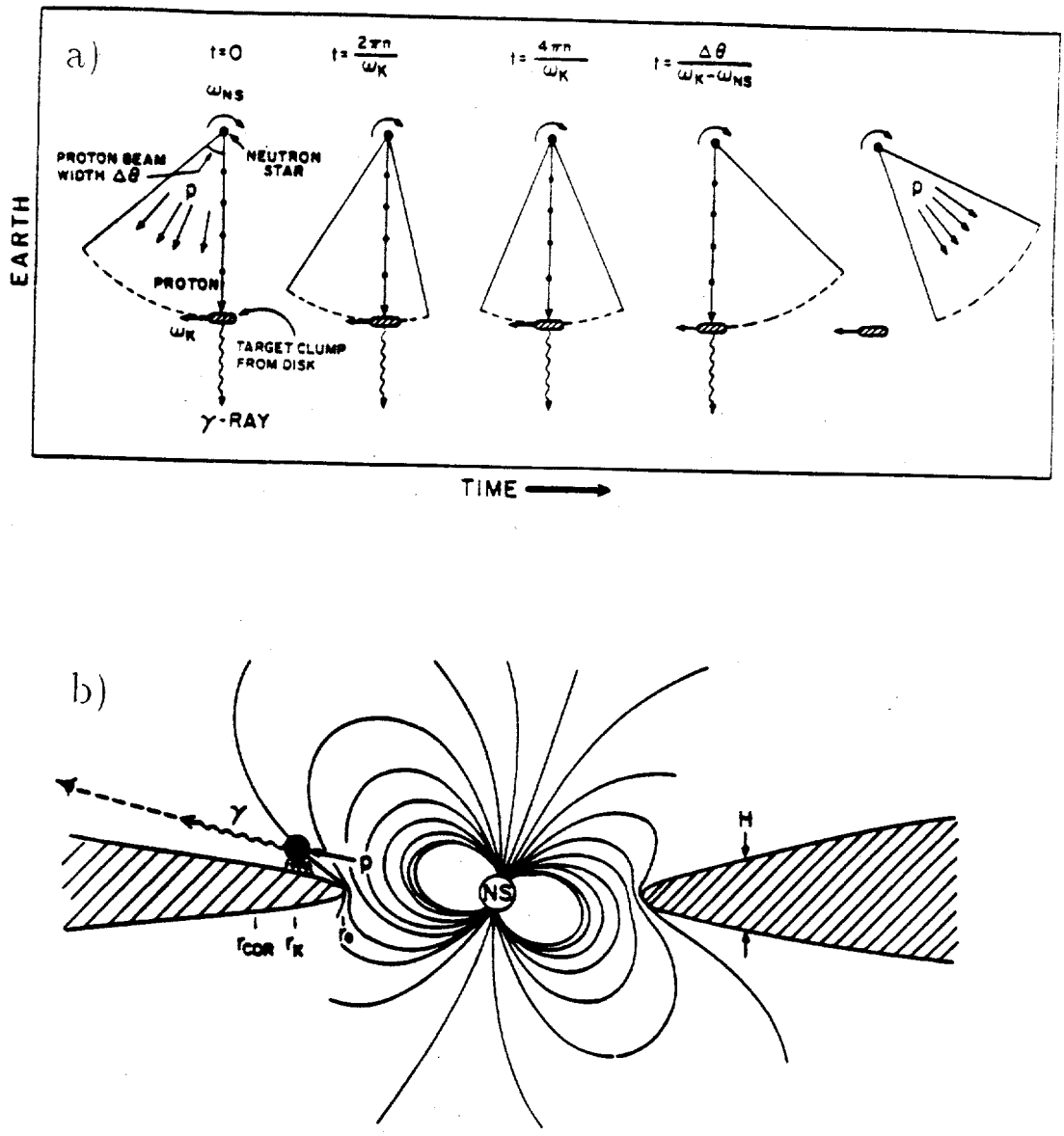

Figure 9.7: Slane and Fry model for producing a blue-shifted periodicity: a) Schematic diagram depicting the interaction of a broad particle beam with target matter orbiting neutron star with period smaller than the rotational period of the star (and particle beam). As time progresses, the target advances in phase with respect to the beam. b) Hypothetical orientation of neutron star and orbiting target with respect to the earth [123].

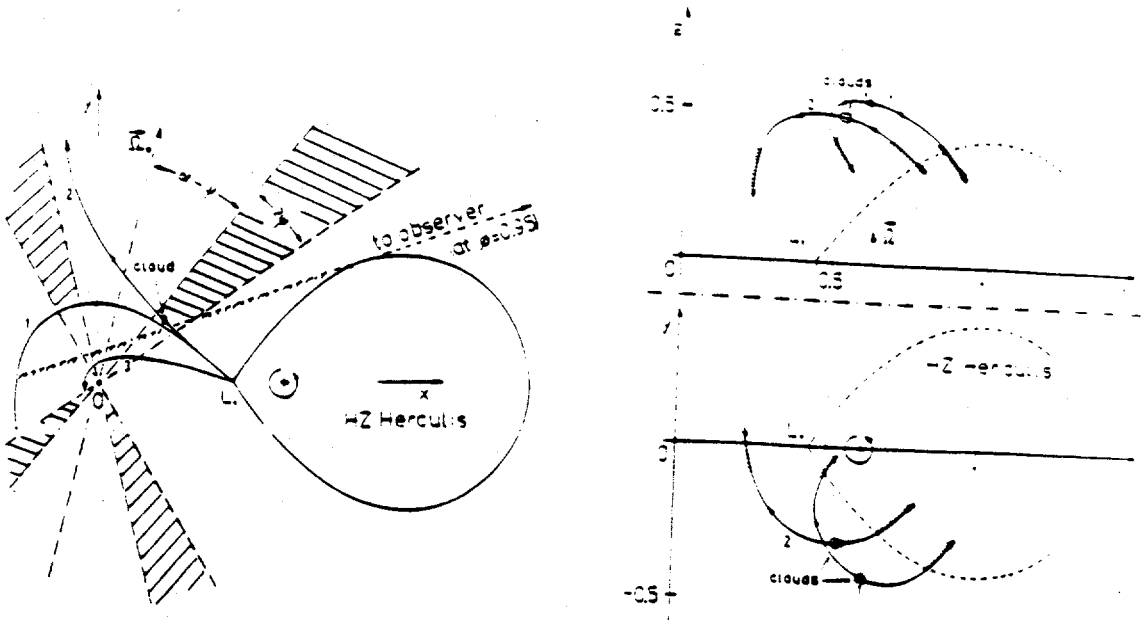

Figure 9.8: Model of Aharonian and Atoyan [124] :

Chapter 10

Conclusion

"I see the world in very fluid, contradictory, emerging, interconnected terms, and with that kind of circuitry I just don't feel the need to say what is going to happen or will not happen."
- Governor Jerry Brown -

Given the ensemble of hypotheses that have been examined in the CYGNUS data set, the chance probability that the Her X-1 data is consistent with background has been estimated to be 0.44%, based on event excess and periodicity studies (chapter 5). These studies have included a search for both pulsed and unpulsed emission from Her X-1 on time scales ranging from minutes to years (chapter 7). The most significant observation remains that of July 24, 1986, and is the basis for the chance probability quoted above. This is also the most significant result of the 4 source hypotheses that have been considered (Her X-1, Crab pulsar/nebula, Cyg X-3, and a collective treatment of others). Therefore, the overall chance probability for the observations of the CYGNUS experiment has been estimated to be $4 \times 0.44\% = 1.8\%$.

An analysis of shower characteristics for events associated with Her X-1 on July 24, 1986 has indicated a different behavior than that expected from background hadronic showers at a chance probability level of 0.1% (chapter 6). Specifically, a steeper radial dependence of the showerfront timing width has been observed. This property might be explained by a model that invokes a forward-peaked and/or a deeply interacting component of the hadronic interaction in the atmosphere.

A review of results from other VHE/UHE experiments regarding Her X-1 has indicated weaknesses in many of the claims of observed emission (chapter 8). However, several observations, particularly those of the Fly's Eye [100] and Whipple [9] collaborations, remain difficult to explain in the context of the null hypothesis. The results from these 2 experiments, taken together with the Haleakala [5] and CYGNUS burst observations of 1986, have been used to estimate the likelihood for correlations with either the 35 day or 1.7 day periodicities associated with Her X-1. This study has yielded chance probabilities of 40% for a potential 35 day correlation, and 7.5% for a 1.7 day dependence.

If VHE/UHE emission from Her X-1 has been observed, the muon content measured by the CYGNUS experiment indicates that the the primary particles responsible for the signal do not interact in a manner consistent with standard predictions for gamma rays. This may also be suggested by the inability to enhance the significance of Her X-1 detections in the Whipple data by selecting gamma-like Cherenkov images [9]. The existence of point-source emission with properties other than those of gamma-rays appears to be consistent with the earlier Kiel observation of Cyg X-3.

The constraints discussed in chapter 9 regarding the mass, charge, cross section and lifetime place considerable limitations on the type of particle that can be responsible for the Her X-1 signal. Consequently, the observations either indicate modified interaction properties of the photon or neutrino, or denote the existence of a new particle species. Current models for new particles generally suffer from a contrived nature that is necessary to avoid limits on such particles obtained from accelerator data [109]. These models also tend to lack plausible production mechanisms at the source that would not also produce copious amounts of VHE/UHE gamma rays, which should also be detected. If strongly-interacting neutrinos arising from a quark sub-structure are responsible [110], it appears that the modified interaction cross section would have to be remarkably close to that of the proton at the detected energies to explain the measured age distribution of source-associated showers (chapter 9). Such an unlikely coincidence would also raise the problem previously discussed regarding a gamma-poor production mechanism at the source.

If the progenitor particle is a gamma-ray with an enhanced photoproduction cross section [115], an extremely rapid departure from the trends indicated by the HERA data would be necessary [119]. In addition, none of the models that invoke modified interaction properties above center-of-mass energies of $\sim$1 TeV appear to be able to explain the lower energy observations of the Whipple experiment in the absence of triggering or analysis biases.

Finally, to reiterate the statements made in chapter 6, the lack of further Her X-1 observations among VHE/UHE experiments in recent years leads to one of three conclusions: **1)** The reported significance levels of previous VHE/UHE observations of Her X-1 have been overestimated and emission at these energies has not been observed; **2)** The reported significance levels of VHE/UHE observations of Her X-1 are generally correct, but constitute statistical fluctuations and emission at these energies has not been observed; **3)** VHE/UHE emission from Her X-1 has been seen in the past, but the emission is of a highly sporadic nature that may only be observed during short time intervals occurring every few years. The results of continued monitoring of point sources will ultimately determine the credibility of claimed observations of VHE/UHE emission from this as well as other sources, although this route is proving to be a long and difficult one.

Appendix A

Simulation of Extensive Air Showers and the CYGNUS Detector

"**sim-u-late** */'sim-yə-lāt/ vb. 1: To assume the outward qualities or appeareance of usually with the intent to deceive."*
- Webster's Dictionary -

Introduction

The description of the simulation is divided into 2 parts: **1)** the generation of extensive air showers ("**raw**" output at detector level); and **2)** the response of the CYGNUS detector. The simulation approach has been made as modular as possible to allow for easy modification of the detector configuration. The final output is in standard data-file format to allow for easy comparison with actual data.

EAS Simulation

The criteria set for the EAS simulation are as follows: **1)** it should follow electrons, gammas, muons, pions and nucleons; **2)** particle energies should be followed below the minimum energy required to trigger each counter ($\sim$1 MeV); **3)** particle arrival times should be known to $\sim$ 1 nanosecond; **4)** correlations between

particle position, energy and arrival time should be preserved; **5)** the simulation should be fast (able to produce ~1000 proton showers of energy ~100 TeV in a day of *real* time using a VAXSTATION 3100).

These requirements have been met by combining an updated version of SHOWERSIM [125] with a library of lower energy electromagnetic sub-showers generated with EGS4 [126].

Nuclear Interaction Model

The default model used for nuclear interactions was the SHOWERSIM standard $W00$, which is based on extrapolations from ISR and SPS collider data. In addition to this, Gaisser's fit to a rising proton cross-section was used. Both of these choices are standard SHOWERSIM options.

Generation of EGS4 Sub-Showers

Several features were implemented in the EGS4 users code for the generation of the sub-shower library: **1)** an accurate accounting of particle transit time in the interaction medium was made; **2)** Wrotniak's fit to the standard U.S. atmosphere was used to alter the air density each time a particle was stepped; **3)** *shower thinning* was used to speed up the calculation and facilitate storage of the sub-showers.

Thinning is a procedure whereby only a fraction of the shower particles are actually followed "blow-by-blow" as a representation of the greater number of particle tracks. A weight is assigned to each particle that is followed to designate the number actually represented. The Hillas prescription [127] was used to determine the probability for a particle to be thinned after each interaction. This probability is given by:

$$P = \frac{E}{E_{thin}} \qquad (A.1)$$

$$where \;\; E_{thin} = minimum(E_{primary} \times \Gamma, E_{parent})$$

Γ is the parameter that determines the extent of the thinning. A random variable is used to decide if a given particle is thinned, in which case it is no longer followed. If it is allowed to continue, it is then given a weight of $\frac{1}{p}$ times the weight of its parent particle. The larger the value of Γ, the greater the thinning and the faster the computation. However, larger values of Γ also increase the fluctuations that are artificially introduced by this procedure. Tests are therefore needed to find a compromise. Figure A.1 shows the fractional standard deviation in the number of electromagnetic particles reaching detection level for a variety of cases as a function of the thinning parameter Γ. Figure A.2 shows the same for the total electromagnetic energy reaching the detector, and figure A.3 shows the computation time per shower versus Γ. The arrow at the bottom of each of these figures indicates the value of Γ that was chosen.

Structure of Sub-Shower Library

The sub-shower library is composed of shower information generated by incident electrons and gammas sampled from 100 different energies (in logarithmic intervals from 5MeV to 200GeV); 39 initial production depths (from 0 to 800 g/cm^2 in steps of 20 g/cm^2); and 10 values of COS(θ_i) (with the initial zenith angles ranging from 0 to 80 degrees). Only those showers with particles surviving to the detection level of 800 g/cm^2 are saved, which results in ~30000 showers. The shower information is saved for a cross section of the shower at the detection level, consisting of a plane perpendicular to the shower axis. For each surviving secondary particle in a given sub-shower, this information includes: **1)** the thinning *weight* that designates the total number of particles it represents; **2)** whether the particle is a photon or electron (positrons are treated as indistinguishable from electrons); **3)** the location (relative to the shower axis); **4)** the energy; and **5)** the arrival time relative to that for a particle traveling along the shower axis with velocity *c*. The resulting sub-shower library comprises ~9 Mb of memory, which is small enough to be stored in internal memory for rapid retrieval. A second "index file" is used to give the record number corresponding to a particular sub-shower type.

The appropriate sub-shower is "attached" whenever an electromagnetic particle in SHOWERSIM drops below 200 GeV. The x and y sub-shower direction cosines are then scrambled to randomize the sub-shower orientation, and the sub-shower is then projected into the detector plane. For a 100 TeV proton-initiated shower, several thousand of these electromagnetic sub-showers are typically attached. Computation time for this type of shower is about 30 CPU seconds on a VAXSTATION 3100.

Sample Output

Figures A.4 through A.10 show some sample distributions generated by the EAS simulation. These include lateral particle density distributions and average energy per particle for proton, gamma, and iron primaries. A sample of the showerfront time-structure is also given. Whenever possible, comparison is made with expectations. In comparing the results, it is interesting to note that the average energy per electromagnetic particle appears to be a composition-dependent quantity. This indicates that electromagnetic calorimetry may be another means (aside from muon content) of distinguishing primary gamma rays from hadrons.

Storage of Simulated Shower Output

Shower simulation information was output relative to the shower plane and radial symmetry was assumed so that showers could be stored in terms of simple, radius-dependent distributions. 30 logarithmically increasing intervals in radius from the core ranging from 1 to 1000 meters were used, with the last interval acting as an overflow bin. Note that this approach implicitly smooths any correlated fluctuations that may have an azimuthal dependence. It also smooths fluctuations introduced by the thinning procedure, thereby removing the first-order side effects of the technique. For each of these radial intervals, the showerfront time-structure is explicitly preserved by a 20-bin histogram of particle arrival times. Other distributions saved include the particle density versus radius; the average radius of particles falling in a given radial bin (for purposes of interpolation); and the average particle

energy as a function of both radius and arrival time. Each of these distributions are saved separately for electrons, gammas, muons, nucleons and pions. Also, for each simulated shower, the type of primary particle, the primary energy, the initial zenith angle from which the shower was thrown, and the depth of the first interaction are stored. This amounts to ~14kb per shower, independent of primary energy (since fixed-length histograms are saved).

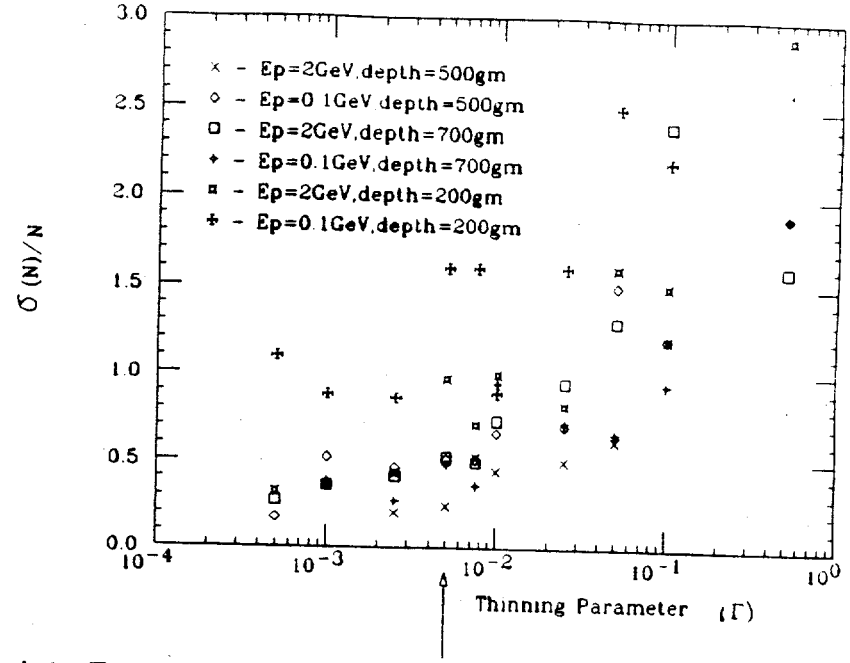

Figure A.1: Fractional standard deviation in the number of particles reaching detection level ($800\frac{gm}{cm^2}$) versus thinning parameter Γ for various simulated electron showers (EGS4). The chosen value of Γ is indicated by the arrow.

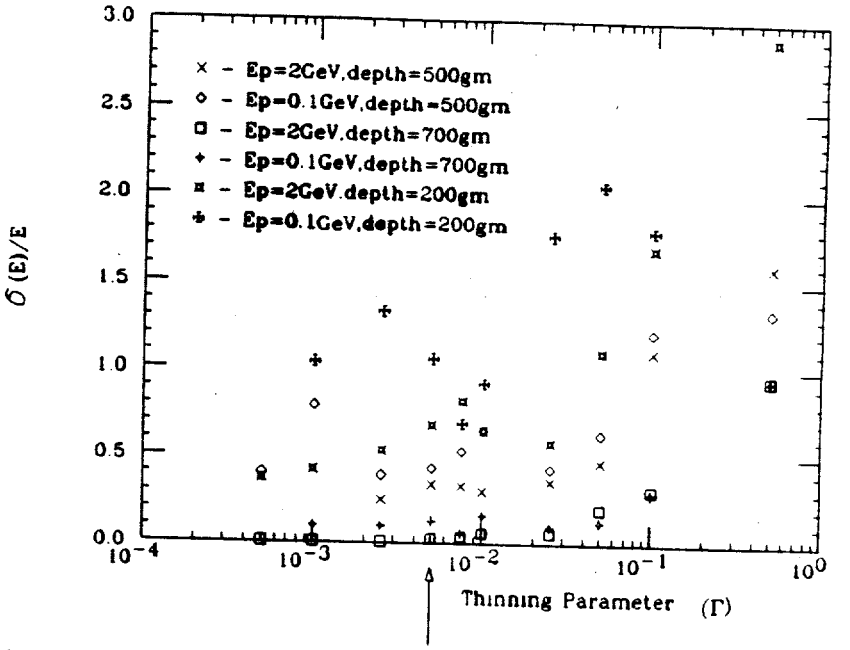

Figure A.2: Fractional standard deviation in the electromagnetic energy reaching detection level versus thinning parameter Γ for various simulated electron showers. The chosen value of Γ is indicated by the arrow.

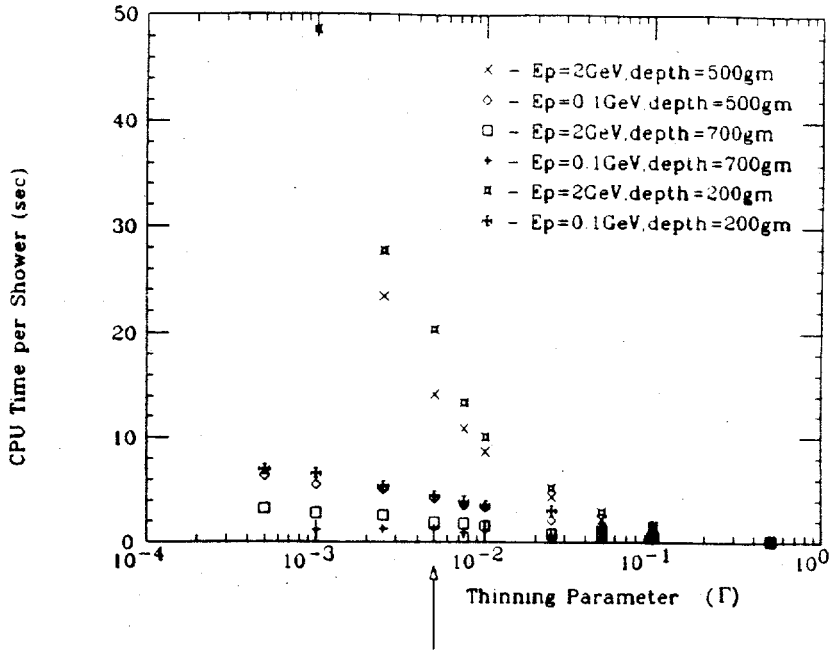

Figure A.3: CPU time per shower computation versus thinning parameter Γ for various simulated electron showers. The chosen value of Γ is indicated by the arrow.

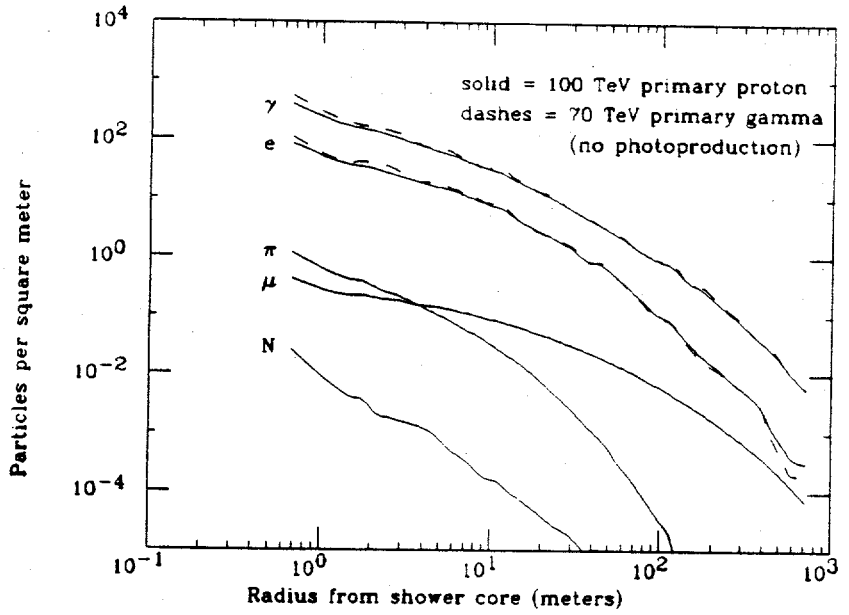

Figure A.4: Lateral particle densities at $800\frac{gm}{cm^2}$ for 100 TeV proton (solid) and 70 TeV gamma (dashes) primaries. The current simulation of gamma-initiated showers does not account for photoproduction.

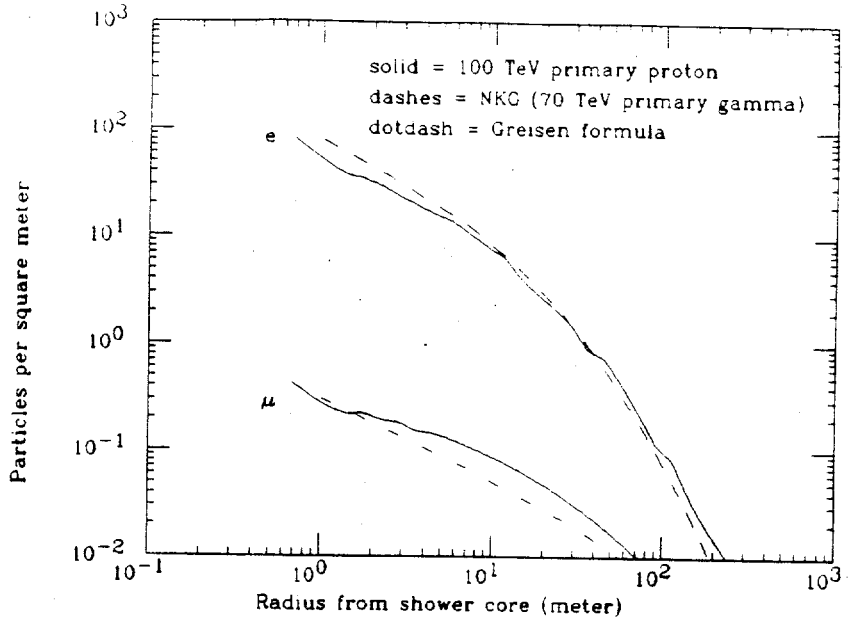

Figure A.5: Lateral electron and muon densities at $800\frac{gm}{cm^2}$ for 100 TeV proton primaries (solid) compared with expectation (dashes). Expectation for the electron component is based on the NKG prediction for a 70 TeV gamma primary, which yields the same size shower at this altitude. The prediction for the muon component is base on the Greisen formula [128].

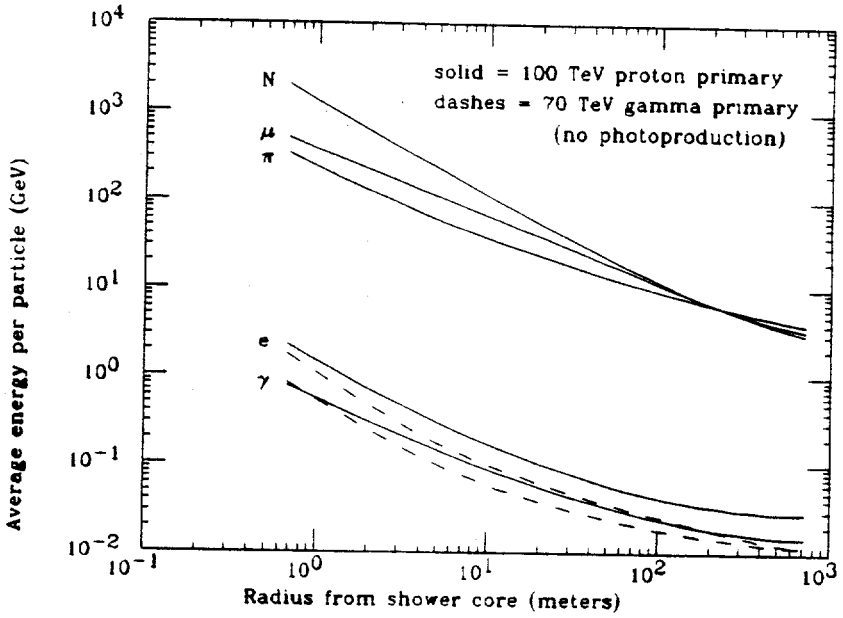

Figure A.6: Average energy per particle versus radius from the shower core for 100 TeV proton (solid) and 70 TeV gamma (dashes) primaries.

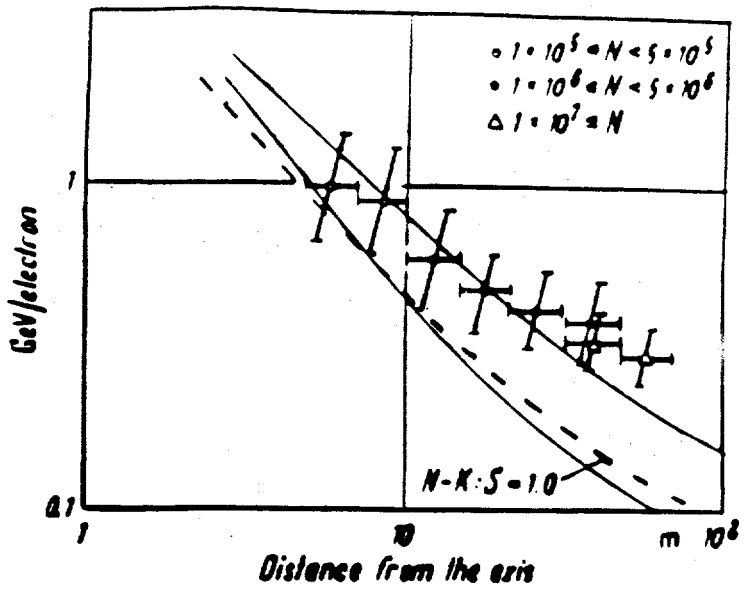

Figure A.7: Average energy of electromagnetic component normalized to the local electron number as a function of radius [129]. Data points are from the Mt. Chacaltaya Laboratory: the dashed line is the theoretical prediction by Nishimura and Kamata for a primary gamma-ray. The solid lines are simulation results scaled to the altitude of Mt. Chacaltaya for proton (upper line), and gamma-ray (lower line) primaries [130].

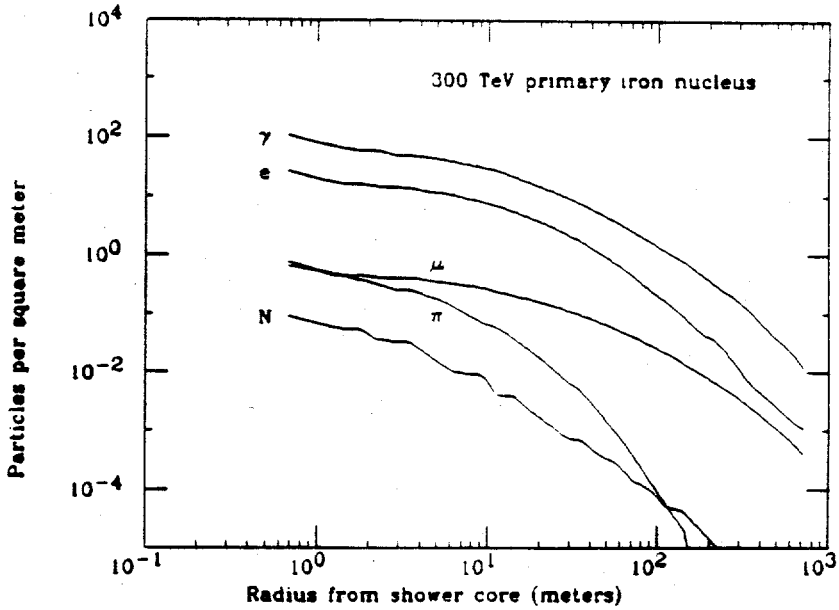

Figure A.8: Lateral particle densities at $800\frac{gm}{cm^2}$ for 300 TeV iron primaries.

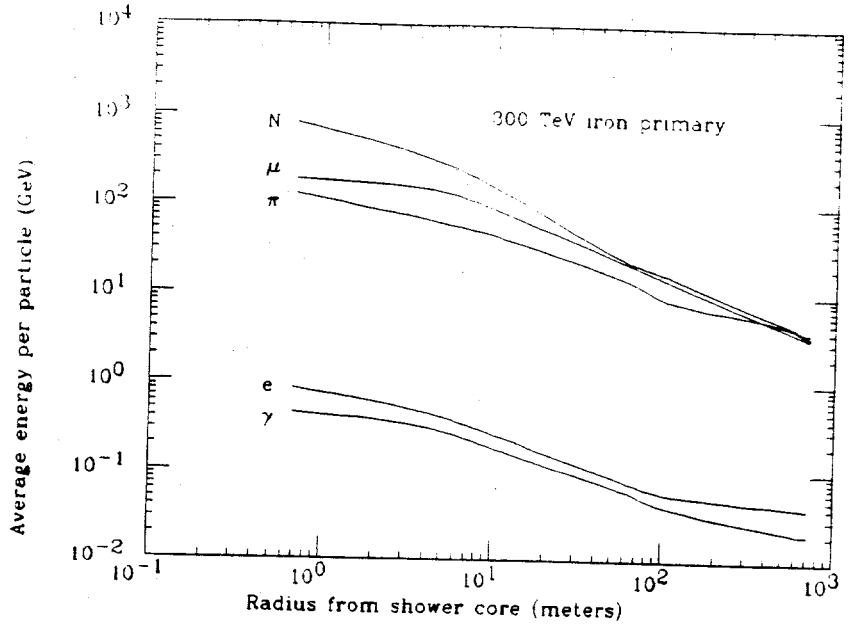

Figure A.9: Average energy per particle versus radius from the shower core for 300 TeV iron primaries.

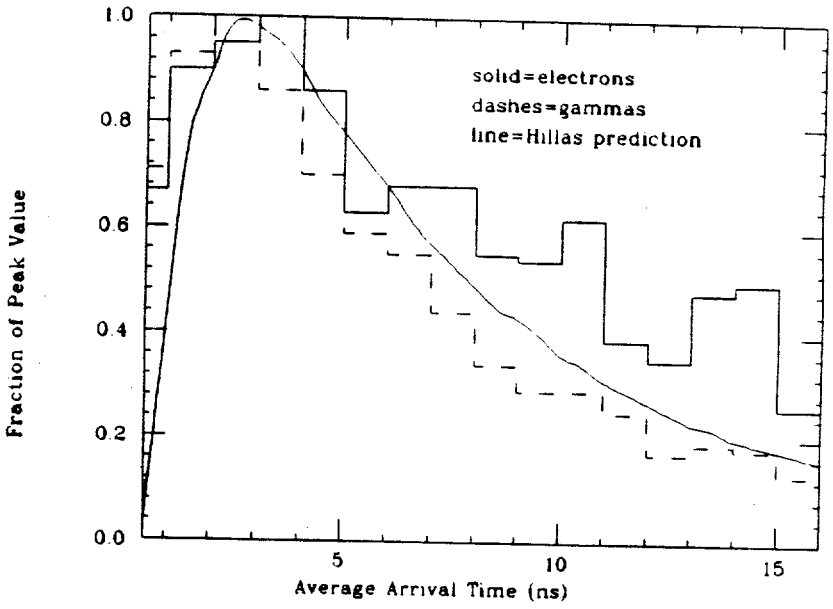

Figure A.10: Electron (solid) and gamma (dashes) showerfront time structure 50 meters from the shower core for 100 TeV proton primaries. The results of an independent calculation by Hillas for gamma-ray primaries is also shown [127].

Simulation of the CYGNUS Detector

Figure A.11 shows the flowchart for the underlying structure of the detector simulation CYGSIM.

Simulation Configuration

The first step is to set up the configuration for the simulation. This involves basic simulation parameters (*e.g.* how many times to use each shower generated according to the previous section), as well as run-specific considerations (*e.g.* which scintillation counters are included and which have lead sheets over them). Each shower is then used several times, sampling from a specified range of core locations relative to the geometric center of the working counters in the array. Scintillator attenuation lengths for the working counters are then generated to account for the degradation in light yield due to the scintillator "ageing" (see below).

Simulation of Scintillation Counter Response

The range of scintillator attenuation lengths, λ, was determined by a separate simulation of an individual counter. The simulation was then compared with tests previously made with a 2-inch diameter Quanticon [131] photomultiplier tube (PMT), which measured the number of photoelectrons generated by a through-going muon in the scintillator. Comparisons were made for 2 cases: **1)** where the inner walls of the counter were white (normal case); and **2)** where the inner walls were black. The simulation was also used to determine the distribution of arrival times as measured by the PMT relative to when a charged particle passes through the scintillator. The light yield of the scintillator was taken to be 6700 photons per MeV [60]; the Quanticon tube efficiency was taken to be ~28%; the distribution of scintillator response times was assumed to be an exponential with a time constant of 4 nanoseconds [60]; and the PMT "jitter" was parametrized by a Gaussian with an exponential tail (fit to an average distribution given in the RCA Handbook [132]).

Results for the attenuation length studies are given in the table below, which shows the number of photoelectrons (pe's) measured and predicted for the various cases.

	Reflectivity	
	90% (white)	0% (black)
Measured	20-25 pe	5-6 pe
Simulation		
λ=6cm	18.9 pe	6.1 pe
λ=7cm	20.4 pe	6.9 pe
λ=8cm	22.5 pe	7.6 pe

Table A.1: # pe's observed per through-going muon: data and simulation.

Based on these results (which are consistent with the apparent optical depth of the scintillator), simulated attenuation lengths are uniformly sampled from 5 to 10 centimeters (the sampling trys to account for the observed non-uniformity in scintillator quality). Figure A.12 shows the distribution of scintillator-PMT transit times also derived from the simulation. This is parameterized in CYGSIM by a Gaussian to the left of the peak, and an exponential to the right (dashed line).

Sampling of Particles

The number of particles striking a given counter is determined for each particle type by interpolating the particle density × scintillator area, and then fluctuating this number according to Poisson statistics. For each of these particles, the arrival time is then sampled and the average energy (E_{avg}) is found from the appropriate distributions. The particle energy is then further sampled using the following empirical parameterization for the energy distribution:

$$P(E) = Ae^{-\alpha\sqrt{E}} \tag{A.2}$$

where α is determined by requiring that the average of the distribution yields E_{avg}, and the normalization constant, A, from requiring the integral over all energies to

be 1. Figures A.13 through A.15 show how the above parameterization fits the full distribution of simulated particle energies (resulting from a proton primary) for electrons, gammas and muons respectively. The general form of this distribution appears to be roughly independent of the radius from the shower core.

Energy Deposition in the Scintillator

Figure A.16 shows distributions resulting from of an EGS4 simulation of energy deposited in scintillator by a through-going electron. As can be seen, the form of this distribution is relatively independent of scintillator thickness if the peak of the distribution is normalized to 1. This form is parameterized by a Gaussian to the left of the peak, and an exponential to the right (solid line). The peak corresponds to 2 MeV/cm times the scintillator thickness. The sampled energy deposition is never allowed to exceed the total energy of the electron. For gammas, the depths for pair-production and Compton interaction are sampled from a parameterization of their cross-sections as a function of energy. The interaction that occurs first (assuming that it occurs within the scintillator) is then simulated. The Compton interaction is assumed to be perfectly elastic (i.e. all of the gamma energy is given to a single electron); the fraction of energy imparted to each electron resulting from pair-production is assumed to be entirely random. The resulting electron energies are then deposited as described above.

A form of the distribution of energy deposition for pions that is very similar to the one previously described was found based on the simulations of Ispirian, Margarian and Zverev [133].

Muons are assumed to deposit exactly the amount of energy expected for an average, through-going, minimum-ionizing particle (2 MeV per centimeter of track length).

Half of the nucleons are assumed to be high-energy neutrons that do not deposit any energy in the scintillator. The other half are assumed to be protons that deposit their energy like muons.

As in the actual experiment, the energy deposition is then defined relative

to the median of the pulse height distribution obtained from single, through-going muons. This distribution was simulated by assuming a $cos^2(\theta)$ dependence of muon flux, calculating the path length and average energy deposited in the scintillator, and adding a Gaussian broadening of ~30% to this energy deposition (due mostly to Poisson fluctuations in the number of photoelectrons produced). The resulting distribution, shown in figure A.17, appears very similar to calibration histograms. The ratio of the peak position to median position is 0.8 .

PMT Response

After each particle has deposited its energy in the scintillator, the number of photoelectrons generated in the PMT is calculated. This involves taking into account the scintillator attenuation length, the solid angle of the PMT as viewed from the interaction site within the scintillator, the PMT efficiency, and reflection from the inner walls of the counter. This number of photoelectrons is then fluctuated according to Poisson statistics, and used to sample the scintillator-PMT transit time. The earliest transit time is added to the particle arrival time and the effective particle number is re-calculated (owing to the additional fluctuation in the number of photoelectrons).

The probability for a direct tube-hit is calculated from the ratio of the area of the PMT face to the area of the scintillator. For each particle, a random variable is used to decide whether a tube-hit occurs. If so, 5 nanoseconds is subtracted from the PMT time.

The earliest time measured by the PMT and the effective particle sum for the counter are then saved.

Electronic Response

Next, the ADC and TDC responses are simulated. Currently, only a crude accounting for electronic response is performed. For the ADC, this entails quantizing the particle number in ADC bins, folding in a 15% calibration uncertainty for converting ADC bins back to particle number, and accounting for any ADC pedestal

uncertainty (these may depend on which run is being simulated). Simulation of the TDC response involves adding in a Gaussian error of ~0.5 nanoseconds to account for TDC pedestal calibration uncertainties. A simulation of electronic "slewing" is not currently implemented.

Array Trigger, Muon Detector and Output

The entire event is then tested to determine whether the array is triggered based on criteria set up in the initial configuration. If a trigger occurs, the number of muons striking the E225 anti-coincidence shield is calculated. This involves sampling the muon density and energy distributions over the projected area of the muon detector, and attenuating the lower energy muons striking each wall according to calculations of the effective overburden [62]. The response of the wire chambers and muon counting algorithm have not been simulated, so the detector is assumed to be 100% efficient up to a "saturation" value of 12 muons. After accounting for the muon detector response, the entire event is output in a standard data-file format and the next event is processed.

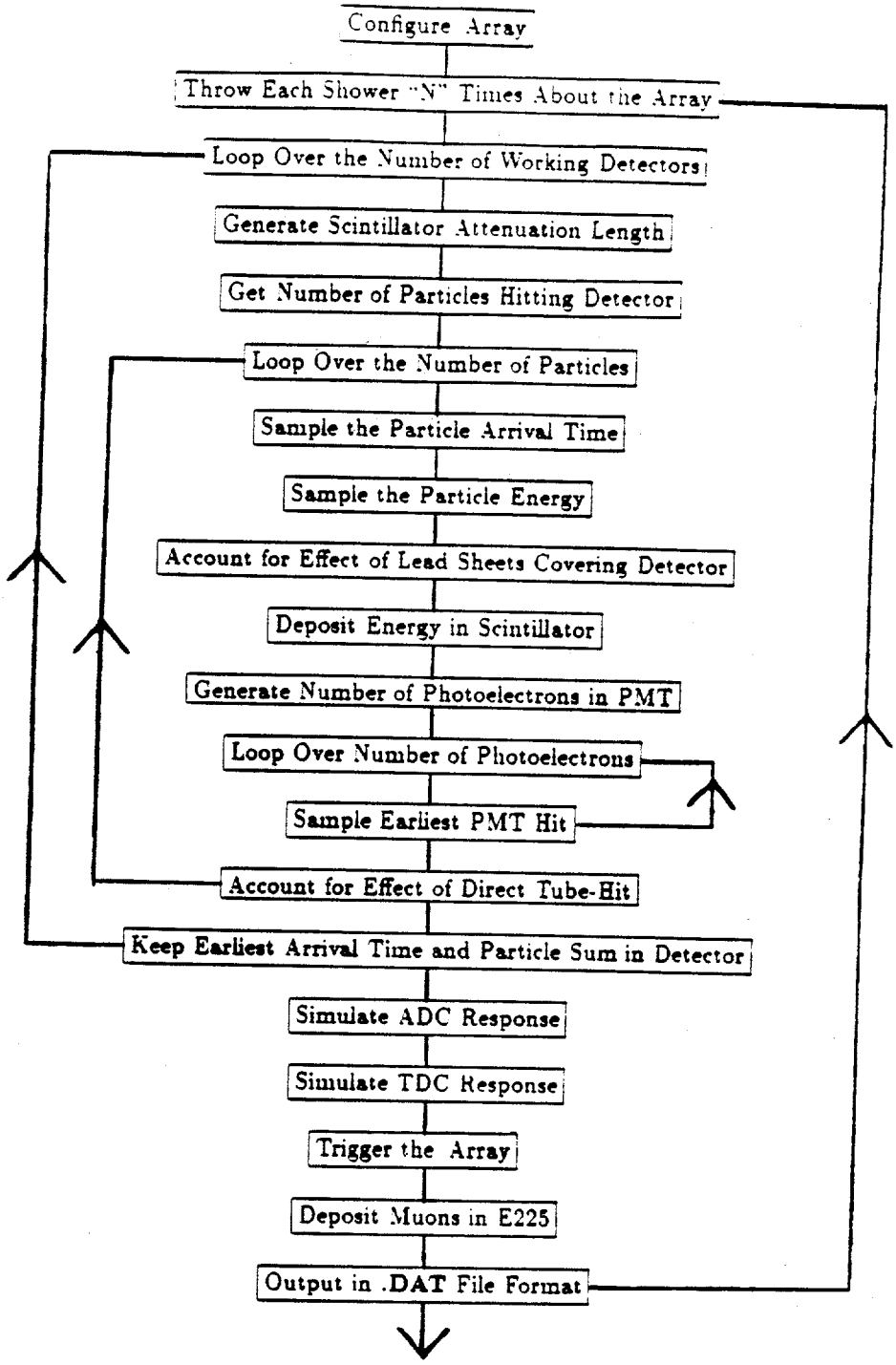

Figure A.11: Logic diagram for detector simulation.

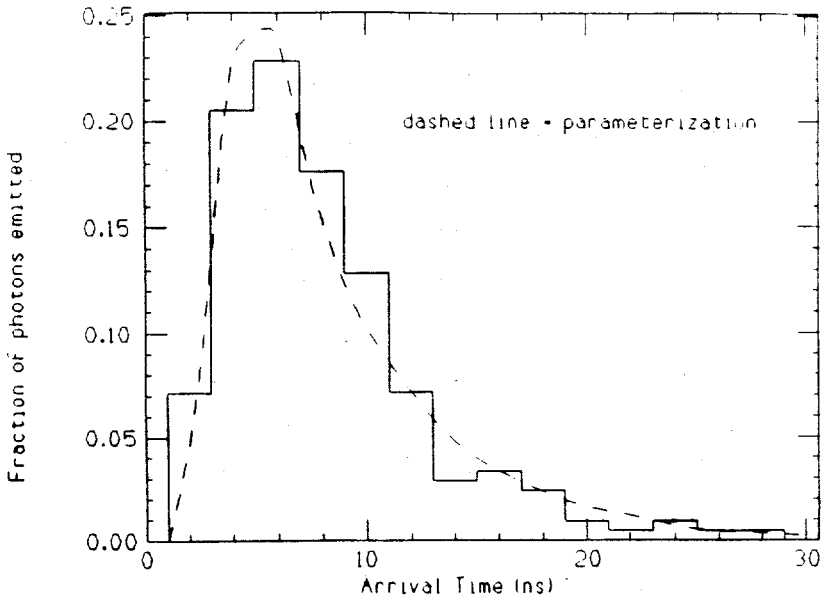

Figure A.12: Simulated distribution of scintillator-PMT arrival times. The dashed line shows the parameterization adopted for use in CYGSIM.

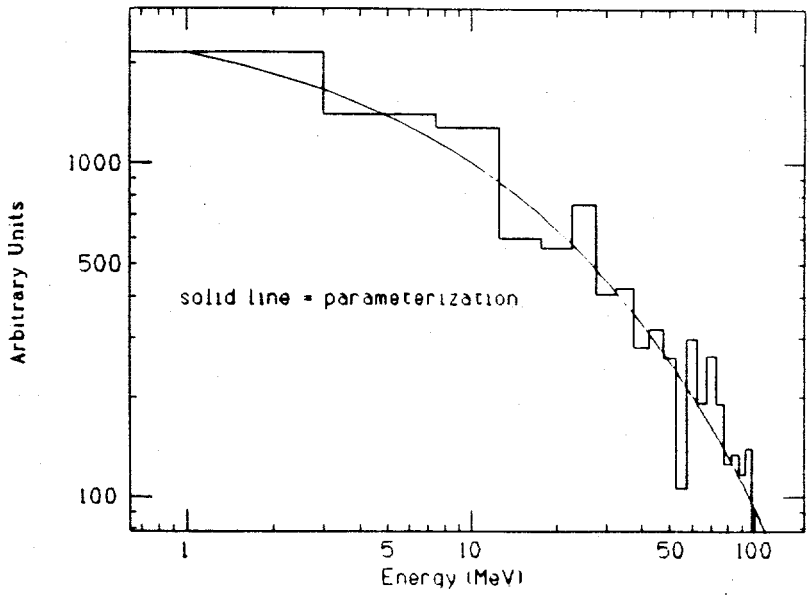

Figure A.13: Simulated distribution of electron energies at a given distance from the shower core. The solid line shows the parameterization adopted for use in CYGSIM.

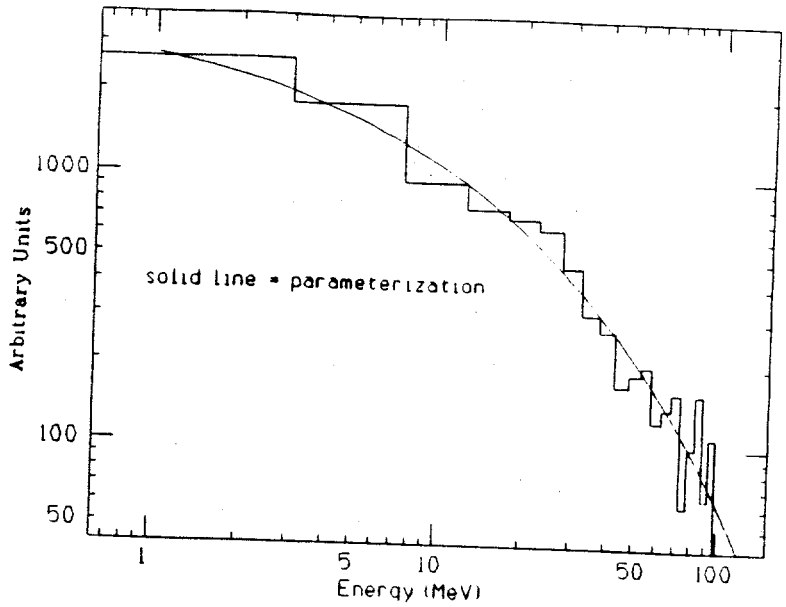

Figure A.14: Simulated distribution of photon energies at a given distance from the shower core. The solid line shows the parameterization adopted for use in CYGSIM.

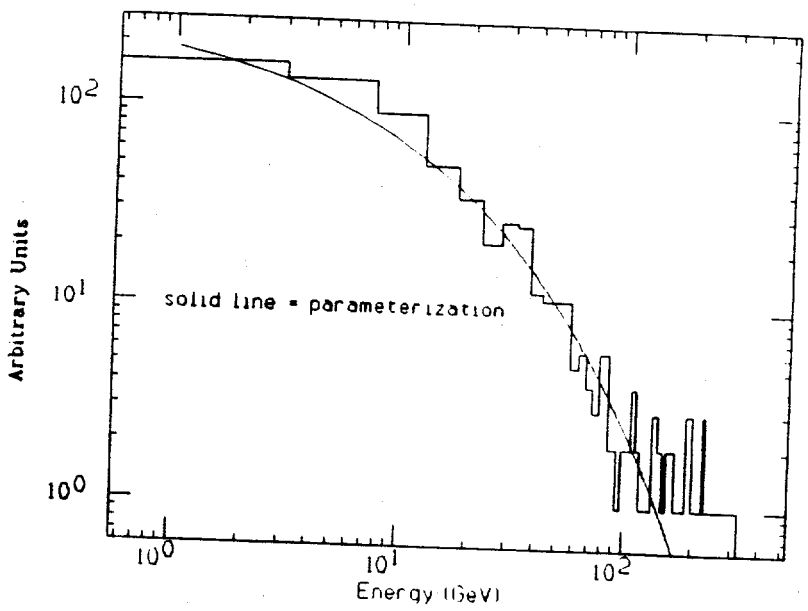

Figure A.15: Simulated distribution of muon energies at a given distance from the shower core. The solid line shows the parameterization adopted for use in CYGSIM.

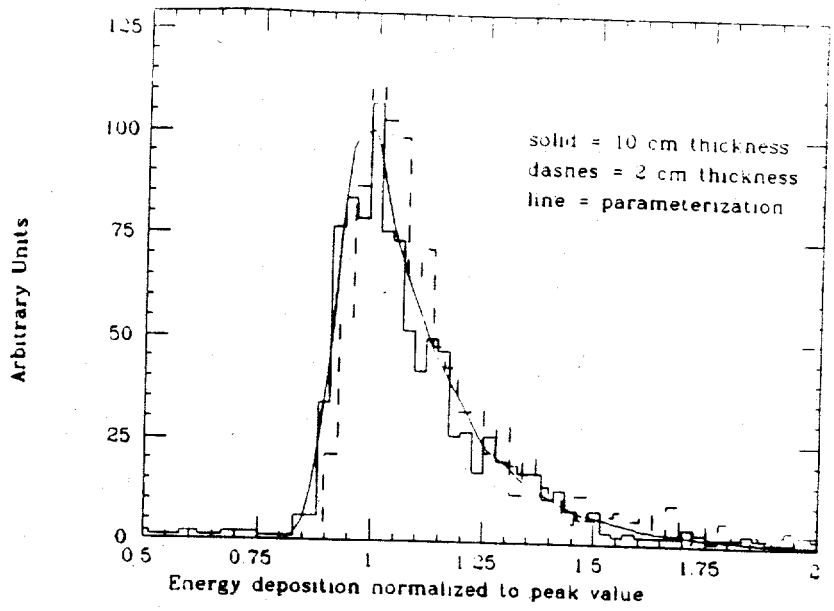

Figure A.16: Simulated distribution of electron energy deposition in plastic scintillator of thickness 10cm (solid) and 2 cm (dashes), each normalized to the peak value. The parameterization adopted for use in CYGSIM is also shown.

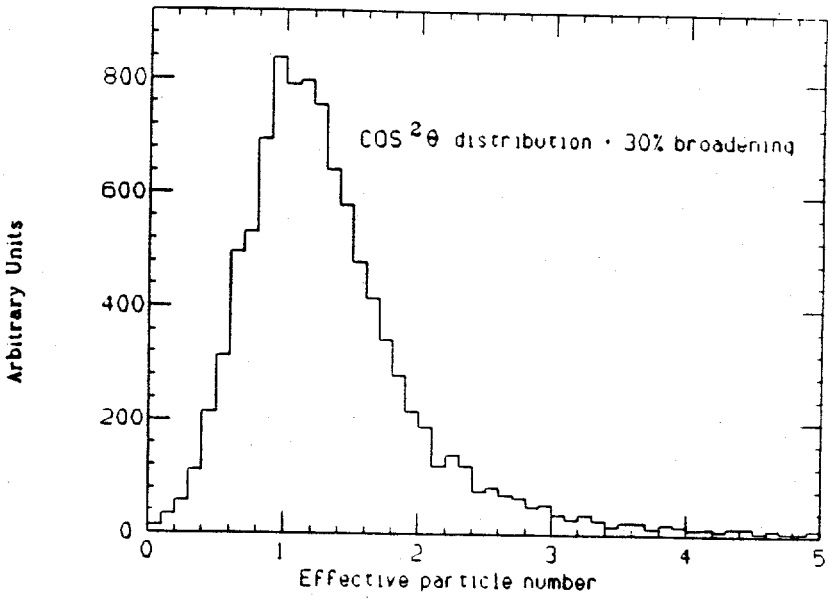

Figure A.17: Simulated distribution of muon energy deposited in plastic scintillator of thickness 10cm.

Results

A simulated data set of 1000 "background" showers was generated by modeling proton-initiated showers sampled from an $E^{-1.7}$ integral energy spectrum starting at 50 TeV, and projected from the zenith. The detector configuration simulated was that of the original 64-counter array as it existed for runs 167-175 (which will be used for comparison). Each shower was used 40 times, with the core location varied over a radius of 200 meters relative to the geometric center of the array. Of the 40000 showers processed by CYGSIM, 556 triggered the array.

The average angular resolution of triggered simulated events was 0.6 degrees, as compared with the measured value of 0.7 degrees obtained from the sun/moon shadow analysis averaged over all array configurations.

Figures A.18-A.31 compare various distributions of simulated events with data. The distributions derived from data were typically based on ~5000 events. These plots are normalized to their total area for comparison.

The first few plots compare the spectra of fitted shower size, shower age, core location, minimum-ionizing particles per counter, and detected muon number. The peak of the size spectrum corresponds to a proton primary energy of ~100 TeV. The relatively large value of reduced χ^2 corresponding to the single-counter particle spectrum (figure A.21) is primarily due to difficulties in matching the values at the highest (overflow bin) and lowest pulse heights (figure A.22), which are sensitive to the precise threshold and saturation values of individual detectors. The large value of reduced χ^2 associated with the age distribution (figure A.19) is not currently understood, but may stem from related issues.

The next set of plots are concerned with showerfront timing fits. Figures A.24-A.26 show distributions of the number of counters used per timing fit, the space-angle difference between fits using odd and even counters (DelEO), and the space-angle between fits using "clockwise" and "anticlockwise" halves of the array (DelCA). Figure A.27 compares the distributions of the ratio of "inner-counter" to "outer-counter" showerfront widths, which is the main parameter of interest in the analysis presented in chapter 6. The relatively large χ^2 values in figures A.24 and

A.26 may be related to the fact that electronic slewing has not been simulated, thus making the standard curvature correction inappropriate for simulated showers. Figures A.28 and A.29 show the time residuals from the shower fit versus pulse height for data and simulation respectively. Figure A.31 is a plot of the standard deviation of measured particle number versus particle number as obtained from comparing data in neighboring counters. The simulated data (shown as crosses) was obtained from running the identical "experiment" with the simulated data set. Note that both sets of data show similar deviations from a $\sqrt{\text{particle \#}}$ dependence. This deviation is principally caused by ADC calibration uncertainties and a limited ability to account for the radial-dependence of the density distribution resulting from core location uncertainties.

Figure A.30 is a plot of the fitted shower size versus the actual number of electrons reaching the ground. Note the linear correlation is systematically shifted lower for the fitted sizes by ~40%. This systematic shift is not related to problems with the fitting algorithm, but is due to **1)** the fact that the simulation follows all electrons with energies as low as 1 MeV, whereas the scintillation counters possess a ~20 MeV threshold for through-going particles, and **2)** that the scintillation counters do not strictly measure electron number, as they are sensitive to the scintillator's attenuation length, fluctuations in energy deposition, gamma-ray and muon interactions, etc.

In addition to "standard background" showers, several other sets of simulated data were generated for various studies. Figures A.32-A.34 show how the age distribution is modified for **1)** protons initiated 400gm/cm^2 deep in the atmosphere, **2)** gamma-initiated showers, and **3)** iron-initiated showers respectively. Comparisons have been made with results from the previous simulation of "standard" proton-initiated showers. The trends observed are as expected, indicating some sensitivity to interaction depth and composition. No significant difference is seen for gamma-initiated (as compared to proton-initiated) showers.

To predict the trigger rate of the array, the following model for composition was used: 4 parts H and He, 2 parts N and Mg, and 1 part Cl and Fe. This mixture is consistent with direct measurements at energies of $\sim 10^5$ Gev/nucleon [134].

In this simple model, no energy-dependent change in the composition is assumed. The rate is then given by:

$$\text{Rate} = \Phi_{CR}(> E) \times \Delta\Omega \times A_{Eff} \tag{A.3}$$

Where $\Phi_{CR}(> E)$ is the all-particle, integral cosmic ray flux above the minimum simulated energy E, taken to be $3 \times 10^{-7} s^{-1} cm^{-2} sr^{-1}$ above 10TeV [134]; $\Delta\Omega$ is the solid angle over which simulated events are generated (typically $2\pi(1 - cos(50°)) = 2.2sr$); and A_{Eff} is the effective area, defined as the area over which simulated shower cores are thrown times the fraction of simulated showers that trigger the array. The following table lists the results for 4 different detector configurations:

Run Number	Simulated Rate (Hz)	Actual Rate (Hz)
171	0.23	0.25
1100	0.75	0.90
1191	2.8	2.7
3000	4.2	3.4

Table A.2: Simulated and actual trigger rate for various runs.

The absolute values of simulated and actual trigger rates match much better than expected from inherent uncertainties in both composition and interaction models. An agreement to within $\sim 50\%$ would be acceptable. The observed agreement in the absolute value of the rate is therefore largely taken as coincidence. However, the scaling of the rate between array configurations is primarily based on known geometry and detector response characteristics, and should therefore be well reflected by the simulation. The largest descrepancy (run 3000) is attributed to difficulties still present in simulating the effects of the lead sheets that were added above the counters in order to pair-convert photons.

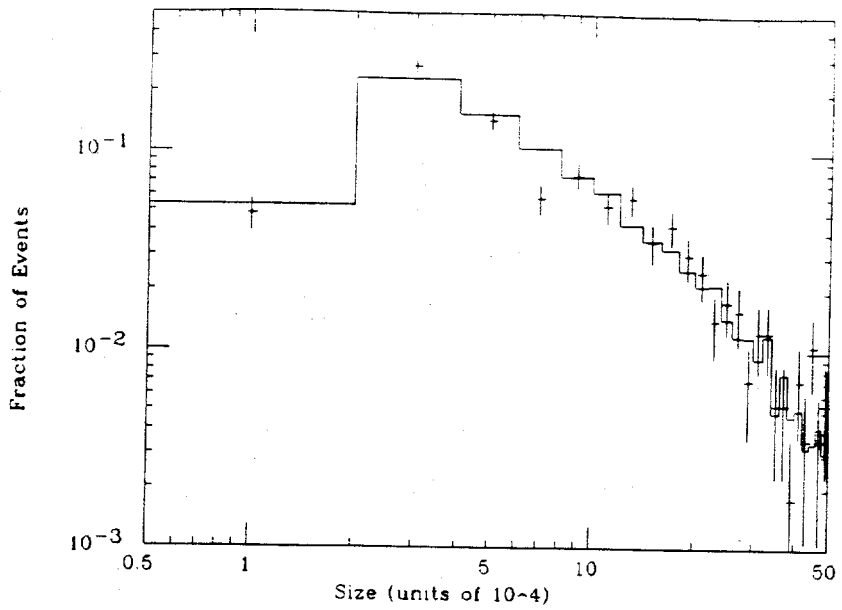

Figure A.18: Simulated (error bars) and measured (solid) distribution of fit sizes (in units of 10^4) for triggered events. The reduced χ^2 is 1.2 for the comparison.

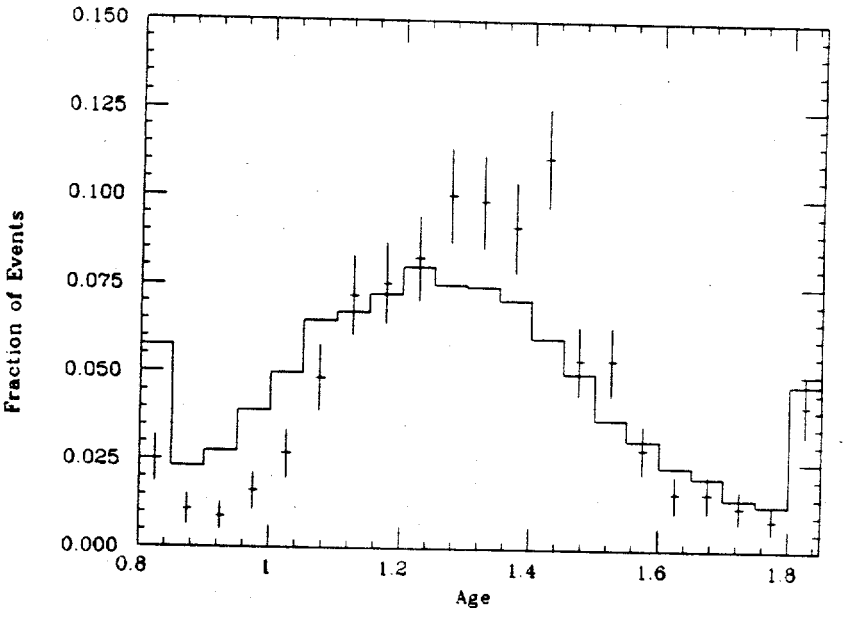

Figure A.19: Simulated (error bars) and measured (solid) distribution of fit ages for triggered events. The reduced χ^2 is 4.6 for the comparison.

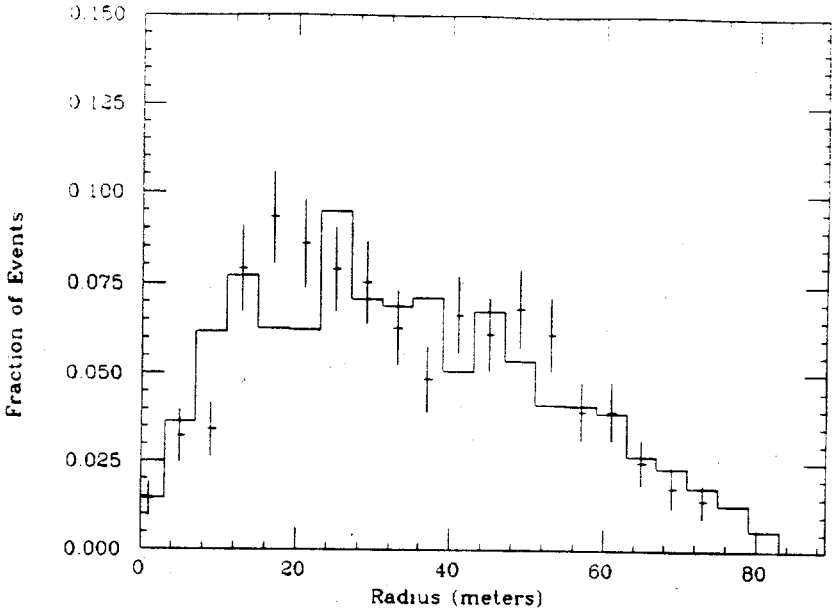

Figure A.20: Simulated (error bars) and measured (solid) distribution of fit core locations relative to the E225 muon detector for triggered events. The reduced χ^2 is 1.8 for the comparison.

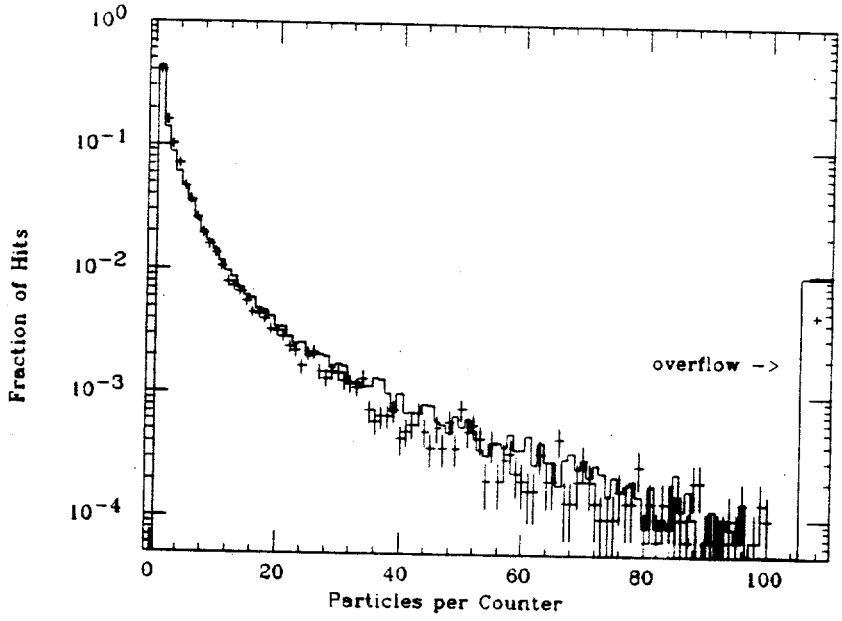

Figure A.21: Simulated (error bars) and measured (solid) single-counter particle spectrum for triggered events. The bin to the far right represent overflows due to counter saturation at large pulse heights. The reduced χ^2 is 3.6 for the comparison.

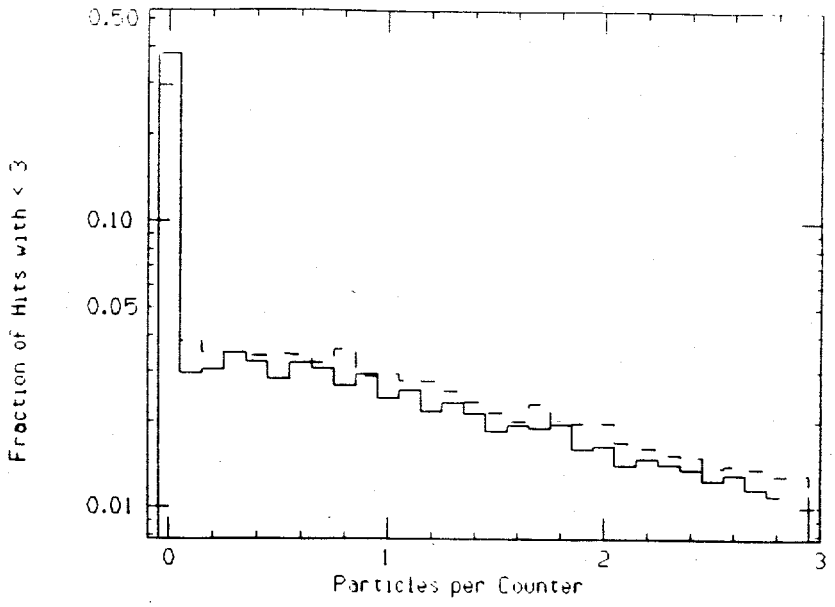

Figure A.22: Simulated (dashes) and measured (solid) single-counter particle spectrum at low pulse height for triggered events.

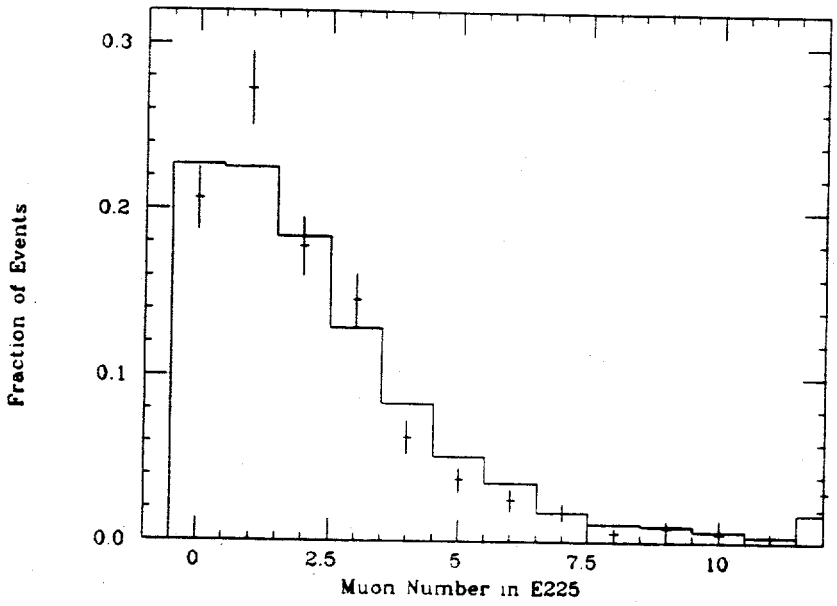

Figure A.23: Simulated (error bars) and measured (solid) distribution of muon number detected in E225. The reduced χ^2 is 1.5 for the comparison.

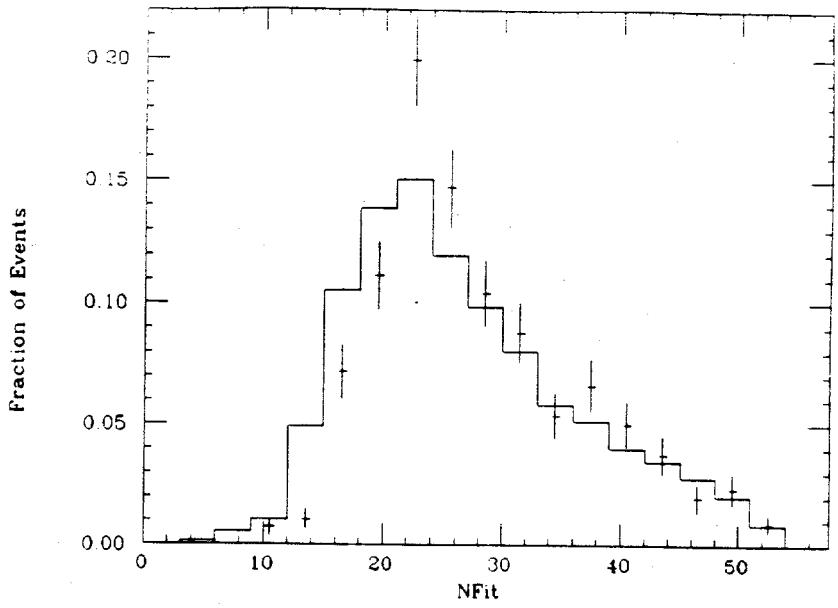

Figure A.24: Simulated (error bars) and measured (solid) distribution of the number of counters that could be used in showerfront timing fits. The reduced χ^2 is 5.2 for the comparison.

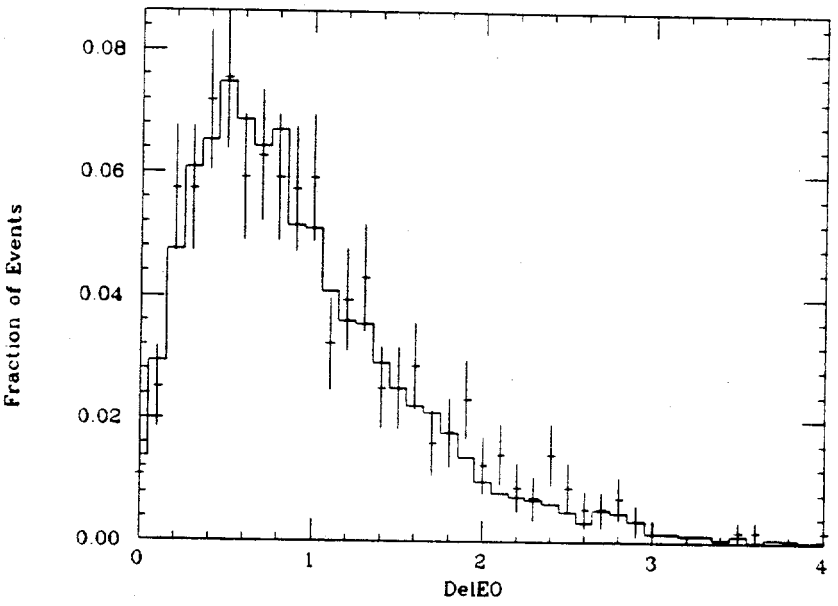

Figure A.25: Simulated (error bars) and measured (solid) distribution of fit space-angle differences between "odd" and "even" counter directional reconstructions. The reduced χ^2 is 0.54 for the comparison.

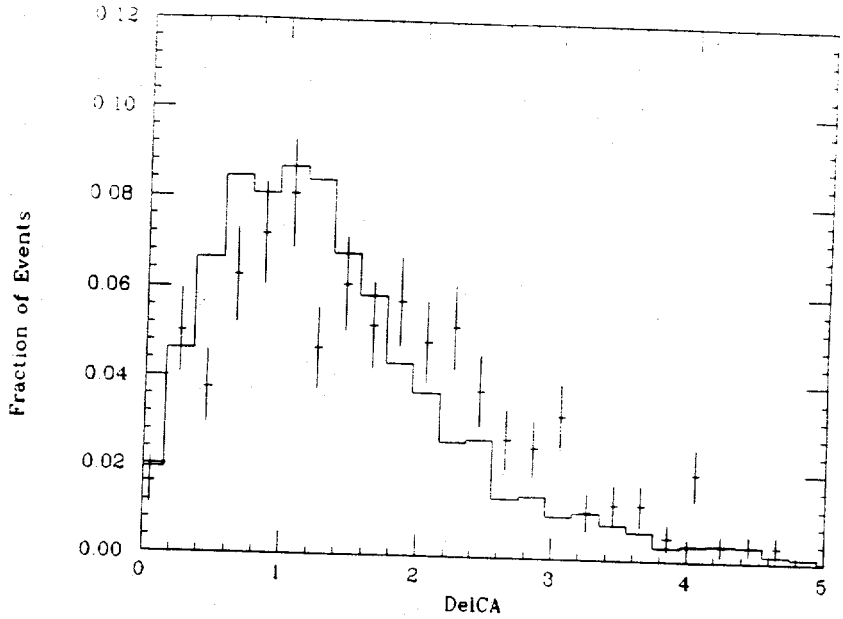

Figure A.26: Simulated (error bars) and measured (solid) distribution of fit space-angle differences between "clockwise" and "anti-clockwise" counter directional reconstructions. The reduced χ^2 is 2.8 for the comparison.

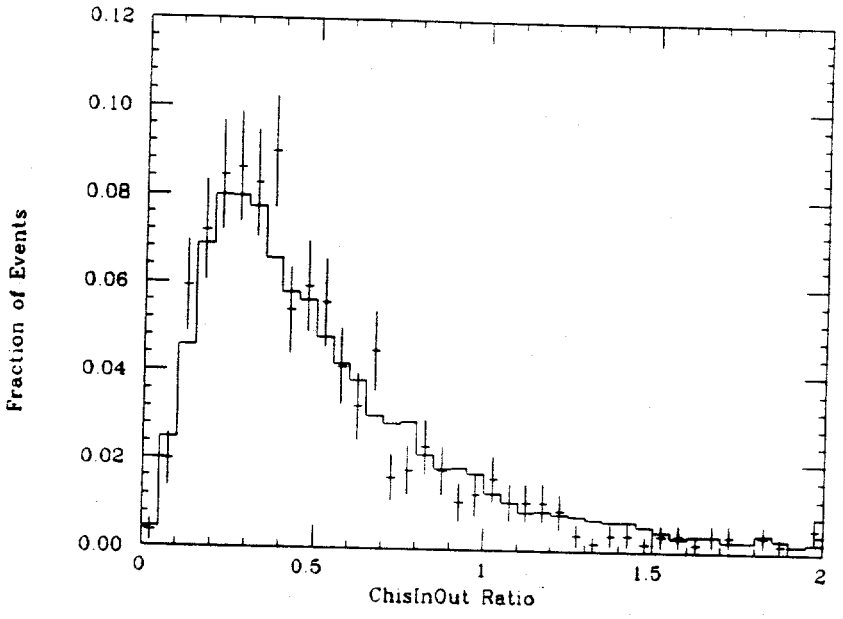

Figure A.27: Simulated (error bars) and measured (solid) distribution of the fit ratio of inner-counter to outer-counter showerfront widths. The reduced χ^2 is 0.54 for the comparison.

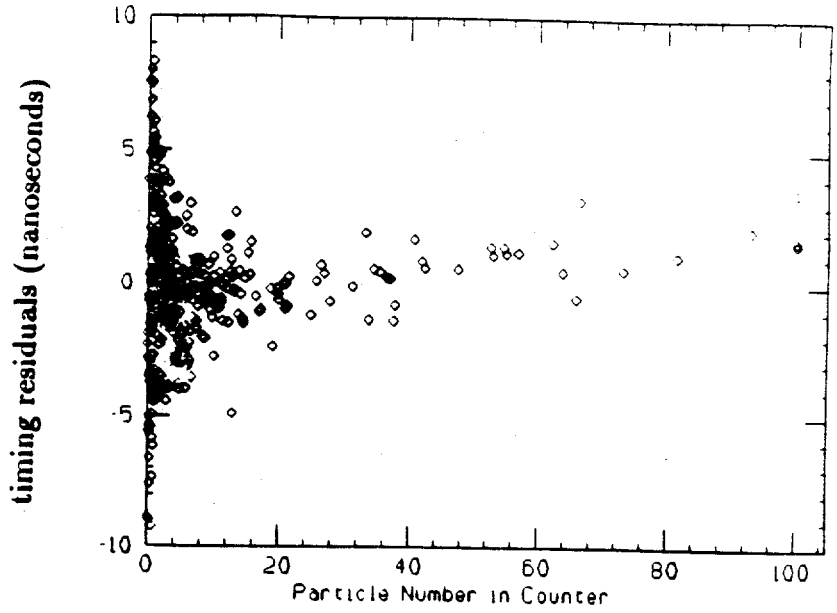

Figure A.28: Measured distribution of counter timing residuals (nanoseconds) relative to the fit showerfront plane as a function of the effective particle number striking that counter. The plot comprises of 10 events of size 10^5.

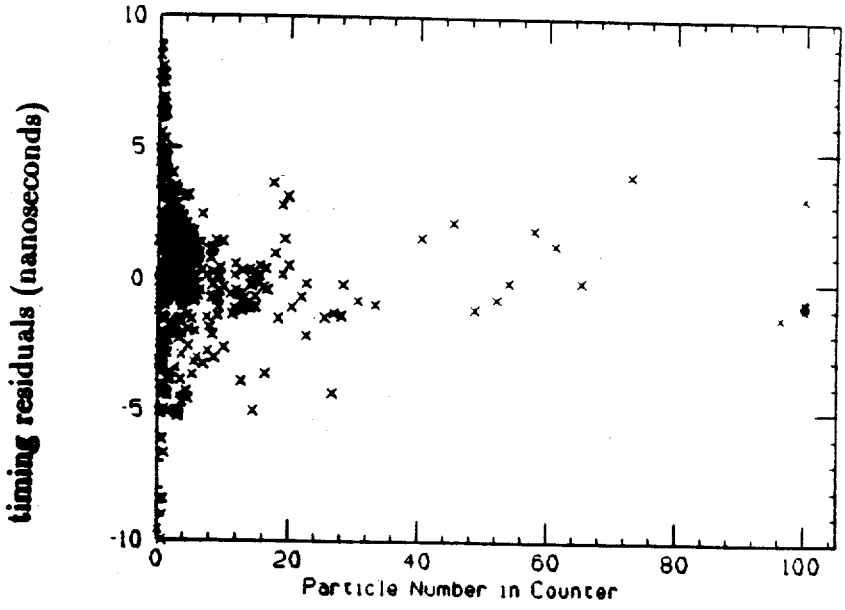

Figure A.29: Simulated distribution of counter timing residuals (nanoseconds) relative to the fit showerfront plane as a function of the effective particle number striking that counter. The plot comprises of 10 events of size 10^5.

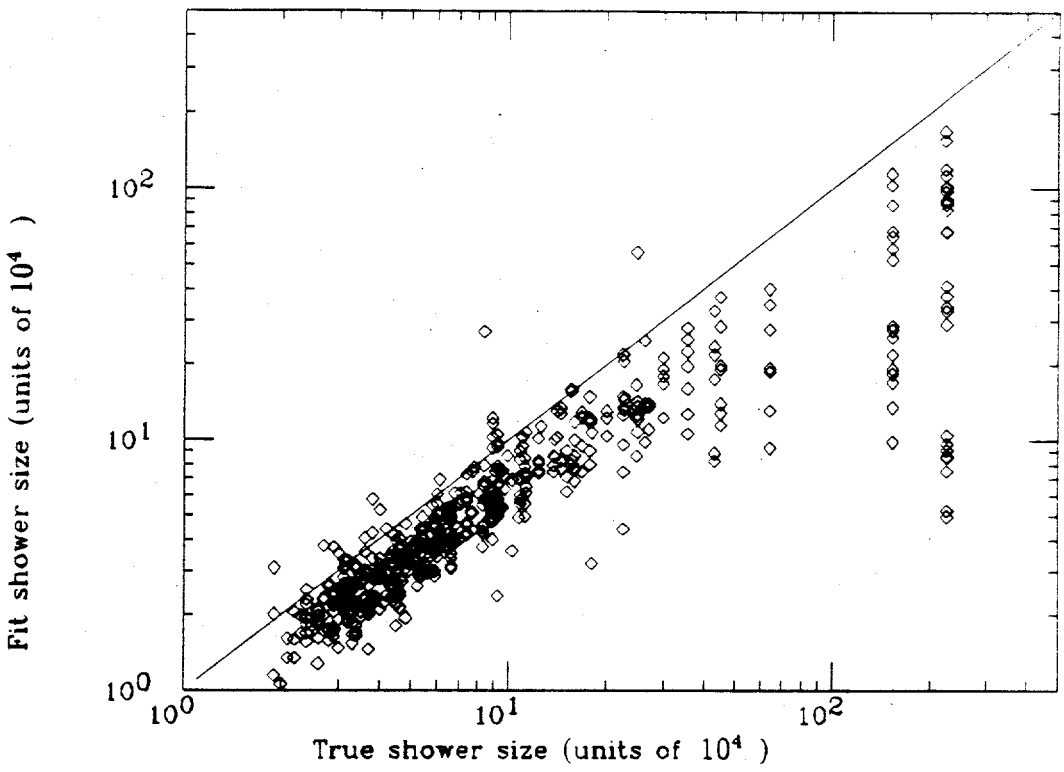

Figure A.30: Fit shower size (in units of 10^4) versus true size (simulation). The solid line shows what is expected for a one-to-one correlation. The observed systematic shift is primarily due to a ~20 MeV threshold for through-going particles associated with the scintillator.

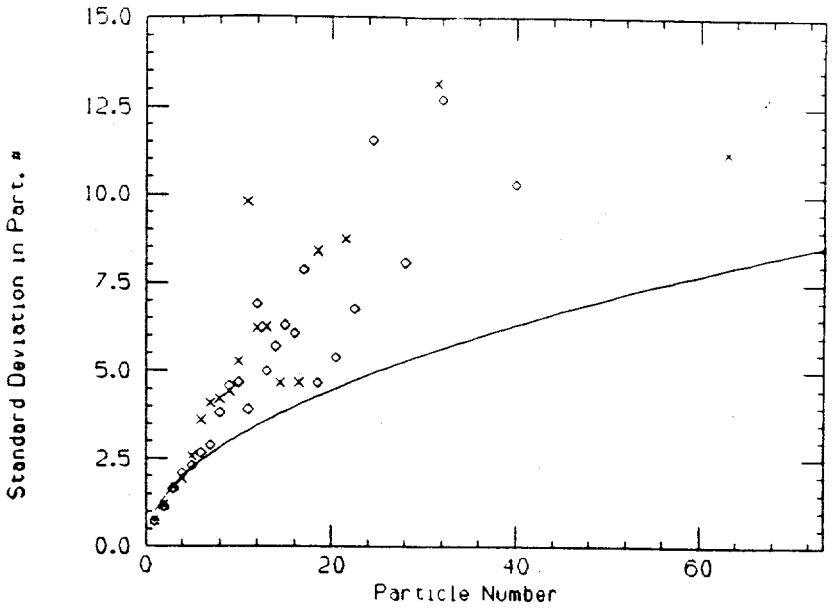

Figure A.31: Inferred standard deviation in the number of effective particle versus average particle number based on side-by-side counter measurements for both data (diamonds) and simulation (crosses). The naive $\sqrt{N}$ prediction is also shown. The observed deviation is principally caused by ADC calibration uncertainties and a limited ability to account for the radial-dependence of the density distribution as a result of core location uncertainties.

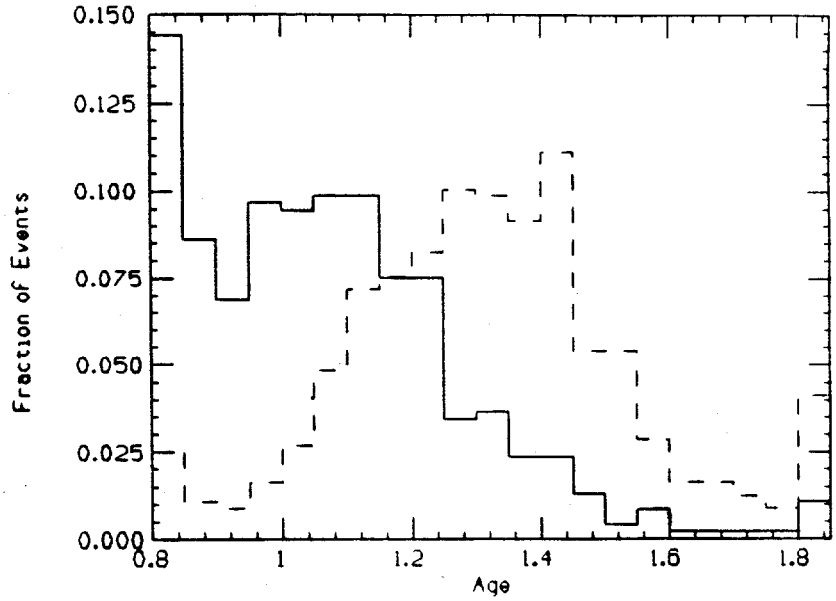

Figure A.32: Simulated distribution of fit ages for triggered proton showers injected at $400\frac{gm}{cm^2}$ (solid) compared to that obtained for typical proton showers (dashes).

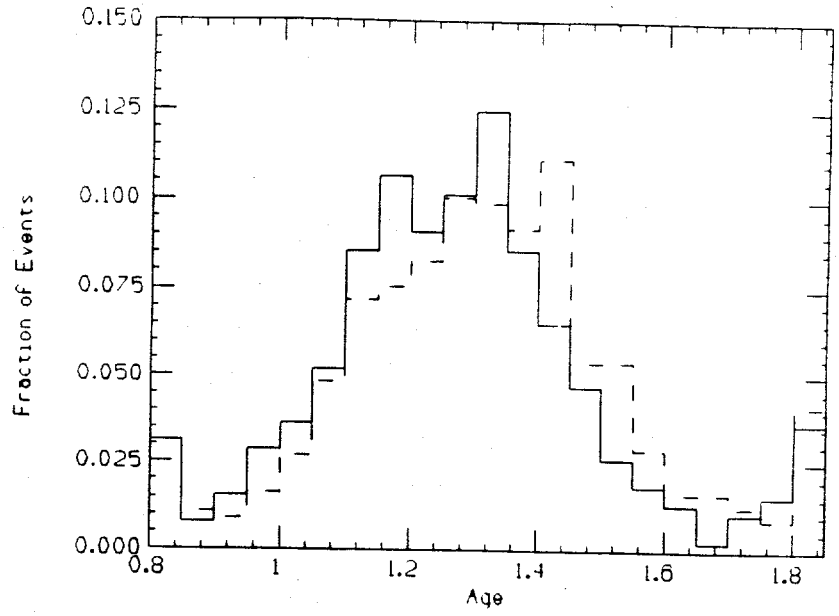

Figure A.33: Simulated distribution of fit ages for triggered gamma-induced showers (solid) compared to that obtained from typical proton showers (dashes).

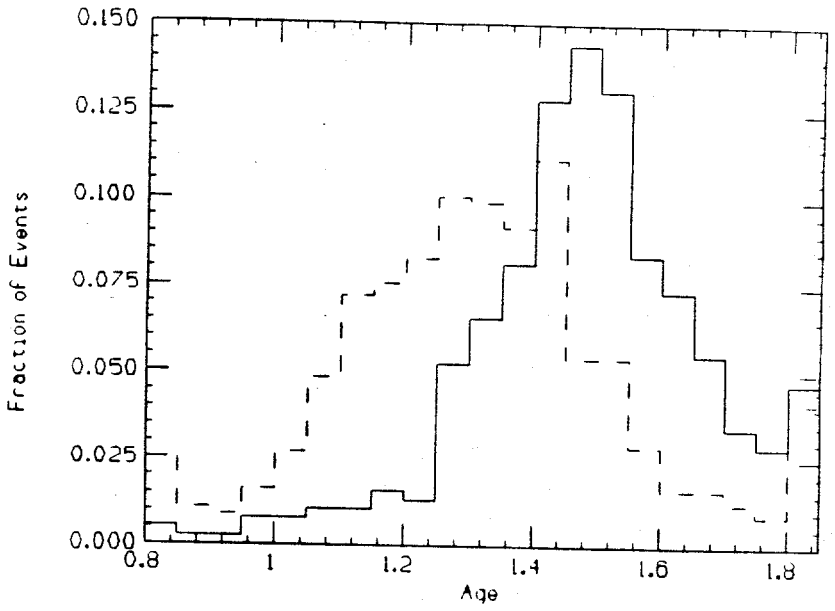

Figure A.34: Simulated distribution of fit ages for triggered iron-induced showers (solid) compared to that obtained from typical proton showers (dashes).

Appendix B

Fitting the Lateral Density Distribution

"Anything that can Gaurang, will Gaurang."

- Stuart Schaller -

Form of the Lateral Density Distribution of Electrons

A theoretical form for the lateral electron density distribution for electromagnetic cascades has been derived by Nishimura and Kamata [129]. In his 1960 article [128], Greisen couched this derivation in a more useful form, now called the "NKG" formula:

$$\rho_e = \frac{N_e}{2\pi {R_0}^2} C(s) \left(\frac{R}{R_0}\right)^{s-2.0} \left(1 + \frac{R}{R_0}\right)^{s-4.5} \qquad \text{(B.1)}$$

where ρ_e is the electron density; N_e is the total number of electrons in the shower ("shower size"); s is the "age" (related to the depth of shower maximum); $C(s) = \frac{\Gamma(4.5-s)}{\Gamma(s)\Gamma(4.5-2s)}$; R_0 is the Moliere scattering radius at the level of observation; and R is the radius from the core as measured in the shower plane.

The theoretical value for R_0 at the altitude of Los Alamos is approximately 100 meters [128], and the average age, s, should be about 1.3 (where a value of 1 would correspond to shower maximum for a gamma-initiated shower). However, several independent simulations of cascade development [135] (including the one

described in this thesis), along with fits to measured lateral electron density distributions, indicate a deviation from the theoretical expectation. Several authors have therefore adopted modified forms for the lateral distribution, the simplest of which is to use the NKG formula with a value for R_0 that is 50% the theoretical value (the theoretical value is ~100 meters in our case). The cause for the discrepancy with theory is not well understood analytically, although it is clearly imbedded within the simulations previously eluded to. This, along with the fact that typical EAS measurements involve fitting to the lateral electron distribution induced by hadronic as opposed to electromagnetic interactions, casts some doubt on the precise physical interpretations of the parameters R_0 and age. Nevertheless, the age parameter is still a measure of the steepness of the lateral distribution for a given shower, and this is related to both the depth of shower maximum relative to the observation level, and to the distribution of transverse momentum inherent to the cascade development. Therefore, the shower age in the modified NKG formula still possesses physical meaning in terms of its sensitivity to the nature of the primary interaction.

Estimation of Shower Parameters

The standard approach to estimating the lateral distribution shower parameters is to perform a simultaneous, 4-parameter fit of the NKG formula to the data in order to determine N_e, s, and the core location (X_c, Y_c). Because of the complex form of the NKG formula (particluarly with regard to X_c and Y_c), an alternate approach has been developed whereby the dependence of each parameter on the lateral distribution is separated out.

The approach is as follows: 1) Use a separate core-locating algorithm to quickly estimate the core position by symmetry. The approach used here involves a linearized approximation to a 2-dimensional Gaussian. 2) Assign uncertainties to the particle density measurements so as to minimize the dependence of the NKG fit on the precision of the core determination. This is done on an event-by-event basis by using the calculated standard deviation from the average particle density in different "radial bins". Specifically, density information within a sliding ± 5 meter

radial bin (concentric with the estimated core position) around the radius of each counter is considered to determine the particle density fluctuations there. Since the lateral distribution asymptotically approaches $\frac{1}{R}$ close to the core, the average density is computed with this weighting factor to reduce density biases within the radial bin. To remain in the fit, a minimum of 3 counters within that radial bin are required to be hit. Saturated counters are removed from the fit as their influence tends to distort the shape of the distribution, which is sufficiently preserved by the remaining counters. This approach tends to weight the influence of particle density measurements according to the degree to which its value is corroborated by other measurements made in the same vicinity. The dependence of the fit on the precise determination of core position is therefore minimized. **3)** Determine the age parameter using the ratios of particle densities at various radii from the core. The ratio of NKG densities is given by:

$$\frac{\rho_{e1}}{\rho_{e2}} = \left(\frac{R_1}{R_2}\right)^{s-2.0} \left(\frac{R_0 + R_1}{R_0 + R_1}\right)^{s-4.5} \tag{B.2}$$

Since the core location has already been determined, this formula lends itself easily to a size-independent solution of s. The best overall value is calculated by taking a weighted average of the ages determined for each computed ratio. In practice, the determination of age via particle density ratios is particularly sensitive to fluctuations. It is found that this technique works more consistently if the radial-binned averages for each counter are used (essentially just a data-smoothing technique). **4)** Finally, solve for the shower size (the only remaining parameter) at each counter and perform another weighted average to find its best value.

This "compartmentalization" decouples parameter dependencies to avoid χ^2 minimization in lieu of more direct calculations and, at the same time, diminishes the effects of core position uncertainties and abhorent counter responses. It therefore results in a very robust approach. Aside from the technique being computationally fast, unforseen perturbations (*e.g.* non-working counters mistakenly included in the fit), will have minimum impact on the determination of shower parameters.

Performance of Fitting Technique

The simulation described in Appendix A was used to generated 500 proton-induced showers, projected from zenith, and passing simulated array trigger conditions corresponding to the configuration employed during the 1986 Hercules X-1 observation. Shower energies were sampled from an $E^{-1.7}$ integral spectrum starting at 50 TeV.

Figure B.1 shows the reconstructed shower size derived as described in the previous section, versus the actual total number of simulated electrons striking the ground (units are in 10^4 particles). The reason for the systematic offset is described in Appendix A. The systematic "turn-over" at larger shower sizes is due to core-location errors associated with cores located outside the physical array boundaries that can, nevertheless, trigger the array.

Figure B.2 shows the same plot for showers reconstructed by a more standard, simultaneous, 4-parameter fit using the Levenberg-Marquardt technique [136]. Note that the differences between this and the previous plot are negligible. This is despite the fact that, as shown in figure B.3, there is a systematic improvement in core location when the simultaneous fit is used. Furthermore, it should be noted that the simulation indicates no noticible difference in the average angular resolution if the better core location is used (the angular dependence on core location enters through the showerfront curvature correction).

Both techniques fail most frequently when there is a large uncertainty in the gradient of measured particle densities, resulting in poor core location and age determinations. Such considerations must clearly be taken into account if one wishes to use shower size estimates to imply something about energy spectra of primary particles.

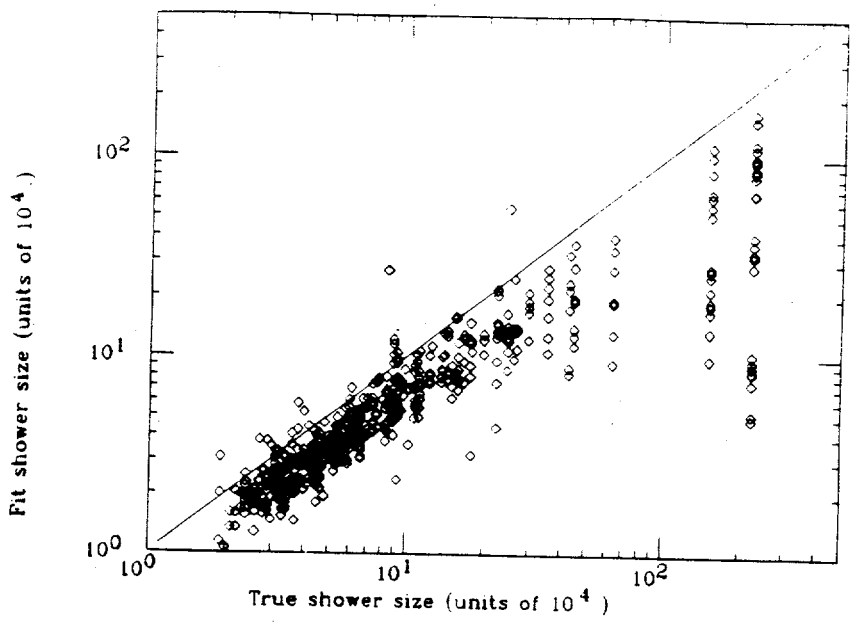

Figure B.1: Fit shower size using "separation" approach (in units of 10^4) versus true size (simulation). The solid line shows what is expected for a one-to-one correlation. The observed systematic shift is primarily due to a ~20 MeV threshold for through-going particles associated with the scintillator.

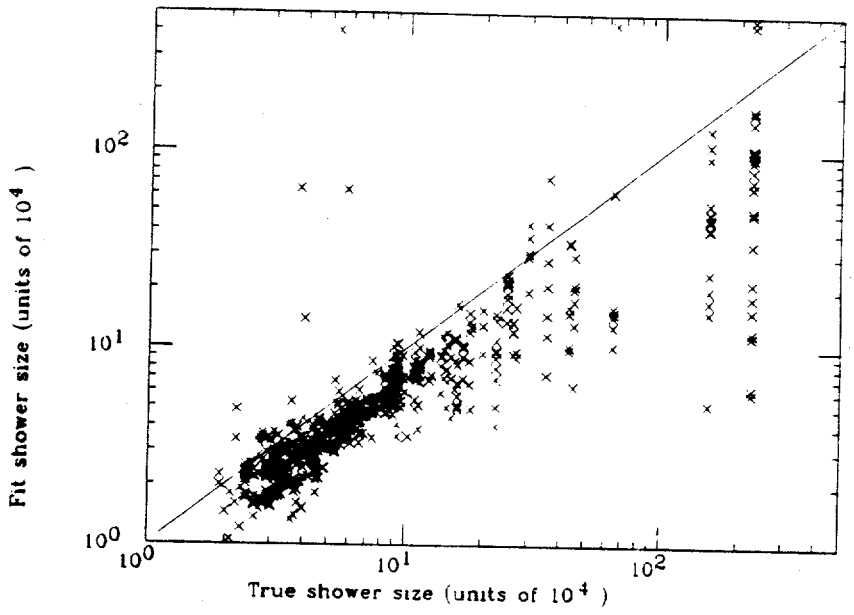

Figure B.2: Fit shower size using 4-parameter minimization (Levenberg-Marquardt) versus true size (simulation).

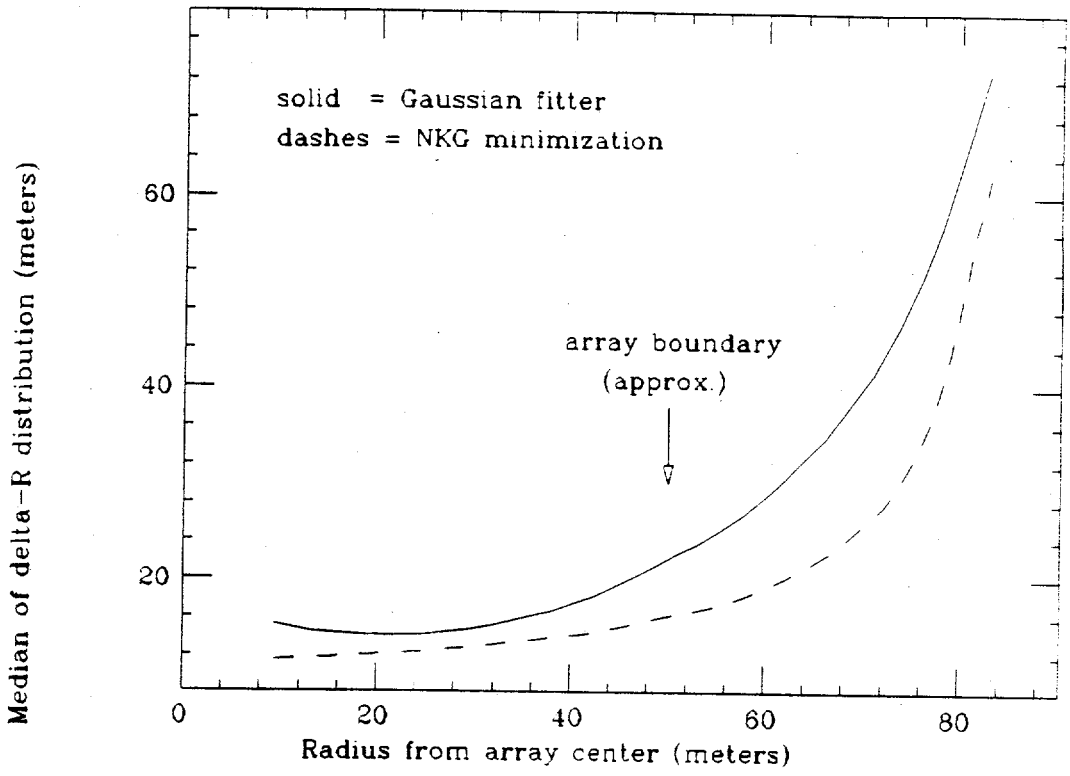

Figure B.3: Median core error (from simulation) versus radius from the geometric center of the array (run 171 array/triggering configuration). The solid line is obtained from a simple ~Gaussian fit, and the dashed line is obtained from a 4-parameter minimization of the NKG formula.

Appendix C

Testing the Distribution of Probabilities

"If this is coffee, please bring me some tea;
but if this is tea, please bring me some coffee."
- Abraham Lincoln -

Given a distribution of calculated chance probabilities, a general question of interest is what procedure should be used in deciding between $H0$ and $H1$ hypotheses. An approach that has typically been used involves simply considering the single most significant episode relative to the total number of entries in the probability distribution (e.g. the probability for the most significant daily excess). However, this method is not sensitive to lower-level emission that may be exhibited by a number of episodes, thus distorting the probability distribution above the tail. On the other hand, while a χ^2 test is sensitive to a distortion in the overall shape of the distribution, it is relatively insensitive to cases where the emission is only manifested in a small fraction of the episodes.

One alternative approach is as follows: Define P_1 to be the smallest chance probability of the distribution, P_2 to be the second smallest, and so on. Given the total number of episodes in the distribution, compute the binomial probabilities for 1 or more episodes to attain a chance probability of P_1 or smaller, 2 or more to attain P_2 or smaller, 3 or more to attain P_3 or smaller...etc. Then choose the most significant of these probabilities and use a Monte Carlo calculation to account for the trial factor associated with this choice. An approximate parameterization for

the trial factor is given below:

$$
\begin{aligned}
Factor &= \alpha + \beta(1 - e^{-\gamma(-log_{10}(P))^{1.4}}) \\
&\textit{where} \\
\alpha &= 0.57 + 2.7 log_{10}(N) \\
\beta &= 1.3N^{0.77} - 2.2 \\
\gamma &= \frac{1}{\sqrt{N}}
\end{aligned}
$$

where P is the most significant binomial probability, and N is the number of episodes tested. This parameterization is valid in for the range $5 \leq N \leq 5000$, and $0.5 \leq -log_{10}(P) \leq 6$. For $N = 1000$, and $P = 10^{-4}$, the calculated factor is 60.

This factor, which can obviously become quite large, may be further reduced in certain cases. For example, there may be instances where it may not be physically meaningful to search through the entire distribution, or where deviations associated with a significant portion of the distribution have already been ruled out by other tests (such as a test for continuous emission). In such cases, the prescription would be to only search through a given fraction of the entire distribution (chosen *a priori*). As an example, the following is a parameterization for the trial factor associated with searching through the upper 10% of a probability distribution (*i.e.* the 10% comprising the smallest chance probabilities in the distribution):

$$
\begin{aligned}
Factor &= \alpha + \beta(1 - e^{-\gamma(-log_{10}(P))^{1.4}}) \\
&\textit{where} \\
\alpha &= 1.4 log_{10}(N) - 0.475 \\
\beta &= 0.15N^{0.77} - 0.88 \\
\gamma &= \frac{3.4}{\sqrt{N}}
\end{aligned}
$$

This parameterization is valid in for the range $50 \leq N \leq 5000$, and $0.5 \leq -log_{10}(P) \leq 6$. For $N = 1000$, and $P = 10^{-4}$, this factor is 19. This factor still lowers the sensitivity compared to the approach of only testing the most significant episode if, indeed, the hypothesis of a single "hot" episode is correct. Therefore, one may wish to perform both tests, choose the most significant result, and pay an additional statistical penalty of 2 for the choice.

A similar approach that has been employed by the Whipple collaboration to test distributions of Rayleigh powers [69] differs only in the specific choice of the test statistic. The statistic used in the Whipple analysis was that of the Fisher test [68]. The specific application involved first choosing a Rayleigh power threshold (RP_{TH}). Then, for each interval corresponding to a Rayleigh power (RP) above this threshold, the probability of achieving the observed power or greater relative to this threshold is calculated. This is just $\frac{P(RP)}{P(RP_{TH})}$, where P is the probability of attaining a power at least as large as RP, *given the total number of intervals searched.* Next, the product of these probabilities is computed, and the chance probability to obtain this product is taken from the statistic $-2log(\sum_i^n \frac{P_i(RP)}{P(RP_{TH})})$, which is distributed like a χ^2 distribution with $2n$ degrees of freedom. Finally, a Monte Carlo calculation was used to determine the trial factor to be assessed for choosing the Rayleigh power threshold that optimizes the significance of the test. This approach tends to be less sensitive to emission scenarios that would result in a cluster of similar burst probabilities (or, in this case, Rayleigh powers), than the approach previously described.

As an example, consider the case where 500 intervals are examined, with two intervals attaining Rayleigh powers of 9 (RP_1) and 10 (RP_2) respectively. Assume that the rest of the distribution behaves exactly as expected, and that no oversampling or period search was performed. The Fisher approach would optimize at a Rayleigh power threshold of 6.2 (corresponding to a probability of $\sim \frac{1}{500}$), and result in a pre-trial (for the threshold optimization) probability of 2.3%. The binomial approach would optimize at a power threshold of 9, and would yield a pre-trial probability of 0.18%. The trial factors for threshold optimization in both tests are comparable. Under this current scenario, the Fisher test would be more sensitive

only when RP_1 is greater than 10, and $RP_2 - RP_1 > 5$, at which point the gain is irrelevant since $H0$ can easily be rejected by either test. Therefore, the binomial test appears to be a better general approach.

Appendix D

Protheroe and Rayleigh Statistics

"The data did not indicate the presence of a signal; so we had to apply statistics."
- Anonymous -

Critical Values of the Protheroe Statistic

The Protheroe statistic [65], used to test for phase-alignment, is defined as:

$$\Upsilon_N = \frac{2}{N(N-1)} \sum_{j=i+1}^{N} \sum_{i=1}^{N-1} \frac{1}{\Delta_{ij} + \frac{1}{N}} \tag{D.1}$$

where

$$\begin{aligned} \Delta_{ij} &= 0.5 - ||\phi_i - \phi_j| - 0.5| \\ N &= \text{number of events} \\ \phi_i &= \text{phase of } i_{th} \text{ event} \end{aligned}$$

The probability distribution for Υ_N cannot be characterized by a simple, closed-form expression due to the fact that the Δ_{ij} terms are not independent. However, the probability distribution of Υ_N can be obtained by Monte Carlo calculation. Such a calculation has been used to extend the previously published table of "critical" Υ_N values to chance probability levels as low as 10^{-7}, for $2 \leq N \leq 200$. This

calculation was based on 10^6 randomly distributed trial phase distributions for each value of N, and a process of data smoothing and extrapolation was then employed to obtain the critical values corresponding to probability levels of 10^{-7}. The resulting extended table is given in the following pages.

Table D.1: Critical Values of the Protheroe Statistic

N	Probability Level								
	0.95	0.75	0.50	0.25	0.10	0.075	0.05	0.025	0.01
2	1.02	1.14	1.33	1.60	1.82	1.86	1.90	1.95	1.98
3	1.51	1.60	1.77	1.98	2.24	2.32	2.41	2.55	2.69
4	1.86	1.99	2.12	2.34	2.60	2.67	2.78	2.94	3.14
5	2.16	2.29	2.43	2.64	2.90	2.98	3.09	3.26	3.48
6	2.43	2.56	2.70	2.91	3.17	3.24	3.35	3.53	3.76
7	2.66	2.80	2.94	3.15	3.40	3.48	3.58	3.77	4.00
8	2.87	3.01	3.15	3.36	3.61	3.68	3.79	3.98	4.21
9	3.06	3.20	3.34	3.55	3.79	3.87	3.98	4.16	4.39
10	3.24	3.38	3.52	3.72	3.97	4.04	4.15	4.32	4.55
11	3.40	3.54	3.68	3.88	4.12	4.20	4.30	4.47	4.71
12	3.54	3.69	3.83	4.03	4.27	4.34	4.44	4.61	4.84
13	3.68	3.83	3.97	4.17	4.40	4.47	4.57	4.74	4.97
14	3.81	3.96	4.10	4.30	4.53	4.60	4.69	4.86	5.08
15	3.94	4.08	4.22	4.42	4.64	4.71	4.81	4.97	5.19
17	4.16	4.31	4.45	4.64	4.86	4.93	5.02	5.18	5.39
20	4.46	4.61	4.75	4.93	5.14	5.21	5.30	5.45	5.65
22	4.64	4.78	4.92	5.10	5.31	5.37	5.46	5.61	5.80
25	4.88	5.02	5.16	5.34	5.54	5.60	5.68	5.82	6.01
27	5.03	5.17	5.30	5.48	5.67	5.73	5.81	5.95	6.13
30	5.23	5.37	5.50	5.67	5.86	5.92	6.00	6.13	6.30
32	5.35	5.50	5.63	5.79	5.98	6.03	6.11	6.24	6.41
35	5.53	5.67	5.80	5.96	6.14	6.19	6.27	6.39	6.56
40	5.79	5.93	6.05	6.21	6.38	6.43	6.50	6.62	6.78
45	6.02	6.16	6.28	6.43	6.60	6.65	6.71	6.83	6.97
50	6.23	6.37	6.48	6.63	6.79	6.84	6.90	7.01	7.15
55	6.42	6.55	6.67	6.81	6.97	7.01	7.07	7.18	7.31
60	6.60	6.73	6.84	6.98	7.13	7.17	7.23	7.33	7.46
65	6.76	6.89	7.00	7.13	7.28	7.32	7.38	7.47	7.59
70	6.91	7.03	7.14	7.27	7.41	7.45	7.51	7.60	7.72
75	7.05	7.17	7.28	7.40	7.54	7.58	7.64	7.73	7.84
80	7.18	7.30	7.40	7.53	7.66	7.70	7.75	7.84	7.95
85	7.30	7.42	7.52	7.65	7.78	7.81	7.86	7.95	8.06
90	7.42	7.53	7.64	7.76	7.88	7.92	7.97	8.05	8.16
95	7.53	7.64	7.74	7.86	7.98	8.02	8.07	8.15	8.25
100	7.63	7.75	7.84	7.96	8.08	8.12	8.16	8.24	8.34
110	7.82	7.94	8.03	8.14	8.26	8.29	8.34	8.41	8.51
120	8.00	8.11	8.20	8.31	8.42	8.45	8.50	8.57	8.66
130	8.16	8.27	8.36	8.47	8.57	8.60	8.65	8.72	8.80
140	8.31	8.42	8.51	8.61	8.72	8.74	8.78	8.85	8.93
150	8.46	8.56	8.65	8.74	8.85	8.87	8.91	8.98	9.06
160	8.59	8.69	8.77	8.87	8.97	9.00	9.03	9.10	9.17
170	8.71	8.81	8.89	8.99	9.08	9.11	9.15	9.21	9.28
180	8.83	8.93	9.01	9.10	9.19	9.22	9.25	9.31	9.38
190	8.94	9.04	9.12	9.20	9.30	9.32	9.35	9.41	9.48
200	9.05	9.14	9.22	9.30	9.39	9.42	9.45	9.51	9.57

N	Probability Level								
	7.5E-03	5E-03	2.5E-03	1E-03	7.5E-04	5E-04	2.5E-04	1E-04	7.5E-05
2	1.98	1.99	1.99	2.00					
3	2.73	2.77	2.83	2.89	2.91	2.92	2.95		
4	3.19	3.27	3.39	3.52	3.56	3.60	3.68	3.75	3.77
5	3.54	3.63	3.78	3.95	4.00	4.08	4.19	4.31	4.34
6	3.83	3.92	4.08	4.29	4.35	4.43	4.57	4.72	4.76
7	4.07	4.17	4.33	4.54	4.60	4.69	4.83	5.07	5.11
8	4.28	4.38	4.54	4.75	4.82	4.92	5.08	5.32	5.37
9	4.46	4.56	4.72	4.94	5.01	5.12	5.28	5.49	5.55
10	4.62	4.72	4.89	5.11	5.18	5.28	5.43	5.65	5.72
11	4.78	4.88	5.04	5.26	5.33	5.43	5.58	5.80	5.87
12	4.91	5.01	5.17	5.39	5.46	5.55	5.71	5.95	6.01
13	5.04	5.13	5.30	5.51	5.57	5.66	5.84	6.06	6.13
14	5.15	5.25	5.41	5.63	5.70	5.79	5.95	6.20	6.27
15	5.26	5.35	5.52	5.73	5.80	5.90	6.04	6.27	6.34
17	5.46	5.55	5.71	5.93	6.00	6.09	6.25	6.42	6.49
20	5.71	5.80	5.96	6.16	6.22	6.31	6.47	6.68	6.74
22	5.86	5.95	6.10	6.30	6.36	6.45	6.59	6.82	6.87
25	6.07	6.15	6.29	6.48	6.54	6.62	6.75	6.95	7.00
27	6.19	6.27	6.41	6.59	6.65	6.73	6.87	7.04	7.09
30	6.36	6.43	6.56	6.74	6.79	6.87	6.99	7.17	7.22
32	6.46	6.53	6.66	6.83	6.89	6.96	7.08	7.27	7.33
35	6.61	6.68	6.80	6.96	7.02	7.09	7.20	7.39	7.44
40	6.82	6.89	7.01	7.15	7.20	7.27	7.38	7.57	7.62
45	7.02	7.08	7.19	7.34	7.39	7.45	7.56	7.73	7.77
50	7.19	7.25	7.36	7.50	7.54	7.61	7.70	7.87	7.92
55	7.35	7.41	7.51	7.64	7.69	7.75	7.85	8.00	8.04
60	7.50	7.55	7.65	7.77	7.81	7.87	7.97	8.10	8.14
65	7.63	7.68	7.78	7.90	7.94	8.00	8.09	8.22	8.25
70	7.76	7.81	7.90	8.01	8.04	8.10	8.20	8.32	8.36
75	7.87	7.92	8.01	8.12	8.15	8.20	8.29	8.40	8.44
80	7.99	8.04	8.12	8.22	8.26	8.30	8.38	8.48	8.52
85	8.09	8.14	8.22	8.32	8.35	8.39	8.47	8.56	8.60
90	8.19	8.23	8.31	8.41	8.44	8.48	8.56	8.64	8.67
95	8.28	8.33	8.40	8.50	8.52	8.56	8.63	8.72	8.75
100	8.37	8.41	8.49	8.58	8.61	8.65	8.71	8.80	8.83
110	8.54	8.58	8.64	8.73	8.76	8.80	8.87	8.94	8.97
120	8.69	8.73	8.79	8.87	8.90	8.93	9.00	9.07	9.10
130	8.83	8.86	8.93	9.01	9.04	9.07	9.13	9.20	9.23
140	8.96	9.00	9.05	9.13	9.15	9.18	9.24	9.32	9.34
150	9.08	9.11	9.17	9.24	9.26	9.30	9.35	9.39	9.41
160	9.20	9.23	9.28	9.35	9.37	9.41	9.46	9.49	9.51
170	9.30	9.33	9.39	9.45	9.47	9.50	9.55	9.62	9.64
180	9.41	9.44	9.49	9.55	9.57	9.60	9.65	9.70	9.72
190	9.50	9.53	9.58	9.64	9.66	9.69	9.74	9.76	9.78
200	9.60	9.62	9.67	9.73	9.75	9.78	9.82	9.86	9.88

N	Probability Level								
	5E-05	2.5E-05	1E-05	7.5E-06	5E-06	2E-06	1E-06	5E-07	1E-07
2									
3									
4	3.81	3.87	3.96	3.99	4.00				
5	4.39	4.48	4.59	4.63	4.67	4.74	4.87	4.95	5.00
6	4.82	4.93	5.06	5.11	5.16	5.24	5.40	5.50	5.74
7	5.18	5.30	5.45	5.51	5.57	5.65	5.83	5.95	6.21
8	5.45	5.58	5.75	5.81	5.87	5.97	6.17	6.30	6.59
9	5.64	5.79	5.98	6.06	6.13	6.24	6.48	6.63	6.97
10	5.81	5.97	6.18	6.26	6.34	6.45	6.70	6.86	7.23
11	5.96	6.13	6.34	6.42	6.50	6.62	6.88	7.04	7.42
12	6.11	6.28	6.51	6.59	6.68	6.80	7.07	7.24	7.63
13	6.23	6.40	6.63	6.72	6.80	6.93	7.20	7.37	7.77
14	6.37	6.53	6.76	6.84	6.92	7.05	7.31	7.48	7.87
15	6.44	6.61	6.83	6.92	7.00	7.13	7.39	7.56	7.95
17	6.59	6.75	6.97	7.05	7.14	7.26	7.52	7.69	8.07
20	6.83	6.97	7.16	7.23	7.30	7.41	7.64	7.78	8.11
22	6.95	7.08	7.26	7.32	7.39	7.48	7.69	7.82	8.13
25	7.08	7.22	7.40	7.46	7.53	7.63	7.85	7.98	8.29
27	7.18	7.31	7.49	7.56	7.63	7.73	7.94	8.08	8.40
30	7.30	7.44	7.62	7.68	7.75	7.85	8.06	8.20	8.51
32	7.40	7.53	7.70	7.76	7.82	7.92	8.12	8.25	8.54
35	7.51	7.63	7.80	7.86	7.92	8.01	8.21	8.33	8.62
40	7.69	7.80	7.96	8.01	8.07	8.15	8.34	8.45	8.72
45	7.84	7.95	8.09	8.15	8.20	8.28	8.45	8.56	8.81
50	7.98	8.08	8.21	8.26	8.31	8.39	8.55	8.65	8.89
55	8.09	8.19	8.32	8.37	8.42	8.49	8.64	8.74	8.97
60	8.19	8.29	8.42	8.46	8.51	8.58	8.73	8.83	9.05
65	8.31	8.39	8.51	8.56	8.60	8.67	8.81	8.89	9.10
70	8.41	8.49	8.61	8.65	8.70	8.76	8.90	8.99	9.19
75	8.49	8.57	8.68	8.73	8.77	8.83	8.97	9.05	9.25
80	8.57	8.65	8.76	8.80	8.84	8.90	9.04	9.12	9.31
85	8.64	8.72	8.83	8.87	8.91	8.97	9.10	9.18	9.37
90	8.72	8.80	8.90	8.94	8.98	9.04	9.17	9.25	9.44
95	8.80	8.87	8.97	9.01	9.05	9.10	9.22	9.30	9.47
100	8.88	8.95	9.05	9.09	9.12	9.18	9.30	9.37	9.54
110	9.01	9.08	9.17	9.21	9.24	9.29	9.40	9.47	9.63
120	9.14	9.20	9.29	9.32	9.36	9.40	9.51	9.58	9.73
130	9.26	9.33	9.41	9.44	9.47	9.52	9.62	9.68	9.83
140	9.38	9.43	9.51	9.54	9.57	9.61	9.70	9.76	9.89
150	9.44	9.50	9.57	9.60	9.62	9.66	9.75	9.80	9.93
160	9.54	9.60	9.67	9.70	9.72	9.76	9.85	9.90	10.03
170	9.67	9.72	9.79	9.81	9.84	9.88	9.96	10.01	10.13
180	9.75	9.80	9.86	9.88	9.91	9.94	10.02	10.07	10.18
190	9.81	9.85	9.91	9.93	9.96	9.99	10.06	10.10	10.21
200	9.91	9.95	10.01	10.03	10.06	10.09	10.16	10.21	10.31

Critical Values of the Rayleigh Power

The Rayleigh "Power", R_p, is defined relative to the Rayleigh statistic, $\bar{R}$, as follows [80]:

$$R_p = N\bar{R}^2 = \bar{S}^2 + \bar{C}^2 \tag{D.2}$$

where

$$\begin{aligned} \bar{C} &= \frac{1}{N}\sum_i^N cos(2\pi\phi_i) \\ \bar{S} &= \frac{1}{N}\sum_i^N sin(2\pi\phi_i) \\ N &= \text{number of events} \\ \phi_i &= \text{phase of } i_{th} \text{ event} \end{aligned}$$

For large values of N (~ 100), and assuming a flat light curve for the null hypothesis, the chance probability to exceed a given Rayleigh power is approximately e^{-R_p}. For values of N as low as ~ 20, the following polynomial correction [81] can be applied to extend the reliable range of this approximation:

$$\begin{aligned} P_{R>R_p} = e^{-R_p}\Bigg[1 &+ \frac{1}{2N}\left(R_p - \frac{{R_p}^2}{2!}\right) + \\ &\frac{1}{12n^2}\left(-R_p + \frac{11{R_p}^2}{2!} - \frac{19{R_p}^3}{3!} + \frac{9{R_p}^4}{4!}\right) \\ &+ \frac{1}{24{R_p}^3}\left(-2R_p - \frac{4{R_p}^2}{2!} + \frac{69{R_p}^3}{3!} - \frac{163{R_p}^4}{4!} + \frac{145{R_p}^5}{5!} - \frac{45{R_p}^6}{6!}\right)\Bigg] \end{aligned} \tag{D.3}$$

For smaller values of N, a Monte Carlo calculation may be used to determine the significance of phase-alignment. The following pages give the critical values of the Rayleigh power, R_p, corresponding to various probability levels based on such a Monte Carlo approach. This calculation was based on 10^8 randomly distributed trial phase distributions for each value of N.

Table D.2: Critical Values of the Rayleigh Power

N	Probability Level								
	0.95	0.75	0.50	0.25	0.10	0.075	0.05	0.025	0.01
2	0.011	0.292	0.999	1.706	1.950	1.971	1.986	1.995	1.998
3	0.085	0.332	0.720	1.557	2.336	2.490	2.652	2.821	2.926
4	0.047	0.327	0.769	1.417	2.323	2.564	2.859	3.244	3.573
5	0.059	0.306	0.744	1.435	2.261	2.523	2.872	3.392	3.922
6	0.053	0.310	0.728	1.429	2.267	2.510	2.856	3.427	4.082
7	0.054	0.304	0.727	1.416	2.281	2.535	2.880	3.444	4.153
8	0.053	0.303	0.721	1.414	2.280	2.542	2.900	3.481	4.198
9	0.053	0.300	0.718	1.410	2.282	2.545	2.909	3.508	4.248
10	0.052	0.299	0.715	1.407	2.285	2.551	2.918	3.525	4.288
11	0.052	0.298	0.713	1.405	2.286	2.554	2.925	3.541	4.319
12	0.052	0.297	0.711	1.404	2.287	2.557	2.931	3.554	4.344
13	0.052	0.296	0.710	1.402	2.288	2.560	2.936	3.564	4.364
14	0.052	0.295	0.708	1.401	2.289	2.562	2.941	3.573	4.381
15	0.052	0.295	0.707	1.400	2.290	2.564	2.944	3.582	4.396
16	0.051	0.294	0.706	1.399	2.291	2.565	2.948	3.588	4.411
17	0.051	0.294	0.705	1.398	2.291	2.567	2.951	3.594	4.423
18	0.051	0.293	0.705	1.397	2.292	2.568	2.953	3.600	4.432
19	0.051	0.293	0.704	1.396	2.292	2.569	2.955	3.604	4.442
20	0.051	0.292	0.703	1.396	2.293	2.570	2.957	3.609	4.450
21	0.051	0.292	0.703	1.395	2.293	2.571	2.959	3.613	4.458
22	0.051	0.292	0.702	1.395	2.293	2.571	2.960	3.616	4.465
23	0.051	0.292	0.702	1.394	2.293	2.572	2.962	3.619	4.471
24	0.051	0.291	0.701	1.394	2.294	2.573	2.963	3.622	4.477
25	0.051	0.291	0.701	1.393	2.294	2.573	2.964	3.624	4.481
26	0.051	0.291	0.700	1.393	2.294	2.574	2.966	3.627	4.486
27	0.051	0.291	0.700	1.393	2.295	2.575	2.967	3.629	4.490
28	0.051	0.291	0.700	1.392	2.295	2.575	2.968	3.631	4.494
29	0.051	0.291	0.699	1.392	2.295	2.575	2.968	3.633	4.498
30	0.051	0.290	0.699	1.392	2.295	2.576	2.969	3.635	4.500
31	0.051	0.290	0.699	1.392	2.295	2.576	2.970	3.636	4.503
32	0.051	0.290	0.699	1.392	2.295	2.576	2.970	3.638	4.506
33	0.051	0.290	0.699	1.391	2.296	2.577	2.971	3.639	4.508
34	0.051	0.290	0.698	1.391	2.296	2.577	2.972	3.641	4.511
35	0.051	0.290	0.698	1.391	2.296	2.577	2.972	3.642	4.513
36	0.051	0.290	0.698	1.391	2.296	2.578	2.973	3.643	4.517
37	0.050	0.290	0.698	1.391	2.296	2.578	2.974	3.644	4.519
38	0.050	0.290	0.698	1.391	2.296	2.578	2.974	3.645	4.522
39	0.050	0.289	0.698	1.390	2.297	2.579	2.975	3.646	4.524
40	0.050	0.289	0.698	1.390	2.297	2.579	2.975	3.647	4.526

N	Probability Level								
	7.5E-03	5E-03	2.5E-03	1E-03	7.5E-04	5E-04	2.5E-04	1E-04	7.5E-05
2									
3	2.944	2.962	2.980	2.991	2.993	2.995	2.997	2.998	
4	3.645	3.726	3.825	3.903	3.919	3.937	3.959	3.976	3.979
5	4.054	4.214	4.432	4.631	4.678	4.734	4.807	4.869	4.884
6	4.259	4.486	4.816	5.151	5.236	5.341	5.485	5.618	5.649
7	4.359	4.631	5.047	5.498	5.618	5.771	5.990	6.207	6.257
8	4.415	4.711	5.181	5.725	5.872	6.068	6.356	6.653	6.728
9	4.469	4.772	5.269	5.869	6.040	6.270	6.610	6.967	7.057
10	4.517	4.829	5.341	5.972	6.157	6.407	6.794	7.213	7.319
11	4.553	4.876	5.407	6.057	6.250	6.512	6.923	7.375	7.492
12	4.583	4.913	5.457	6.131	6.333	6.606	7.035	7.516	7.641
13	4.607	4.944	5.498	6.193	6.398	6.674	7.116	7.616	7.739
14	4.629	4.970	5.536	6.247	6.461	6.750	7.206	7.723	7.858
15	4.646	4.991	5.567	6.291	6.509	6.804	7.270	7.790	7.927
16	4.662	5.013	5.596	6.332	6.555	6.859	7.341	7.895	8.040
17	4.676	5.029	5.618	6.365	6.587	6.893	7.380	7.932	8.076
18	4.688	5.044	5.641	6.393	6.619	6.928	7.418	7.974	8.116
19	4.699	5.058	5.660	6.419	6.650	6.963	7.463	8.030	8.170
20	4.710	5.071	5.675	6.443	6.676	6.996	7.504	8.074	8.223
21	4.718	5.080	5.691	6.470	6.702	7.023	7.536	8.133	8.286
22	4.727	5.092	5.704	6.487	6.724	7.046	7.565	8.147	8.298
23	4.734	5.101	5.716	6.504	6.740	7.067	7.597	8.185	8.338
24	4.740	5.108	5.727	6.521	6.759	7.083	7.607	8.207	8.361
25	4.746	5.115	5.737	6.534	6.776	7.105	7.632	8.231	8.389
26	4.752	5.123	5.746	6.544	6.789	7.124	7.667	8.278	8.433
27	4.756	5.130	5.755	6.558	6.800	7.137	7.672	8.288	8.453
28	4.761	5.135	5.764	6.569	6.816	7.150	7.696	8.320	8.481
29	4.766	5.139	5.770	6.580	6.826	7.164	7.709	8.330	8.497
30	4.770	5.144	5.777	6.591	6.837	7.179	7.728	8.357	8.524
31	4.772	5.148	5.783	6.597	6.846	7.184	7.726	8.333	8.493
32	4.776	5.153	5.791	6.608	6.855	7.197	7.745	8.368	8.528
33	4.778	5.155	5.794	6.617	6.866	7.210	7.762	8.381	8.545
34	4.782	5.160	5.801	6.626	6.880	7.229	7.790	8.436	8.604
35	4.785	5.165	5.804	6.631	6.884	7.234	7.797	8.433	8.600
36	4.788	5.169	5.811	6.636	6.891	7.240	7.802	8.437	8.599
37	4.791	5.172	5.815	6.647	6.899	7.252	7.814	8.464	8.631
38	4.795	5.176	5.821	6.653	6.905	7.259	7.817	8.458	8.631
39	4.797	5.179	5.825	6.657	6.913	7.267	7.830	8.455	8.614
40	4.799	5.182	5.830	6.665	6.921	7.272	7.838	8.477	8.642

N	Probability Level								
	5E-05	2.5E-05	1E-05	7.5E-06	5E-06	2.5E-06	1E-06	5E-07	1E-07
2									
3									
4	3.983	3.987	3.990	3.990	3.990	3.991	3.991	3.992	3.992
5	4.900	4.919	4.933	4.936	4.938	4.941	4.943	4.944	4.944
6	5.686	5.730	5.763	5.770	5.777	5.784	5.789	5.790	5.792
7	6.317	6.393	6.449	6.461	6.472	6.483	6.492	6.494	6.496
8	6.817	6.926	7.013	7.032	7.051	7.070	7.082	7.087	7.090
9	7.161	7.305	7.409	7.430	7.448	7.469	7.484	7.488	7.490
10	7.440	7.595	7.715	7.739	7.762	7.783	7.798	7.804	7.810
11	7.628	7.816	7.955	7.981	8.004	8.035	8.055	8.061	8.066
12	7.794	7.992	8.140	8.167	8.194	8.226	8.246	8.253	8.258
13	7.887	8.085	8.231	8.258	8.287	8.316	8.334	8.342	8.346
14	8.014	8.225	8.381	8.414	8.446	8.481	8.504	8.513	8.518
15	8.098	8.306	8.472	8.503	8.533	8.565	8.586	8.591	8.598
16	8.217	8.449	8.621	8.656	8.689	8.729	8.751	8.762	8.767
17	8.254	8.490	8.650	8.682	8.713	8.751	8.773	8.779	8.785
18	8.286	8.512	8.679	8.711	8.739	8.771	8.790	8.796	8.802
19	8.352	8.585	8.766	8.801	8.833	8.870	8.891	8.901	8.908
20	8.408	8.650	8.823	8.854	8.885	8.921	8.942	8.948	8.952
21	8.472	8.721	8.900	8.938	8.974	9.009	9.030	9.035	9.040
22	8.480	8.722	8.903	8.939	8.973	9.005	9.028	9.034	9.040
23	8.527	8.768	8.949	8.982	9.019	9.053	9.074	9.081	9.087
24	8.551	8.791	8.966	8.999	9.033	9.070	9.098	9.104	9.108
25	8.588	8.843	9.020	9.055	9.087	9.122	9.144	9.150	9.158
26	8.639	8.892	9.083	9.119	9.155	9.197	9.225	9.231	9.236
27	8.645	8.883	9.067	9.097	9.130	9.165	9.184	9.191	9.197
28	8.681	8.948	9.132	9.168	9.205	9.240	9.261	9.267	9.273
29	8.692	8.956	9.143	9.176	9.218	9.253	9.274	9.282	9.291
30	8.728	8.983	9.175	9.213	9.246	9.284	9.311	9.318	9.324
31	8.681	8.923	9.096	9.133	9.164	9.196	9.219	9.226	9.232
32	8.728	8.987	9.164	9.199	9.234	9.267	9.289	9.296	9.301
33	8.734	8.982	9.164	9.196	9.229	9.268	9.291	9.297	9.302
34	8.811	9.082	9.280	9.320	9.357	9.392	9.415	9.422	9.428
35	8.801	9.065	9.268	9.307	9.347	9.384	9.405	9.410	9.415
36	8.801	9.058	9.251	9.284	9.316	9.355	9.375	9.384	9.389
37	8.845	9.105	9.303	9.338	9.372	9.412	9.442	9.453	9.459
38	8.833	9.080	9.266	9.305	9.341	9.377	9.402	9.407	9.413
39	8.822	9.079	9.274	9.309	9.346	9.381	9.406	9.412	9.416
40	8.841	9.101	9.289	9.325	9.363	9.401	9.426	9.432	9.438

Appendix E

Parameterizations for Showerfront Curvature and Timing Widths

"Scales and clocks are not to be trusted
to decide anything that's worth deciding."
- Finley Peter Dunne -

Introduction

During the development of an extensive air-shower, the effects of multiple scattering at larger radii from the core result in an increasing width and overall curvature of the showerfront. Since each scintillation counter is used to record only the earliest measured arrival time, detector sampling effects in regions of low particle density tend to enhance the apparent radial dependence of these showerfront properties. Measurements of the effective showerfront width and curvature are also influenced by the nature of the electronic response, such as time slewing for low pulse-heights due to the risetime of the PMT pulse. These effects therefore lead to an effective showerfront curvature and thickness.

The effective curvature is currently parameterized in the CYGNUS event reconstruction procedure by the conical form [59] :

$$\delta T = \frac{\alpha R}{\sqrt{N}} \qquad \text{(E.1)}$$

where δT is the relative, curvature-induced delay time with respect to a plane normal to the shower direction; R is the radius from the shower core; N is the measured pulse height in terms of an equivalent number of minimum-ionizing particles; and α is an empirically-determined constant. The best fit values of α have been found to be $0.2\frac{ns}{m}$ for detectors in the original CYG I configuration, and $0.15\frac{ns}{m}$ for those same detectors when covered by $\sim$1 radiation length of lead (used to increase detection efficiency by pair-converting photons associated with the air-shower).

The showerfront width has typically not been directly used in associating a relative weight to various measurements when fitting the shower direction, but instead the following *ad hoc* weighting scheme was applied [59] :

$$\text{Weight} = \begin{cases} 0 & \text{if } N < 1 \\ \frac{N-0.5}{4.5} & \text{if } 1 < N < 5 \\ 1 & \text{if } N > 5 \end{cases} \qquad \text{(E.2)}$$

where, once again, N is the measured pulse height in terms of an equivalent number of minimum-ionizing particles. The exclusion of measurements involving pulse heights below 1 particle tends to reduce the effects of slewing. In addition to this, measurements with arrival times that deviate by more that 8 nanoseconds from an initial fit to the showerfront are eliminated when the final fit is performed.

Based on an detailed examination of the timing residuals from showerfront fits, a new weighting scheme based on a parameterization for the effective showerfront thickness and an improved form for the curvature has been derived.

Showerfront Curvature

The parameterization of showerfront curvature has been separated into two parts: the first depends only on pulse height and is believed to be primarily due to electronic slewing; the second depends on both pulse height and radius from the shower core and is believed to be primarily due to sampling and "true" curvature of the showerfront. The parameterizations are as follows:

Detectors	"Slewing" Correction (ns)	"Sampling" Correction (ns)
CYG I without lead	$\frac{2.2}{\sqrt{N}} + 1.8e^{-0.05N}$	$0.12R_m N^{-0.25}$
CYG I with lead	$\frac{2.2}{\sqrt{N}} + 1.8e^{-0.05N}$	$0.10R_m N^{-0.28}$
CYG II with lead	$\frac{2.2}{\sqrt{N}} + 2.4e^{-0.05N}$	$0.10R_m N^{-0.28}$
SIMULATION (CYG I without lead)	0	$0.15R_m N^{-0.32}$

Table E.1: Parameterization of showerfront curvature correction.

where N is the pulse height in terms of particle number, and R_m is the radius from the shower core in meters. To apply the appropriate timing correction, both terms should be subtracted from the measured arrival time in each detector. Since these are relative time corrections, they are arbitrary to within an additive constant. These formulas are shown graphically in figures E.1-E.4. Figure E.1 compares the CYG I, no-lead configuration with simulation results. Figures E.2-E.4 compare old and new parameterizations for each of the 3 configurations described above.

The fact that the first term of the correction does not change for the CYG I data when lead is added, and that this term can be set to zero for the simulated data set, is consistent with the interpretation that this represents the effect of the electronic slewing.

Showerfront Thickness

Similarly, the parameterization of showerfront thickness has been separated into radius-dependent and radius-independent parts. The former accounts for the increasing thickness of the showerfront with increasing distance from the core, and the latter represents some intrinsic minimum width that is partially dependent on scintillator-PMT and showerfront sampling. The showerfront thickness is represented in terms of σ, which has been defined according to the span of timing residuals that account for 68% of the measurements, centered on the median of the distribution. The parameterizations for σ are as follows:

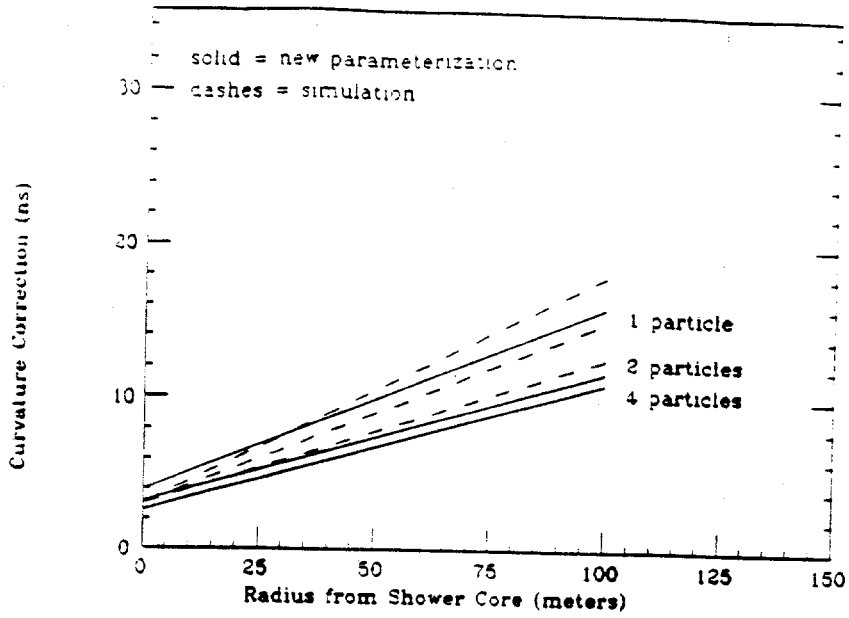

Figure E.1: Curvature correction (ns) versus radius from the shower core (m) for 1, 2, and 4 detected particles. Solid lines are based on a fit to the data, dashed lines are from simulation. The detector configuration is CYG I, without lead.

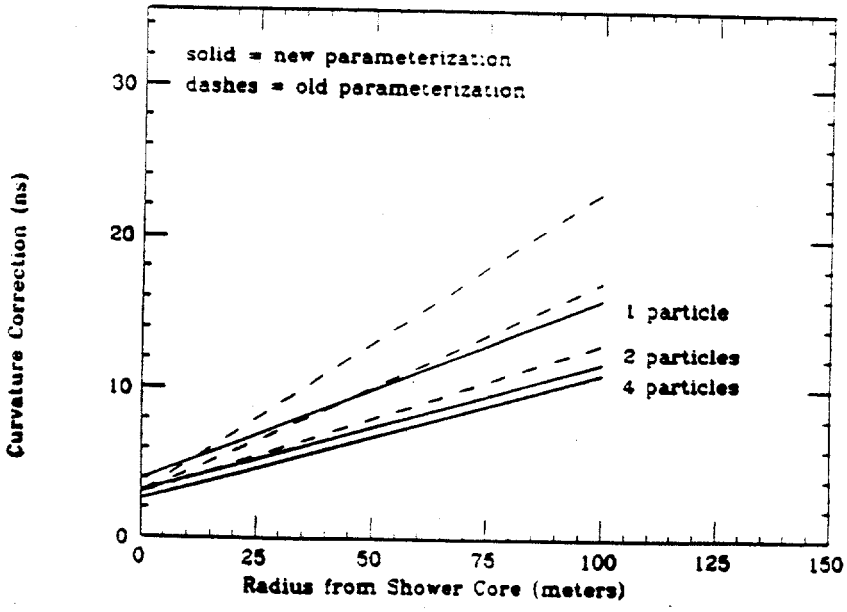

Figure E.2: Old and New curvature correction (ns) versus radius from the shower core (m) for 1, 2, and 4 detected particles. Solid lines show the new parameterization, dashed lines show the old parameterization. The detector configuration is CYG I, without lead.

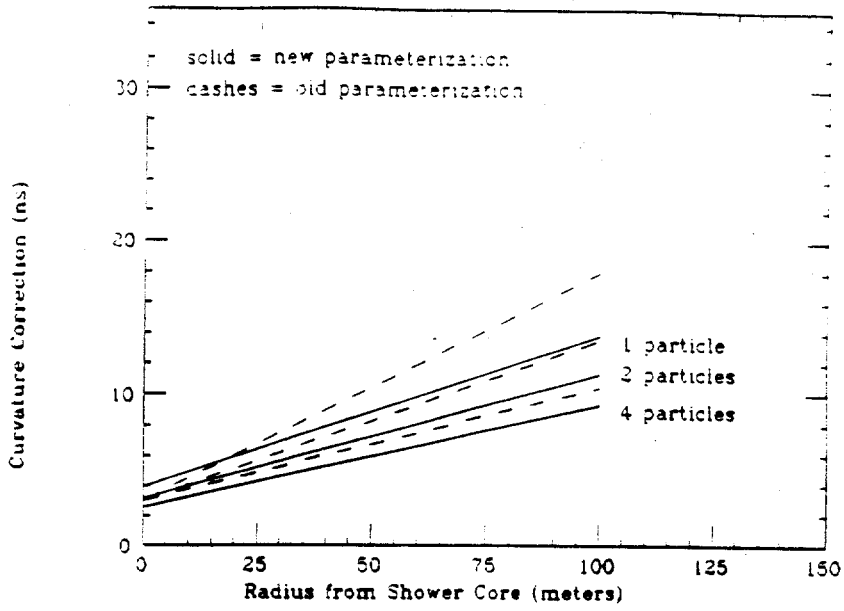

Figure E.3: Old and new curvature correction (ns) for CYG I lead-covered counters versus radius from the shower core (m) for 1, 2, and 4 detected particles. Solid lines show the new parameterization, dashed lines show the old parameterization.

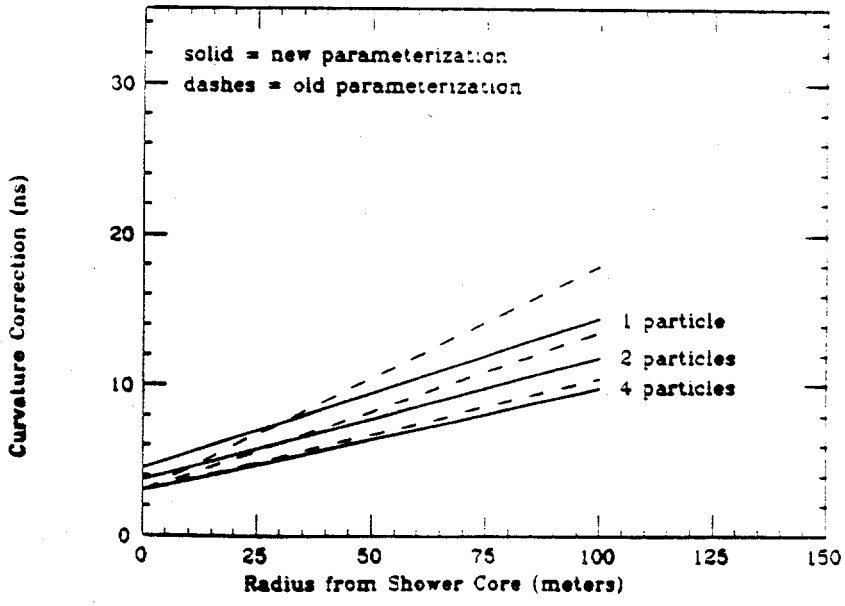

Figure E.4: Old and new curvature correction (ns) for CYG II lead-covered counters versus radius from the shower core (m) for 1, 2, and 4 detected particles. Solid lines show the new parameterization, dashed lines show the old parameterization.

Detectors	Radius-Independent Term (ns)	Radius-Dependent Term (ns)
CYG I without lead	$0.95 + 2.3e^{-0.62N}$	$(0.0064 + \frac{0.022}{\sqrt{N}})R_m$
CYG I with lead	$0.54 + 2.64e^{-0.75N}$	$(0.016 + \frac{0.013}{\sqrt{N}})R_m$
CYG II with lead	$0.89 + 5.5e^{-0.81N}$	$0.018R_m$
SIMULATION (CYG I without lead)	$0.80 + 2.8e^{-0.70N}$	$(0.0083 + \frac{0.024}{\sqrt{N}})R_m$

Table E.2: Parameterization of showerfront thickness.

The addition of both terms gives σ of the showerfront measurement in nanoseconds.

Figure E.5 compares the CYG I, no-lead configuration with simulation results. Figure E.6 compares results involving lead conversion-sheets for CYG I and CYG II counters.

A slight change in the parameterization of σ is expected between CYG I data with lead versus CYG I data without lead owing to the sampling of different fractions of the electron and photon showerfront. An increased intrinsic width of the distribution of timing residuals for CYG II data is expected due to the slower response-time of scintillator in that array. The fact that the second term no longer appears to depend noticibly on the measured pulse height may be due to the greater uncertainty in core location for CYG II events, making it more difficult to discern the nature of the radial dependence. This argument would not effect the curvature analysis as much since the radial dependence in that case is greater, and is therefore easier to discriminate.

Potential Effect on Angular Resolution

Based on the results previously presented, the following alteration to shower fitting procedures is proposed: **1)** Apply the new forms of the showerfront curvature correction to the appropriate cases; **2)** Apply a $\frac{1}{\sigma^2}$ weighting scheme to the timing-fit procedure, where σ is as previously defined; **3)** Throw out "bad" timing hits from

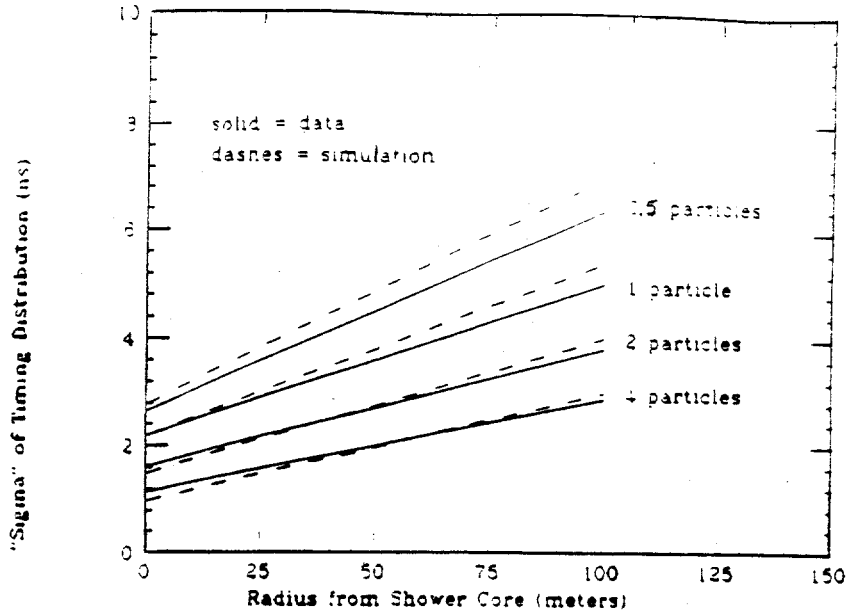

Figure E.5: Showerfront thickness (ns) versus radius from the shower core (m) for 0.5, 1, 2, and 4 effective minimum-ionizing particles. Solid lines are based on a fit to the data, dashed lines are from simulation. The detector configuration is CYG I, without lead.

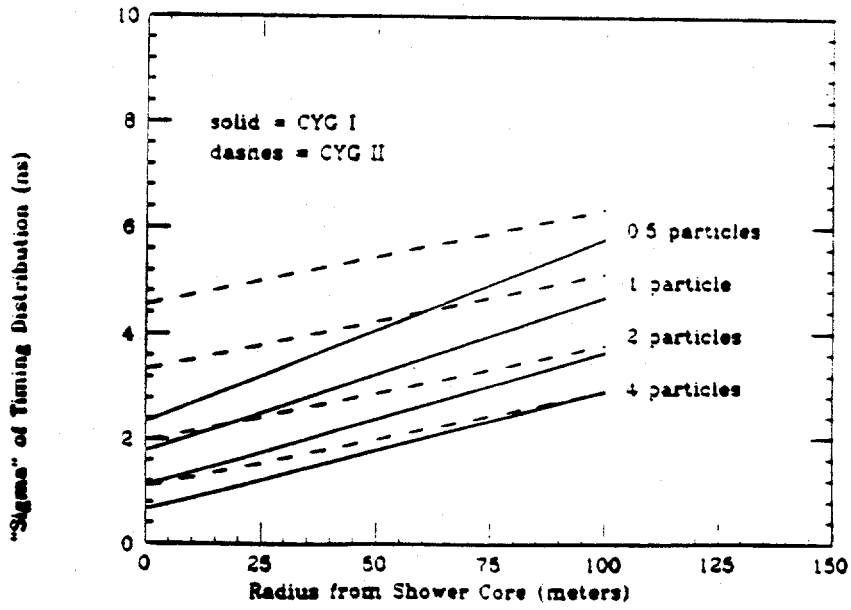

Figure E.6: Showerfront thickness (ns) for lead-covered counters versus radius from the shower core (m) for 0.5, 1, 2, and 4 effective minimum-ionizing particles. Solid lines are based on a fit to the CYG I data, dashed lines are from CYG II.

the fit if they deviate from zero by more than 3 standard deviations or ~10 nanoseconds, whichever is smaller, in order to remove the extreme non-Gaussian tails of the distributions; **4)** Since these new parameterizations have been based on data with pulse heights as low as 0.5 particles, counters with pulse heights this small should be included in showerfront fits.

This procedure has been applied to a set of 510 simulated proton showers interacting with a 64 counter, non-leaded array (old configuration). Figure E.7 compares the distribution of space-angle differences from the true direction for fits involving old and new algorithms. These studies indicate a ~15% improvement in the angular resolution, based on the decreased value of the distribution median when the new algorithm is applied. Since the current trigger conditions of the CYGNUS detector allow showers that involve a larger percentage of low pulse-height measurements, the new algorithm may result in a greater relative improvement for this data since the improvement in parameterizations are enhanced at low pulse heights.

These results regarding angular resolution are preliminary, pending a reanalysis of the cosmic-ray shadow of the sun and moon [70] using shower directions reconstructed according to this alternate approach. Therefore, for the purposes of this thesis, the new parameterizations are not used for angular reconstruction. They will, however, be employed to investigate showerfront properties associated with specific events of interest.

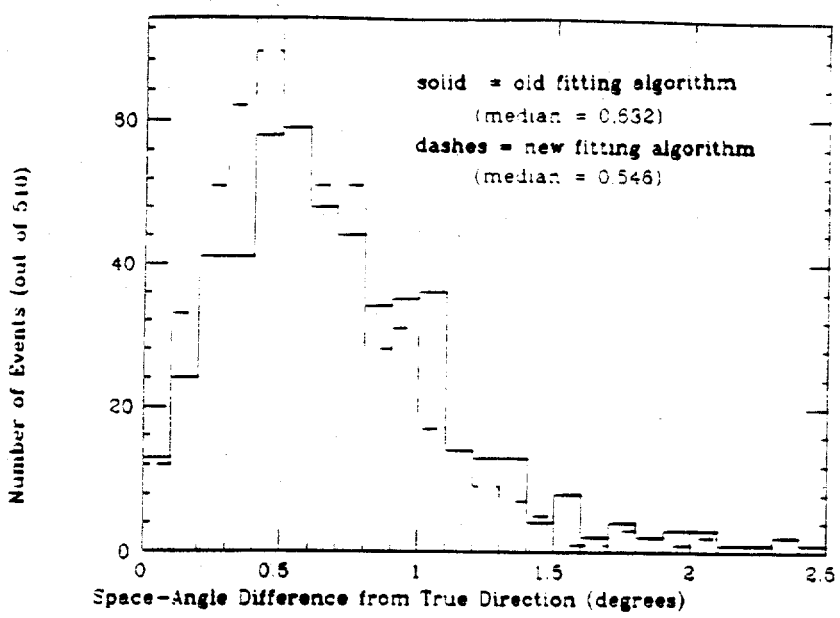

Figure E.7: Histogram of simulated space-angle differences between the fit and true shower directions using the old (solid) and new (dashes) algorithms. The distribution medians for the old and new algorithms are 0.63 and 0.55 degrees, respectively.

Appendix F

Details of CYGNUS Array Configurations/Modifications

"The real question for 1988 is
whether we're going to go forward
to tomorrow or past to ... the back!"
- Dan Quayle -

Table F.1: Relative Detector Locations as of 1992

Counter	X (ft)	Y (ft)	Z (ft)	Counter	X (ft)	Y (ft)	Z (ft)
CYGNUS I							
1	161.0	92.1	-0.6	2	-11.9	-6.4	55.9
3	14.4	-31.2	54.9	4	-7.3	-61.7	-6.8
5	-11.8	-26.4	55.1	6	14.9	16.8	55.5
7	38.1	-0.3	22.5	8	38.2	-18.5	22.5
9	41.7	-46.2	-0.3	10	206.4	52.5	-0.6
11	-17.0	-91.5	-6.7	12	-42.3	-54.2	8.9
13	-42.5	-31.5	54.9	14	-43.1	-11.5	55.8
15	-11.9	16.6	55.5	16	-12.0	31.5	55.0
17	77.7	-11.2	13.7	18	23.2	-97.8	-6.8
19	-63.5	-31.4	55.0	20	70.2	39.3	-0.1
21	75.4	-56.9	-4.5	22	-61.8	-67.0	8.1
23	-63.8	16.4	55.5	24	38.0	18.4	22.5
25	101.7	9.1	5.2	26	2.2	-117.5	-9.0
27	-84.3	-31.8	55.0	28	36.8	57.1	0.5
29	42.1	-109.2	-7.3	30	-30.5	-105.9	9.1
31	-46.8	58.5	45.0	32	121.7	38.2	-0.8

Counter	X (ft)	Y (ft)	Z (ft)	Counter	X (ft)	Y (ft)	Z (ft)
33	97.8	-75.0	-4.4	34	-104.6	-77.2	-3.6
35	-115.8	16.2	55.6	36	-0.3	100.4	6.3
37	77.5	51.4	-0.1	38	122.8	-27.2	9.5
39	77.0	-101.8	-6.2	40	22.5	-151.1	-16.7
41	-19.6	-150.3	-8.8	42	-82.3	-106.0	9.1
43	-115.6	-31.8	55.0	44	-88.1	53.4	45.8
45	-28.2	97.8	38.5	46	27.9	-73.7	-6.8
47	121.6	58.3	-0.4	48	167.5	22.2	-2.2
49	150.1	-68.6	-4.6	50	116.8	-106.4	-3.5
51	62.4	-151.3	-10.3	52	-52.8	-151.0	-7.7
53	-123.7	-112.2	-2.6	54	-170.2	-27.2	55.2
55	-147.7	16.2	55.5	56	-134.9	58.1	45.0
57	-66.5	97.8	38.4	58	-111.4	97.4	38.4
59	155.7	-118.8	-2.0	60	154.6	-21.2	1.4
61	124.9	-157.4	-0.3	62	42.7	-192.2	-20.5
63	-38.3	-202.3	-8.8	64	-103.6	-152.3	-16.4
65	209.3	-73.5	-9.2	66	197.5	-161.6	-2.9
67	115.4	-209.7	-1.5	68	29.2	-212.2	-25.1
69	187.7	-44.8	-18.1	70	194.9	8.9	-17.4
71	268.1	-125.4	-13.5	72	222.1	-256.9	-37.2
73	67.1	-305.3	-26.6	74	-109.1	-204.2	-22.3
75	-160.6	-160.3	-1.4	76	-56.5	-228.6	-25.3
77	-1.9	-182.6	-22.9	78	105.4	-179.7	0.1
79	-115.6	-287.1	-23.1	80	126.8	-160.8	-0.4
81	35.6	-335.8	-24.0	82	237.3	-99.9	-11.6
83	195.0	-124.4	-6.3	84	253.6	-59.1	-20.6
85	162.6	-194.1	-1.8	86	44.3	-275.6	-26.9
87	157.3	-141.4	-0.5	88	251.9	-178.8	-18.8
89	215.1	-208.3	-22.6	90	162.6	-239.9	-17.3
91	160.1	-272.3	-30.1	92	124.4	-284.3	-26.1
93	123.0	-239.4	-9.4	94	88.8	-213.1	-10.6
95	88.6	-257.0	-22.1	96	46.0	-227.4	-25.9
97	247.1	-282.9	-37.2	98	309.7	-242.5	-32.2
99	350.0	-218.5	-30.8	100	262.8	-230.7	-35.5
101	330.0	-198.2	-30.8	102	369.3	-188.1	-29.3
103	328.6	-138.2	-21.3	104	346.7	-105.1	-20.9
105	309.5	-60.5	-20.6	106	342.9	-61.9	-20.1
107	320.2	-3.8	-17.0	108	282.5	34.2	-16.3
CYGNUS II							
121	758.8	101.9	-9.6	122	820.1	58.6	0.0
123	643.0	126.3	10.9	124	709.0	76.6	0.0
125	753.9	18.2	-29.0	126	816.9	-24.2	0.0
127	559.0	46.2	15.9	128	622.5	9.5	0.0
129	682.1	-32.6	-21.1	130	747.0	-57.7	0.0

Counter	X (ft)	Y (ft)	Z (ft)	Counter	X (ft)	Y (ft)	Z (ft)
131	816.0	-108.2	-43.4	132	531.3	-33.7	0.0
133	594.5	-74.2	3.9	134	725.4	-141.5	-16.6
135	629.2	-132.6	-19.9	136	535.8	-139.4	-14.4
137	510.9	113.0	18.4	138	410.2	124.6	-37.6
139	447.3	12.3	12.3	140	482.0	19.8	8.3
141	348.8	106.2	8.3	142	391.2	70.2	-36.5
143	416.3	15.1	4.1	144	450.8	-30.1	11.2
145	485.5	-89.1	4.3	146	280.2	89.2	-41.1
147	338.9	59.2	-1.4	148	375.7	-22.6	-3.1
149	398.1	-80.2	-16.6	150	438.0	-91.7	14.9
151	418.0	-133.8	-14.0	152	474.2	-165.6	12.2
153	487.4	188.3	22.6	154	502.3	281.2	6.4
155	457.8	236.1	24.4	156	413.7	187.9	5.0
157	517.1	374.9	27.4	158	485.2	330.8	-11.1
159	423.2	299.2	26.5	160	381.9	236.2	-14.5
161	347.8	194.6	16.3	162	536.3	473.2	-2.9
163	518.0	431.3	27.5	164	446.7	388.7	-10.8
165	392.0	355.7	28.0	166	370.0	291.3	24.4
167	319.0	256.0	16.9	168	280.6	195.8	20.8
169	559.5	184.0	19.3	170	648.6	181.9	26.5
171	726.0	198.9	12.3	172	822.6	179.1	21.0
173	923.9	223.7	14.1	174	580.4	263.1	25.2
175	663.0	273.7	19.0	176	751.2	260.8	28.8
177	844.1	251.0	14.8	178	599.0	341.7	22.6
179	713.6	329.1	21.0	180	841.9	327.5	7.5
181	566.8	439.0	25.9	182	666.7	409.6	12.9
183	756.3	411.6	21.0	184	645.1	506.9	8.9
185	1041.3	176.5	8.9	186	1236.8	171.6	20.5
187	1133.0	220.2	7.4	188	1330.9	219.3	16.1
189	1044.5	272.1	12.1	190	1226.3	267.8	23.8
191	958.4	299.3	15.1	192	1133.2	327.4	18.4
193	1332.6	314.2	-2.3	194	1052.1	363.3	23.6
195	1240.6	396.4	-5.9	196	944.7	390.8	19.6
197	1121.6	431.0	1.1	198	849.6	449.1	2.5
199	1031.1	457.8	3.5	200	942.4	502.3	2.8
201	933.8	130.2	7.2	202	1122.8	126.7	5.0
203	1318.3	126.2	-0.3	204	1034.7	70.8	5.7
205	1229.7	73.0	-5.3	206	957.8	20.1	8.3
207	1132.8	13.7	-11.5	208	1312.6	33.4	12.4
209	1036.0	-51.2	-12.7	210	1230.8	-34.7	14.7
211	948.8	-102.4	-21.1	212	1146.0	-79.3	3.2
213	1071.3	-167.6	-31.3	214	1217.6	-148.0	2.4
215	938.9	-210.3	-25.2	216	1066.4	-262.3	-0.1

Table F.2: History of Major Detector Modifications

Date	Run	Change/Status
4/2/86	62	taping cuts: minimum of 1 detector with > 8 particles counters operational: 1-64, excluding 1,10,17,20,24,25,28 32,36-38,47,48,60
6/20/86	135	taping cuts: minimum of 8 detector with > 3 particles
6/30/86	144	counters 20,24,28,37 added
9/3/86	218	taping cuts: minimum of 9 detector with > 3 particles
10/1/86 -11/16/86	247 -296	E225 flash-chamber data available (smart triggers only)
12/6/86	319	counters 10,32,47,48 added
12/26/86 -1/12/87	340 -363	E225 flash-chamber data available (smart triggers only)
1/22/87	373	muon data from E645 available
1/23/87	374	taping cuts: minimum of 10 detector with > 2 particles
1/29/87	382	taping cuts: minimum of 7 detector with > 3 particles
1/30/87	383	counter 46 relocated
2/4/87	390	taping cuts: minimum of 7 detector with > 2 particles
2/20/87	406	taping cuts: minimum of 8 detector with > 2 particles
3/20/87	437	E225 flash-chamber data available (smart triggers only)
3/31/87	448	taping cuts: minimum of 6 detector with > 2 particles
4/1/87	450	counter 21 relocated
4/7/87	457	counter 46 relocated
4/28/87	477	TDCs replaced for counters 9-16
5/14/87	493	counter 60 relocated end of muon data from E645
6/16/87	529	counters 21,48 relocated
7/7/87 -10/4/87	550 -630	array calibration for ADC pedestals
7/9/87	552	ADC/TDC split changed from 1/4 to 1/7 for counters 49-64
7/9/87	555	ADC/TDC split changed from 1/4 to 1/7 for remaining counters
7/10/87	556	new pulse height conversions: counters 4,9,18,21,29,53,62
7/13/87	559	new pulse height conversions: counters 33,41
7/17/87	560	new pulse height conversions: counters 12,22,30,34,42,46,61,63
7/29/87	572	counter 42 removed

Date	Run	Change/Status
9/28/87	625	counters 21,24,28,36,48,59,61 relocated
10/4/87	630	array calibration for ADC pedestals
10/7/87	633	counters 64-96 added
10/9/87	637	counter 76 turned off
10/15/87	643	counter 76 turned back on
10/16/87	644	counters 75,76,81 recalibrated
10/19/87	647	counter 11 turned off
10/20/87	648	counter 1 turned back on
10/21/87	649	counter 11 recalibrated
10/23/87	652	counters 36,38 added
10/25/87	654	counter 39 TDC offset corrected
10/28/87	658	counters 17,25 added counter 46 recalibrated
10/29/87	659	counter 1 added counter 10 recalibrated and relocated
11/25/87	690	taping cuts: minimum of 8 detector with > 2 particles
11/26/87	691	taping cuts: minimum of 10 detector with > 2 particles
11/30/87	695	new ADC module for counters 85-96
12/4/87	700	counters 1-84 calibrated for pulse-height conversion
1/6/88	732	counters 85-96 calibrated for pulse-height conversion
1/26/88	750	end of E225 flash-chamber data
3/21/88	800	counters 85-96 calibrated for pulse-height conversion recalibration of TDC time-conversion factors
2/25/88	805	counter 18 relocated adjacent to counter 29
4/2/88	811	counter 18 returned to previous location
4/5/88	815	calibration of pulse-height conversion for counter 18
4/20/88	827	calibration of pulse-height conversion for counters 2,5,13
5/10/88	846	active TDC delays replaced by passive delays
5/22/88	860	new values of ADC pedestals values: counters 1-96
6/21/88	889	calibration of pulse-height conversion for counters 34,88
7/5/88	904	calibration of pulse-height conversion for counters: 71,74,76,77,80,81,82,86,96
7/6/88	905	calibration of pulse-height conversion for counter 49
7/13/88	912	counters 97-108 added, but not calibrated
7/21/88	920	counter 80 removed
7/26/88	926	counters 1,20,28,32,37,47 relocated
9/11/88	975	new values of pulse-height conversions: counters 1-108

Date	Run	Change/Status
10/23/88 -10/31/88	1030 -1040	new values of pulse-height conversions, ADC pedestals TDC offset adjustment due to change to passive delays
11/11/88	1054	counters 97-108 calibrated
12/1/88	1076	TDC offset adjustment for counters 81-88
1/10/89	1119	new values of ADC pedestals values: counters 1-96
3/9/89	1172	lead sheet on counter 18 (beginning of lead tests) counter 18 relocated adjacent to counter 29
3/10/89	1173	lead sheet on counter 29
3/16/89	1178	lead sheets removed from counters 18 and 29
3/17/89	1179	counter 18 moved back to previous location
5/22/89	1245	lead sheets on counters 4,11,18,46
5/23/89	1246	lead sheets on counters 61,67,78,85
5/24/89	1247	all lead sheets removed
5/31/89	1257	two layers of lead sheets on counters 4,46,11,18
6/1/89	1258	test deployment: lead sheets on 28 scattered counters
6/28/89	1289	lead sheets deployed on all counters
7/20/89	1315	installation of GPS satellite clock
9/7/89	1375	10-fold trigger, no additional taping cuts (25 Hz)
9/7/89	1376	12-fold trigger, no additional taping cuts (10Hz)
9/7/89	1377	10-fold trigger, taping cuts: 8 counters with > 1 particle
9/8/89	1378	taping cuts turned off (permanently), 12-fold trigger
9/9/89	1379	taping cuts turned back on
9/11/89	1382	taping cuts turned off
9/13/89	1385	20-fold trigger
11/7/89 -11/9/89	1446 -1448	CYGNUS I calibration
12/14/89	1484	CYGNUS II tests
12/18/89	1490	Anasazi muon information written to tape
1/9/90	1516	counter 71 moved and turned off
1/25/90	1532	counter 71 replaced
2/15/90	1555	E645 muon detector installed
3/14/90	1586	data now written to Exabyte instead of magtape automated "run-handler" now operating (~5 runs/day)
3/15/90	1599	triggers from both CYG I and CYG II (with Anasazi info)
3/19/90	1620	CYGNUS II permanantly turned on
4/17/90 -4/19/90	1737 -1743	CYGNUS I calibration

Date	Run	Change/Status
5/4/90	1804	Anasazi calibration
5/7/90	1815	automatic "watchdog timer" calling unit installed
5/10/90	1830	counters 80 and 97 calibrated
5/15/90	1854	counter 70 relocated
5/24/90	1889	E645 muon detector now also triggered by CYGNUS II
8/28/90 -8/29/90	2246 -2250	CYGNUS I calibration
8/30/90	2254	water-Cherenkov test pool in data stream
10/17/90	2419	end of E645 muon data
10/20/90	2429	"morgue" muon counters installed in old E645 location
10/31/90	2469	"morgue" muon information in data stream
12/14/90	2626	"morgue" muon counters calibrated
4/9/91 -4/10/91	3055 -3058	CYGNUS II calibration
4/16/91 -4/17/91	3075 -3081	CYGNUS I calibration
5/3/91	3141	counter 103 calibrated
5/14/91 -5/16/91	3182 -3192	water-Cherenkov pool tests
10/9/91	3730	CYGNUS I calibration
10/15/91	3755	CYGNUS II calibration
12/13/91	3976	5 water-Cherenkov pools in data stream

Appendix G

Calculation of Flux Limits

*"**outcome**, n. a particular type of dissapointment."*

- Ambrose Bierce -

Limits on the Number of Expected Signal Events

The observed number of on-source events compared to the number expected for pure background can be used to derive an upper limit for the maximum number of expected signal events that would be consistent with the signal hypothesis at a given confidence level. This has been accomplished by first defining the *source probability density function* as follows:

$$G(S) = \int_0^\infty P(N_{on}|S+B)P(B_{off}|B)dB \qquad \text{(G.1)}$$

where S is the average number of source events seen at the earth (this is the parameter that we ultimately wish to set a limit on); B is the average background level; N_{on} is the total number of events observed in the on-source bin; and B_{off} is the average background level inferred from off-source bins. $P(N_{on}|S+B)$ is the probability that the number of expected events is $S+B$, given the observation N_{on}. $P(B_{off}|B)$ is thus the probability that the true, average, background level is B, given the observation B_{off}. These probabilities are simply given according to Poisson statistics as follows:

$$P(N_{on}|S+B) = \frac{e^{-(S+B)}(S+B)^{N_{on}}}{N_{on}!} \qquad \text{(G.2)}$$

and

$$P(B_{off}|B) = \frac{e^{-\beta}\beta'}{(\beta')!} \tag{G.3}$$

where $\frac{1}{\alpha}$ is the number of off-source bins used to find the average B_{off} (the same definition as that of Li and Ma [75]); $\beta = \frac{B}{\alpha}$; and $\beta' = \frac{B_{off}}{\alpha}$. Since the actual background level is not known, the integral in equation G.1 is over all possible background scenarios, weighted by the probability for that scenario, given the observation B_{off}.

The upper limit is then calculated by finding the value of S such that

$$1 - \mathrm{CL} = \frac{\int_S^\infty G(S)dS}{\int_0^\infty G(S)dS} \tag{G.4}$$

where CL is the desired confidence level, and the integral probability on the right-hand side is normalized over the space of all possible source hypotheses. Note that this follows the so-called "Baysian" approach [137] [138], which finds the value of S_{lim} such that 100 × CL% of the source strengths that would result in N_{on} or less are bounded by S_{lim}. In contrast, the Classical philosophy attempts to find a value of S_{lim} in a manner that would correctly bound the true value of S 100 × CL% of the time, if the experiment were to be repeated. In fact, as will be discussed below, the two approaches are equivalent. Therefore, the value of S_{lim} is unambiguous.

There has been much discussion in the literature regarding whether the calculation of an upper limits should be couched as a "Classical" or a "Baysian" question. Much of this discussion is based on a fundamental misconception, since questions are neither truely "Classical" or "Baysian." The approach used to answer a particular question may be couched either in terms of a sum over possible measurements ("Classical"), or in terms of a sum over possible source models ("Baysian"). Bayes theorem states that the two approaches are *equivalent*. The value derived for S_{lim} must be the same for either approach, since descrepancies cannot result from a philosophical difference in the statement of the same question. Typically, the reason for apparent descrepancies lay in an improper generalization of the Classical approach from the zero-background case. However, Zech has shown that a properly normalized Classical approach yields identical answers to the Baysian method [139].

Returning to equation G.4, following a suitable change of variables and repeated application of the following integral (obtained by repeated integration by

parts):

$$\int_A^\infty e^{-x}x^m dx = e^{-A}m!\sum_{i=0}^{m}\frac{A^i}{i!} \tag{G.5}$$

one obtains [140]:

$$1 - \mathrm{CL} = \frac{\beta}{\gamma} \tag{G.6}$$

where

$$\beta = e^{-S_{lim}}\sum_{i=0}^{N_{on}}\sum_{j=0}^{i}\frac{i!}{j!(i-j)!}\left[S_{lim}^{i-j}(\frac{\alpha}{1+\alpha})^j\right]\left[\frac{(j+\frac{B_{off}}{\alpha})!}{i!}\right] \tag{G.7}$$

and

$$\gamma = \sum_{i=0}^{N_{on}}\left[(\frac{\alpha}{1+\alpha})^i!\right]\left[\frac{(i+\frac{B_{off}}{\alpha})!}{i!}\right] \tag{G.8}$$

For a given value of confidence level, CL, the value of S_{lim} can then be found through a standard root-finding algorithm.

Conversion to a Flux Limit

A confidence level of 90% has been chosen for quoting flux limits. Following the prescription previously described, the value of S_{lim} can be converted to a 90% confidence limit on the fraction of on-source events that could be attributed to signal by simply dividing by N_{on}. The limit on gamma-ray source flux can then be expressed as:

$$\Phi_{lim} = \frac{S_{lim}}{N_{on}} \times \frac{\Phi_{CR}\Omega}{0.72R_\gamma} \tag{G.9}$$

where Φ_{CR} is the all-particle cosmic ray flux; Ω is the solid angle subtended by the source bin; R_γ is a correction factor to account for the relative efficiency for triggering on gamma-induced showers versus typical background showers above a given energy; and the value of 0.72 accounts for the fact that the bin size chosen should contain 72% of the signal, on average.

Recent measurements by the JACEE collaboration [134], indicate an integral background cosmic-ray flux of:

$$\Phi_{CR} = (1.8 \pm 0.5) \times 10^{-5} {E_{TeV}}^{-1.76\pm0.09} cm^{-2}s^{-1}sr^{-1} \tag{G.10}$$

Simulations (Appendix A) indicate that the median energy of triggered events has changed from ~130 TeV to ~70 TeV throughout the course of the experiment. For consistency, fluxes will be quoted above an energy of 100 TeV throughout this thesis.

Source bins typically subtend a solid angle of $\Omega = 1.2 \times 10^{-3} sr$, and simulations indicate an average value for R_γ of ~2.5 for sources at the declination of Her X-1.

Appendix H

Generalized *A Priori* Hypothesis Weighting

"Was the choice a priori ? Mmmmmmmm...
I'd rather not answer that question."
- An Anonymous Astrophysicist -

Chapter 5 discusses a method of placing calculated probabilities for various hypotheses in context by ranking emission scenarios according to *a priori* theoretical or experimental biases. When choosing the most significant result from a number of hypothesis tests, a more general procedure can be employed to account for the assignment of *a priori* weights of arbitrary value to each hypothesis.

Consider the set of chance probabilities:

$$P_1, P_2, ...P_n \tag{H.1}$$

corresponding to the tests of n hypotheses. Assign to these hypotheses the relative rankings

$$\alpha_1, \alpha_2 ... \alpha_n \tag{H.2}$$

where the rankings are expressed as a fraction of the total number of hypotheses, so that $\sum_i \alpha_i = 1$. Larger values of α correspond to more probable hypotheses. We now wish to redistribute the total number of trials (1 for each hypothesis) according to the the assigned ranks. Specifically, the number of trials assigned to a given hypothesis

should be inversly proportional to its rank, so that fewer trials are assessed for the more likely hypotheses. This is accomplished by defining a set of new quantities:

$$Q_1, Q_2, ...Q_n \tag{H.3}$$

where

$$Q_i = 1 - (1 - P_i)^{\frac{1}{a_i n}} \tag{H.4}$$

The smallest value of Q is then selected (corresponding to the most significant rank-corrected result), and a trial factor is assessed for the total number of hypotheses considered (n). The final chance probability is then given by:

$$P_f = 1 - (1 - Q)^n = 1 - (1 - (1 - (1 - P)^{\frac{1}{an}}))^n = 1 - (1 - P)^{\frac{1}{a}} \tag{H.5}$$

While the Q values are *not* distributed as proper probabilities under the null hypothesis (*i.e.* uniformly between 0 and 1), the P_f values are.

In practice, there is rarely enough detailed information to warrant the degree of ranking for VHE/UHE studies that this method is capable of providing. The simpler, diagramatic approach discussed in chapter 5 is therefore recommended for most applications. However, the technique presented here may be useful for analyses such as correlation studies, where the results for one set of data are used to rank tests to be performed in another, independent set of data.

Bibliography

[1] M. Samorski and W. Stamm, *Proc. of 18th Int'l Conf. on Cosmic Rays* (Banglore), **11**, 244 (1983)

[2] J. Lloyd-Evans *et al.*, Nature, **305** , 784 (1983)

[3] B. L. Dingus *et al.*, Phys. Rev. Lett., **61** (17), 1906 (1988)

[4] R. C. Lamb *et al.*, Ap. J. Lett., **328**, L13 (1988)

[5] L. K. Resvanis *et al.*, Ap. J. Lett., **328**, L9 (1988)

[6] R. J. Protheroe, Proc. 20th Int'l Cosmic Ray Conf., **8**, 21 (1988)

[7] T. C. Weekes *et al.*, Ap. J., **342**, 379 (1989)

[8] T. C. Weekes *et al.*, IAU Circular No. 5522 (1992)

[9] P. T. Reynolds *et al.*, Ap. J., **382**, 640 (1991)

[10] J. P. Ostriker and J. E. Gunn, Phys. Rev. Lett., **22**, 728 (1969)

[11] P. Goldreich and W. H. Julian, Ap. J., **157**, 869 (1969)

[12] N. I. Shakura and R. A. Sunyaev, Astr. and Ap., **24**, 337 (1973)

[13] P. Ghosh and F. K. Lamb, Ap. J. Lett., **223**, L83 (1978)

[14] A. K. Harding, *Arkansas Gamma-Ray and Neutrino Workshop '89*, Nuc. Phys. B (Proc. Suppl.), **14A**, ed. G. B. Yodh, D. C. Wold and W. R. Kropp (North-Holland), 3 (1990)

[15] P. A. Sturrock, Ap. J., **164**, 529 (1971)

[16] M. A. Ruderman and P. G. Sutherland, Ap. J., **196**, 51 (1975)

[17] K. S. Cheng, C. Ho and M. A. Ruderman, Ap. J., **300**, 500 (1986)

[18] R. V. E. Lovelace, Nature, **262**, 649 (1976)

[19] R. D. Blandford, *The Galactic Center*, ed. G. R. Riegler and R. D. Blandford (AIP: New York) 177 (1982)

[20] G. Chanmugam and K. Brecher, Nature, **313**, 767 (1985)

[21] M. A. Ruderman *et al.*, Ap. J., **343**, 292 (1989)

[22] E. Fermi, Ap. J., **119**, 1 (1954)

[23] D. Eichler and W. T. Vestrand, Nature, **318**, 345 (1985)

[24] P. Kiraly and P. Meszaros, Ap. J., **333**, 719 (1988)

[25] D. Kazanas and D. C. Ellison, Nature, **319**, 380 (1986)

[26] A. K. Harding and T. K. Gaisser, Ap. J., **358**, 561 (1990)

[27] J. I. Katz and I. A. Smith, Ap. J., **326**, 733 (1988)

[28] E. Fermi, Phys. Rev., **75**, 1169 (1949)

[29] Y. M. Wang, Ap. Space Sci., **121**, 193 (1986)

[30] E. Schrier *et al.*, Ap. J. Lett., **172**, L79 (1972)

[31] H. Tannanbaum *et al.*, Ap. J. Lett., **174**, L143 (1972)

[32] J. Trümper *et al.*, Ap. J. Lett., **219**, L105 (1978)

[33] H. Ögelman, *et al.*, Space Science Reviews, **40**, 347 (1985)

[34] J. E. Deeter, P. E. Boynton and S. H. Pravdo, Ap. J., **247**, 1003 (1981)

[35] J. Middleditch and J. Nelson, Ap. J., **208**, 567 (1976)

[36] R. Staubert, M. Bezler and E. Kendziorra, Astr. and Ap., **117**, 215 (1983)

[37] R. Giacconi *et al.*, Ap. J., **184**, 227 (1973)

[38] F. K. Lamb, C. J. Pethick and D. Pines, Ap. J., **184**, 271 (1973)

[39] J. E. Pringle and M. J. Rees, Astr. and Ap., **21**, 1 (1972)

[40] M. Gil'fanov *et al.*, Sov. Astron. Lett., **15**, 4 (1989)

[41] A. Fabian, J. Pringle and M. Rees, Nature, **244**, 212 (1973)

[42] B. Cooke and C. Page, Nature, **256**, 712 (1975)

[43] C. Jones and W. Forman, Ap. J. Lett., **209**, L131 (1976)

[44] J. I. Katz, Nature Phys. Sci., **246**, 87 (1973)

[45] J. W. Roberts, Ap. J., **187**, 575 (1974)

[46] J. A. Petterson, Ap. J. Lett., **201**, L61 (1975); Ap. J., **218**, 783 (1977)

[47] K. Brecher, Nature, **239**, 325 (1972)

[48] D. Pines, C. J. Pethick and F. K. Lamb, Sixth Texas Symposium on Relativistic Astrophysics (1972)

[49] D. Q. Lamb *et al.*, Ap. J. Lett., **198**, L21 (1975)

[50] J. Trümper *et al.*, Ap. J. Lett., **300**, L63 (1986)

[51] A. N. Parmar *et al.*, Nature, **313**, 119 (1985).

[52] F. Nagase *et al.*, *Proc. Am. Inst. Phys. Conf.*, ed. S. Woosley, **115**, 131 (1983)

[53] R. Meyhandan *et al.*, Ap. J., **391**, 236 (1992)

[54] J. N. Bahcall and N. A. Bahcall, Ap. J. Lett., **178**, L1 (1972)

[55] W. Forman, C. A. Jones and W. Liller, Ap. J. Lett., **177**, L103 (1972)

[56] A. Davidsen *et al.*, Ap. J. Lett., **177**, L97 (1972)

[57] J. Middleditch, C. R. Pennypacker and M. S. Burns, Ap. J., **274**, 313 (1983)

[58] J. Middleditch, Ap. J., **275**, 278 (1983)

[59] D. E. Alexandreas *et al.*, Nucl. Instr. and Meth. in Phys. Research, **A311**, 350 (1992)

[60] G. W. Clark, F. Scherb and W. B. Smith, Review of Scientific Instruments, **28 (6)**, 433 (1957)

[61] R. C. Allen *et al.*, Phys. Rev. Lett., **55**, 2401 (1985)

[62] R. C. Allen *et al.*, Nucl. Instr. and Meth. in Phys. Research, **A311**, 368 (1992)

[63] B. L. Dingus, Ph.D. thesis, University of Maryland, Los Alamos report no. LA-11431-T (1988)

[64] J. Glenn and G. Allen, CYGNUS internal memo (in preparation).

[65] R. J. Protheroe, Astr. Express, **1**, 137 (1985); Proc. 20th Int'l Cosmic Ray Conf., **3**, 485

[66] D. A. Lewis, R. C. Lamb and S. D. Biller, Ap. J., **369**, 479 (1991)

[67] W. T. Eadie, "Statistical Methods in Experimental Physics," Cambridge University Press, New York (1971)

[68] R. A. Fisher, *Statistical Methods for Research Workers*, (Oliver and Boyd: Edinburgh and London) (1958)

[69] D. A. Lewis, *Arkansas Gamma-Ray and Neutrino Workshop '89*, Nuc. Phys. B (Proc. Suppl.), **14A**, ed. G. B. Yodh, D. C. Wold and W. R. Kropp (North-Holland), 299 (1990)

[70] D. E. Alexandreas *et al.*, Phys. Rev. D, **43**, 1735 (1991)

[71] G. L. Cassiday *et al.*, Phys. Rev. Lett., **62**, 383 (1989)

[72] D. E. Alexandreas *et al.*, Ap. J. Lett., **383**, L53 (1991)

[73] D. E. Alexandreas *et al.*, Ap. J. (to be published)

[74] J. Matthews *et al.*, Nucl. Phys. Proc. Suppl., **14A**, 211 (1990)

[75] T. P. Li and Y. Q. Ma, Ap. J., **272**, 317 (1983)

[76] S. S. Wilks, *Mathematical Statistics*, (John Wiley and Sons: New York) (1962)

[77] D. E. Alexandreas *et al.*, submitted to Ap. J.

[78] D. E. Alexandreas *et al.*, submitted to Nucl. Instr. and Meth. in Phys. Research

[79] M. Potter, CYGNUS internal memo No. 25

[80] K. V. Mardia, *Statistics of Directional Data*, (London: Academic) (1972)

[81] J. A. Greenwood and D. Durand, Ann. Math. Stat., **26**, 233 (1955)

[82] J. L. Uretsky, Nucl. Instr. and Meth. in Phys. Research, **A300**, 351 (1991)

[83] R. Bucceri, *Proc. of the Workshop on Tech. in U.H.E. Gamma-Ray Astr.* (La Jolla), 98 (1985)

[84] O. C. De Jager, Ph.D. thesis, Potchefstroom University (1987)

[85] O. C. De Jager, J. W. H. Swanepoel and B. C. Raubenheimer, Astr. and Ap. **221**, 180 (1989)

[86] J. Middleditch, R. C. Puetter and C. R. Pennypacker, Ap. J., **267**, 313 (1987)

[87] P. W. Gorham, Ph.D. thesis, University of Hawaii (1986)

[88] K. J. Orford, Exper. Astr., **1**, 305 (1991)

[89] J. Middleditch, Ph.D. thesis, LBL Report No. 3639 (1975)

[90] P. O. Slane, Ph.D. thesis, University of Wisconsin (1988)

[91] M. O. Stephens, Journal of Royal Stat. Soc., **B32**, 115 (1970)

[92] J. C. Dowthwaite *et al.*, Nature, **309**, 691 (1984)

[93] P. M. Chadwick *et al.*, *Proc. NATO Workshop on Very High Energy Gamma-Ray Astronomy*, ed. K. E. Turver (Dordrecht: Reidel) **199**, 121 (1987)

[94] S. K. Gupta *et al.*, Ap. J. Lett., **354**, L13 (1990)

[95] M. E. Ash, I. I. Shapiro and W. B. Smith, Astr. and Ap., **72**, 338 (1967)

[96] S. K. Gupta and S. C. Tonwar, J. Phys. G, **17**, 1271 (1991)

[97] S. K. Gupta and S. C. Tonwar, private communication

[98] H. S. Rawat *et al.*, Proc. 21st Int'l Cosmic Ray Conf., **2**, 104 (1990)

[99] P. R. Vishwanath *et al.*, Ap. J., **342**, 489 (1989)

[100] R. M. Baltrusaitis *et al.*, Ap. J. Lett., **293**, L69 (1985)

[101] J. W. Elbert, private communication

[102] P. M. Chadwick *et al.*, *Proc. 19th Int'l Cosmic Ray Conf.* (La Jolla), **1**, 251 (1985)

[103] **M. F.** Cawley *et al.*, Ap. J., **296**, 185 (1985)

[104] **A. M.** Hillas, *Proc. 19th Int'l Cosmic Ray Conf.* (La Jolla), **3**, 445 (1985)

[105] M. F. Cawley *et al.*, *Proc. 19th Int'l Cosmic Ray Conf.* (La Jolla), **3**, 453 (1985)

[106] L. K. Resvanis *et al.*, Nucl. Instr. and Meth. in Phys. Research, **A269**, 297 (1988)

[107] C. Sinnis, private communication.

[108] P. T. Reynolds, Ph.D. thesis, University College Dublin (1989)

[109] J. Collins *et al.*, Phys. Rev. D, **39**, 1318 (1989)

[110] G. Domokos and S. Nussinov, Phys. Lett. B, **187**, 372 (1987)

[111] G. Domokos and S. Kovesi-Domokos, Phys. Rev. D, **38**, 2833 (1988)

[112] S. Mrenna, Phys. Rev. D, **45**, 2371 (1992)

[113] S. Karakula and J. Wdowzcyk, Acta Phys. Pol., **23**, 231 (1963)

[114] J. Procureur and J. Stamenov, J. Phys. G, **13**, 1579 (1987)

[115] M. Drees and F. Halzen, Phys. Rev. Lett., **61**, 275 (1988)

[116] D. Duke and J. Owens, Phys. Rev. D, **26**, 1600 (1982)

[117] M. Drees and K. Grassie, Z. Phys. C, **28**, 451 (1985)

[118] T. Gaisser *et al.*, Phys. Lett. B, **243**, 444 (1990)

[119] D. Krakauer, private communication

[120] H. Abramowicz *et al.*, Phys. Lett., **B269**, 465 (1991)

[121] J. Middleditch, private communication.

[122] K. S. Cheng and M. A. Ruderman, Ap. J. Lett., **337**, L77 (1989)

[123] P. Slane and W. Fry, Ap. J., **342**, 1129 (1989)

[124] F. Aharonian and A. Atoyan, Ap. J., **381**, 220 (1991)

[125] J. A. Wrotniak, *SHOWERSIM/85,* Department of Physics, University of Maryland

[126] W. O. Nelson, H. Hirayama and D. W. O. Rogers, *The EGS4 Code System,* SLAC Report 265, December 1985

[127] A. M. Hillas, *Proc. 19th Int'l Cosmic Ray Conf.* (Paris), **8**, 193 (1981)

[128] K. Greisen, Ann. Rev. of Nuc. Sci., **10**, 63 (1960)

[129] K. Kamata and J. Nishimura, Suppl. Prog. Theoret. Phys., **6**, 93 (1958)

[130] S. D. Biller, G. B. Yodh and R. C. Lamb, *Proc. 22nd Int'l Cosmic Ray Conf.* (Dublin), **1**, 520 (1991)

[131] RCA type number C31034.

[132] R. W. Engstrom, *Photomultiplier Handbook*, RCA, 1980

[133] K. A. Ispirian, A. T. Margarian and A. M. Zverev, Nuclear Instruments and Method, 117 (1974) p. 125-129

[134] T. H. Burnett *et al.*, Ap. J. Lett., **383**, L53 (1991)

[135] A. M. Hillas and J. Lapikens, *Proc. 15th Int'l Cosmic Ray Conf.* (Plovdiv), 8, 460 (1977)

[136] W. H. Press *et al.*, *Numerical Recipes*, (Cambridge University Press: New York) (1986)

[137] O. Helene, Nucl. Instr. and Meth. in Phys. Research, **212**, 319 (1983)

[138] R. J. Protheroe, Astr. Express, **1**, 33 (1984)

[139] G. Zech, Nucl. Instr. and Meth. in Phys. Research, **A277**, 608 (1989)

[140] **C. Sinnis, internal** CYGNUS memo (in preparation)

Bibliography
(alphabetical)

[120] H. Abramowicz *et al.*, Phys. Lett., **B269**, 465 (1991)

[124] F. Aharonian and A. Atoyan, Ap. J., **381**, 220 (1991)

[70] D. E. Alexandreas *et al.*, Phys. Rev. D, **43**, 1735 (1991)

[72] D. E. Alexandreas *et al.*, Ap. J. Lett., **383**, L53 (1991)

[73] D. E. Alexandreas *et al.*, Ap. J. (to be published)

[78] D. E. Alexandreas *et al.*, submitted to Nucl. Instr. and Meth. in Phys. Research

[59] D. E. Alexandreas *et al.*, Nucl. Instr. and Meth. in Phys. Research, **A311**, 350 (1992)

[77] D. E. Alexandreas *et al.*, submitted to Ap. J.

[61] R. C. Allen *et al.*, Phys. Rev. Lett., **55**, 2401 (1985)

[62] R. C. Allen *et al.*, Nucl. Instr. and Meth. in Phys. Research, **A311**, 368 (1992)

[95] M. E. Ash, I. I. Shapiro and W. B. Smith, Astr. and Ap., **72**, 338 (1967)

[54] J. N. Bahcall and N. A. Bahcall, Ap. J. Lett., **178**, L1 (1972)

[100] R. M. Baltrusaitis *et al.*, Ap. J. Lett., **293**, L69 (1985)

[130] S. D. Biller, G. B. Yodh and R. C. Lamb, *Proc. 22nd Int'l Cosmic Ray Conf.* (Dublin), **1**, 520 (1991)

[19] R. D. Blandford, *The Galactic Center*, ed. G. R. Riegler and R. D. Blandford (AIP: New York) 177 (1982)

[47] K. Brecher, Nature, **239**, 325 (1972)

[83] R. Bucceri, *Proc. of the Workshop on Tech. in U.H.E. Gamma-Ray Astr.* (La Jolla), 98 (1985)

[134] T. H. Burnett *et al.*, Ap. J. Lett., **383**, L53 (1991)

[71] G. L. Cassiday *et al.*, Phys. Rev. Lett., **62**, 383 (1989)

[103] M. F. Cawley *et al.*, Ap. J., **296**, 185 (1985)

[105] M. F. Cawley *et al.*, *Proc. 19th Int'l Cosmic Ray Conf.* (La Jolla), **3**, 453 (1985)

[102] P. M. Chadwick *et al.*, *Proc. 19th Int'l Cosmic Ray Conf.* (La Jolla), **1**, 251 (1985)

[93] P. M. Chadwick *et al.*, *Proc. NATO Workshop on Very High Energy Gamma-Ray Astronomy*, ed. K. E. Turver (Dordrecht: Reidel) **199**, 121 (1987)

[20] G. Chanmugam and K. Brecher, Nature, **313**, 767 (1985)

[17] K. S. Cheng, C. Ho and M. A. Ruderman, Ap. J., **300**, 500 (1986)

[122] K. S. Cheng and M. A. Ruderman, Ap. J. Lett., **337**, L77 (1989)

[60] G. W. Clark, F. Scherb and W. B. Smith, Review of Scientific Instruments, **28 (6)**, 433 (1957)

[109] J. Collins *et al.*, Phys. Rev. D, **39**, 1318 (1989)

[42] B. Cooke and C. Page, Nature, **256**, 712 (1975)

[56] A. Davidsen *et al.*, Ap. J. Lett., **177**, L97 (1972)

[34] J. E. Deeter, P. E. Boynton and S. H. Pravdo, Ap. J., **247**, 1003 (1981)

[84] O. C. De Jager, Ph.D. thesis, Potchefstroom University (1987)

[85] O. C. De Jager, J. W. H. Swanepoel and B. C. Raubenheimer, Astr. and Ap., **221**, 180 (1989)

[63] B. L. Dingus, Ph.D. thesis, University of Maryland, Los Alamos report no. LA-11431-T (1988)

[3] B. L. Dingus *et al.*, Phys. Rev. Lett., **61** (17), 1906 (1988)

[111] G. Domokos and S. Kovesi-Domokos, Phys. Rev. D, **38**, 2833 (1988)

[110] G. Domokos and S. Nussinov, Phys. Lett. B, **187**, 372 (1987)

[92] J. C. Dowthwaite *et al.*, Nature, **309**, 691 (1984)

[117] M. Drees and K. Grassie, Z. Phys. C, **28**, 451 (1985)

[115] M. Drees and F. Halzen, Phys. Rev. Lett., **61**, 275 (1988)

[116] D. Duke and J. Owens, Phys. Rev. D, **26**, 1600 (1982)

[67] W. T. Eadie, "Statistical Methods in Experimental Physics," Cambridge University Press, New York (1971)

[23] D. Eichler and W. T. Vestrand, Nature, **318**, 345 (1985)

[101] J. W. Elbert, private communication

[132] R. W. Engstrom, *Photomultiplier Handbook*, RCA, 1980

[41] A. Fabian, J. Pringle and M. Rees, Nature, **244**, 212 (1973)

[28] E. Fermi, Phys. Rev., **75**, 1169 (1949)

[22] E. Fermi, Ap. J., **119**, 1 (1954)

[68] R. A. Fisher, *Statistical Methods for Research Workers*, (Oliver and Boyd: Edinburgh and London) (1958)

[55] W. Forman, C. A. Jones and W. Liller, Ap. J. Lett., **177**, L103 (1972)

[118] T. Gaisser *et al.*, Phys. Lett. B, **243**, 444 (1990)

[37] R. Giacconi *et al.*, Ap. J., **184**, 227 (1973)

[40] M. Gil'fanov *et al.*, Sov. Astron. Lett., **15**, 4 (1989)

[64] J. Glenn and G. Allen, CYGNUS internal memo (in preparation).

[11] P. Goldreich and W. H. Julian, Ap. J., **157**, 869 (1969)

[87] P. W. Gorham, Ph.D. thesis, University of Hawaii (1986)

[13] P. Ghosh and F. K. Lamb, Ap. J. Lett., **223**, L83 (1978)

[81] J. A. Greenwood and D. Durand, Ann. Math. Stat., **26**, 233 (1955)

[136] W. H. Press *et al.*, *Numerical Recipes*, (Cambridge University Press: New York) (1986)

[94] S. K. Gupta *et al.*, Ap. J. Lett., **354**, L13 (1990)

[96] S. K. Gupta and S. C. Tonwar, J. Phys. G, **17**, 1271 (1991)

[128] K. Greisen, Ann. Rev. of Nuc. Sci., **10**, 63 (1960)

[97] S. K. Gupta and S. C. Tonwar, private communication

[14] A. K. Harding, *Arkansas Gamma-Ray and Neutrino Workshop '89*, Nuc. Phys. B (Proc. Suppl.), **14A**, ed. G. B. Yodh, D. C. Wold and W. R. Kropp (North-Holland), 3 (1990)

[26] A. K. Harding and T. K. Gaisser, Ap. J., **358**, 561 (1990)

[137] O. Helene, Nucl. Instr. and Meth. in Phys. Research, **212**, 319 (1983)

[135] A. M. Hillas and J. Lapikens, *Proc. 15th Int'l Cosmic Ray Conf.* (Plovdiv), **8**, 460 (1977)

[127] A. M. Hillas, *Proc. 19th Int'l Cosmic Ray Conf.* (Paris), **8**, 193 (1981)

[104] A. M. Hillas, *Proc. 19th Int'l Cosmic Ray Conf.* (La Jolla), **3**, 445 (1985)

[133] K. A. Ispirian, A. T. Margarian and A. M. Zverev, Nuclear Instruments and Methods, 117 (1974) p. 125-129

[43] C. Jones and W. Forman, Ap. J. Lett., **209**, L131 (1976)

[129] K. Kamata and J. Nishimura, Suppl. Prog. Theoret. Phys., **6**, 93 (1958)

[25] D. Kazanas and D. C. Ellison, Nature, **319**, 380 (1986)

[113] S. Karakula and J. Wdowzcyk, Acta Phys. Pol., **23**, 231 (1963)

[44] J. I. Katz, Nature Phys. Sci., **246**, 87 (1973)

[27] J. I. Katz and I. A. Smith, Ap. J., **326**, 733 (1988)

[24] P. Kiraly and P. Meszaros, Ap. J., **333**, 719 (1988)

[119] D. Krakauer, private communication

[49] D. Q. Lamb *et al.*, Ap. J. Lett., **198**, L21 (1975)

[38] F. K. Lamb, C. J. Pethick and D. Pines, Ap. J., **184**, 271 (1973)

[4] R. C. Lamb *et al.*, Ap. J. Lett., **328**, L13 (1988)

[69] D. A. Lewis, *Arkansas Gamma-Ray and Neutrino Workshop '89*, Nuc. Phys. B (Proc. Suppl.), **14A**, ed. G. B. Yodh, D. C. Wold and W. R. Kropp (North-Holland), 299 (1990)

[66] D. A. Lewis, R. C. Lamb and S. D. Biller, Ap. J., **369**, 479 (1991)

[75] T. P. Li and Y. Q. Ma, Ap. J., **272**, 317 (1983)

[18] R. V. E. Lovelace, Nature, **262**, 649 (1976)

[2] J. Lloyd-Evans *et al.*, Nature, **305** , 784 (1983)

[80] K. V. Mardia, *Statistics of Directional Data*, (London: Academic) (1972)

[74] J. Matthews *et al.*, Nucl. Phys. Proc. Suppl., **14A**, 211 (1990)

[53] R. Meyhandan *et al.*, Ap. J., **391**, 236 (1992)

[89] J. Middleditch, Ph.D. thesis, LBL Report No. 3639 (1975)

[121] J. Middleditch, private communication.

[35] J. Middleditch and J. Nelson, Ap. J., **208**, 567 (1976)

[58] J. Middleditch, Ap. J., **275**, 278 (1983)

[57] J. Middleditch, C. R. Pennypacker and M. S. Burns, Ap. J., **274**, 313 (1983)

[86] J. Middleditch, R. C. Puetter and C. R. Pennypacker, Ap. J., **267**, 313 (1985)

[112] S. Mrenna, Phys. Rev. D, **45**, 2371 (1992)

[52] F. Nagase *et al.*, *Proc. Am. Inst. Phys. Conf.*, ed. S. Woosley, **115**, 131 (1983)

[126] W. O. Nelson, H. Hirayama and D. W. O. Rogers, *The EGS4 Code System*, SLAC Report 265, December 1985

[33] H. Ögelman, *et al.*, Space Science Reviews, **40**, 347 (1985)

[88] K. J. Orford, Exper. Astr., **1**, 305 (1991)

[10] J. P. Ostriker and J. E. Gunn, Phys. Rev. Lett., **22**, 728 (1969)

[51] A. N. Parmar *et al.*, Nature, **313**, 119 (1985).

[46] J. A. Petterson, Ap. J. Lett., **201**, L61 (1975); Ap. J., **218**, 783 (1977)

[48] D. Pines, C. J. Pethick and F. K. Lamb, Sixth Texas Symposium on Relativistic Astrophysics (1972)

[79] M. Potter, CYGNUS internal memo No. 25

[39] J. E. Pringle and M. J. Rees, Astr. and Ap., **21**, 1 (1972)

[114] J. Procureur and J. Stamenov, J. Phys. G, **13**, 1579 (1987)

[138] R. J. Protheroe, Astr. Express, **1**, 33 (1984)

[65] R. J. Protheroe, Astr. Express, **1**, 137 (1985); Proc. 20th Int'l Cosmic Ray Conf., **3**, 485 (1988)

[6] R. J. Protheroe, Proc. 20th Int'l Cosmic Ray Conf., **8**, 21 (1988)

[98] H. S. Rawat *et al.*, Proc. 21st Int'l Cosmic Ray Conf., **2**, 104 (1990)

[131] RCA type number C31034.

[5] L. K. Resvanis *et al.*, Ap. J. Lett., **328**, L9 (1988)

[106] L. K. Resvanis *et al.*, Nucl. Instr. and Meth. in Phys. Research, **A269**, 297 (1988)

[108] P. T. Reynolds, Ph.D. thesis, University College Dublin (1989)

[9] P. T. Reynolds *et al.*, Ap. J., **382**, 640 (1991)

[45] J. W. Roberts, Ap. J., **187**, 575 (1974)

[1] M. Samorski and W. Stamm, *Proc. of 18th Int'l Conf. on Cosmic Rays* (Banglore), **11**, 244 (1983)

[12] N. I. Shakura and R. A. Sunyaev, Astr. and Ap., **24**, 337 (1973)

[107] C. Sinnis, private communication.

[140] C. Sinnis, internal CYGNUS memo (in preparation)

[16] M. A. Ruderman and P. G. Sutherland, Ap. J., **196**, 51 (1975)

[21] M. A. Ruderman *et al.*, Ap. J., **343**, 292 (1989)

[30] E. Schrier *et al.*, Ap. J. Lett., **172**, L79 (1972)

[90] P. O. Slane, Ph.D. thesis, University of Wisconsin (1988)

[123] P. Slane and W. Fry, Ap. J., **342**, 1129 (1989)

[36] R. Staubert, M. Bezler and E. Kendziorra, Astr. and Ap., **117**, 215 (1983)

[91] M. O. Stephens, Journal of Royal Stat. Soc., **B32**, 115 (1970)

[15] P. A. Sturrock, Ap. J., **164**, 529 (1971)

[31] H. Tannanbaum *et al.*, Ap. J. Lett., **174**, L143 (1972)

[32] J. Trümper *et al.*, Ap. J. Lett., **219**, L105 (1978)

[50] J. Trümper *et al.*, Ap. J. Lett., **300**, L63 (1986)

[82] J. L. Uretsky, Nucl. Instr. and Meth. in Phys. Research, **A300**, 351 (1991)

[99] P. R. Vishwanath *et al.*, Ap. J., **342**, 489 (1989)

[29] Y. M. Wang, Ap. Space Sci., **121**, 193 (1986)

[7] T. C. Weekes *et al.*, Ap. J., **342**, 379 (1989)

[8] T. C. Weekes *et al.*, IAU Circular No. 5522 (1992)

[76] S. S. Wilks, *Mathematical Statistics*, (John Wiley and Sons: New York) (1962)

[125] J. A. Wrotniak, *SHOWERSIM/85*, Department of Physics, University of Maryland

[139] G. Zech, Nucl. Instr. and Meth. in Phys. Research, **A277**, 608 (1989)